## *A study of particles close to the core of extensive air showers using a flash tube chamber*

Cooper, D. A.

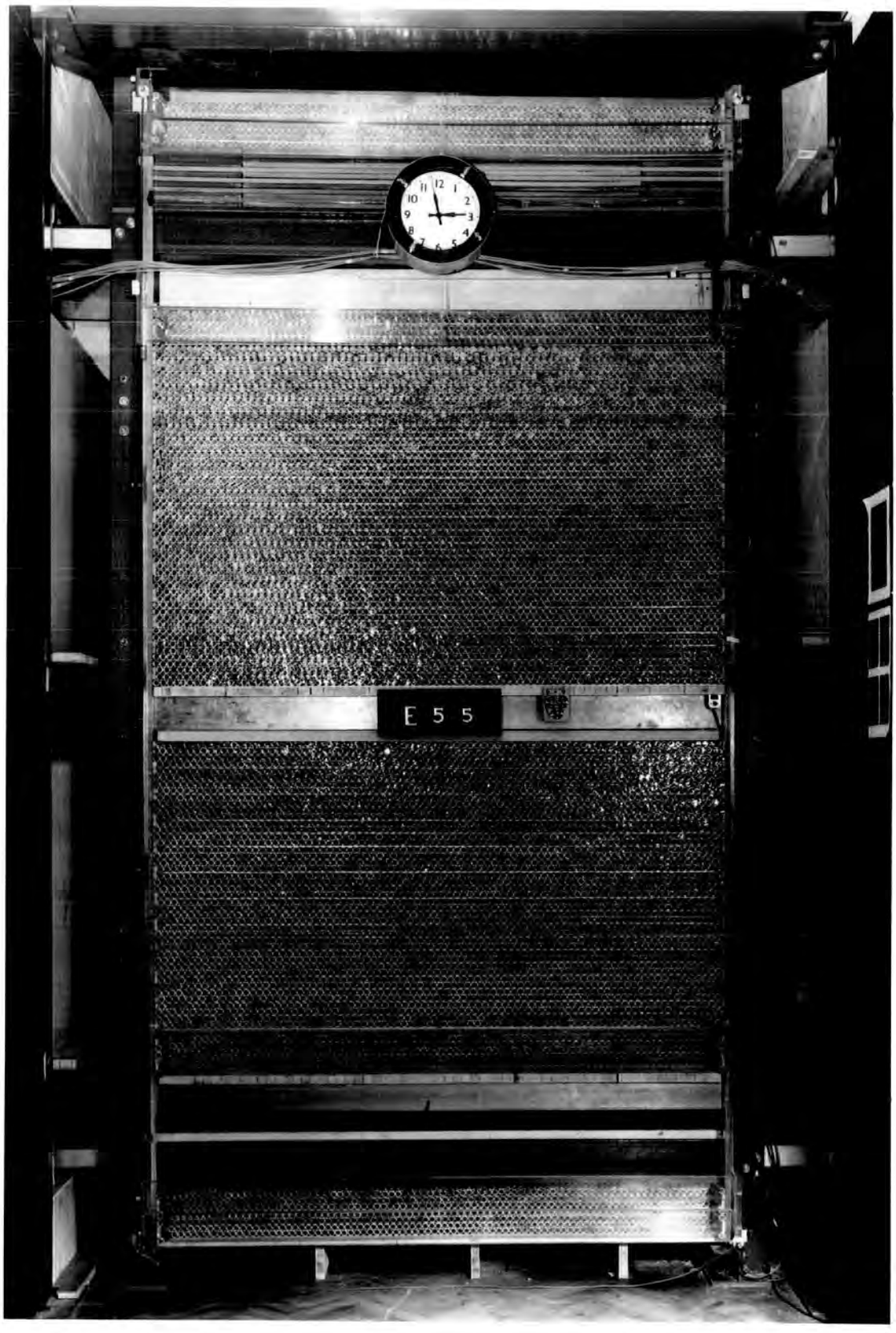
E 5 5

PLATE 1

FRONTISPIECE

FRONT VIEW OF THE FLASH TUBE CHAMBER

# A STUDY OF PARTICLES CLOSE TO THE CORE OF EXTENSIVE AIR SHOWERS USING A FLASH TUBE CHAMBER

by

D. A. Cooper, B.Sc.

A thesis submitted to the

University of Durham

for the Degree of Doctor of Philosophy

September 1974

CONTENTS

## ABSTRACT

A search for particles carrying an electric charge one third that of the electronic charge (quarks) has been carried out close to the core of extensive air showers. The search was conducted at sea-level using a large volume flash tube chamber. The technique employed utilised the sensitivity of flash tubes to particle ionisation. Air showers were selected by requiring the local electron density above the detector to exceed 40 $m^{-2}$. With this trigger the apparatus has been operated for 2570 hours. No definite quark tracks have been observed, the upper limit on the quark flux being set at $8.0 \times 10^{-11}$ $cm^{-2} sec^{-1} st^{-1}$.

In the same experiment, the energy spectra of charged and neutral nuclear-active particles in extensive air showers of mean shower size $2.0 \times 10^{5}$ has been measured. A method has been developed for estimating the energies of the particles from the width of the nuclear-electromagnetic cascade resulting from the interactions, as measured in flash tubes below the absorbers. The results have been related to extensive air shower characteristics, in particular to the nuclear-physical aspects of very high energy collisions.

The flash tube chamber has been modified to allow the relationship between the width of the nuclear-electromagnetic cascade and the energy of the interacting particle to be established. The experiment, utilising the flux of unaccompanied hadrons in the near-vertical direction, has also allowed the energy spectrum of these particles to be determined up to energies of 1TeV.

## PREFACE

This thesis describes the work performed by the author in the Physics Department of the University of Durham while he was a Research Student under the supervision of Dr. F. Ashton.

A large volume flash tube chamber has been used to study particles close to the core of extensive air showers. In particular, a search for quarks has been carried out and a study of hadrons has been performed.

The author has shared with his colleagues the collection of data, and for some parts of the work the data reduction and analysis, and has been responsible for the calculations and data interpretation described in the thesis.

The quark search has been reported by Ashton et.al. (1973a). Other aspects of the work have also been reported:- Ashton et.al. (1973 b,c, d,e,f,g, and h).

# CHAPTER 1

# INTRODUCTION

## 1.1 Historical background

The beginning of the twentieth century saw many advances in the field of physics. Thomson had discovered the electron in 1897 and the alpha-particle scattering experiments of Geiger and Marsden had led Rutherford to postulate the nuclear model of the atom in 1911. A coherent picture of atomic structure was emerging (although there were still many problems to be solved). The photoelectric effect had provided evidence for the quantisation of energy, which led to great advances in theoretical physics.

One instrument which had played an important part in experimental work of the period was the electrometer, a charge-sensitive device capable of detecting ionising radiation. It had been noticed by several workers that a charged electrometer would discharge slowly, in the absence of any of the radioactive sources used in experiments and without irradiation by ultra-violet light. Indeed, the discharge occurred even if the electrometer was sealed in a light-tight lead-lined container. It was shown by Hess in 1912 that the ionising radiation responsible for this effect was not due totally to natural radioactivity in the earth, by flying a balloon containing electrometers to a height of several kilometers. The ionisation was seen to decrease initially as the effect of the earth's radioactivity decreased, but then increased significantly at greater heights. It was argued, however, that this could be due not to external radiation, but to radioactive gases high in the atmosphere or the effects of thunderstorms. It was Millikan, who in a series of experiments from 1923 to 1926, proved beyond doubt that the radiation really was external to the earth. By studying the amount of ionisation as a function of depth below water in lakes at different altitudes he

was able to show that the decrease in the radiation with increasing depth could only be explained in terms of a downward flux of ionising radiation which he called "cosmic rays".

Since the only types of radiation known at that time were $\alpha$, $\beta$, and $\gamma$ radiation, the cosmic rays were assumed initially to be high energy photons, since $\alpha$ and $\beta$ rays would be unable to traverse the whole atmosphere. Geomagnetic effects showed that this was not the case. A world-wide survey organised by Compton, at sea-level and at mountain altitudes, showed that the intensity decreased as the equator was approached, consistent with the radiation being composed of charged "corpuscles" rather than photons. It had been predicted, from calculations by Stormer on the trajectories of charged particles in magnetic fields, that if the primary particles were of predominantly one charge then there should be an asymmetry in the flux of particles in the east-west direction. In 1933, several experiments found evidence for this effect, there being an excess from the west. This implied that the primaries were mainly positive particles, presumably protons.

An effect first noticed by Rossi in 1932 (Rossi, 1932, 1933a and 1933b) was the high coincidence rate which occurred when two or more Geiger-Muller (GM) tubes were placed side by side below an absorber of say, lead. Important results found by Rossi were that the rate of coincidences was greater below lead than below the same amount of absorber (in $g.cm.^{-2}$) of iron or aluminium. The ratio's found for these rates were, for lead: iron: aluminium, 4:2:1 respectively. In addition, as the thickness of absorber was increased the rate of coincidences first increased rapidly until a maximum was reached, after which there was a slow decrease as more absorber was added. This was the first observation of the electron-photon cascade.

The understanding of this cascade process relied upon another discovery in cosmic rays, by Anderson. This was the positron, Dirac's postulated "positive electron" - the antiparticle of the electron.

Dirac's theory predicted that positrons and electrons should be produced in pairs, as had been observed in cloud chambers when photons of high energy passed through dense absorbers. Oppenheimer studied the process and concluded that this "pair production" by photons took place in the field of a nucleus, and Bethe and Heitler were able to produce a full theory of the process. With the understanding of this effect and also that of the radiative loss of electrons (bremstrahlung) which Bethe and Heitler also produced a theory to explain, the cascade process could to a large extent be understood. If a photon, say, is incident on a dense absorber, it will after some distance produce an electron-positron pair. The positron will either annihilate (at low energies) or, like the electron, will radiate photons. These photons in turn will produce more electron-positron pairs, and this process will continue until a cascade of particles and photons builds up. The cascade dies out when the electrons and positrons have insufficient energy to produce photons efficiently and their energy is dissipated in excitation of the atomic electrons. The Compton effect was also known at this time, and could be included in the cascade theory, but as a low energy effect, was realised not to be of primary importance. This cascade theory was first developed by Bhabha and Heitler. The process has assumed considerable importance in high energy particle physics since its discovery, as a method of detecting particles and estimating their energy.

Thus the cascades could be understood, but it was not until the discovery of muons by Neddermeyer and Anderson in 1937 that the uncertainty regarding the origin of the cascades was removed. The muons were measured to have a mass of approximately 200 electron masses, and on the average were found to occur in almost equal numbers as positive and negative particles. This charge ratio implied that the muons were secondary particles (confirmed when their short lifetime was discovered), and this implied that the primary positive particles were interacting in the atmosphere to produce these secondaries. It was realised that large

numbers of particles might be produced in these interactions, and that the cascade processes observed in dense materials could also occur in air. Now it had been noticed that coincidences occurred sometimes between detectors placed large distances apart, and led Auger (1938) to undertake an examination of this effect. This led to the discovery of extensive air showers (EAS). Auger found that the showers consisted mainly of electrons, up to $10^6$ particles being present in a single shower, spread over distances of hundreds of metres. In addition, he found that the showers contained a core of very high energy particles which were capable of producing large cascades below layers of lead.

We now know that EAS consist of three main components: electrons, muons, which constitute about 1% of the total number of particles and extend to even greater distances than the electrons, and a core of strongly interacting particles such as pions, protons (and antiprotons), neutrons (and antineutrons) and kaons.

Using cosmic rays much was learned about nuclear physics. The discovery of the neutron by Chadwick in 1932 in a series of laboratory experiments with radioactive materials had already produced a deeper understanding of atomic structure. In the cosmic radiation the phenomenon of associated production and the existence of "strange" particles was discovered in experiments conducted by Rochester and Butler (1947). The pi-meson was discovered by Lattes, Occhialini and Powell in 1947 when this group exposed nuclear emulsion plates to cosmic rays at mountain altitudes and observed the decay of pions into muons (the dominant process for the production of the muons seen at sea-level). The pion was later associated with the Yukawa particle, the theoretical particle predicted to explain the binding force between nucleons. Nuclear interactions were seen in nuclear emulsions, the study of these yielding a great deal of information. Up to the present day, cosmic rays have played an important part in the study of high energy physics. Recently accelerators have extended the energy region over which they can study

interactions to energies of the order of $10^{12}$ eV (ISR), and in this region they are capable of superior measurements owing to the high fluxes available. Thus it has become necessary for cosmic ray physicists wishing to investigate nuclear physics to concentrate on very high energy interactions.

Cosmic rays have been useful in providing information of astrophysical significance. By flying balloons with nuclear emulsion payloads to great heights, and more recently using satellites, it has been possible to study the primary cosmic radiation directly up to energies of $10^{12}$ - $10^{13}$ eV/nucleon. The primary particles are found to be mainly protons, but with small numbers of heavier nuclei extending up to uranium and perhaps beyond (Fowler et al. 1973). In addition, weak fluxes of $\gamma$-rays and electrons have been found to exist. The mass composition has yielded important information on the history of the cosmic radiation, its origin and subsequent passage through space. The amount of fragmentation which occurs can be related to the age of the cosmic rays and provide information not only on the source of cosmic rays but also on the magnetic fields through which they have travelled. However, while much has been learned by studying the primary particles, their origin is not yet established. Information at higher energies than those accessible to balloon or satellite measurements is needed. The limitations on detector size do not allow primaries of energy much greater than $10^{12}$eV to be studied. This is because of the steeply falling energy spectrum (the intensity decreases as $E^{-2.6}$ from $10^{12}$ eV to $3.10^{15}$ eV and $E^{-3.2}$ above $3.10^{15}$ eV). Thus above this energy indirect measurements have been used. These include estimation of the spectrum from sea-level fluxes of muons at intermediate energies ($10^{12}$-$10^{14}$ eV) and the study of extensive air showers at higher energies. These indirect methods rely on a knowledge of the interaction processes occurring in the atmosphere. Questions that remain to be answered include : What is the primary composition in this very high energy region, and does the energy spectrum

cut-off at about $10^{20}$ eV., due to interactions with the 2.7°K background radiation?

Very large EAS arrays have been built to record the highest energy showers, and at the present time the highest energies reached correspond to about $10^{20}$ eV, with no indication of a cut-off, although techniques are being developed which could improve the situation; in particular the observation of atmospheric Cerenkov and scintillation light, produced as the air showers propagate through the atmosphere.

However, the energies available in smaller air showers are still far in excess of those at accellerators, and these showers, while not being frequent, are much more so than the larger showers. Thus these smaller showers are suitable for studying very high energy nuclear-physical processes. In addition, the mass composition of the primary particles at these energies is still unknown, and information would be very valuable in helping to answer some of the questions posed by astrophysics.

## 1.2 The Quark Search

Science attempts to explain the physical world by unifying facts deduced from observations. It attempts, in other words, to reduce the number of independent variables in a system to a few, more fundamental ones. Thus if an underlying law or symmetry can be found to combine a set of variables, the system can be more accurately described, and hence the scientist's understanding of the system has increased. In just this way, the discovery that matter is composed of molecules, that molecules are made up of numbers of atoms, and that atoms consist of a few "elementary" particles, have all been advances in knowledge.

Now while the discovery of the constituents of atoms has greatly clarified the physicist's picture of the world, over the past 30 years the number of these elementary particles known has increased rapidly. Thus it is natural to ask :- Is there an underlying symmetry from which all of these particles can be constructed? One attempt to explain the

structure of elementary particles along these lines is the Quark theory, discussed in Chapter 3 of this thesis, which postulates three fundamental particles, quarks, to be the basic building blocks of matter. Because of the obvious importance of determining whether these quarks really exist, an experiment, described in Chapter 4, has been carried out to search for these particles in the secondary cosmic radiation. For reasons discussed in Chapter 3, the search was carried out close to the core of EAS, assuming the quarks, if they exist, to be produced in the very high energy interactions of the primary cosmic rays with the atmosphere. Chapter 2 describes the experimental arrangement of the flash tube chamber used in the search.

## 1.3 Nuclear-active Particles in EAS

As was mentioned earlier, at the very highest energies the flux of cosmic ray particles is too low for direct observation of their nuclear interactions. They can be detected, however, by the extensive air showers which result, and a study of the secondary hadrons at sea-level can yield information about the interaction characteristics. The energy spectra and relative numbers of the different components of the hadron flux are related to their production mechanisms. In addition, it might be expected that a study of these parameters might yield information on the primary mass composition.

Therefore, the flash tube chamber has been used to study these particles in extensive air showers, using the method of measuring the cascades produced when the hadrons interact in lead and iron absorbers. A technique has been developed for estimating the energy of the interacting particle which involves measuring the width of the cascade below the absorber. In Chapter 5 the theory of these cascades is developed, enabling the number of cascade particles produced below the absorber to be related to the energy of the interacting particle. Chapter 6 describes the experimental determination of the relationship between the number of cascade particles present and the width of the cascade. For

this determination, the flux of unaccompanied hadrons at sea-level, in the near-vertical direction, was utilised.

Chapter 7 describes the results obtained in the EAS experiment and also the analysis and subsequent interpretation of those results in terms of the shower properties mentioned.

# CHAPTER 2

# THE FLASH TUBE CHAMBER AND EXTENSIVE AIR SHOWER EXPERIMENT

## 2.1 Introduction

The flash tube chamber described below is primarily a visual detector of cosmic ray particles at sea-level. It enables the tracks of individual particles to be observed, and records the interactions which these particles undergo in the chamber - much as a cloud chamber does, but without the limitations on the sensitive volume usually imposed on cloud chambers.

The flash tube chamber selection mechanisms allow single penetrating particles to be observed, or alternatively Extensive Air Showers (E.A.S.) in which the local electron density above the chamber exceeds a preselected value.

## 2.2 The Flash Tube Chamber

### 2.2.1 Experimental Arrangement

In Figure 2.1 can be seen a scale diagram of the flash tube chamber. A total of 10748 flash tubes have been incorporated. These are cylindrical soda glass envelopes filled with Neon gas (98%) and Helium gas (2%) to a pressure of 60 cms. Hg. Each tube is 2 metres in length, of mean internal diameter 1.58 cms. and mean external diameter 1.78 cms. Alternate layers contain 84 and 85 tubes, the tube positions being staggered with respect to the ajoining layers. Every tube is covered with polythene sleeving to inhibit light transfer to neighbouring tubes.

Above every second layer of tubes are aluminium electrodes, 0.122 cms. in thickness, 3.3 cms apart. In the section F2 and F3 (Figure 2.1) the area of the electrodes is 2.94 $m^2$, while in F1a, F1b, F4a and F4b the electrodes are shorter in depth by 30 cms, and cover an area of 2.48 $m^2$.

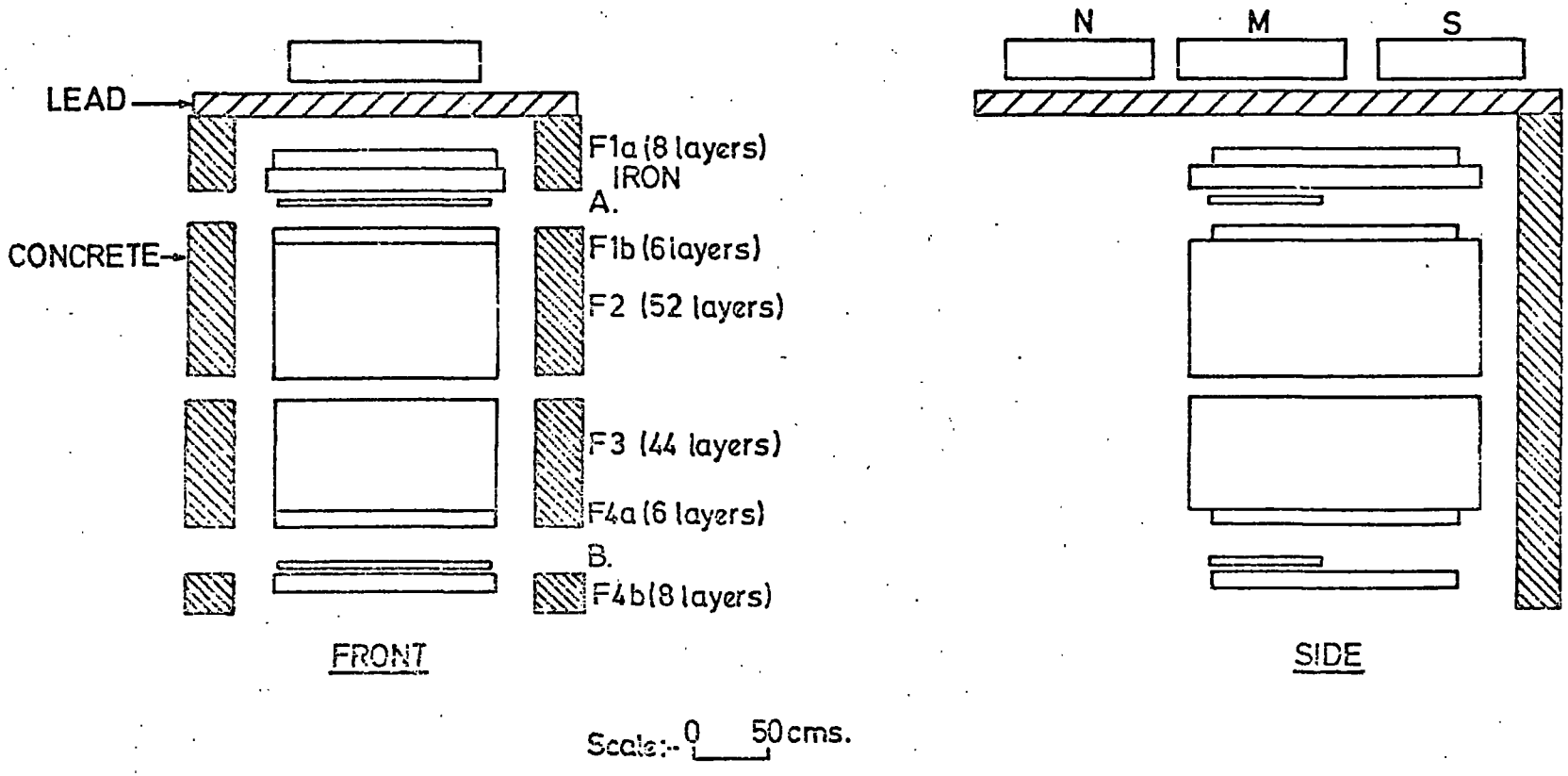


Figure 2.1 Scale diagram of the flash tube chamber.

The 15 cms. of steel situated between F1a and F1b allows electromagnetic bursts to be studied in the chamber, identification of the parent particle being possible in F1a. It also helps in the identification of penetrating particles.

Directly below the iron, and also below F4a, are the plastic scintillators A and B, of area 1.05$m^2$ and thickness 5 cms., each viewed by five 53AVP photomultiplier tubes and one 56AVP tube (Figure 2.2). These two scintillators, in coincidence, were used to select single penetrating particles (muons).

The steel plates, flash tubes and plastic scintillators are contained in an inner framework of steel girders, while around the chamber itself is a larger enclosure consisting of 30 cm. thick walls of barytes concrete and a roof of 15 cm. of lead supported by steel plates of thickness 1.3 cms. This absorber is designed to cut out the soft component (electrons) in extensive air showers while allowing penetrating particles to pass through the chamber.

Above the lead are three large liquid scintillators which form the air shower selection system. These scintillators (Figure 2.3) are each of area 1.24 $m^2$, depth 15 cms., and are each viewed by two EMI 9583B photomultiplier tubes.

The whole chamber is light-tight, allowing the use of a camera without a shutter. This means that the camera is continuously sensitive, the film being wound on by one frame after each event.

2.2.2 The High Voltage Pulsing System

When a trigger occurs a high voltage pulse must be applied to the electrodes, creating the necessary electric field across the neon flash tubes such that in tubes containing ionisation due to the recent passage of a charged particle, the neon gas will break down and a visible discharge will occur in the tube.

This high voltage pulse is produced by the circuitry shown in Figure 2.4. The 5 volt trigger pulse is used to trigger a thyristor, producing an output of +300 volts. This pulse is fed into a high voltage pulse transformer, the output of which produces the trigger

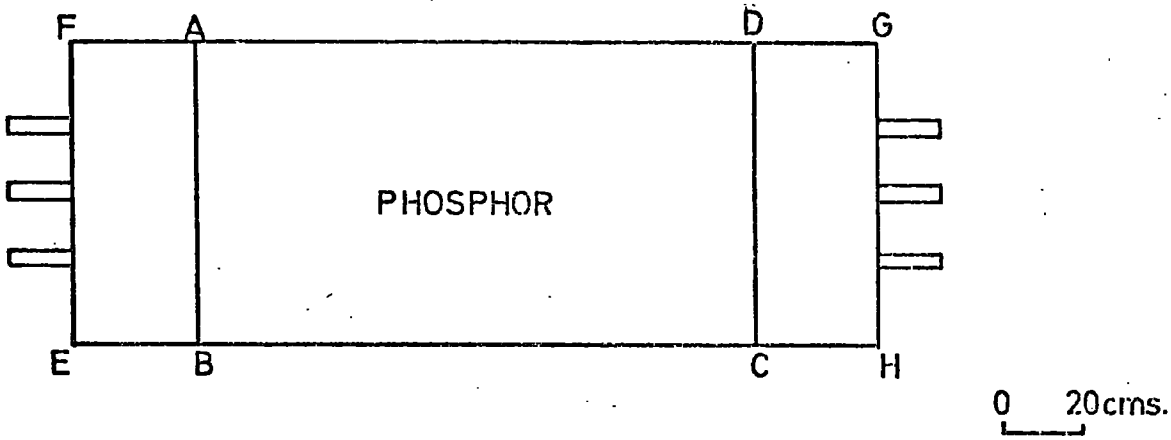


A B C D = Plastic scintillator
A B E F, C D G H = Perspex light guides

Figure 2.2. A plastic scintillation counter

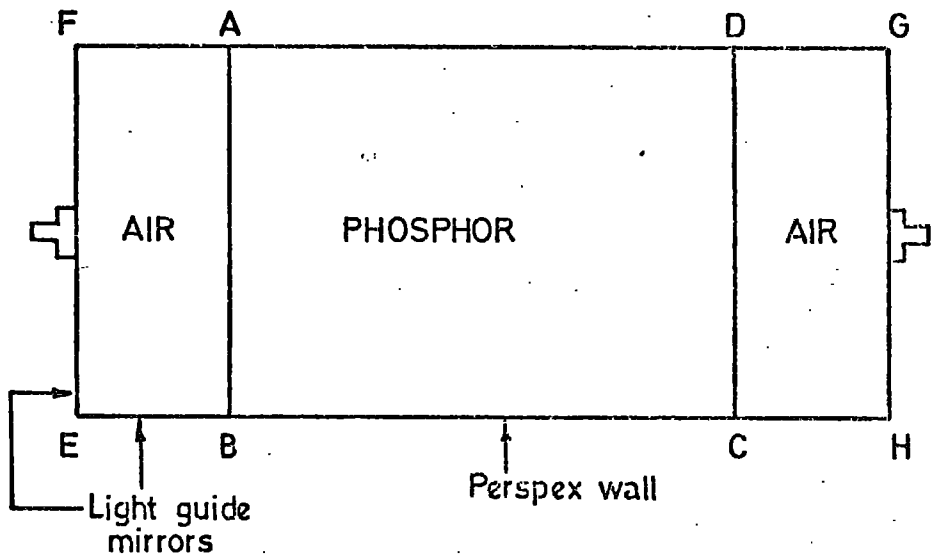


Figure 2.3. A liquid scintillation counter

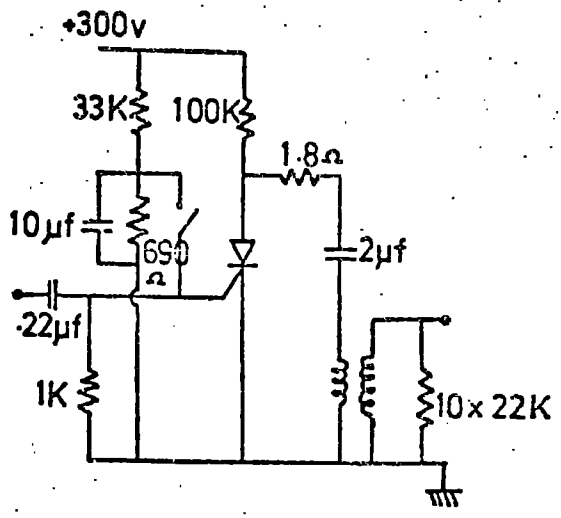


Figure 2.4. H.T. Pulsing Unit

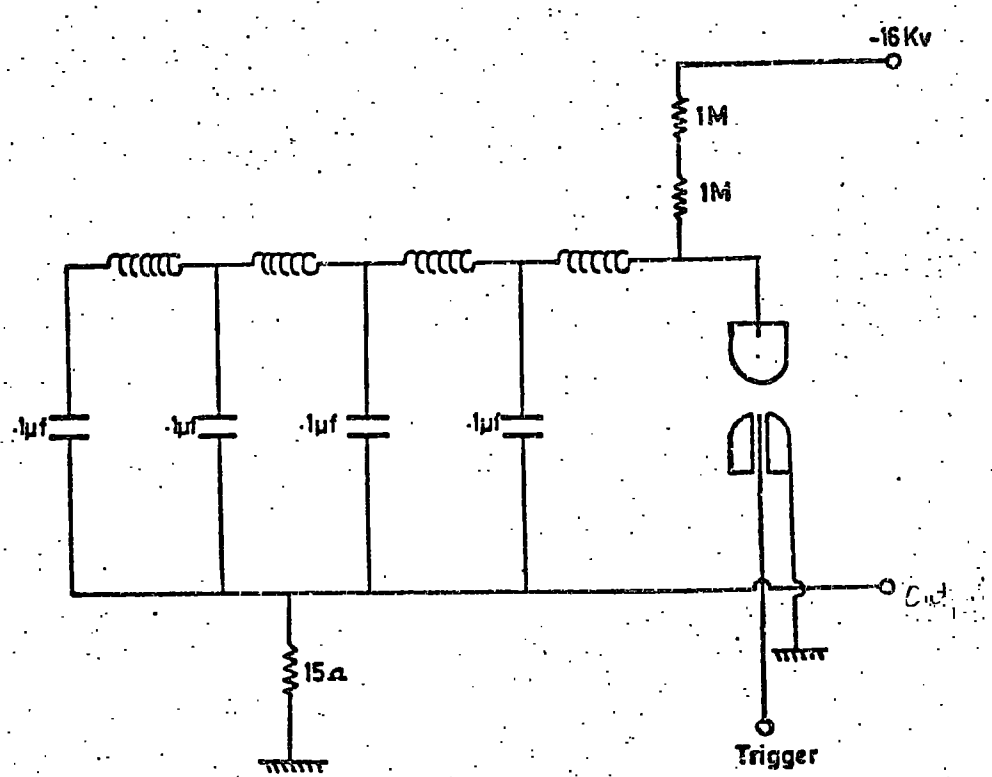


Figure 2.5. Spark gap and delay line

pulse for the "Trigatron" spark gap.

A voltage of 16 kV. is applied across the main spark gap, the trigger spark causing the gap to break down largely by the production of photoelectrons (Sletten and Lewis, 1956).

The pulse applied to the electrodes is approximately rectangular, of height 8 kV. and length 10 $\mu$S. It is produced by the circuit shown in Figure 2.5. When the main gap of the Trigatron breaks down, the lumped circuit transmission line discharges through its characteristic impedence, producing a rectangular pulse for a time $2n\sqrt{LC}$ (for n. identical L, C stages (Elmore and Sands, 1949)). The transmission line employed has four elements, each of capacitance $C = 0.1\,\mu F$ and of inductance $L = 22\,\mu H$. The capacity of the flash tube chamber which this unit supplies is $0.087\,\mu F$.

2.2.3 Properties of Flash Tubes

An ionising particle passing through a flash tube produces along its track positive ions, electrons and excited gas atoms. Lloyd (1960), has discussed the problem and concludes that only the electrons which are produced initially can cause the discharge. He concludes that positive gas ions and metastable neon atoms do not contribute to the probability of a discharge occurring, and similarly the resonance and non-resonance photons produced can have little or no effect.

Lloyd sets up diffusion equations for the electrons produced, and solves them for the probability of a discharge occurring if a high voltage pulse is applied to the tube a time $T_D$ after traversal by the ionising particle. He expresses the probability of a discharge occurring (the internal efficiency) as a function of $D.T_D/a^2$ (where D is the diffusion coefficient of thermal electrons and a the internal radius of the tube) with a $F_1\ Q_1$ as a parameter, $F_1$ being the probability that a single electron produces an avalanche (independent of position) and $Q_1$ the probability per unit track length of the

primary particle producing a free electron. The term $Q_1$ is thus the only parameter dependent on the charge of the particle, and is related to the ionisation loss of the particle in the gas, a function of the square of the electric charge. This forms the basis of the use of the flash tube chamber in the search for quarks, since the term $a F_1 Q_1$ is 1/9th. (for a quark of charge e/3) of that for a charge e particle.

Hence the internal efficiency variation has been calculated (for the flash tubes used in the chamber) as a function of time delay, and is shown in Figure 2.6. In order to determine the best value of the parameter $af_1Q_1$, single muons were selected by the plastic scintillators A and B in coincidence (Figure 2.7), and the tracks were photographed in the flash tubes for different time delays.

2.2.4 Determination of the Efficiency-Time Delay Function

In order to determine the internal efficiency of a flash tube for a particle of charge e, single muons were allowed to traverse the sensitive volume of the chamber, defined as the 96 layers of flash tubes comprising F2 + F3. As mentioned above, the muons were selected by the coincidence arrangement shown in Figure 2.7.

When a trigger occurs and a high voltage pulse is applied across the flash tubes, a cycling system is set into operation which triggers microswitches controlling fiducial lights on the chamber, illumination for the clock, and also the winding on of the camera film. This operation lasts for approximately 7 seconds, which is also long enough to allow the high voltage pulsing unit to recover. It was found convenient to impose a dead time of 30 seconds after each event, this dead-time being applied by means of an RC - controlled decay circuit which switched a relay, earthing the signal line.

The time delay $T_D$ was varied, and a series of events were photographed at each $T_D$.

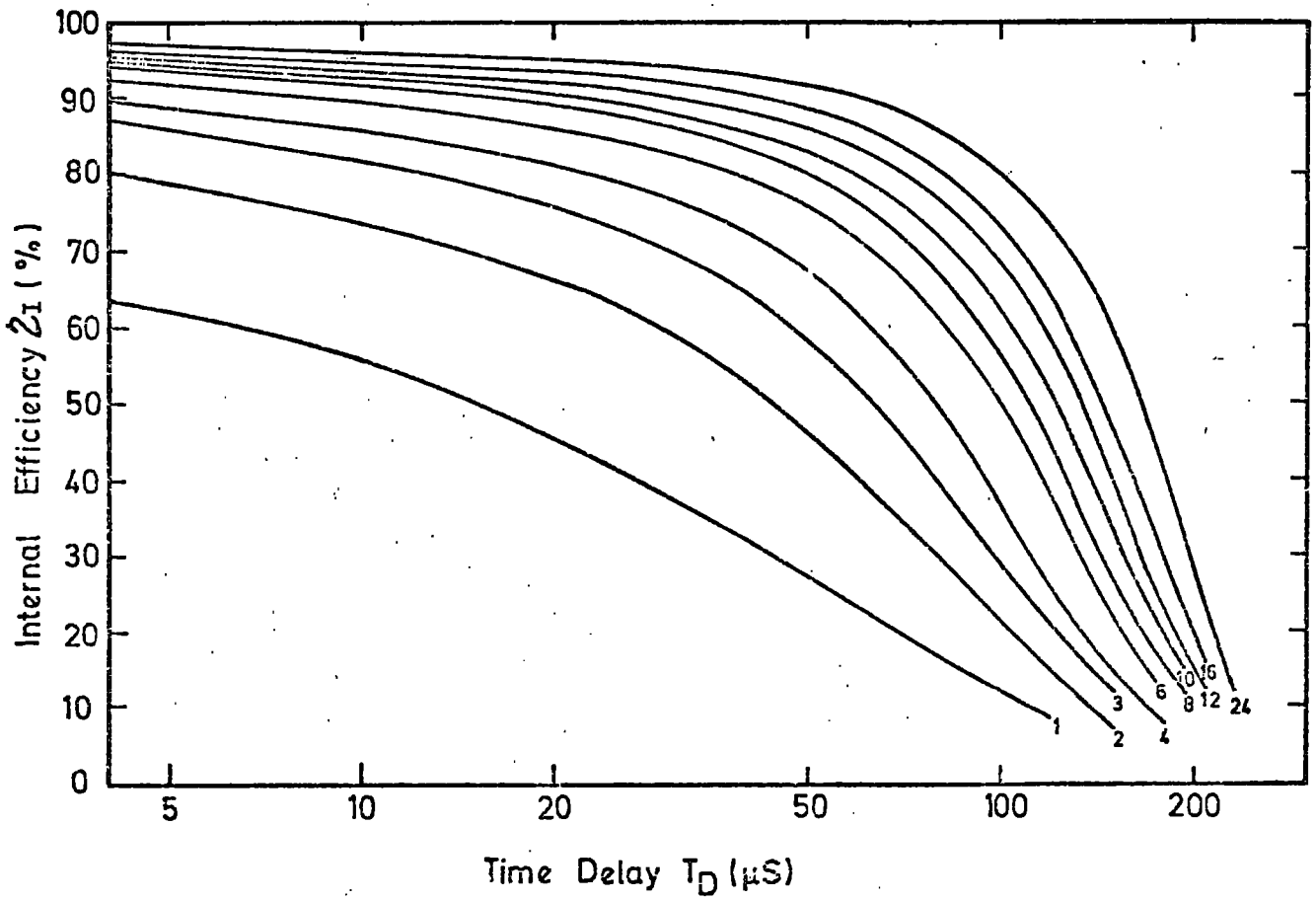


Figure 2.6 Predicted variation of the internal efficiency of flash tubes as a function of the time delay. The numbers by each curve refer to the value of the parameter $af_1q_1$.

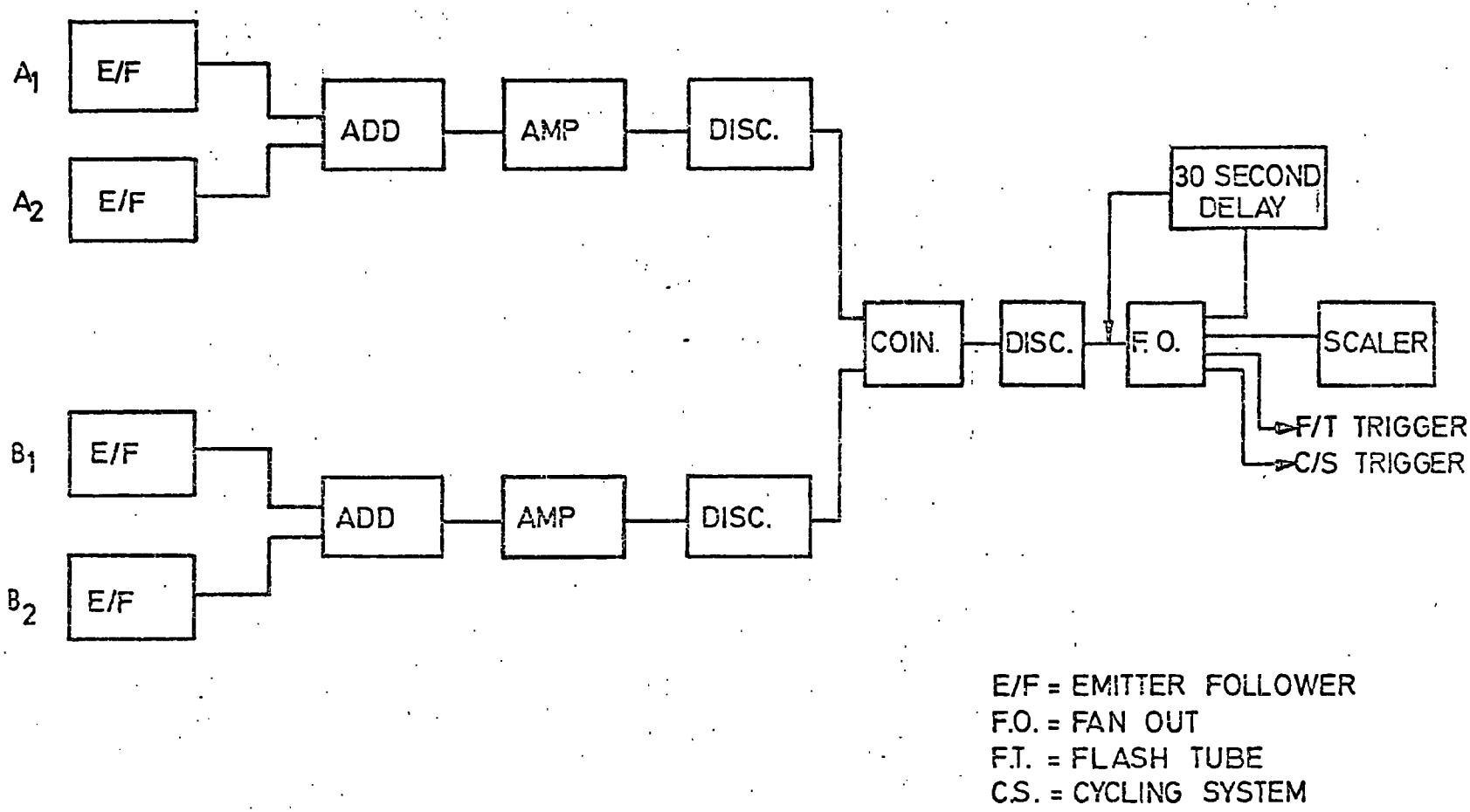


Figure 2.7 The single particle selection system.

The films obtained were projected onto a scanning table, which allowed the muon tracks photographed to be analysed in detail. The method used was to count the number of flashes along a track in the sensitive volume F2 + F3. This number, divided by the number of layers (96), is the layer efficiency ($\eta_L$). To convert this to an internal efficiency ($\eta_I$) the layer efficiency is multiplied by the ratio of the total area covered by the flash tubes to the sensitive area.

Thus $\eta_I = (1.81/1.58).\ \eta_L = 1.145\ \eta_L$

The criterion adopted for an acceptable track was that it must traverse not only the whole of F2 + F3, but must also appear in F1 and F4. This latter requirement ensures that muons do not traverse the front or rear edges of the chamber, since it has been shown by Ashton et. al. (1971) that a tube may flash with a reduced efficiency if the ionising particle passes through the tube a small distance beyond the electrode edge.

Figure 2.8 shows the distribution of the number of flashed tubes ($N_f$) for different time delays. Now the variation of layer efficiency would be expected to be a binomial distribution for an array of randomly positioned tubes. Since in the present experiment the layers are not independent of each other, a deviation from a pure binomial distribution would be expected.

For randomly positioned tubes the standard deviation $\sigma_f$ should be of the form

$$\sigma_f = \left[np(1-p)\right]^{\frac{1}{2}}$$

where n is the number of layers and p is the probability of a tube in any layer flashing. Now p is just the layer efficiency $\eta_L$, hence

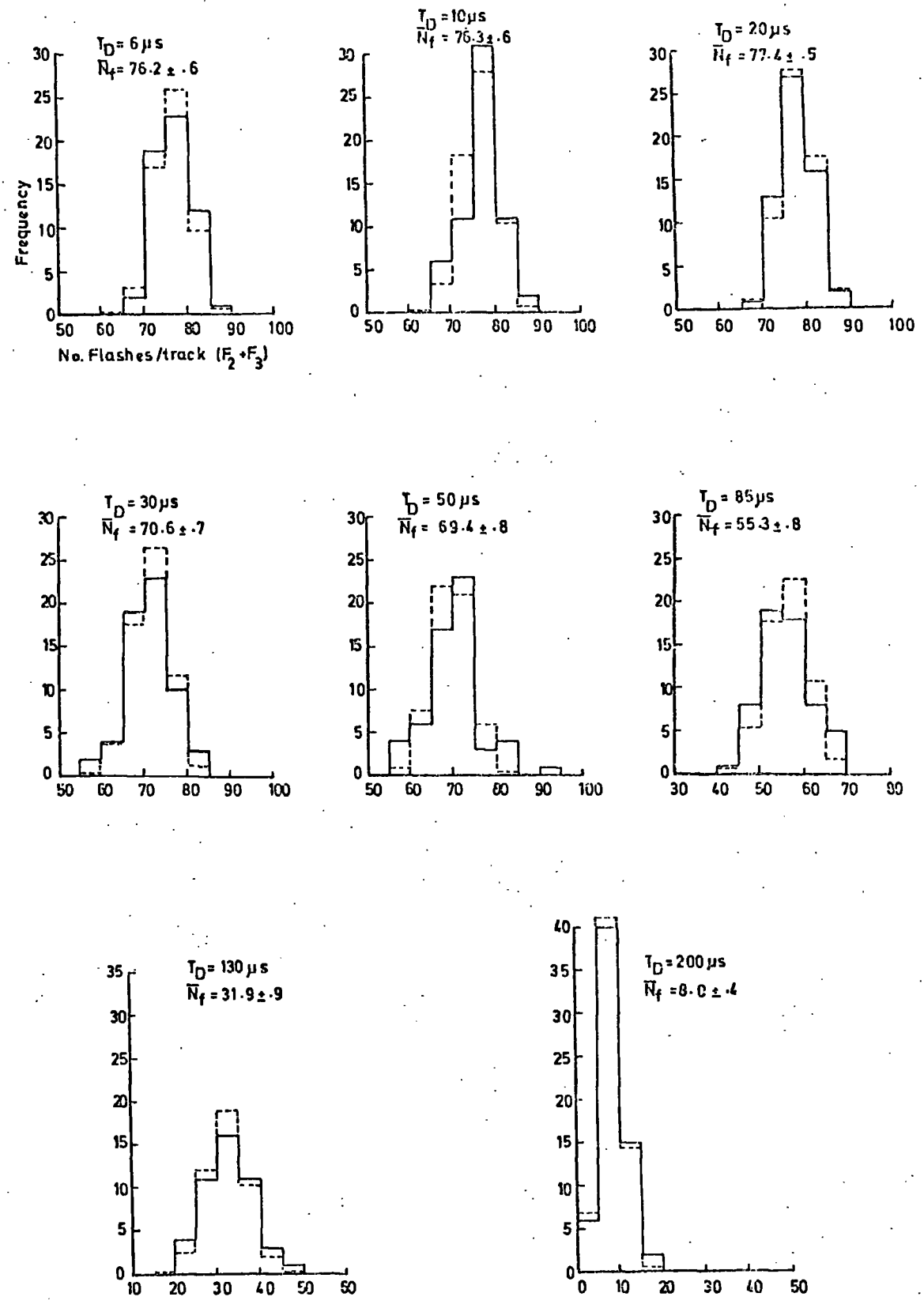


Figure 2.8. The distribution of the number of flashed tubes along a track ($N_f$) for different time delays, $T_D$. The dashed histograms refer to the expected distribution for a binomial distribution.

we can write :-

$$\sigma_f = \left[ n \eta_L (1-\eta_L) \right]^{\frac{1}{2}}$$

This function is plotted in Figure 2.9. The experimental points refer to the distributions shown in Figure 2.8.

It can be seen that the agreement obtained is reasonable. This is an important result as regards the quark experiment, since large non-random fluctuations in $\eta_L$ could result in a track produced by a charge e particle simulating a quark track.

In Figure 2.10 the results are expressed as the internal efficiency ($\eta_I$) as a function of time delay ($T_D$). Also shown is the best fit to the experimental points of Lloyd's parameter $aF_1Q_1$. The value obtained was $aF_1Q_1 = 9 \pm 1$. This leads to a value of $aF_1Q_1 = 1.0 \pm 0.1$ for quarks of charge e/3, assuming that they have the same Lorentz factor. (It is a reasonable assumption that the theory is applicable to quark tracks, since $Q_1$ is the only variable involved, $f_1$ being independent of the number of electrons in the tube).

The results obtained substantiate the theory and lend confidence to the technique employed in the quark experiment.

## 2.3 The Local Electron Density Trigger

### 2.3.1 Characteristics of the Trigger

In order to investigate the properties of a local density trigger, calculations were performed to determine the mean shower size and mean core distance of showers selected by the detector. These were also investigated as a function of the number of muons passing through the chamber.

These calculations permit results obtained with the flash tube chamber to be applied to the general properties of extensive air showers, once the selection bias has been unfolded.

The calculations were carried out numerically. A sea-level

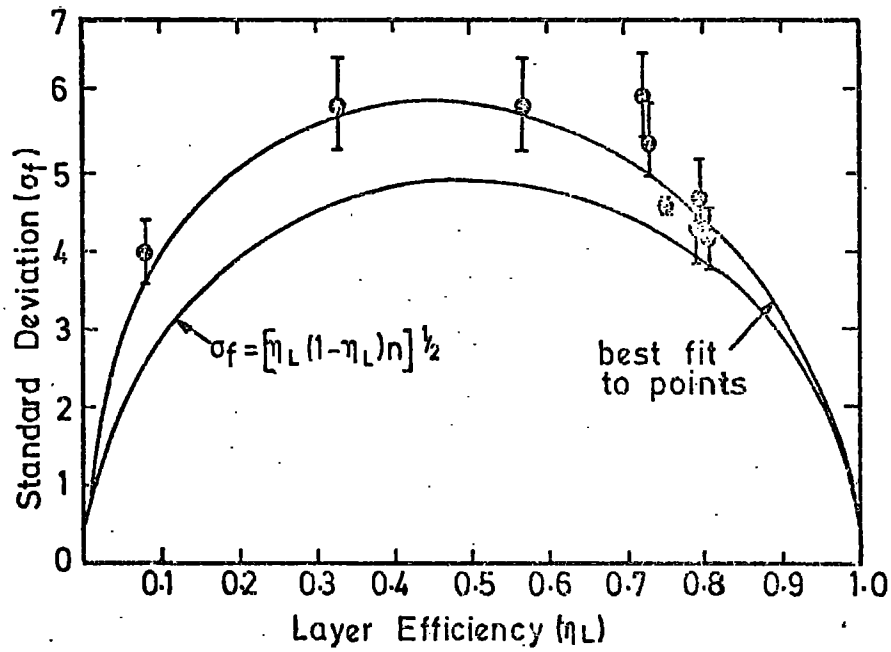


Figure 2.9. The distribution in the standard deviation, $\sigma_f$, of the number of flashed tubes as a function of the layer efficiency, $\eta_L$. The experimental points are compared with the expected distribution for a random stacking arrangement.

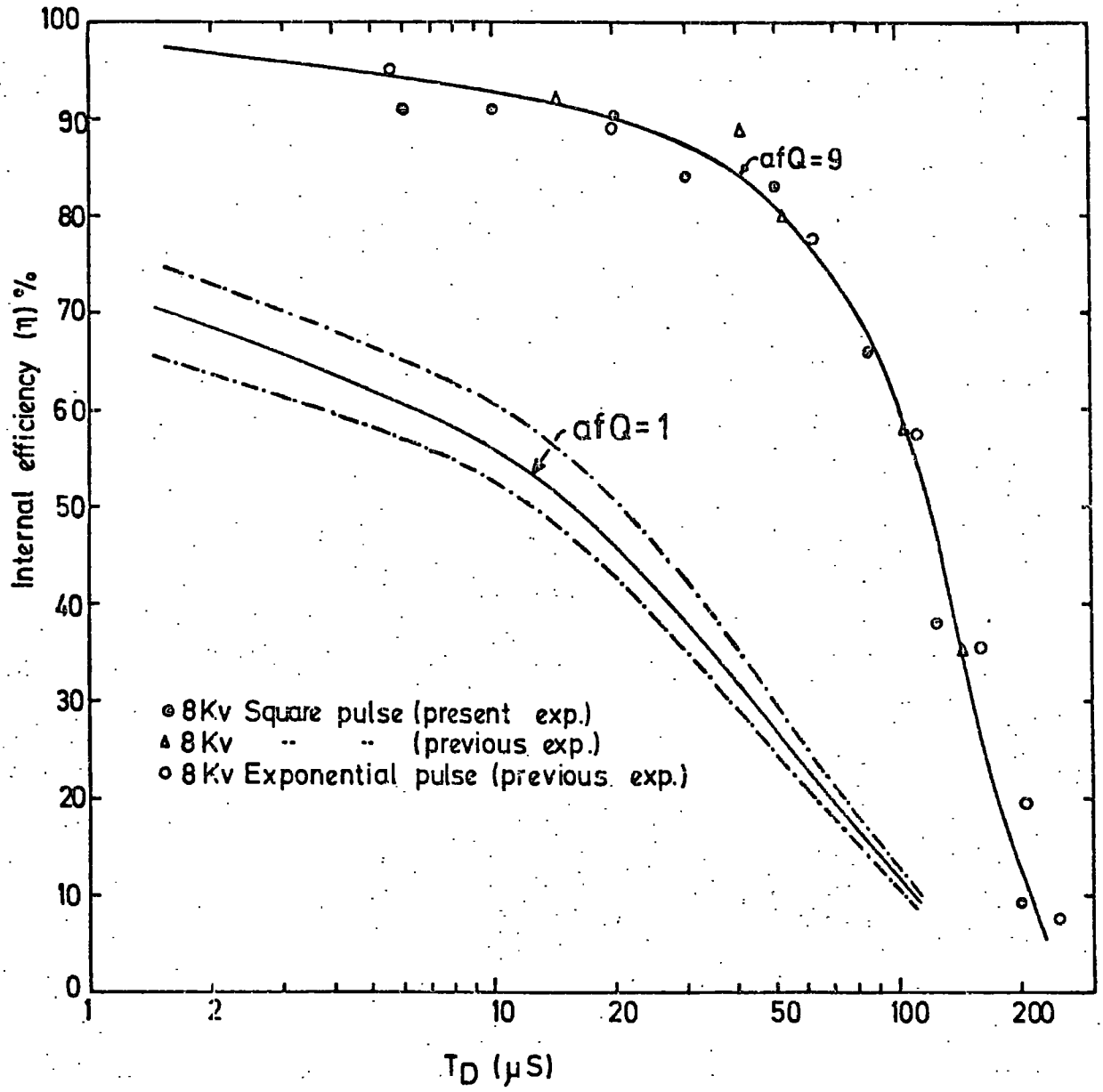


Figure 2.10. The variation of the internal efficiency of the flash tubes as a function of time delay, $T_D$. The points refer to experimental measurements. The full curve is the theoretical prediction with $af_1Q_1=9$, and corresponds to the best fit to the experimental points. Also shown is the $af_1Q_1=1$, which corresponds to a particle of charge e/3. The curves -.- indicate the latitude of uncertainty.

number spectrum of the form

$$F(\geq N_e) = 0.6\ N_e^{-1.815} + 0.60\ \log N_e\ m^{-2}.sec.^{-1}st^{-1}.$$

was assumed (Cocconi (1961)).

The lateral distribution functions for electrons and muons at sea-level that were used were those of Greisen (1960). Namely, for electrons:-

$$f(N_e,r) = \frac{0.4\ N_e}{r_1^2} \left(\frac{r}{r_1}\right)^{0.75} \left(\frac{r_1}{r+r_1}\right)^{3.25} \left(1 + \frac{r}{11.4\ r_1}\right) m^{-2}$$

where $r_1$ is the cascade length in air (=79 metres), and for muons:-

$$g(N_e,r) = 18\ (N_e/10^6)^{0.75}\ r^{-0.75}\ (1.+r/320)^{-2.5}\ m^{-2}$$

$N_e$ is the electron shower size and r is the radial distance from the core in metres.

The rate of triggers where the local electron density exceeds $\Delta e$, and the muon density at the detector exceeds $\Delta\mu$, is given by:-

$$R(>r\ ,>\Delta e,>\Delta\mu) = \int_r^\infty 2\pi r' I\left(>\frac{\Delta e}{f(r')}\ ,>\left(\frac{\Delta\mu}{g(r')}\right)^{1.33}\right)dr'$$

$$\text{and } R(>N_e,>\Delta e,>\Delta\mu) = \int_{r_{min}}^\infty 2\pi r' I\left(>\frac{\Delta e}{f(r')}\ ,>\left(\frac{\Delta\mu}{g(r')}\right)^{1.33}\right)dr'$$

where $N_e = \dfrac{\Delta e}{f(r)}$, $f(r')$ is the lateral structure function for electrons and $g(r')$ is the lateral structure function for muons. $N_e$ is related to the muon density by the formula:

$$N_e = \left(\frac{\Delta\mu}{g(r)}\right)^{1.33}$$

This function was evaluated for $\Delta e \geq 40 m.^{-2}$, the result being

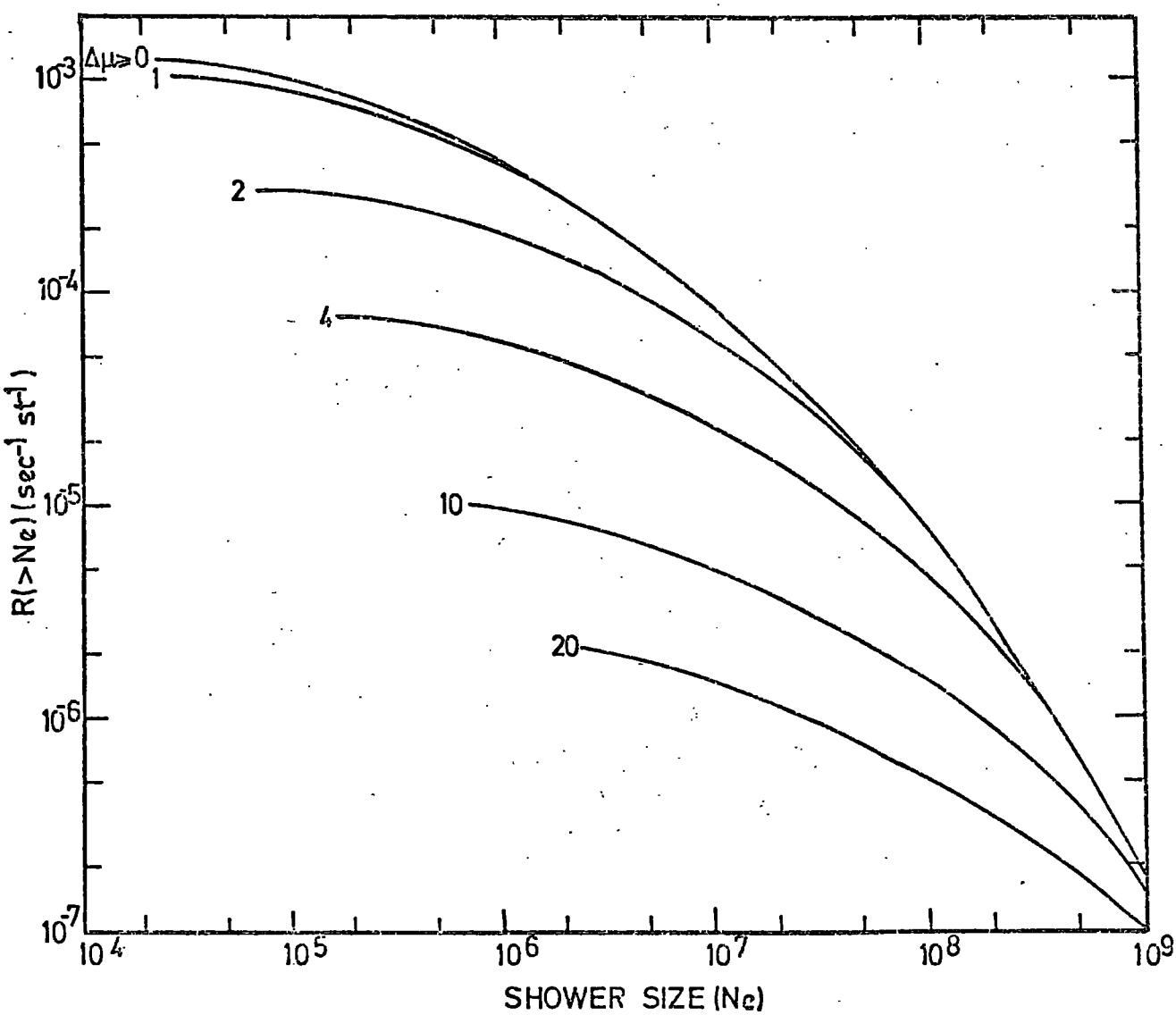


Figure 2.11. The predicted rate of triggers produced at a detector by showers of size ($\geq$Ne) in which the local electron density at the detector exceeds 40 $m^{-2}$, and the muon density exceeds $\Delta\mu\, m^{-2}$.

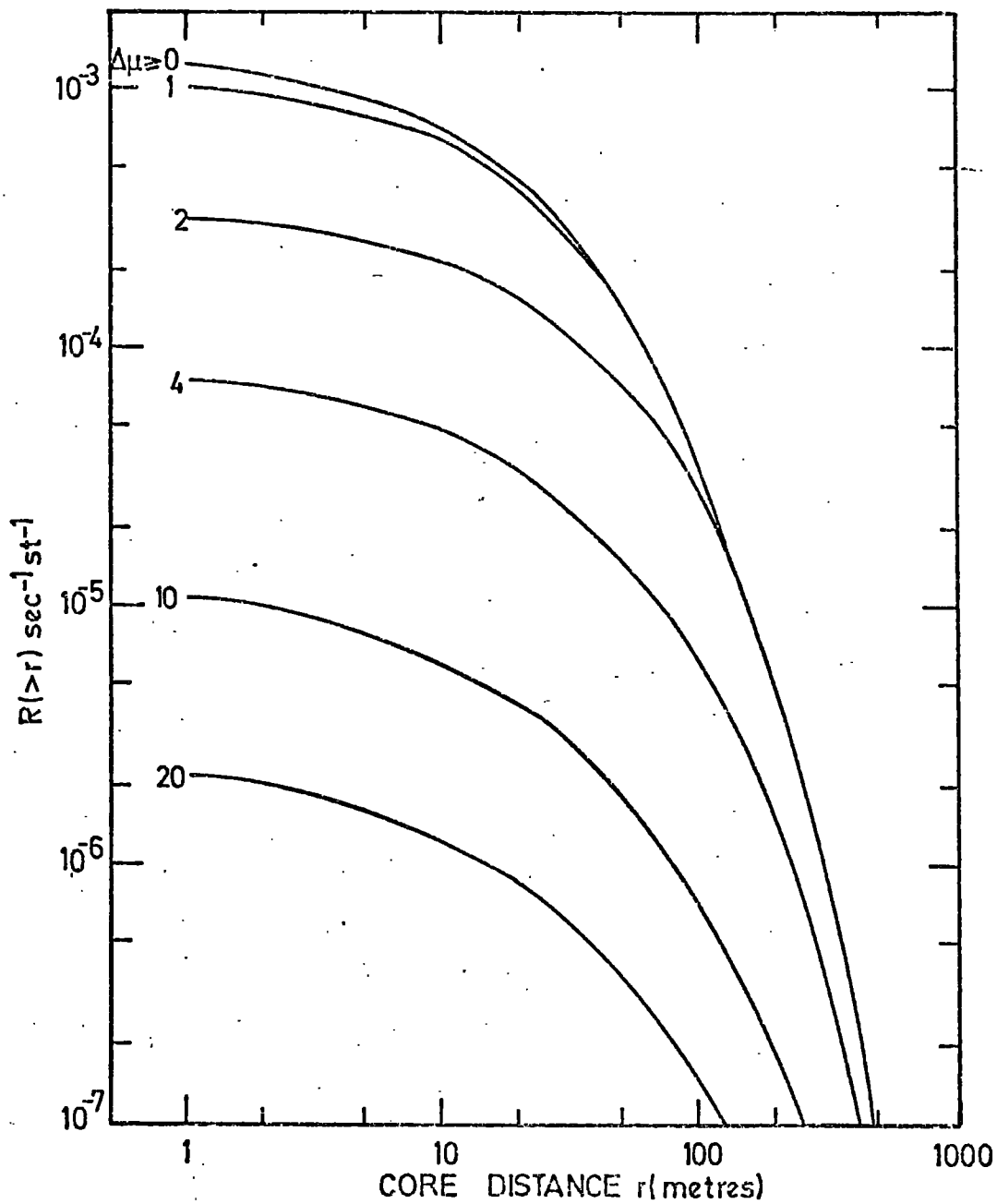


Figure 2.12. The predicted rate of triggers produced at a detector by showers at a distance ($>r$) from the detector in which the local electron density at the detector exceeds $40m^{-2}$, and the muon density exceeds $\Delta\mu m^{-2}$.

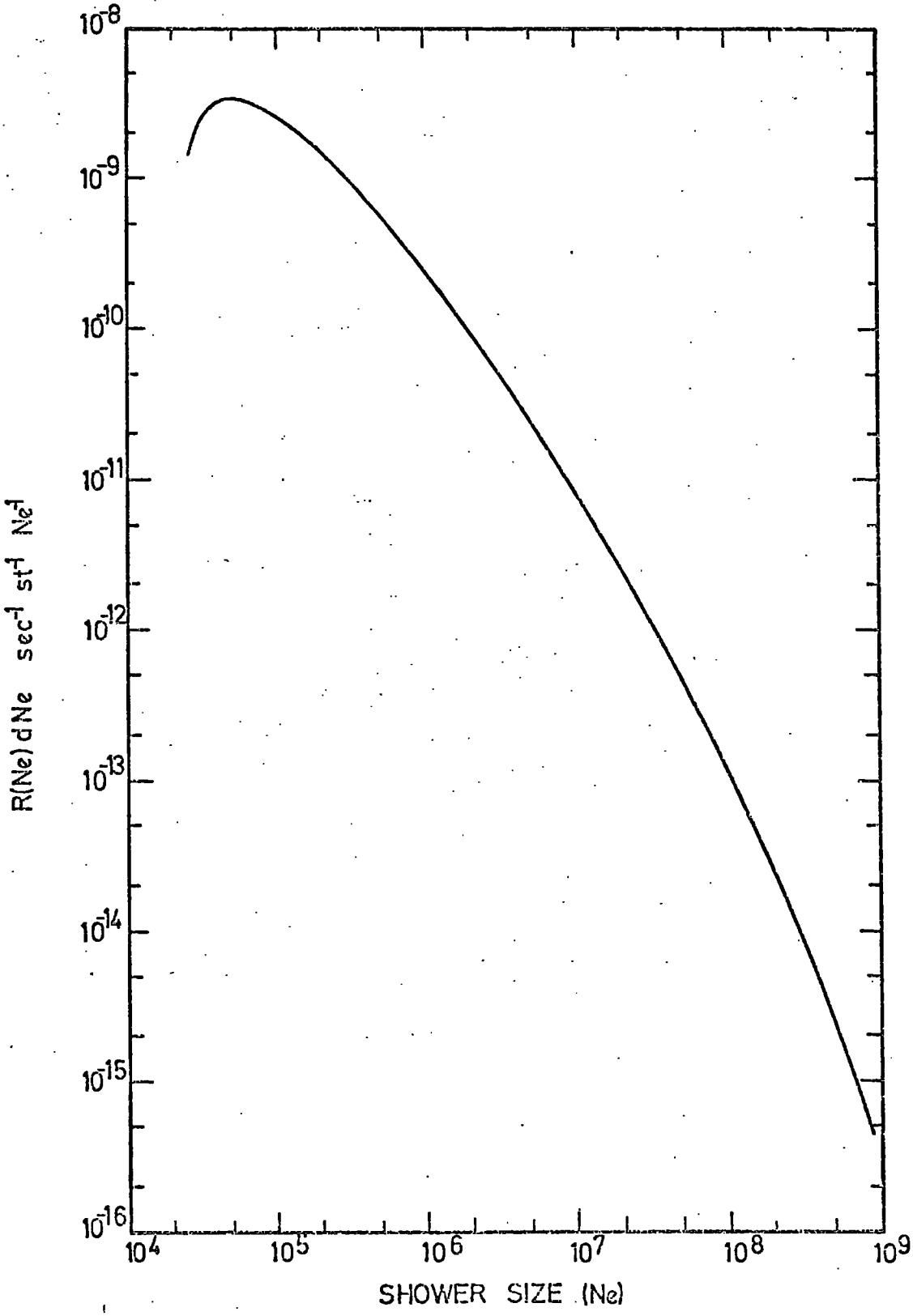


Figure 2.13. The rate of triggers produced at a detector by showers of size Ne in which the local electron density at the detector exceeds 40 $m^{-2}$

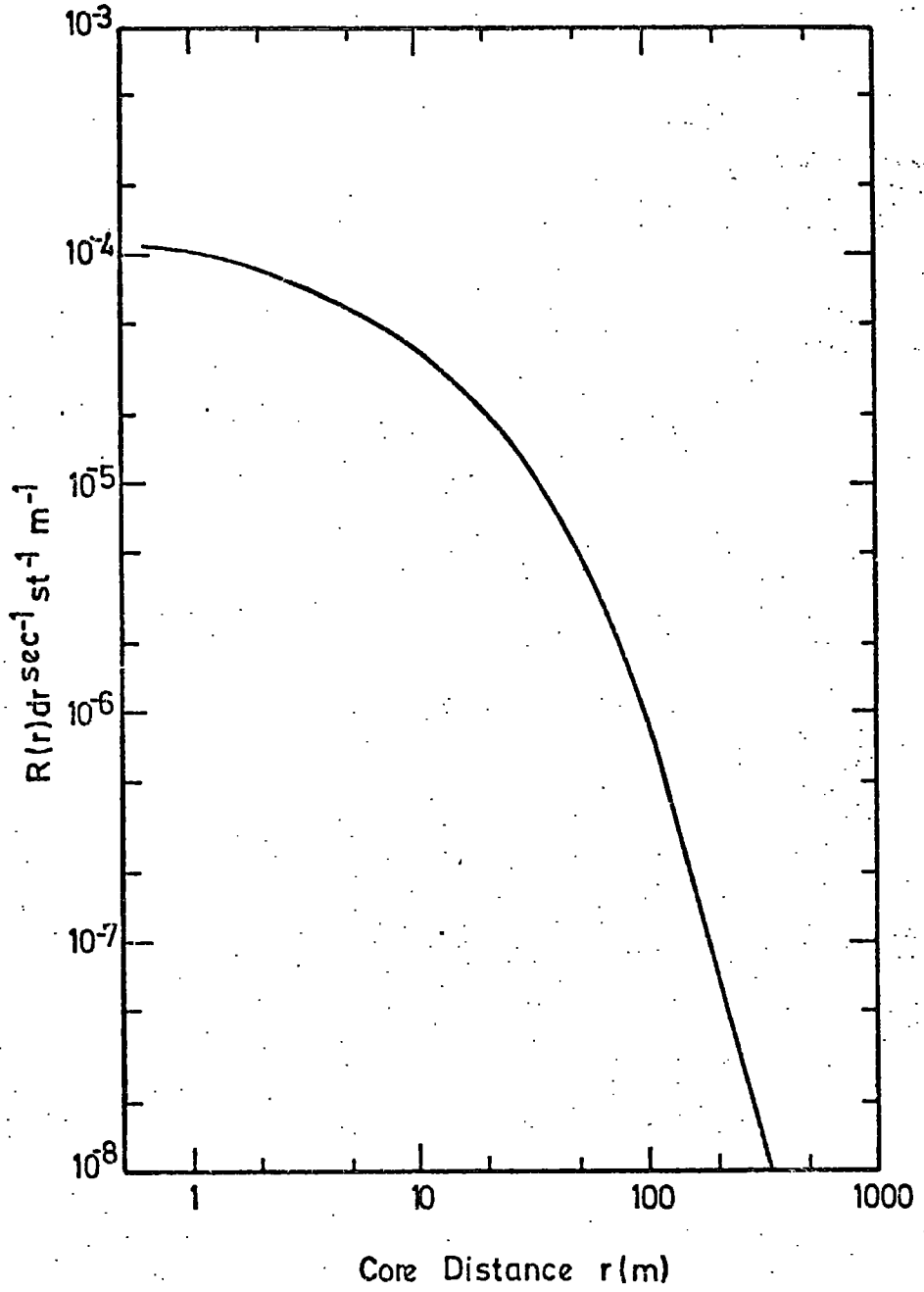


Figure 2.14. The rate of triggers produced at a detector by showers at a distance r metres from the detector, in which the local electron density at the detector exceeds 40 $m^{-2}$.

shown in Figures 2.11 and 2.12. The curves labelled $\Delta\mu \geqq 0$ correspond to no muon density requirement being imposed. Figures 2.13 and 2.14 show the differential forms of these curves, from which it can be seen that the mean shower size selected by the requirement $\Delta e \geqq 40 m.^{-2}$ is $2.0.10^5$, and the mean core distance 4.6 metres.

2.3.2 Setting up the Trigger

The three liquid scintillators used for the selection system were described in section 2.2.1. Figure 2.15 shows the logic for the E.A.S. trigger. After determining the single particle pulse height distributions for relativistic charge e particles (Figure 2.16) using a geiger telescope to select near-vertical particles, the discriminator threshold was set to correspond to 50 particles through each scintillator (i.e. 50 times the single particle mean), a density per scintillator of approximately 40 $m^{-2}$.

## 2.4 Production of Electron-Photon Cascades in the Chamber

When high energy particles pass through matter, photons and electrons of high energy can be produced by the interactions of these particles with the medium.

In the case of hadrons, inelastic collisions with target nuclei create new particles, mainly charged ($\pi^{\pm}$) and uncharged ($\pi^{o}$) pions. The $\pi^{o}$'s decay very rapidly into two photons. These can generate electrons and positrons which in turn generate more photons. In this way a cascade of electrons, positrons and photons is built up. In addition, the charged pions created in the initial interaction can go on to interact themselves, adding to the cascade.

Similarly, high energy muons can transfer a fraction of their energy to either electrons or photons, again producing a cascade if the energy input is sufficient. A more detailed discussion of the physical processes occurring in the cascades is given in Chapter 4.

These cascades provide a means of detecting high energy particles.

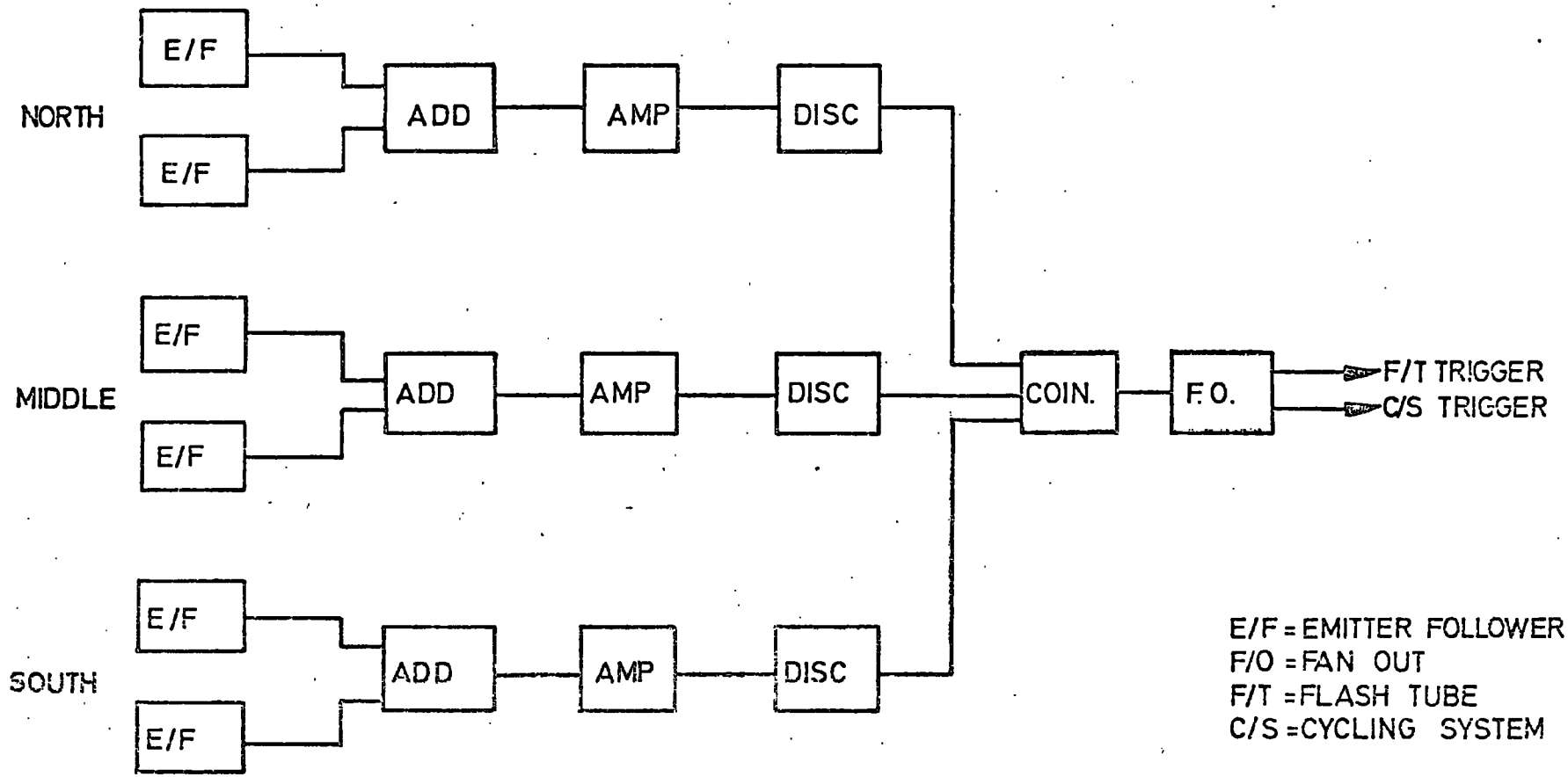


Figure 2.15 The Extensive Air Shower selection system.

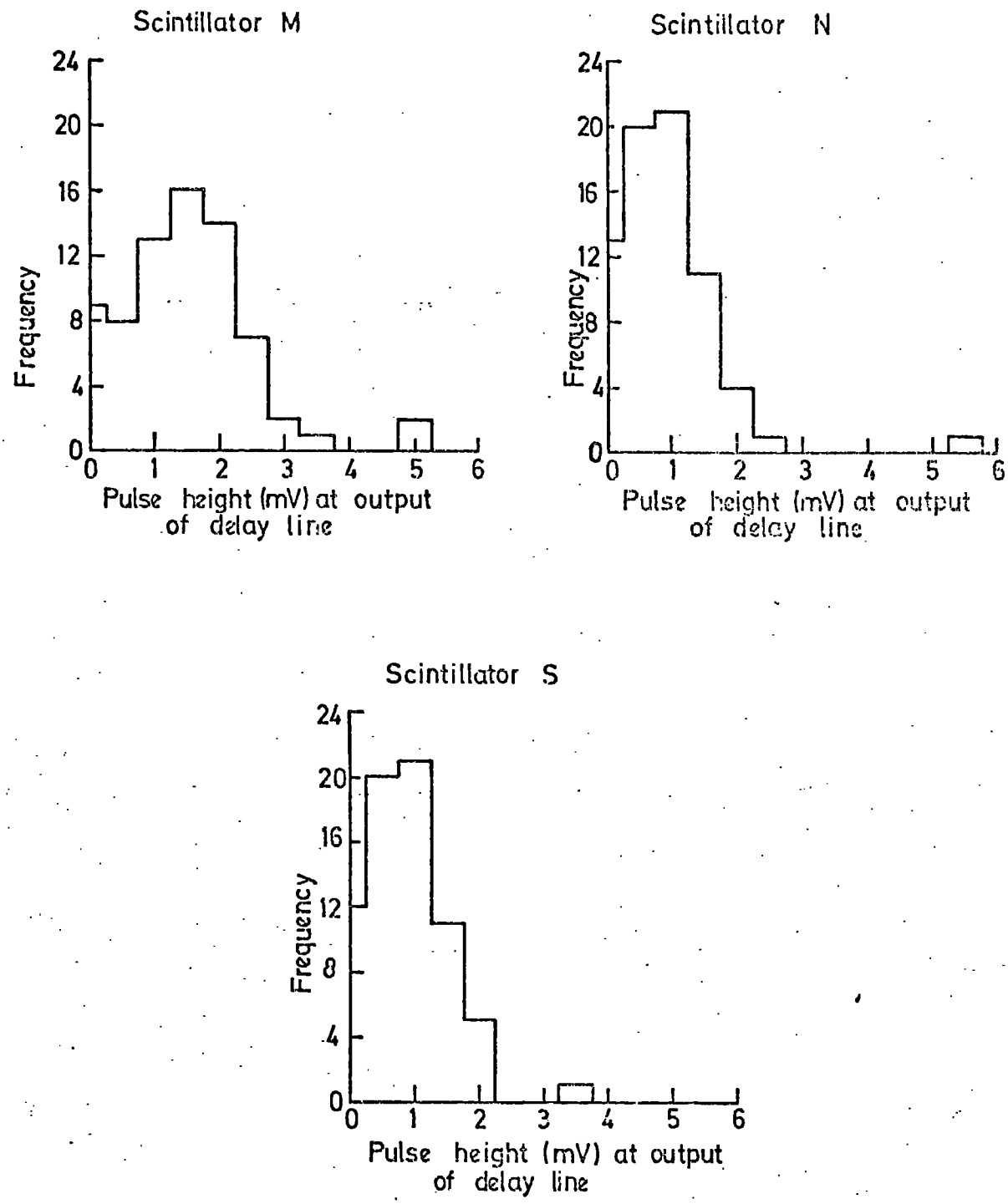


Figure 2.16 Single particle pulse height distributions for three liquid scintillators.

Furthermore, if the cascade process is understood, it is possible to estimate the energy of the interacting particle. An attempt has been made to relate parameters of the cascades which can be measured in the flash tube chamber to the energy of the interacting particle.

This technique has been used to study properties of hadrons in E.A.S. For these measurements the lead roof and the iron layer between Fla and Flb acted as energy converters in which the cascades could develop.

## 2.5 The Extensive Air Shower Experiment

### 2.5.1 Calibration for the Quark Search

For the e/3 quark search, the time delay $T_D$ was chosen to be 20$\mu$S, this being the optimum, allowing the resolution of charge e/3 particles from charge e particles whilst avoiding background problems due to the flashing of spurious tubes in the chamber.

Detailed knowledge of the shape of the muon efficiency distribution was necessary, especially of the low efficiency tail (if any). Hence using the trigger of Figure 2.7, with $T_D$ = 20$\mu$S, single muons were selected and their tracks photographed. A total of 1,046 events were obtained, and these were analysed as described in 2.2.4. The distribution of the number of flashes along the track ($N_f$) is shown in Figure 2.17. The shape was quite satisfactory, since although quarks of charge 2e/3 could not be resolved from the muon peak, the expected position of charge e/3 particles should be well separated from it.

### 2.5.2 Details of the Experiment

It was decided that the optimum electron density on which to trigger was $\geq 40\ m^{-2}$, from considerations of a preliminary experiment (Ashton et al., 1971) and from the calculations described in 2.3.1. In 2.3.2 the experimental arrangement was described.

The chamber was operated in this mode from October 1972 to June 1973 for a total running time of 2,570 hours. During this time

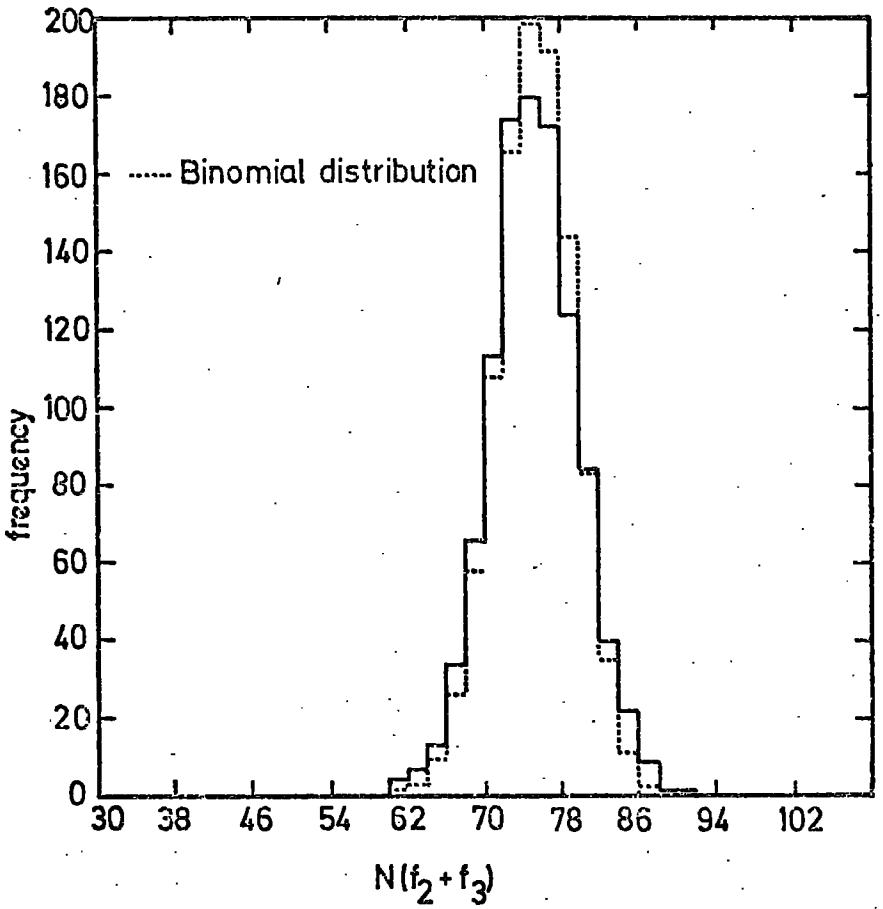


Figure 2.17. The single particle calibration distribution. The distribution of the numbers of flashes ($N(f_2+f_3)$). along a track for 1,046 events for which the time delay $T_D$ was 20 μs. The dashed histogram refers to the expected binomial distribution. The mean value of $N(f_2+f_3)$ obtained was 74.77±.14. Maximum value of $N(f_2+f_3)$ = 96.

12,057 triggers occurred, and were recorded on the series of films E1 to E69.

# CHAPTER 3

## DEVELOPMENT OF THE QUARK THEORY AND PREVIOUS EXPERIMENTS

### 3.1 Origin of the Quark Theory

#### 3.1.1 The Fermi-Yang Model

By 1949 the number of "elementary" particles which had been observed experimentally had grown rapidly. No longer could matter be considered to be built up only of electrons, protons and neutrons. This simple picture had been replaced by one in which there was a bewildering number of new particles, which could be classified as follows:-

Baryons:- strongly interacting , relatively heavy particles such as nucleons, having half integral spin angular momentum (fermions) and baryon number B = +1 for particles, B = -1 for antiparticles.

Mesons:- intermediate mass particles including pions and kaons, having integral spin momentum (bosons) and B = 0. Mesons also interact strongly.

Leptons:- these are light fermions such as electrons and neutrinos which do not interact strongly.

Photon:- the quantum of the electromagnetic field, the photon is a massless boson.

Certain conservation laws had been observed experimentally, laws which determine what interactions may occur. Hence, energy and momentum were observed to be conserved absolutely in all interactions. Similarly, charge was again found to be absolutely conserved, and the conservation of parity, baryon number and isospin in strong interactions were other important rules which had been discovered.

Fermi and Yang (1949) considered that as more new particles were found to exist, the probability that they were all truly elementary

particles decreased. From consideration of the above conservation laws, they postulated that all of the strongly interacting particles (hadrons) could in fact be built up from four basic particles - the proton and neutron, and their antiparticles. Bosons with B = 0, integral spin and integral isospin could be built up, and baryons with B = 1, half-integral spin and half-integral isospin could likewise be constructed.

This theory was inadequate, however, to explain the strange particles.

3.1.2 Strangeness and the Gell-Mann-Nishijima Relation

Rochester and Butler (1947) observed a new class of particles in a cloud chamber exposed to the cosmic radiation. It appeared that these particles were only produced in pairs in strong interactions, but then decayed via the weak interaction. Gell-Mann (1953) and Nakato and Nishijima (1953) postulated the idea of associated production, and this led to the concept of strangeness in strong interactions. Thus hadrons were given a new quantum number (S), where S is related to Q the charge of the particle, $T_3$ the third component of isospin, and B the baryon number by the equation

$$Q = T_3 + Y/2 \qquad \text{where } Y = B + S \text{ is the hypercharge.}$$

This is the Gell-Mann - Nishijima relation.

Since S for the proton and neutron is zero, it immediately became necessary to postulate a strange particle of $S = \pm 1$ as a third building block.

3.1.3 The Sakata Model and SU(3)

Goldhaber (1956) suggested that the three elementary particles should be n p K, but this theory was not successful. Sakata (1956) suggested the n p $\lambda$ triplet, and this model was developed by several other workers (for example Ikeda, Ogawa and Ohnuki, 1959). The model was successful when applied to bosons, but had some difficulties

in explaining the observed baryon states, predicting the wrong mass multiplet structure.

Predictions of the mass multiplet structure were based upon group theoretical arguments. Using group theory, invariants of symmetry operations can be evaluated, invariants of a particular transformation forming multiplets and hence allowing conservation laws to be postulated, minor symmetry - breaking producing structure within a multiplet. The symmetry group which includes isospin and strangeness is SU(3). Invariants are found by evaluating the irreducible representations formed by taking the direct product of tensors of which the components are identified with the triplet n p $\lambda$ and their antiparticles. In the Sakata model bosons are formed by particle - antiparticle pairs, hence evaluating the direct product gives:-

$$3 \otimes \bar{3} = 8 \oplus 1$$

(where a bar indicates an antiparticle, $\otimes$ means direct product and $\oplus$ means direct sum) i.e. singlet and octet states are formed, as had been found experimentally. However, when the theory was applied to baryons the wrong multiplet structure was predicted, since in the Sakata model a baryon should be constructed from two particles and an antiparticle to conserve baryon number. Hence:-

$$3 \otimes \bar{3} \otimes 3 = 15 \oplus 6 \oplus 3 \oplus 3$$

However the multiplets 15,6,3, and 3 are not observed experimentally. It was Gell-Mann (1962) and Ne'eman (1961) who realised that although the Sakata model predicted the wrong baryon mass multiplets, the alternative reduction

$$3 \otimes 3 \otimes 3 = 10 \oplus 8 \oplus 8 \oplus 1$$

gave experimentally observed symmetries.

This led them to postulate the "Eightfold Way", so called since it involved eight conserved quantities. However, this symmetry required the existence of a fundamental triplet. No existing particles

could be members of this triplet.

3.1.4 The Eightfold Way and the Quark Model

It was Goldberg and Ne'eman (1963) who realised that the model proposed by Gell-Mann and Ne'eman was consistent with a model in which the basic triplet each had baryon number $B = \frac{1}{3}$. From the Gell-Mann - Nishijima relation this implies fractional hypercharge and charge.

Not until 1964 did Gell-Mann (1964) and Zweig (1965) independently seriously propose this as a realistic model. Gell-Mann gave the triplet particles the name "Quarks". The basic properties of quarks are as shown in Table 3.1. The quoted lifetimes are estimated from observations of the decays of particles such as neutrons ($\beta^-$ decay) and the $\Lambda^0$, although the decay of quarks in the bound state is not necessarily the same as that of free quarks, so the lifetimes quoted must be regarded as tentative only.

Figure 3.1 shows how mesons can be built up from the quark triplet, called by analogy with the Sakata model, n p $\lambda$ quarks, and in Figure 3.2 the construction of the low-lying baryon octet and decuplet states can be seen.

3.2 Predictions of the Quark Model

3.2.1 Mass Splitting within a Multiplet

The fact that particles belonging to a particular multiplet do not all have degenerate mass values implies a breaking of SU(3) symmetry, in the same way that non-conservation of isospin in electromagnetic interactions causes splitting of isospin multipliets such as the proton-neutron doublet. The mass differences as the hypercharge Y is varied are much greater (~146 MeV) than those observed as the electric charge (Q) is varied (for example $\pi^+ - \pi^0 \approx 1$ Mev. ). This implies that invariance under subgroup SU(2) (isospin) rotations is much less badly broken than under the complete SU(3) symmetry (Squires, 1970).

| Symbol | Q | Spin | $T_3$ | B | S | Mass | Decay schemes and lifetimes |
|---|---|---|---|---|---|---|---|
| p | +2/3e | 1/2 | +1/2 | 1/3 | 0 | M | stable |
| n | -1/3e | 1/2 | -1/2 | 1/3 | 0 | M | $\longrightarrow p + e^- + \bar{\nu}_e$ minutes |
| $\lambda$ | -1/3e | 1/2 | 0 | 1/3 | -1 | M+146MeV | $\longrightarrow p + \pi^-$ or $n + \pi^o$ $\}\sim 10^{-10}$ secs. |
| $\bar{p}$ | -2/3e | 1/2 | -1/2 | -1/3 | 0 | M | stable |
| $\bar{n}$ | +1/3e | 1/2 | +1/2 | -1/3 | 0 | M | $\longrightarrow \bar{p} + e^+ + \nu_e$ minutes |
| $\bar{\lambda}$ | +1/3e | 1/2 | 0 | -1/3 | +1 | M+146MeV | $\longrightarrow \bar{p} + \pi^+$ or $\bar{n} + \pi^o$ $\}\sim 10^{-10}$ secs. |

Table 3.1

Expected properties of quarks. The symbols representing the quantum numbers are explained in the text.

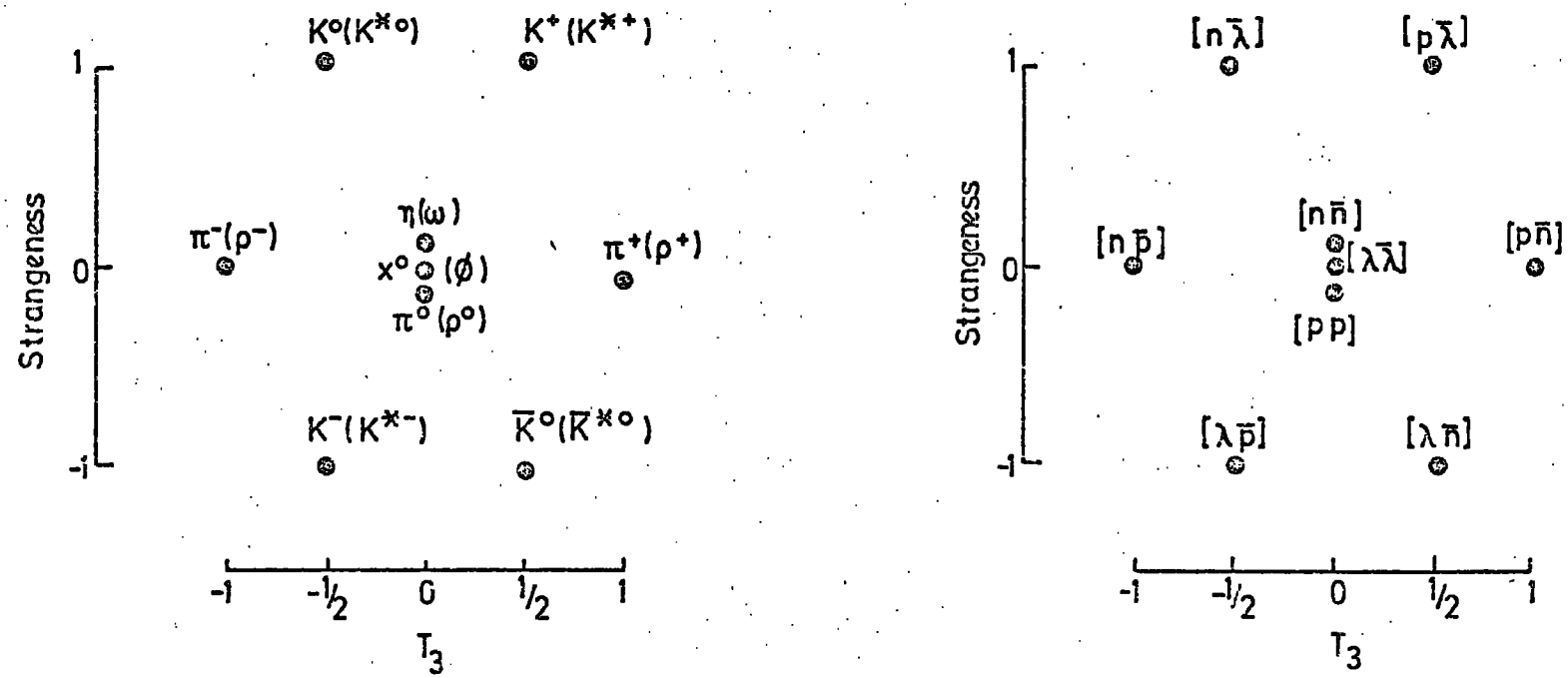


Figure 3.1 The construction of the two lowest meson nonets in the quark model.

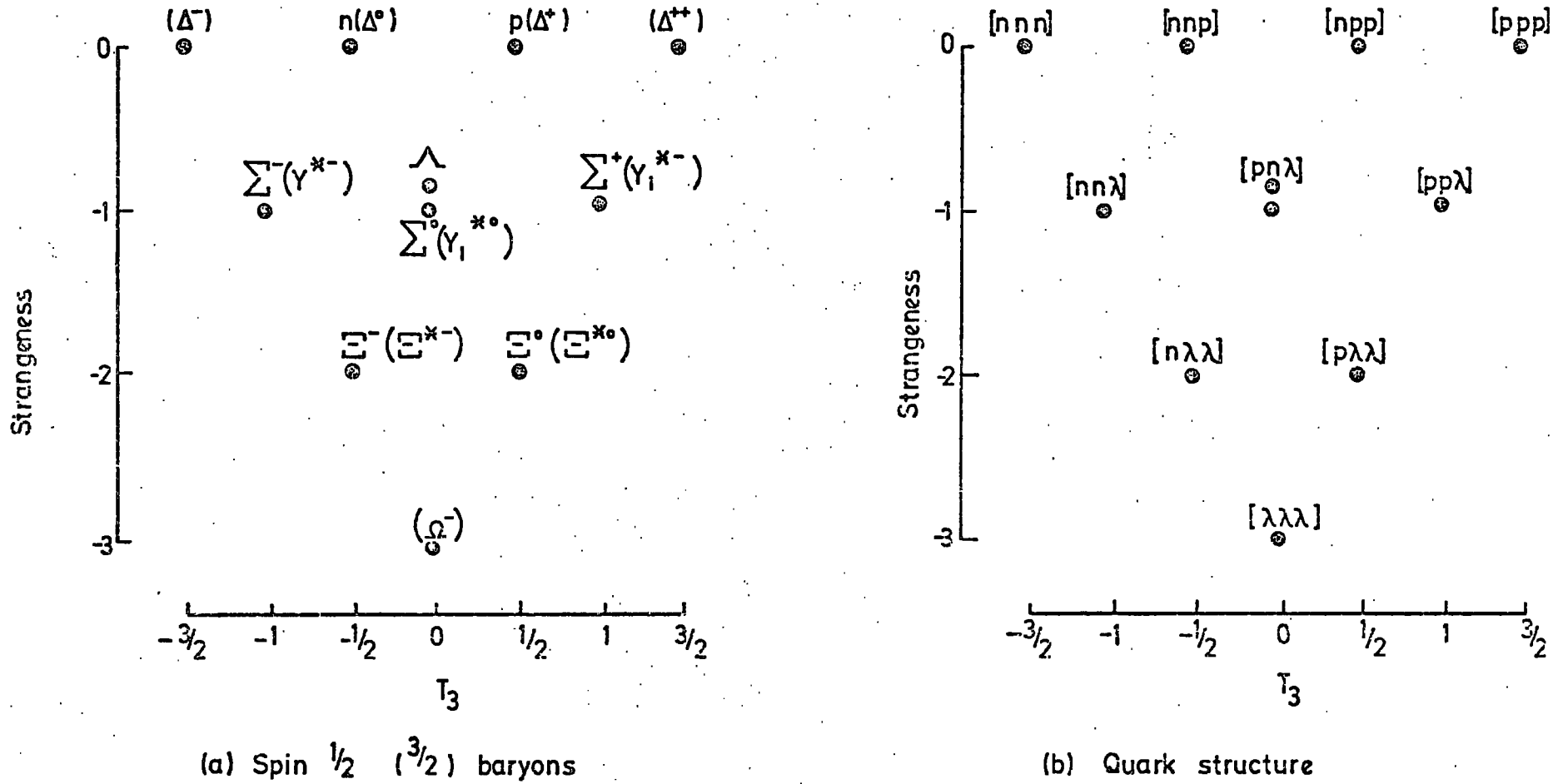


Figure 3.2 The construction of baryon octets and decuplets in the quark model.

The mass splitting between different isospin multiplets (Q = constant) follows naturally from the quark model if the $\lambda$ quark is assumed to be heavier by 146 MeV than the n and p quarks. From Figures 3.1 and 3.2 it can be seen that increasing S by one corresponds to the replacement of an n or p quark by a $\lambda$ quark. This enabled the accurate prediction of the mass of the $\Omega^-$ particle to be made (Zel'dovitch 1965).

Higher mass multiplets can be accounted for by taking into consideration the spin orientation of the quarks. Allowing the spin vectors to be parallel or antiparallel produces the higher mass states. The group representing this enlarged set of quantum numbers is SU(6).

The "supermultiplets" predicted by SU(6) are, for mesons and baryons respectively (Kokkedee, 1969) :-

$$6 \otimes \bar{6} = 35 \oplus 1 = (1,0) \oplus (1,1) \oplus (8,0) \oplus (8,1)$$

and $6 \otimes 6 \otimes 6 = 70 \oplus 70 \oplus 56 \oplus 20$

$$= (1,1/2) \oplus (8,1/2) \oplus (8,3/2) \oplus (10,1/2)$$
$$\oplus (1,1/2) \oplus (8,1/2) \oplus (8,3/2) \oplus (10,1/2)$$
$$\oplus (8,1/2) \oplus (10,3/2)$$
$$\oplus (1,3/2) \oplus (8,1/2)$$

(where the first number in the brackets indicates the number of independent states in a multiplet and the second figure the angular momentum of the multiplet states).

3.2.2 Allowed values of Isospin and Charge

The question arises as to why the maximum value of isospin should be 3/2 and maximum strangeness be (-3). This again follows naturally from the quark model, since quarks consist of a non-strange isospin doublet with I = 1/2 and a strange singlet (S = -1) with I = 0.

3.2.3 Collision Processes and the Quark Model

Experimentally it is found that the pion-proton total scattering cross-section ($\sim$ 22mb) is approximately two-thirds of the proton-proton

total cross-section (~33 mb). This has a very straightforward explanation in the quark model, if quarks are considered to interact as though free particles and the total scattering amplitude is just the sum of independent, single quark-quark scattering amplitudes. At low energies the relation breaks down, presumable due to the fact that quark-antiquark scattering is stronger than quark-quark scattering. Taking account of this produces reasonable agreement with experiment.

In inelastic scattering processes it can be considered that only one quark in each hadron is "active", the others being spectators and unable to exchange electric charge or strangeness. This forbids reactions such as

$$\pi^- p \rightarrow \varphi^\circ B \quad (\text{where B is any baryon})$$

since the $\varphi^\circ$ is composed in the quark model of $\lambda\bar{\lambda}$, hence both the mesons quark and antiquark ($\bar{p}n$) would have to simultaneously change states, violating the scattering rule above. The reaction is in fact not seen to occur.

The quark model has also been successfully applied to other scattering processes (Lipkin, 1968).

It should be noted that a free quark - proton total scattering cross-section might, from these arguments, be expected to be one-third of the proton-proton cross-section. This is of importance when considering the propagation of quarks in matter, with reference to the detection of free quarks.

3.2.4 The Proton-Neutron Magnetic Moment Ratio

Assuming the magnetic moments of quarks to be proportional to their charge such that $\mu_p = 2/3\ \mu_1$; $\mu_n = -1/3\ \mu_1$ and $\mu_\lambda = -1/3\ \mu_1$ (where $\mu_1$ is unknown), and calculating the probabilities of the proton and neutron being in allowed spin states, the ratio of the average magnetic moment of the neutron (pnn) to the average magnetic moment of the proton (ppn) is given by

$$\frac{\mu_N}{\mu_p} = \frac{-2/3\,\mu_1}{\mu_1} = -0.667$$

Experimentally the ratio is found to be

$$\frac{\mu_N}{\mu_p} = -0.685$$

which is in reasonable agreement.

The theory does not predict the absolute values of the magnetic moments.

## 3.3 Predicted Properties of Quarks

### 3.3.1 Free Quark Production Mechanisms

Although several of the predictions of the quark model have been successful, it is still not clear whether quarks have physical existence or are purely mathematical abstractions.

From consideration of the binding energies between quarks it seems that quarks must have masses of several GeV/$c^2$ (see for example Wazed, 1965). Hence if quarks do exist as free particles they can probably only be produced in this state in high energy nucleon-nucleon interactions. Possible production mechanisms are

$$N + N \rightarrow 3\,q + 3\,q$$

$$N + N \rightarrow N + 3\,q$$

$$N + N \rightarrow N + N + q + \bar{q}$$

$$\pi + \pi \rightarrow q + \bar{q} + q + \bar{q}$$

$$\pi + \pi \rightarrow \pi + q + \bar{q}$$

The first three types of interaction are central collisions in which the total centre of mass energy can go into quark production. The last two types represent peripheral interactions between virtual pions from the "clouds" surrounding the interacting nucleons. In these peripheral interactions only a fraction $m_\pi/M_N$ (=0.15) is available for quark production. In Figure 3.3 can be seen the threshold kinetic

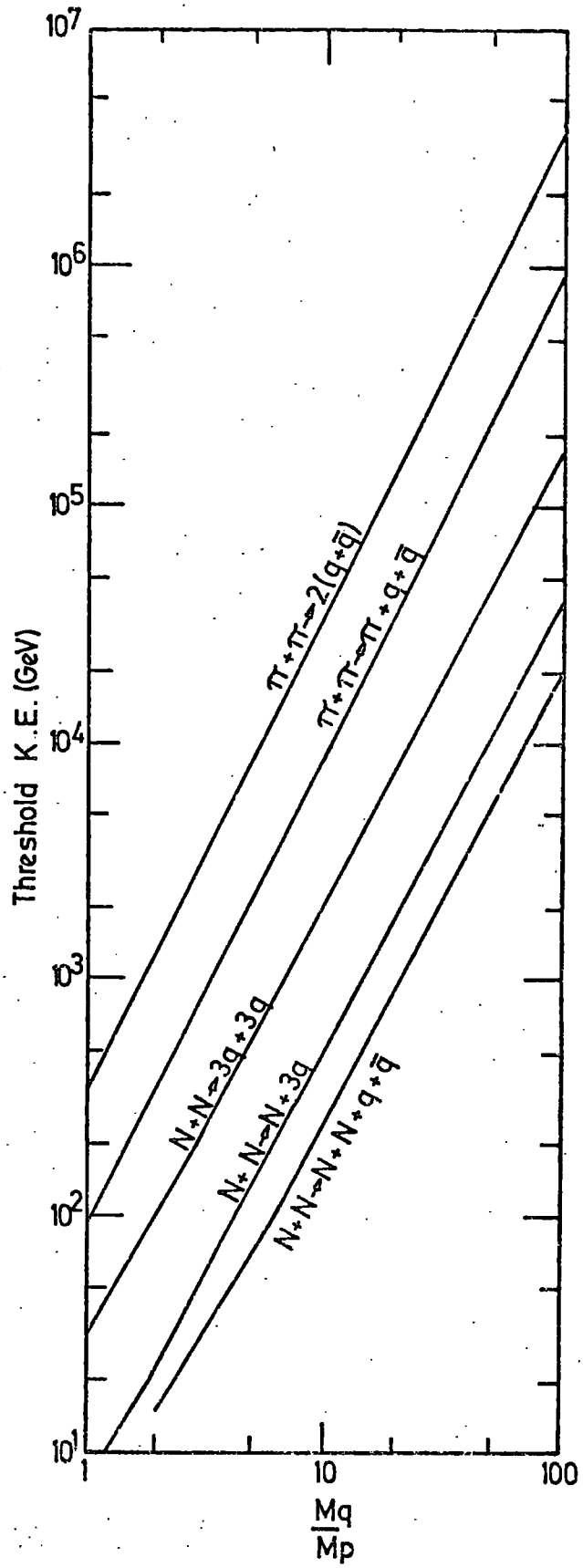


Figure 3.3. Threshold kinetic energy for quark production in nucleon-nucleon collisions. After Ashton (1973a).

energy for quark production by these five mechanisms as a function of the quark mass (Ashton, 1973).

The quark-antiquark pair production process likely to dominate is shown in Figure 3.4. This process can be treated using a thermodynamic model (Maksimenko et. al.,1966 and Hagedorn et al., 1968), and when applied to baryon-antibaryon pair production shows good agreement with experiment up to 30 GeV.

Assuming that the quark-antiquark pair have sufficient energy at production to separate before annihilation we can predict the threshold energy of the process. From Figure 3.3, since the quark-antiquark pair are produced in a virtual $\pi-\pi$ collision, the threshold energy of the incident nucleon in the laboratory system for the pair to be produced, is (Ashton, 1973)

$$2\left[\left(\frac{M_q}{M_\pi}\right)^2 - 1\right] \text{Gev.}$$

Hence we require an estimate of the free quark mass in order to obtain the threshold energy for quark production via this mechanism. This of course is of relevance to the design of experiments to search for quarks, especially searches carried out at accelerators.

3.3.2 Quark Mass Estimate

In order to obtain a rough estimate of the quark mass, Morpurgo (1967) has considered the quark-antiquark bound state in the form of mesons. He considers the quark-antiquark pair to be bound in a cylindrically symmetric potential well of radius r. Vector meson exchange provides the binding between the pair, and the range of the binding force to be, say $(M_p)^{-1} \approx (5m_\pi)^{-1}$. The lowest bound state will have the mass of the pion. Calculating the minimum de Broglie wavelengths which can resonate in this potential well, Morpurgo predicts the s, p, d energy levels of the system to be $25\ m_\pi^2\alpha/Mq$, with $\alpha=(3.14)^2,(4.5)^2$ and $(5.76)^2$ for the three states respectively. From experiment it is known that the mass difference of even and odd angular momentum multiplets is

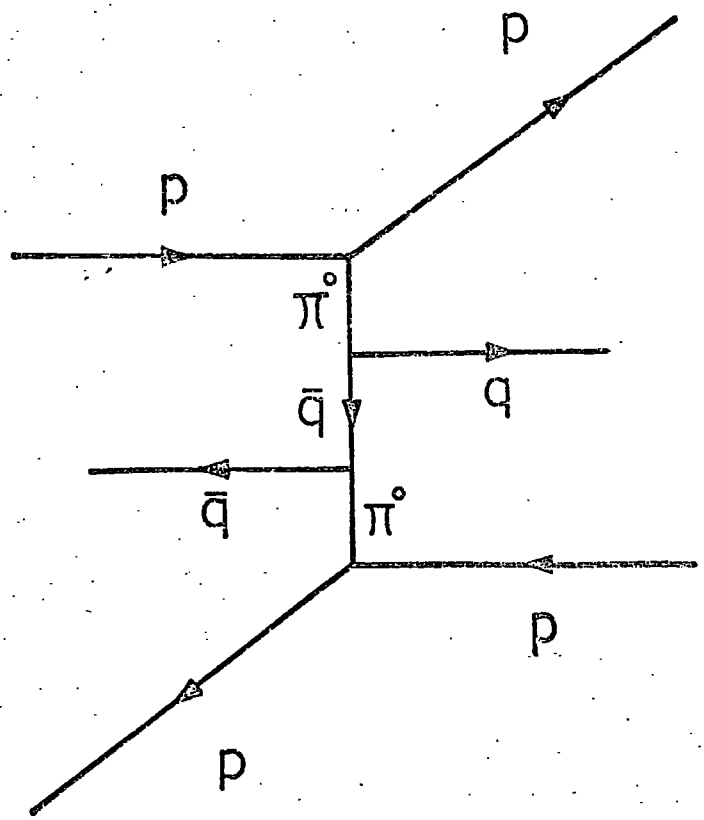


Figure 3.4. Quark-antiquark pair production in a high energy proton-proton collision.

approximately 500 MeV/$c^2$. Hence comparing this with Morpurgo's result gives Mq $\approx$ 10 GeV/$c^2$. It must be noted, however, that as the range of the binding force is altered, Mq varies. Since this range is not known, all that can be said is that the likely mass range is of the order of several GeV/$c^2$ to several tens of GeV/$c^2$.

Lipkin (1973), however, suggests that both vector and scalar potentials should be present in quark dynamics. The vector potential provides an attractive force between quark-antiquark pairs, but a repulsive force for quark-quark interactions. Hence a scalar potential (weaker than the vector potential) providing an attractive force between both quark-quark and quark-antiquark pairs is necessary to explain the baryon and meson states.

Thus, in the bound state quarks are characterised by an effective mass $m_{eff}$, where

$$m_{eff} = m - S_o/c^2.$$

$S_o$ is the value of the scalar potential at the bottom of the potential well. He therefore suggests that if experiments are performed on bound quarks, the mass of the free quark cannot be determined since $S_o$ is an unknown parameter.

Applying this argument to Morpurgo's treatment, $M_{q(eff)}$, thus allowing nothing to be said about the free quark mass. It should also be noted that Morpurgo's calculation is non-relativistic.

3.3.3 Predicted Properties of Free Quarks

If quarks do exist as free particles, what properties do they exhibit, and in particular, what properties are the most accessible to experiment ?

Perhaps the most obvious property on which to base an experimental search is the charge of the quarks. The identification of particles with fractional charge would be taken as very strong evidence for the

existence of quarks. From section 3.1 it is to be expected that at least one quark (the p quark) should be stable, and the n quark probably would have a relatively long lifetime, so if they are produced in high energy nucleon-nucleon collisions they should travel sufficiently far from their point of origin to allow detection. The stability of the p quark also suggests that it may be found in matter, and could therefore be detected by searches aimed in this direction.

If quarks exist as free particles they are almost certainly heavy (at least several times the proton rest mass), otherwise they would be more abundant. This property, along with that of fractional charge, is perhaps the one most accessible to investigation by experiment.

From section 3.2.3, quarks probably have an interaction length for strong interactions of about three times the proton. This, combined with the fact that the ionization loss is less than that of a charge e particle and for a given energy it's range is greater because of it's mass, suggests that quarks should propagate further through matter than other particles. This suggests that, say in a search in Extensive Air Showers, it should be possible to absorb most of the accompaniment without attenuating the quark flux too greatly. Hence underground experiments or experiments with absorber covering the apparatus suggest themselves. An alternative would be to observe large angle showers, where the increased amount of atmosphere acts as an additional absorber.

3.3.4 Difficulties of the Quark Model

Several questions concerning the quark model remain to be answered. Why is it that, while quarks individually have non-integer charge in terms of the electronic charge, all observed particles have integer charge? Also, if the basic unit of charge is e/3 then it is difficult to explain how the electron has unit charge, since experimentally it is found that the magnetic moment of the electron agrees very precisely with that predicted by quantum electrodynamics under the assumption

that the electron is a point particle. To give the electron structure by assuming it to be composed of leptonic quarks of fractional charge would invalidate the theoretical treatment, and the agreement would be lost.

Most observed hadrons fit very well into the scheme predicted by the simple quark model, but there have been suggestions of violations, although the existence of none of these resonances has been proved definitely.

It is difficult also, to see why quarks and antiquarks do not combine to form exotic states such as $qqqq\bar{q}$ baryons or $qq\bar{q}\bar{q}$ mesons. Exotic states are those which are apparently forbidden in nature, but while the quark model provides a convenient description of them, as above, it does not explain their non-existence. Similarly, there is nothing in the quark model to stop an antiquark combining with three quarks, yet this state is not observed. A possible solution to these questions is that quark binding forces saturate.

Another problem arises when one considers the consequences of the quarks being fermions. Consider the $\Delta^{++}$, which consists of three p quarks in the same state. The Pauli Exclusion Principle states that the total wavefunction for the system must be antisymmetric for a system of fermions. Now since the spin and isospin wavefunctions are symmetric for the $\Delta^{++}$, the spatial wavefunction must be totally antisymmetric. This is difficult to achieve for the ground state such as the $\Delta^{++}$, where no orbital spin contribution arises.

This form of argument has led to the postulation of a modified quark model in which there are three types of each quark, forming a combination of nine fundamental particles.

## 3.4 Coloured Quarks and other Models

Giving quarks colour removes the difficulties imposed by the exclusion principle, if the principle is generalised to include colour.

The baryon state can then be defined as totally antisymmetric in it's colour wavefunction. Unfortunately, while no other baryon states are produced in this way, the multiplicity of meson states increases from 9 in the ground state to 81, since each quark and antiquark in the meson can have any colour without violating the exclusion principle. To overcome this it is then necessary to assume that for meson states the colour wavefunction is totally symmetric.

Since the symmetry group has now been enlarged beyond the basic SU(3) or SU(6) symmetry, there is more freedom allowed in choosing the charges of the quarks. The Han-Nambu model (1965) consists of quarks all of which have integral charge :-

$$Q_1^p = Q_2^p = +1$$

$$Q_1^n = Q_1^\lambda = Q_2^n = Q_2^\lambda = Q_3^p = 0$$

$$Q_3^n = Q_3^\lambda = -1$$

The concept of integral quark charge follows more naturally from this model than in an earlier model proposed by Bacry et al., (1964), which required that the Gell-Mann- Nishijima relation be modified to

$$Q = T_3 + Y/2 + D/3$$

where D was a new additive quantum number.

Similarly, the theory of Bjorken and Glashow (1964) requires a modification of the Gell-Mann - Nishijima relation. In this theory "charmed" quarks, different from the basic quark triplet, are added to the triplet to define a new conserved quantity, "charm". Charmed quarks are assumed to have a much higher mass than the three basic quarks, explaining why bound states of charmed quarks have so far not been seen.

Other "fundamental particle" theories have been proposed. Two are quite similar. One, due to Schwinger (1968), suggests the existence

of magnetic monopoles, which leads naturally to an explanation of why electric charge is quantized. An alternative theory due to Yock (1973), proposes that the fundamental particles carry high electric charge as opposed to Schwinger's model in which the particles have high magnetic charge. Both theories require six sub-nuclear particles. They will be discussed in a little more detail in section 3.6.6.

## 3.5 The Parton Model

A more general approach to the problem of sub-nuclear structure has been proposed by Feynman (1969), in which nucleons and other hadrons are composed of partons. This theory envisages the hadron to consist of a large number of point-like constituents. This approach is useful in the application of current algebra to particle-particle interactions. It is assumed that the internal motions of partons are on a time-scale comparable with the transit time of light, thus allowing little or nothing to be said about the instantaneous state of the hadron's constituents. The parton picture can however be applied usefully if the hadron is considered to be moving with almost the speed of light relative to some frame of reference. Time dilation then allows the parton motions to be slowed to any extent, hence allowing them to be "seen" as point particles. This model has been used extensively to account for the results of lepton-hadron deep inelastic scattering (section 3.6.5).

Now the parton model is a general model which can be applied to different specific types of sub-nuclear particles. Hence it is possible to construct a quark-parton model (for example Bjorken, 1973) in which in addition to the triplet of quarks of the Gell-Mann - Zweig (GMZ) model there is also an undefined number of quark-antiquark pairs forming a core. These "current" quarks are therefore totally different from the "constituent" quarks of the GMZ model, since in the constituent quark model there can only be three particles composing a baryon, say.

In addition, as has been mentioned, in the constituent quark model used for hadron spectroscopy the non-relativistic approximation is made, while the current quark model considers an ultra-relativistic infinite momentum frame. A further difficulty in reconciling the two types of quark model is that current quarks are predicted to have low mass (~300 MeV - see Bussian, 1974), while the hadron spectrum has been built up from heavy constituent quarks. Experimental searches have been undertaken at accelerators and in cosmic rays in order to attempt to provide definite answers about sub-nuclear structure.

## 3.6 Previous Searches for Quarks

### 3.6.1 Introduction

Since the advent of the quark theory in 1964, numerous searches have been carried out to search for these particles. These searches can be subdivided as follows.

1. Searches in Stable Matter
2. Spectroscopic Searches
3. Searches at Accelerators
   - (a) Proton - target nucleon interactions
   - (b) Proton - proton colliding beams
   - (c) Lepton - hadron deep inelastic scattering
   - (d) Electron - positron annihilation experiments
4. Searches in Cosmic Rays
   - (a) Sub-relativistic massive particles
   - (b) Delayed particles in Extensive Air Showers
   - (c) Fractionally charged particles
     - (i) Unaccompanied
     - (ii) Accompanied, selected by E.A.S. trigger

These various searches will be briefly summarised.

### 3.6.2 Searches for Quarks in Stable Matter

Geophysical searches have been motivated by the possibility that

if a constant flux of quarks (produced in primary cosmic ray proton interactions with the atmosphere) has been incident on the surface of the earth throughout the earth's history, then a detectable concentration of quarks should have built up in various surface materials, assuming that at least one quark is stable. Adopting a model for the production and propagation of quarks in the atmosphere (for example Adair and Price, 1966), quark concentrations in different materials have been calculated (Cooke et al., 1969, Nir, 1967). Under varying assumptions, experimenters have adopted different samples, ranging from sea-water (Chukpa et al. 1966, Rank 1968, and Cook et. al. 1969), meteorites (Chukpa et al., 1966) and rock (Cook et al., 1969), to pellets of niobium (Johnson 1969, and Hebard and Fairbank 1970).

The results of terrestrial searches, with concentration limits reached, are shown in Table 3.2. Only one group (Hebard and Fairbank, 1970) have reported positive results, in an experiment employing a magnetic levitation method to determine the charge on a niobium pellet. The experiment is, however, to be repeated with stricter control of the experimental conditions. According to Cook et. al (1969), a quark concentration of the order of $10^{-20}$ - $10^{-23}$ quarks/nucleon in surface rock, or $10^{-23}$ - $10^{-28}$ quarks/nucleon in sea-water corresponds to an unchanging sea-level intensity over the last $5.10^{9}$ years of about $10^{-9} cm^{-2} sec^{-1} st^{-1}$. This assumes a quark mass of the order of $5\ GeV/c^{2}$.

3.6.3 Spectroscopic search for Quarks in the Solar Chromosphere

Examinations of the emission line spectrum of the solar atmosphere have been conducted in an attempt to observe transitions due to quarked atoms, that is, nuclei with a -e/3 quark attached. Sinanoglu et.al.(1966) have studied the far ultraviolet end of the spectrum and identified three predicted lines of quarked carbon and nitrogen atoms. Similarly Vainshtein et.al. (1966) looked for and identified lines predicted for quarked calcium and magnesium atoms. It has been shown, however,

| Method | Sample | Concentration limit | Reference |
|---|---|---|---|
| Surface evaporation | Air | $< 5. 10^{-27}$ | Chukpa et.al (1966) |
| | Seawater | $< 3. 10^{-29}$ | |
| | Meteorite | $< 1. 10^{-16}$ | |
| Magnetic levitation | Iron | $< 4. 10^{-19}$ | Stover et.al. (1966) |
| Oil drop | Oil | $< 1. 10^{-20}$ | Rank (1968) |
| Ultraviolet spectroscopy | Seawater | $< 1. 10^{-18}$ | |
| | Seaweed, oysters and plankton | $< 1. 10^{-17}$ | |
| Magnetic levitation | Graphite | $< 1. 10^{-17}$ | Braginskii et.al. (1968) |
| Surface evaporation mass spectrometer | Air | $< 1. 10^{-24}$ | Cook et.al. (1969) |
| | Rock | $< 1. 10^{-23}$ | |
| Magnetic levitation | Niobium | $< 1. 10^{-19}$ | Johnson (1969) |
| Magnetic levitation | Graphite | $< 2. 10^{-18}$ | Morpurgo et.al. (1970) |
| Magnetic levitation | Niobium | $< 2. 10^{-20}$ | Hebard et.al. (1970) |

Table 3.2.

Summary of geophysical searches for quarks, based on a review by Cook et.al.(1969). The concentration limits quoted are in terms of the number of quarks/nucleon.

by Bennett (1966) that the lines are more likely to be weak dipole transitions of normal, "unquarked" atoms.

Postulating the existence of quark atoms in which a +2e/3 quark aquires an orbital electron, Leacock et.al.(1968) have searched for the characteristic emission lines of such an atom in the solar photosphere, but obtained only an upper limit of $<10^{-9}$ for the photospheric abundance relative to hydrogen of the quark atom.

3.6.4 Searches at Proton Accelerators

A large number of quark searches have been carried out at accelerators since 1964. The experiments employing proton beams have been of two main types:- protons incident on a target at rest in the laboratory system (targets of various metals have been used; see Table 3.3), and proton-proton colliding beams. The detectors used have been principally bubble chambers and plastic scintillation counters. Where bubble chambers were used, bubble densities were counted to yield the ionisation of the particle, and in scintillation counter experiments the particles were required to traverse several counters in which dE/dx measurements were made. A large number of counters are needed ($\geq 6$) in order to minimise fluctuation effects which could make a charge e particle appear to be fractionally charged.

The cross-section upper limits obtained from these experiments are displayed in Figure 3.5. See Table 3.3 for a key to the experiments, and for references describing the experiments.

In all cases the limits refer to the reactions

$$N + N \rightarrow N + N + q + \bar{q}$$

$$N + N \rightarrow N + q(+2/3) + q(+2/3) + q(-1/3)$$

For the pair production process the cross-section limit has been calculated assuming an isotropic centre of mass angular distribution and four-body phase space.

The thermodynamic model prediction is that mentioned in section 3.3.1.

| Label used in Fig.3.6. | Experiment | Primary beam energy (GeV). | Target | Mean of detection |
|---|---|---|---|---|
| B | Blum et.al (1964) | 27.5 | Cu | Bubble chamber ($H_2$) |
| C | Bingham et.al (1964) | 21.0 | Cu | Bubble chamber ($C_2F_5Cl$) |
| D | Dorfan et.al. (1965) | 30.0 | Be,Fe | Time of flight |
| E | Leipuner et.al. (1964) | 28.0 | Be | dE/dx (scintillator) |
| F | Franzini et.al. (1965) | 30.0 | W | Electrostatic separator and time of flight |
| G | Antipov et.al. (1969) | 70.0 | Al | dE/dx(scintillator) and time of flight |
| H | Allaby et.al. (1969) | 27.0 | Be | dE/dx(scintillator and spark chamber) |
| I | Nash et.al. (1974) | 200,300 | Be | dE/dx (scintillator) |
| J | Bott-Bodenhausen et.al.(1972) | ISR* 52GeV in CMS | - | dE/dx (scintillator) |

Table 3.3.

Quarks searches at proton accelerators. A key to Figure 3.6. The curves labelled (1) and (2) in Figure 3.6. are the predictions of the thermodynamic model of Hagedorn (1968). Curve (1) is for particles which are ground states of a series of resonances, curve (2) for particles not having this property.

*The CERN proton-proton intersecting storage rings.

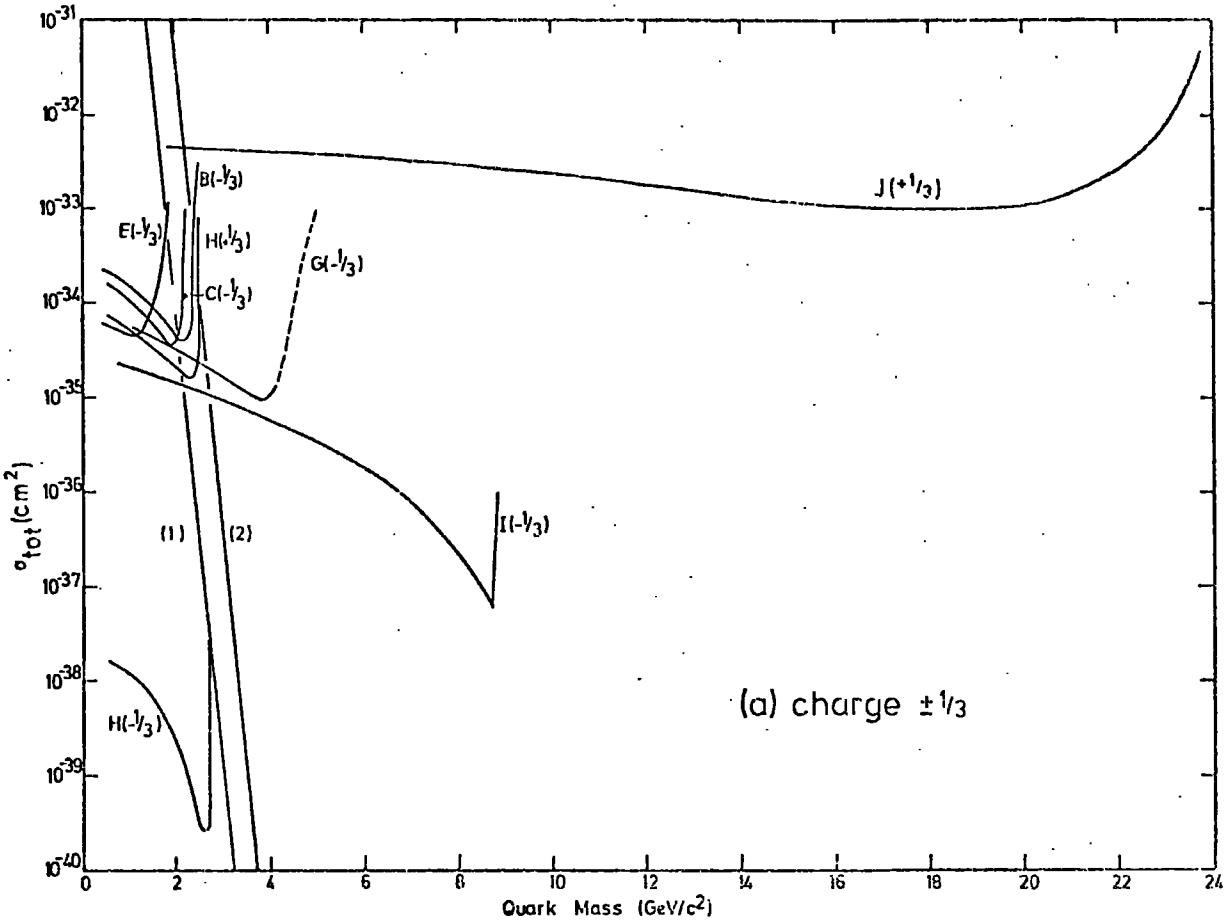


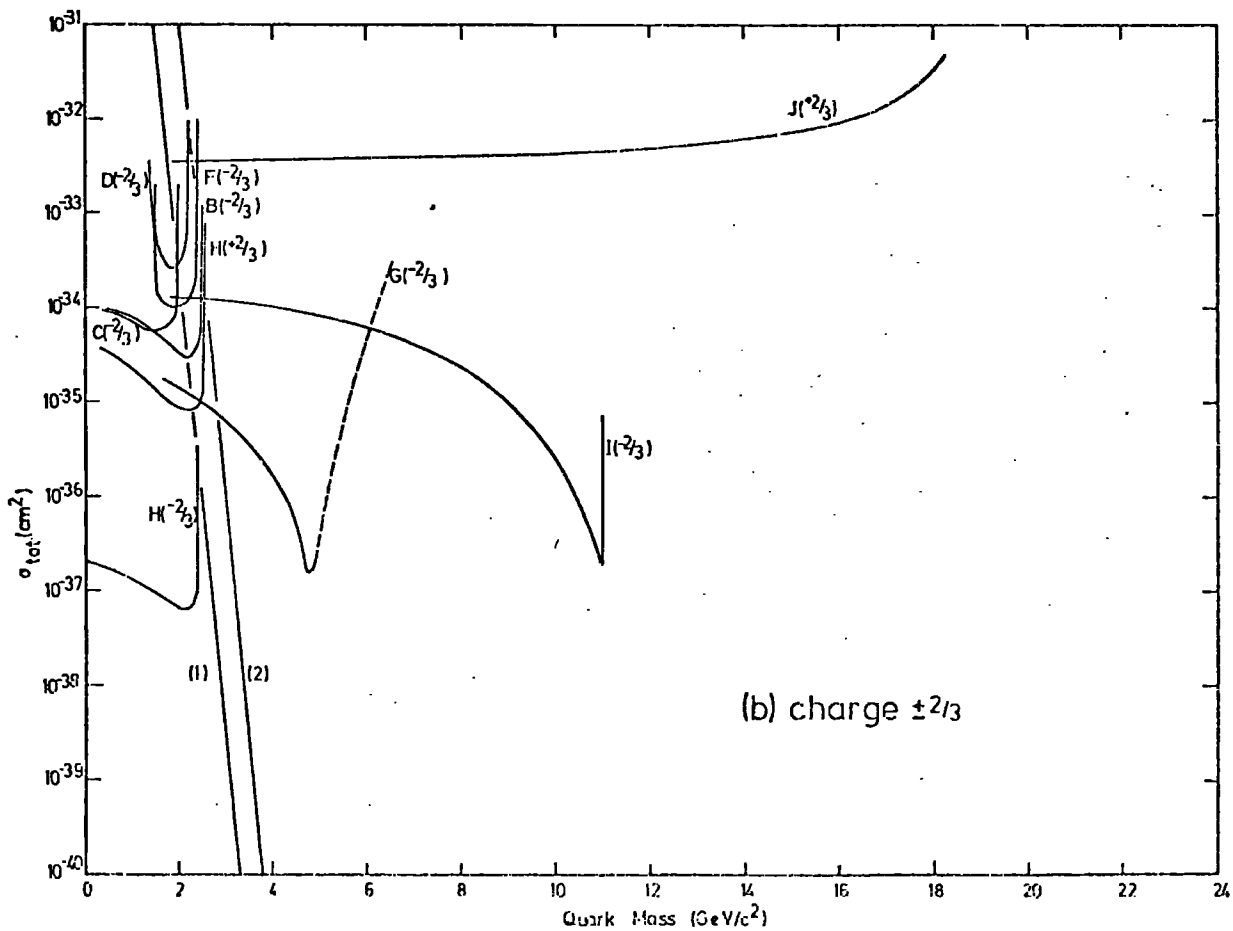


Figure 3.5. A compilation of available data on upper limits for the quark production cross-sections from proton accelerators. See Table 3.3 for key. The cross-sections have all been calculated assuming an isotropic centre of mass distribution and four body phase space. Thermodynamic model predictions are included.

3.6.5. Lepton - Hadron Deep Inelastic Scattering

Interest has, relatively recently, been directed towards experiments which are able to directly probe the structure of nucleons. This is achieved by studying the scattering of high energy point particles (leptons) on protons, neutrons and deuterons. At sufficiently high energies the scattering is deep inelastic and can probe down to distances of the order of $10^{-15}$cm. The process is represented by the diagrams of Figure 3.6.

As mentioned in section 3.5, in the infinite momentum limit scattering should occur from single partons as if they are point particles. In electron-proton scattering experiments the electron energy loss ( $\nu$ ) in it's collision with the proton is measured. If the proton has no substructure, the energy loss distribution of the electron should reflect this, providing merely a measurement of the proton momentum. However, if the proton is composed of partons, the scattering distribution of the electrons should reflect the momentum distribution of the individual partons. It has been shown by Bjorken (1969) that for a point-like parton structure, the structure functions describing deep inelastic scattering should be a function only of the ratio $\nu/q^2$, where the square of the four-momentum transfer $q^2=EE'\sin^2(\vartheta/2)$ and E is the incident electron energy, E the scattered electron energy. As a result the inelastic cross-section decreases smoothly with $q^2$. The same result applies to neutrio (antineutrino - nucleon scattering and is known as Bjorken scaling.

Several experiments have been performed using electron and neutrino beams of sufficiently high energies to approach the Bjorken limit, and these have indeed found scaling to apply. For details of the eN experiments, see for example Bloom et.al.(1969), Miller et.al.(1972), Dakin et.al.(1973), and for the results from $\nu$N, $\bar{\nu}$N experiments, see Eichten et.al.(1973), Benvenuti et.al.(1973) and Barish et.al. (1973).

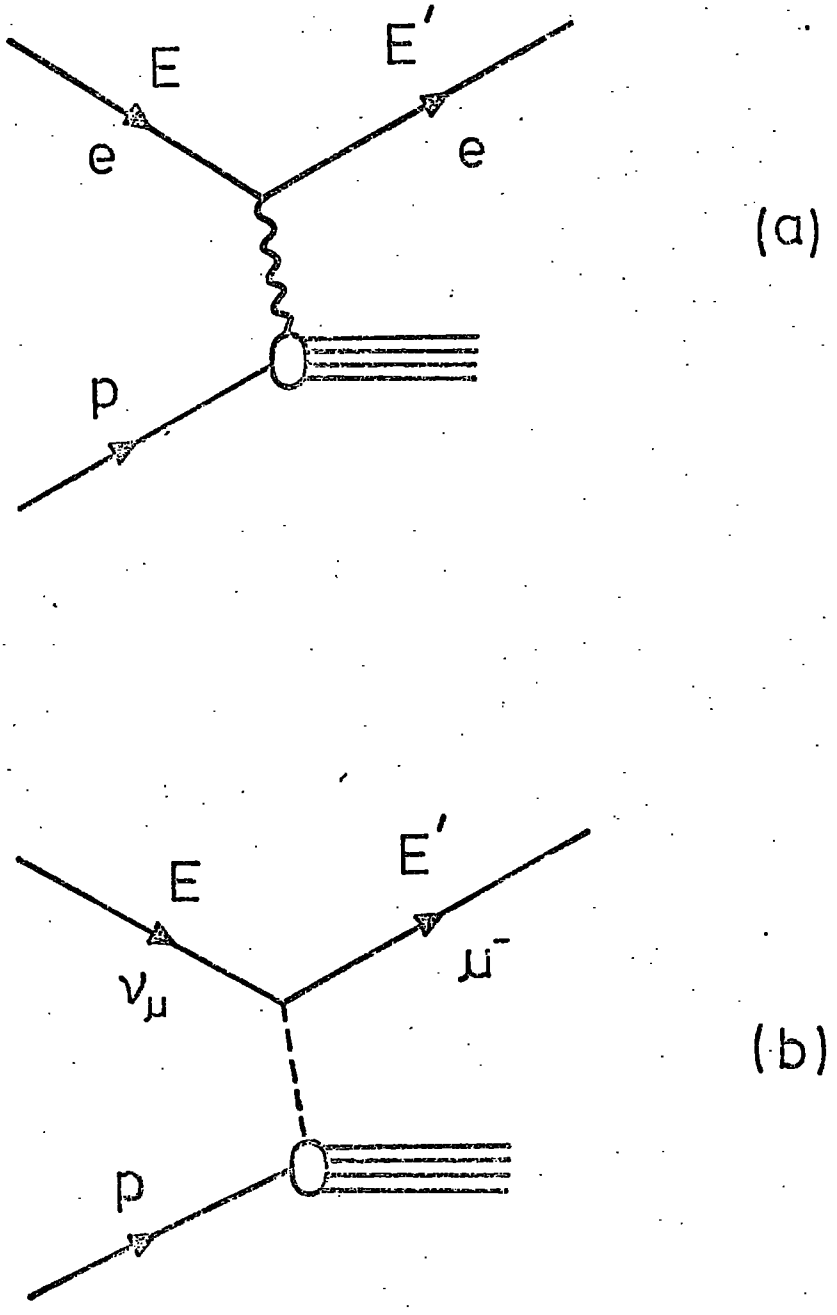


Figure 3.6. Leptron-hadron deep inelastic scattering. (a) represents electron scattering and is an electromagnetic interaction; (b) represents neutrino scattering and occurs via the Fermi(weak) interaction.

These results have been explained by several authors in terms of a quark parton model (QPM). In the experiment of Dakin et.al. (1973), a large excess of positive hadrons over negative hadrons, all predominantly pions, was observed to be produced. Dakin et.al. interpret this in terms of the QPM by assuming that the virtual photon preferentially interacts with a p quark (the cross-section is predicted to be proportional to the square of the quark charge), which then fragments producing an excess of positive pions.

Kurti et.al.(1971) use a QPM to compare with the MIT - SLAC results, in which the three Gell-Mann - Zweig quarks form valence quarks carrying the total quantum numbers of the nucleon, and an indefinite number of quark-antiquark pairs form a core bound by gluons. Interactions should occur with the valence quarks only. A similar QPM is suggested by Gronau et.al.(1973). Both theories agree approximately with the results of lepton-hadron deep inelastic scattering. That is, they predict point-like sub-nuclear particles within the nucleons with spin 1/2, and predict approximately the correct form for the deep inelastic scattering electromagnetic structure functions for the proton and neutron.

Recently, however, it has been suggested that scaling should break down for large $q^2$ as the experiments probe deeper into the structure of the nucleon. Chanowitz and Drell (1973) speculate that the binding force between partons is supplied by the exchange of massive gluons, and that the partons are surrounded by gluon clouds, hence having structure. The dimensions of this field provide an estimate of the gluon mass. The parton structure $G(q^2)$ can be represented by

$$G(q^2) = (1 + q^2/M_C^2)^{-1}$$

such that the Bjorken scaling result is modified to

$$\nu W_2 \xrightarrow[q^2 \to \infty]{} F_2(-q^2/M\nu).\ G(q^2)$$

where $W_2$ is one of the electromagnetic structure functions describing deep inelastic scattering discussed earlier, and the terms $\nu$, $q^2$ have the same notation as defined above. The other structure function, $W_1$, is similarly modified.

This behaviour is not apparent from results on electron-nucleon scattering since the values of $q^2$ reached extend only to 10 GeV$^2$, but the results of $\nu$N and $\bar{\nu}$N experiments (Benvenuti et.al.1973 and Barish et.al., 1973) could indicate a breakdown of scaling at distances $\lesssim 4.10^{-15}$cms. Barger (1974) interprets the NAL data of Barish et.al. in terms of a gluon mass $M_G \sim 10$ GeV, but this must be very tentative. More data is required at high four-momentum transfers.

Experiments on lepton-hadron deep inelastic scattering, then, seem to confirm that there exist within nucleons fundamental particles, partons, which are consistent with quarks in that they have spin 1/2 (i.e. fermions). Clear results concerning measurements of the parton charge have yet to be obtained.

3.6.6 Electron-Positron Annihilation Experiments

The above results, then, seem to support some form of quark theory, and it seemed that a reasonably consistent picture of nucleon structure was emerging. Recent results from experiments on $e^+e^-$ annihilation with multi-hadron production have cast doubt on the correctness of two of the models, the naiive quark model and the coloured quark model.

Assuming the validity of a quark parton model, the production of hadron final states would go via the channel shown in Figure 3.7, to be compared with the channel for muon pair production. The diagram drawn for hadron production is the one-photon exchange process, in which a quark-antiquark pair are produced as an intermediate stage.

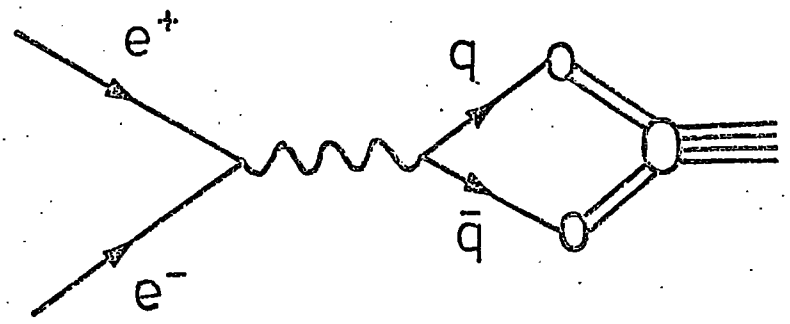


(a)

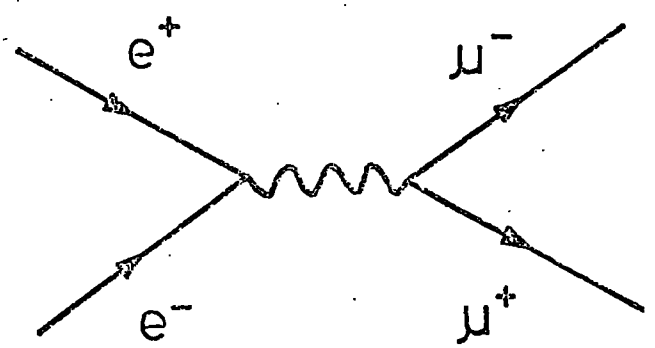


(b)

Figure 3.7. Electron-positron annihilation diagrams in which (a) quark-antiquark are produced which then fragment to produce hadrons, and (b) a muon pair is produced.

Now a quantity R can be defined, where

$$R = \frac{\sigma_{tot}\,(e^+e^- \longrightarrow \text{hadrons})\ 1\gamma}{\sigma_{tot}(e^+e^- \longrightarrow \mu^+\mu^-)}$$

To obtain this ratio from the quark model, the cross-sections for $q\,\bar{q}$ and $\mu^+\mu^-$ production are assumed (in the asymptotic region) to be proportional to the square of the particle charge summed over all possible channels. Thus R is obtained, for the naiive quark model, as

$$R = \frac{(2/3)^2 + (1/3)^2 + (1/3)^2}{(1)^2} = 2/3$$

The coloured quark model of Han-Nambu (1965), with three times as many of each type of quark, yields the value R = 2.

More generally, considering spin :-

$$R = \sum_{\substack{\text{spin } \frac{1}{2} \\ \text{partons}}} q_i^{\,2} + 1/4 \sum_{\substack{\text{spin } 0 \\ \text{partons}}} q_i^{\,2}$$

(Bjorken, 1973) where $q_i$ is the parton charge for partons of spin 1/2 and spin 0. Since the process $e^+e^- \longrightarrow \mu^+\mu^-$ is well understood theoretically (from quantum electrodynamics), the ratio R is accessible to experiment. Several experiments have recently been carried out to measure this quantity. See Litke et.al.(1973) for a complication of data and references. Figure 3.8 is taken from the paper of Litke et.al. and shows the experimental points. Also shown are the constant lines representing the asymptotic value of R predicted by the two quark theories mentioned above. Even if the asymptotic region has not yet been reached, it is difficult to see how agreement between either of these theories and experiment can be found. Presumably

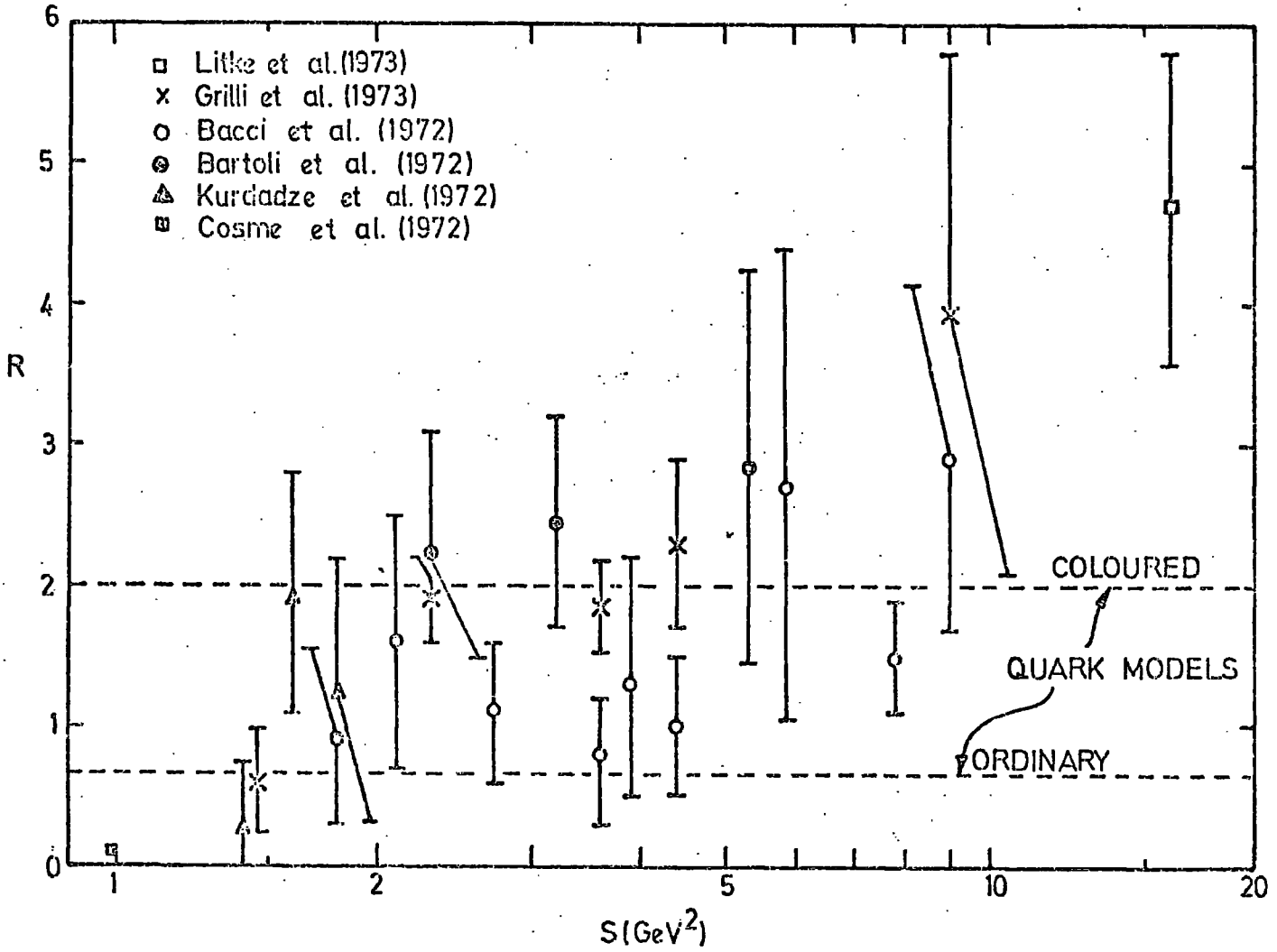


Figure 3.8. $R = \sigma(e^+e^- \rightarrow \text{hadrons}) / \sigma(e^+e^- \rightarrow \mu^+\mu^-)$ versus the square of the centre-of-mass energy S. The dashed lines give the predictions of R for ordinary and coloured quarks. After Litke et.al.(1973).

quark parton models could produce a higher asymptotic value of R. For a comprehensive review of theories related to this field, see Bjorken (1973).

In section 3.4 the models of Yock and Schwinger were mentioned, in which the fundamental particles are, respectively, highly electrically charged and highly magnetically charged. Yock (1974) suggests that these two models predict behaviour for R which is consistent with the experimental results obtained so far. In addition, Yock's model quite naturally produces a form factor for parton structure since his partons are in fact the original Yukawa particles, which themselves are composed of quarks (high Z).

Obviously these two fields of research, lepton-hadron deep inelastic scattering and electron-positron annihilation are now producing important results as regards the structure of hadrons, and it is necessary for further experiments to be performed in these fields, extending the measurements to higher energies. These experiments are at present in progress.

3.6.7 Searches in Cosmic Rays

While accelerator searches have been able to put very low limits on the cross-section for the production of free quarks of mass less than a few GeV, energy limitations have made it impossible so far to extend the search to high quark masses (several tens of GeV). This has been the motivation for the large number of searches carried out since 1964 in cosmic rays, where energies several orders of magnitude above those at accelerators are available.

The quark searches in cosmic rays have been of the following types:-

(a) searches for sub-relativistic massive particles

(b) delayed particles in Extensive Air Showers (E.A.S.)

(c) searches for unaccompanied fractionally-charged particles

(d) searches for fractionally-charged particles close to E.A.S. cores.

(a) Searches for sub-relativistic heavy-mass particles.

These searches have relied on time of flight and range measurements. Franzini et.al.(1968) operated this type of detector at large zenith angles. Obtaining no signal, they quoted an upper limit of $2.2.10^{-8}$ $cm^{-2}sec^{-1}st^{-1}$. Another experiment looking at large zenith angles (Kasha et.al., 1968), and including a magnet for determination of the particle momentum, again found a negative result and quoted an upper limit of $2.4.10^{-8}cm^{-2}sec^{-1}st^{-1}$. The lowest limit obtained by the velocity/range technique is that of Ashton et.al.(1969), who quoted an upper limit of $4.9.10^{-10}cm^{-2}sec^{-1}st^{-1}$. More recently, Galper et.al. (1970), operating under 80 cms. concrete, obtained an upper limit of $3.4.10^{-8}cm^{-2}sec^{-1}st^{-1}$. A positive result has, however, been reported by Yock (1973). Using a similar telescope to that used by Ashton et.al. but under 600 $g.cm^{-2}$ concrete (see Alcock et.al., 1974), two strange events (identified as due to massive particles) have been observed in a preliminary experiment, corresponding to a flux of approximately $2.10^{-9}cm^{-2}sec^{-1}st^{-1}$.

(b) Delayed particles in EAS

The basis of this method is that if quarks are produced in high energy interactions of a primary proton with air nuclei they should be present in EAS (assuming sufficient energy goes into the nuclear-electromagnetic cascade to produce an air shower that survives to sea-level). Now if quarks are massive they will lag behind the shower front, which can be considered to form a spherical shell of thickness 3 metres. Typically, the time delay ( $\Delta t$) between the arrival of the shower front and the arrival of any quarks produced at a height H (the point of first interaction) is

$$\Delta t = \frac{H}{\beta_q c} - \frac{H}{c} \approx \frac{H}{c} \cdot \frac{1}{2\gamma_q^2}$$

assuming that the shower front is moving with almost the velocity of

light (c).

The delays should range from zero up to ~100ns, depending on the model adopted for the production of the quarks and hence the energy of the quark.

Several experiments have been performed in an attempt to detect delayed massive particles. Discrimination against low energy shower particles which could also exhibit large time delays is necessary, this usually being achieved by either measuring directly the energy of the delayed particle or operating underground and hence imposing a threshold energy requirement on the particles.

Kelly (1969) has made an exhaustive survey of experiments up to 1969, and later searches have been reviewed by Jones (1971). Most experiments produced negative or unclear results. Only the Turin group (Dardo et.al., 1968, 1972) and the Tata Institute group (Tonwar et.al., 1971, 1973) have reported positive results, other groups producing upper limits on the flux of delayed particles of about $10^{-10}cm^{-2}sec^{-1}st^{-1}$. The Turin group obtained a signal at a level of a few times $10^{-8}cm^{-2}sec^{-1}st^{-1}$, two orders of magnitude above the upper limits set by the other groups. However having no visual detector it is possible that the delayed events were due to showers produced locally by muons in the rock. More recently, Clark et.al.(1973) have produced a new estimate of the flux of $2\pm1 \cdot 10^{-9}cm^{-2}sec^{-1}st^{-1}$. Tonwar et.al. do not give any flux figures in their latest paper (Tonwar et.al., 1973), but they observed two events with energies of 36 and 28 GeV and delayed by 41ns and 25ns respectively. For energy determination of the delayed particles the Tata group employ a multiplate cloud chamber, scintillators being used to measure the time delay.

(c) Searches for unaccompanied, fractionally-charged particles.

This area has produced the most numerous experiments of any in searches for quarks in cosmic rays. All have employed energy loss

techniques, relying on the assumption that the energy loss of a charged particle by ionisation is proportional to the square of the charge. In general several layers of detectors were employed to minimise the effects of fluctuations, the detectors consisting of scintillation counters, proportional counters and chambers, or spark chambers. All experiments have yielded negative results. For reviews of these experiments see Kelly (1969), Sitte (1970) and Jones(1970, 1971). The lowest intensity limits imposed so far are:-

| Charge | Flux limit($cm^{-2}sec^{-1}st^{-1}$) | Experiment |
|---|---|---|
| e/3 | $< 0.57.10^{-8}$ | Chin et.al. (1971) |
| 2e/3 | $< 0.8 .10^{-8}$ | Ashton et.al. (1968) |

It should be noted that since these experiments reject all events in which there is accompaniment, the energy of the proton (say) causing the initial interaction is limited to about $5.10^{12}$eV, this figure being derived from consideration of the lateral distribution of electrons in air showers (Ashton, 1973b). Ashton concludes that this would correspond to an upper limit for the quark mass of 7.5 GeV/$c^2$.

(d) Searches for fractionally-charged particles in EAS.

In order to attempt to detect quarks if their mass is greater than 7.5 GeV/$c^2$, it is necessary to look close to the core of air showers of relatively high primary energy ($\lesssim 10^{14}$ - $10^{15}$eV). This requires the use of visual detectors, enabling individual particle tracks to be observed and the ionisation estimated. Counters cannot be used since the accompaniment would cause events to be rejected.

The Sydney group were the first to perform an experiment in which they looked close to air shower cores using cloud chambers triggered by a local electron density detector system. They reported positive results at a flux level of $5.10^{-10}cm^{-2}sec^{-1}\ st^{-1}$ for charge 2e/3 particles (Cairns et.al., 1969 and McCusker and Cairns, 1969).

| Technique | Local electron density trigger requirement ( e) | Flux obtained $\times 10^{10} cm^{-2} sec^{-1} st^{-1}$ e/3 | 2e/3 | References |
|---|---|---|---|---|
| Cloud chamber | $> 154\ m^{-2}$ | - | ~5 | Cairns et.al.(1969) |
| Cloud chamber | $> 150\ m^{-2}$ | - | < 0.5 | Hazen (1971) |
| Cloud chamber | $> 86\ m^{-2}$ | < 3.0 | < 0.3 | Clark et.al.(1971) |
| Flash tube chamber | $> 40\ m^{-2}$ | < 2.6 | - | Ashton et.al.(1971) |
| High pressure cloud chamber (28 atoms.He) | $> 60\ m^{-2}$ | < 40 | - | Evans et.al.(1971/72) |

Table 3.4

The status of the quark search in experiments looking close to the core of EAS, as of 1972.

This result was criticised by several authors (Adair and Kasha 1969, Rahm and Louttit 1970, Fraunfelder et.al. 1970, Kiraly and Wolfendale 1970), but was sufficient to stimulate interest in the technique, several groups initiating similar searches.

Most groups adopted cloud chambers similar to McCusker's for their detectors, and also used a local density trigger . No definite quarks have so far been observed by any other group. Indeed, McCusker observed no more candidates in another two years after having made improvements to his detector.

Table 3.4 shows the situation as it was in 1972 as regards the quark search close to the cores of EAS.

However, the fundamental importance of quarks if any exist was felt to be sufficient to justify a further search in air showers, since this seemed to be the most fruitful area to investigate. Hence in 1970 the flash tube chamber described in Chapter 2 was built by Ashton and King. An exploratory experiment was reported by Ashton et.al. (1971). Chapter 4 describes a detailed experiment performed at Durham to search specifically for e/3 charge particles.

# CHAPTER 4

## THE QUARK EXPERIMENT

### 4.1 Introduction

It was shown in Chapter 2 that the flash tube chamber is sensitive to particles of charge e/3 but not to charge 2e/3 particles, since these cannot be resolved from the distribution of charge e particles. Hence the search was directed towards the detection of e/3 quarks, and since it appears that the most fruitful area for a search of this kind is close to the core of extensive air showers (see Chapter 3 for discussion), the trigger for the present experiment was designed for this purpose.

Near the core of EAS the density of particles is high, so while the soft component (electrons and photons) can be absorbed above the detector by the lead shield, good spatial resolution is necessary to enable the tracks of individual particles to be studied in the presence of other particles. The flash tube chamber has a resolution in the projected plane of approximately 2 cms. (the diameter of a flash tube) for each track, hence satisfying this criterion. The aim of the present experiment was to look for particles which produced tracks in the chamber having a low number of flashes along the track, corresponding to the particles having produced less ionisation in the flash tubes on their passage through the chamber. These tracks were then examined in order to determine whether or not they satisfied the requirements of a track produced by a particle of charge e/3.

The time delay $T_D$ (the time between the particles passing through the chamber and the high voltage pulse being applied to the electrodes between the layers of flash tubes) was chosen to be 20$\mu$S, this being considered to be the optimum, allowing wide separation of e/3 quark tracks from the efficiency distribution of charge e particles while being sufficiently short to ensure that the quark tracks were not lost

in the background due to spuriously flashing tubes (or tubes which flash because of residual radioactivity in the glass of the tube).

## 4.2 Basic Experimental Data

With the local electron density trigger set at a lower threshold of 40 particles per square metre, in a running time of 2570 hours a total of 12,057 triggers occurred, each event being recorded photographically. The analysis procedure consisted of projecting the negative obtained onto a scanning table, where each event could be examined in detail. The reconstructed event was reduced relative to it's size in real space by the ratio 1:4.5.

An acceptable track was one which produced at least one flash in F1 and F4 (see Figure 2.1). This ensures, since the defining layers F1 and F4 are shorter than the measuring layers F2+F3, that the track has passed through F2+F3 within the volume of flash tubes covered by electrodes.

The number of flashes in F2+F3 ($N_f$) along a track was then measured if the track was accompanied by a parallel track (within $\pm 5^\circ$ in the projected plane) of projected length greater than 60 cms. If the track was obviously of low efficiency ($< 60$ flashes) it was measured irrespective of whether or not it had an accompanying parallel track. A small-scale diagram of all measured events was made. The high efficiency tracks (produced in general by muons) thus provided a calibration for charge e particle tracks.

Table 4.1 shows a summary of the data, with a breakdown into the multiplicity of measurable tracks per event.

As can be seen from Table 4.1, a total of 4501 tracks were measured, the distribution in the number of flashes ($N_f$) being shown in Figure 4.1. The arrows indicating the expected positions of plateau and minimum ionising particles of charge e were calculated from the paper of Crispin and Fowler (1970), who give the most probably ionisation loss in neon as a function of muon momentum. It was assumed that the median momentum

| Number of measurable tracks per photograph (n) | Number of Photographs (N) | N x n |
|---|---|---|
| 1 | 1604 | 1604 |
| 2 | 758 | 1516 |
| 3 | 254 | 762 |
| 4 | 84 | 336 |
| 5 | 42 | 210 |
| 6 | 7 | 42 |
| 7 | 3 | 21 |
| 8 | 0 | 0 |
| 9 | 0 | 0 |
| 10 | 1 | 10 |
| TOTAL | 2753 | 4501 |

Table 4.1. The frequency distribution of the number of triggers N having n measurable tracks, from a total of 12,057 photographs obtained in a running time of 2570 hours.

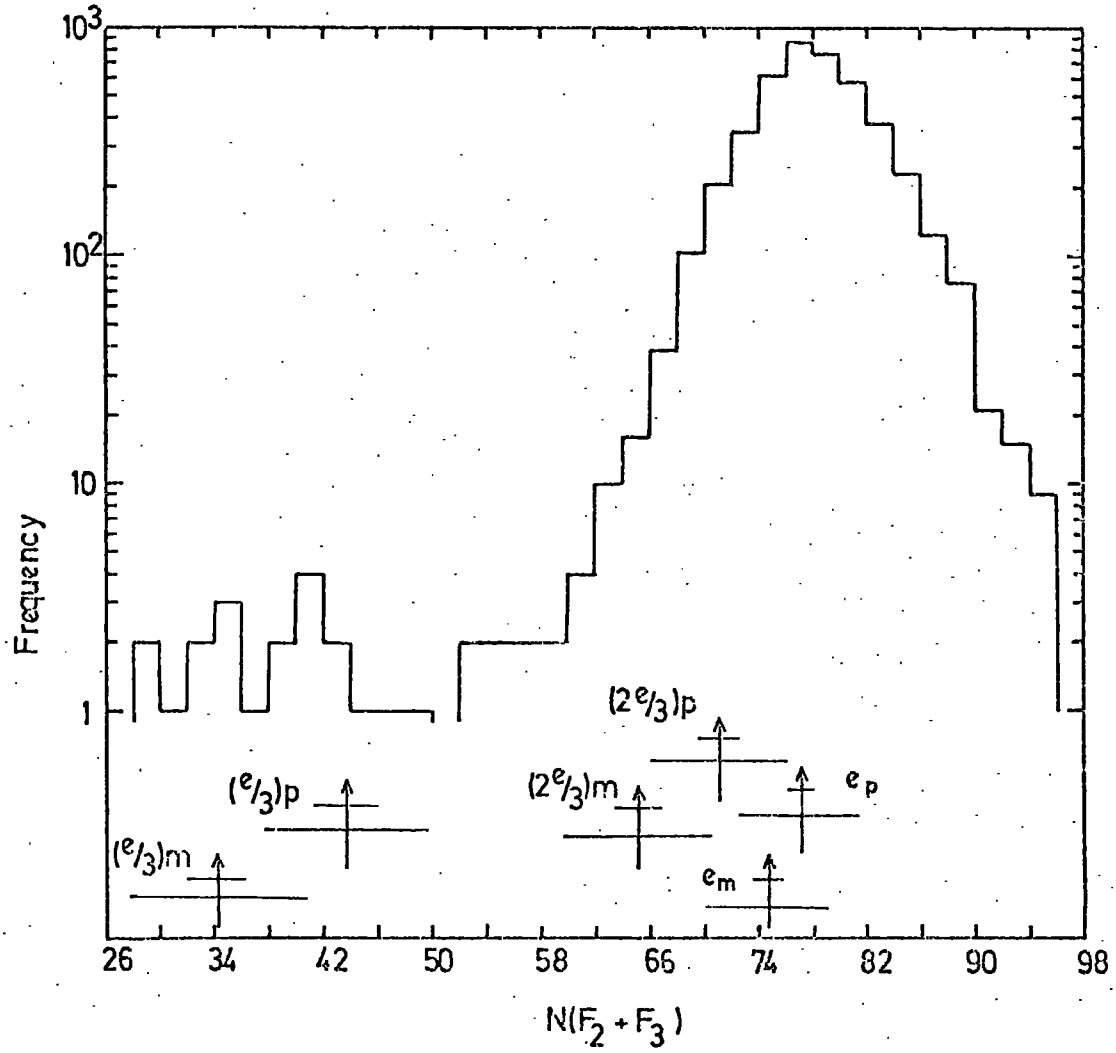


Figure 4.1 The frequency distribution of the number of flashes $N(F_2+F_3)$ along a track in the 96 layers of flash tubes. Tracks with $N(F_2+F_3) > 60$ were only measured if they had at least one other shower track parallel ($\pm 5^\circ$) to it of length >60 cms. The arrows indicate the expected positions for minimum and plateau ionising e, 2e/3 and e/3 particles. The small bars indicate the uncertainty in this position and the large bars indicate the width of the distribution. The total number of tracks measured was 4501. $\bar{N}=78.11\pm.07$, $\sigma=4.73$.

of the muons used in the calibration run described in Chapter 2 was 2.1 GeV/c (derived from the spectrum of Hayman and Wolfendale, 1962). Now the Lloyd parameter ($af_1Q_1$) fitting muons of this energy was found to be $9 \pm 1$ (Figure 2.10), hence knowing the ratio of the amount of ionisation produced by these muons to that of plateau and minimum ionising muons (from Crispin and Fowler), the Lloyd parameter appropriate to these cases could be calculated and hence the expected value of $N_f$ could be estimated. The expected positions for e/3 and 2e/3 quarks are obtained by dividing the Lloyd parameter calculated for charge e particles by 1/9th. and 4/9th. respectively, since the value of the Lloyd parameter is proportional to the charge squared of the traversing particle. The widths expected for the distributions indicated in Figure 4.1 were calculated assuming the standard deviation of the distributions to follow the experimental curve drawn in Figure 2.9.

It can be seen from Figure 4.1 that 20 tracks were observed whose $N_f$ value was less than the one standard deviation upper limit of 50 for plateau ionising e/3 quarks. It was estimated that the lowest density track that would be seen with the scanning technique employed would be approximately $N_f = 20$, whilst the lowest expected $N_f$ value for an e/3 quark (at a one standard deviation level) would be 28. Hence all e/3 quark tracks not obscured by other tracks or by electromagnetic cascades produced in the shielding should be recorded with almost 100% efficiency. The 20 quark candidates were examined in detail in an attempt to determine whether they are tracks produced by genuine quarks.

## 4.3 Consideration of Background Effects

### 4.3.1 Reduction in flashing efficiency due to a clearing field

When breakdown of the gas occurs in a neon flash tube, large numbers of electrons and positive ions remain after cessation of the pulse. Many of these adhere to the glass wall of the tube. The time

for neutralisation of these charges to occur can be of the order of minutes, being determined largely by the surface resistance of the glass. While these electrons and positive ions remain uncombined they can give rise to an electric field within the tube. This field is sufficiently strong to sweep from the gas any new ions produced by the passage of another ionising particle within the time needed for neutralisation to occur. This has the effect of reducing the internal efficiency. Hence if a particle passes through the flash tube chamber a short time after a dense shower has triggered the chamber, the particle will be seen to have a smaller number of flashes along it's track. In order to avoid the possibility that this effect could make an ordinary shower track appear as a track due to a quark, the effect was studied in some detail so as to allow the elimination of any quark candidate produced by this mechanism. In events which followed a dense shower, tracks or parts of tracks were examined and the reduction in efficiency, if any, measured. The results are shown in Figure 4.2. For comparison the results obtained by Ashton et.al.(1971) at a time delay of 40 μs are also shown.

In particular the quark candidates were checked to see whether any had been produced by this effect. It was concluded that none had.

4.3.2 The rate of background muons

The major background effect is due to incoherent muons which traverse the chamber immediately before the chamber is triggered by an air shower. For a background muon to have an efficiency in the range $N_f$ = 28 - 50 requires that it had traversed the chamber in the period 103 - 144 μS before the air shower trigger occurs (see Figure 2.10). It is therefore necessary to estimate the probability of a muon traversing the chamber in this period.

Assuming a minimum momentum of 0.78 GeV/c for muons to traverse the flash tube chamber within the geometrical acceptance, from the sea-level vertical muon momentum spectrum of Hayman and Wolfendale

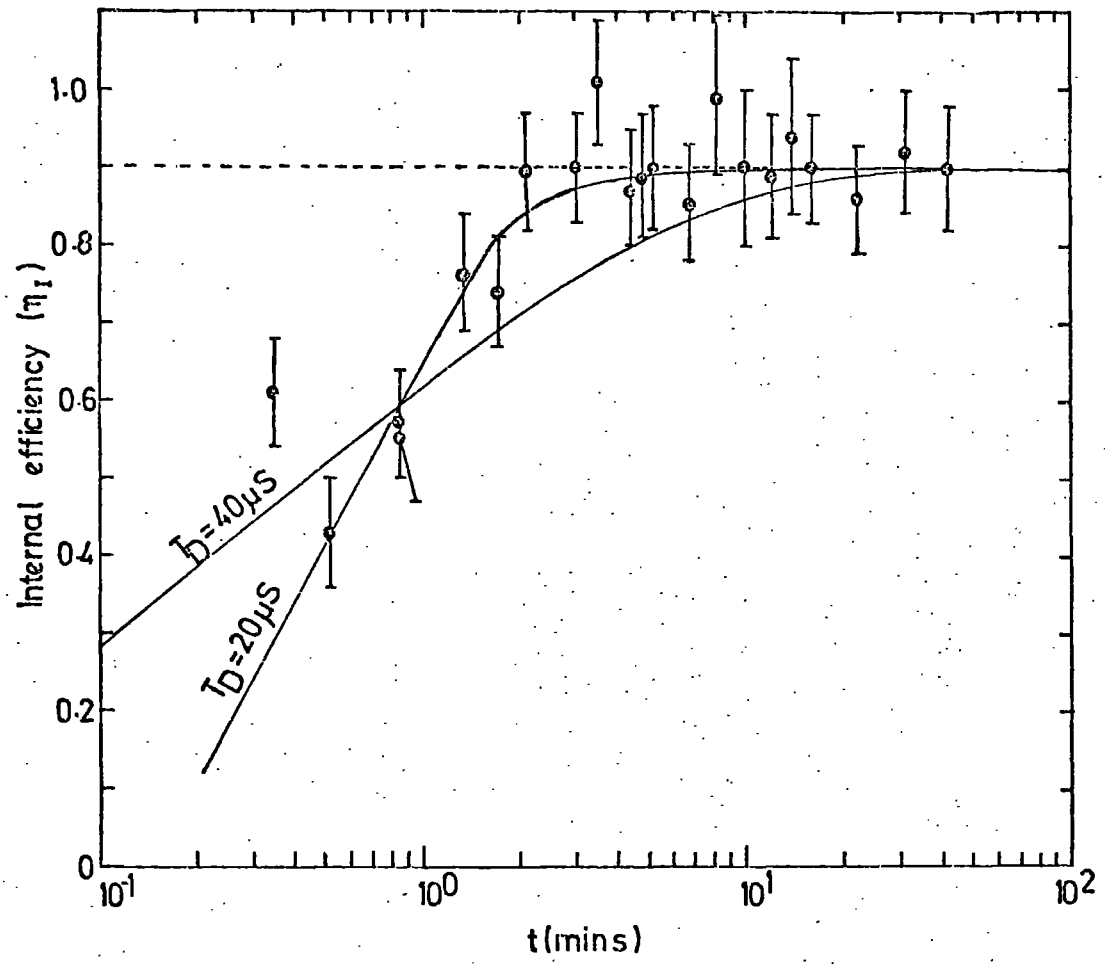


Figure 4.2 The effect of the remnant clearing field on the internal efficiency of the flash tubes as a function of time. The experimental points were obtained at a time delay $T_D$ = 20 μs.

the flux of muons through the chamber should be $6.3.10^{3} cm^{-2} sec^{-1} st^{-1}$. [This should be compared with a measurement of the coincidence rate for the plastic scintillators A and B of $11.5 \pm 0.4$ $sec^{-1}$. For this geometry (see Figure 2.1) the calculated rate using the above flux is 11.2 $sec^{-1}$, in good agreement]. Using this figure the flux of incoherent muons through the whole chamber, within the acceptance geometry for measurable tracks, was calculated to be 104.2 $sec^{-1}$. In addition, it can be shown that the probability distribution for a background muon track to produce a track with $N_f$ in the quark region (28-50) should be flat (Appendix A).

Since quarks are expected to arrive more or less parallel to the shower direction, only the low efficiency tracks which were within $\pm 5^{\circ}$ to the shower direction were accepted. Hence it is necessary to estimate the number of background muon tracks which would satisfy this additional criterion. In order to calculate this quantity, approximately 500 events were scanned to evaluate the proportion of events which could have contained a background track simulating a quark, i.e. the proportion of events in which there was a shower track of length $> 60$ cms. in F2+F3 and which was free from obscuration. This was estimated to be 0.312, giving a number for the total number of photographs which could have contained a background track of 12,057x0.312=3,760 events.

Hence the total sensitive time for incident incoherent muons to simulate a quark (that is, have traversed the chamber between 103-144 μS before the air shower trigger and have at least one shower track of length $> 60$ cms. in F2+F3 in the event) is $3760 \times 41.10^{-6} = 0.154$ seconds.

The maximum angle for the acceptance of a track is $36^{\circ}$, therefore the probability of a random background muon being within $\pm 5^{\circ}$ of a shower track (assuming a flat angular variation for the muon intensity) is 5/36. Thus the expected number of background tracks simulating quarks is given by $104.2 \times 0.154 \times 5/36 = 2.2$.

Now when the angular restriction is placed on the 20 quark candidates with $N_f$ in the range 28 - 50, the number is reduced to 6. This distribution is shown in Figure 4.3.

4.3.3 The number of knock-on electrons along a track

Since the probability of a particle producing a knock-on electron (KO) is proportional to the square of the charge of the particle, it is to be expected that quark tracks should have significantly less KO's than those of charge e particles. Now knock-on electrons are a noticeable feature of muon tracks observed in the flash tubes, hence this technique should provide a means of identifying genuine quark tracks.

In order to test the sensitivity of the flash tubes to knock-on electrons, the 1,046 muon tracks obtained at a time delay of 20 μs during the calibration run described in section 2.5.1 were scanned, the angle of emission and range of the electrons being measured. To obtain an approximate value for the energy of an electron, electrons were assumed to lose energy only by ionisation (a reasonable approximation below the critical energy, ~25 MeV), being about 1 MeV per flash tube traversed. Only projected angles and track lengths could be measured, this limiting the resolution. The results are shown in Figures 4.4 and 4.5. From 1,046 muon tracks measured, the number of knock-on electrons of energy >3 MeV produced in the 96 layers of F2+F3 was found to be 388. Figure 4.5 shows that the energy distribution has essentially the correct form. The large scatter in the points shown in Figure 4.4 is presumably due to multiple scattering of the tracks, which is considerable at low energies, and also to the fact that we are dealing with projected angles. Because of the multiple scattering, below ~3 MeV it is not possible to estimate energies with any accuracy.

Now for application to the identification of quark tracks, knock-on electrons of energy less than 3 MeV need to be utilised in order to increase counting statistics. Since individual energy measurements

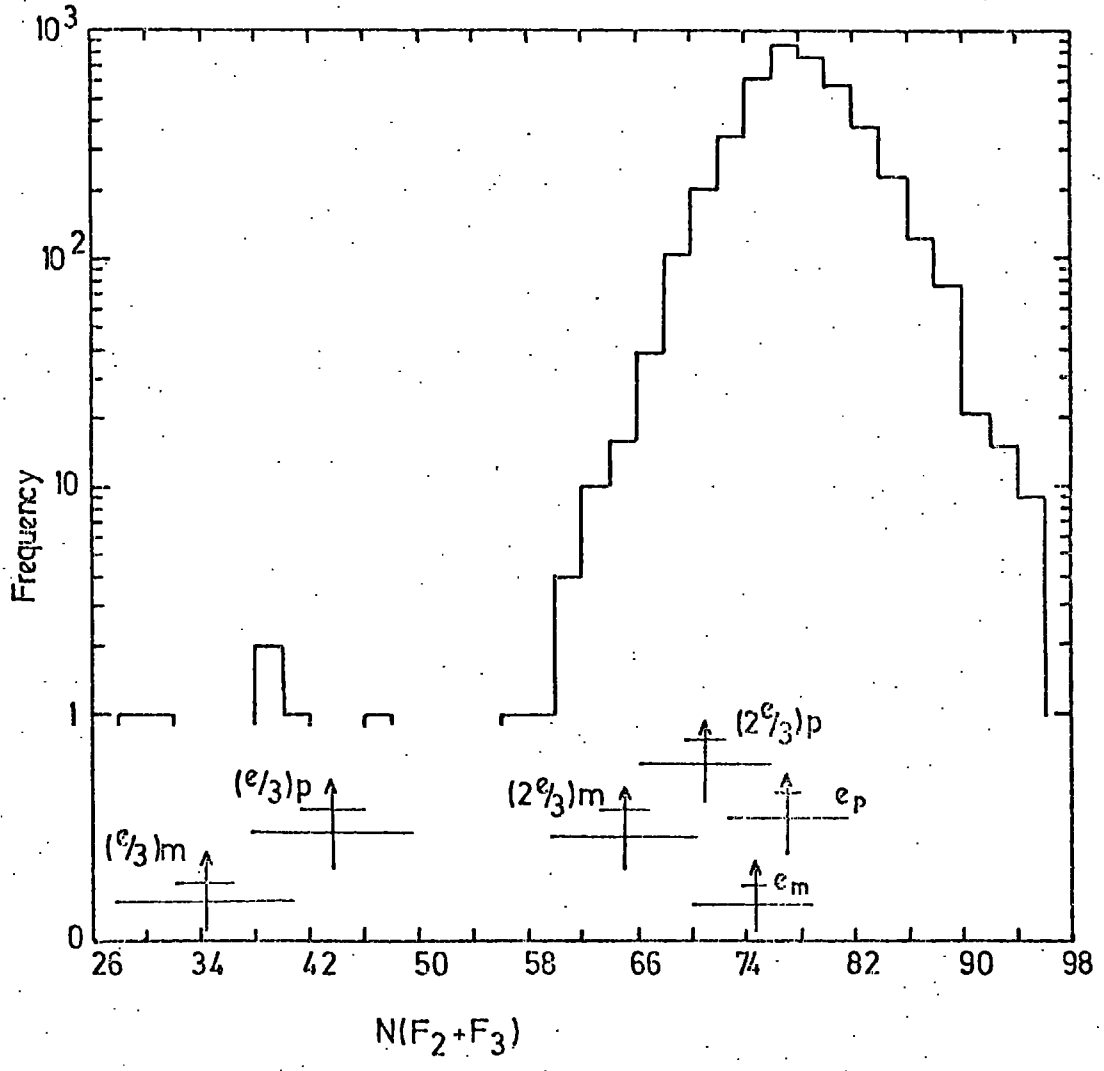


Figure 4.3 As Figure 4.1 but with an added requirement placed on all events with $N(F_2+F_3) < 60$ that they must be parallel to within $\pm 5^o$ to other shower tracks.

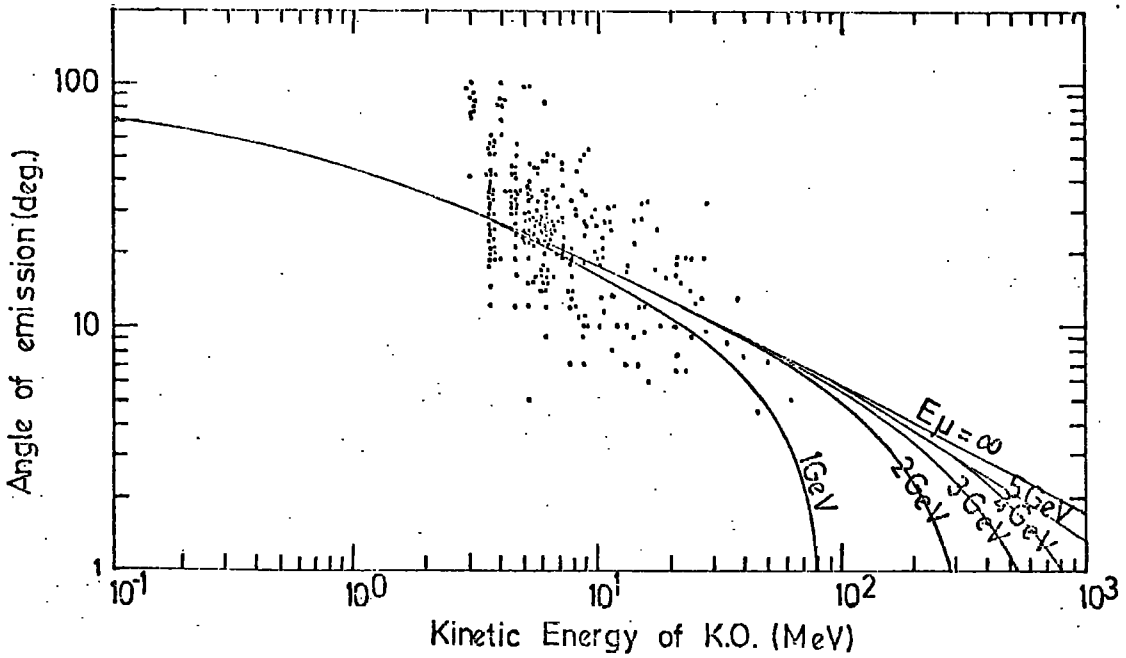


Figure 4.4 Scatter plot showing the correlation between recoil angle and electron energy. The energies Eμ refer to the primary muon energy.

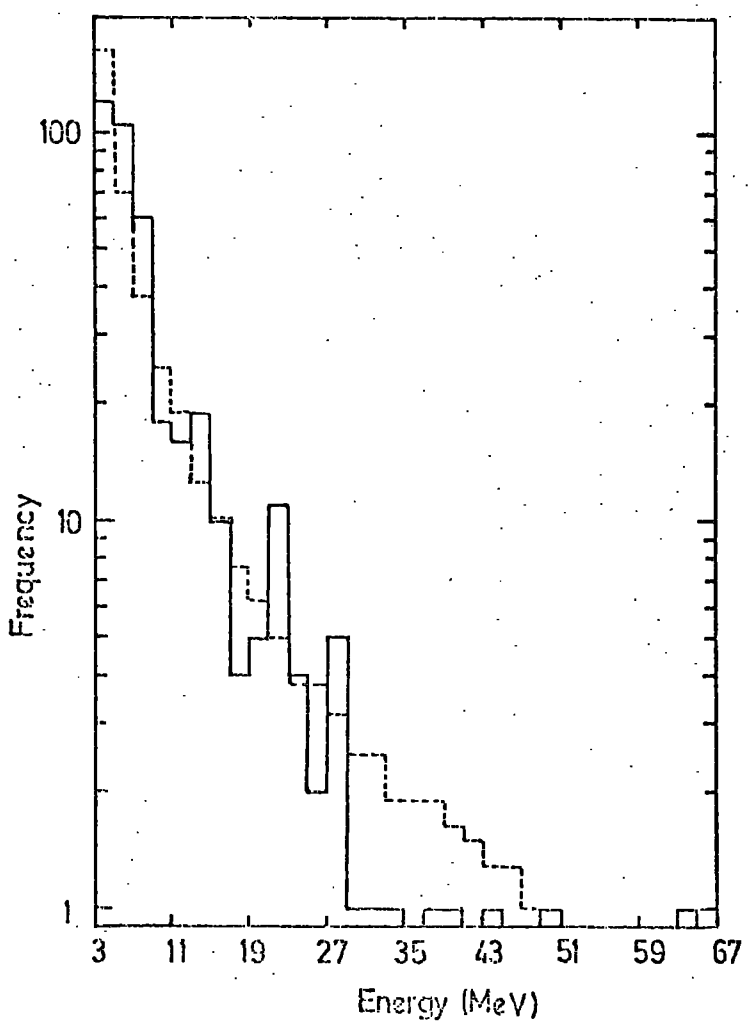


Figure 4.5 The integral energy spectrum of knock-on electrons. The dashed histogram shows the predicted distribution

in this region are not possible, it was decided to adopt the technique of counting single flashes adjacent to the track. For an electron to flash one tube off the parent track requires approximately 1 MeV, hence the predicted number per track is given by

$$\varphi(E,\ E') = \frac{2Cm_e c^2}{\beta^2} \int_{E'=1MeV}^{\infty} \frac{dE'}{E'^2}$$

where $C = \frac{\pi N Z}{A} r_e^2 = 0.15 \frac{Z}{A}$ (g cm$^{-2}$) (Rossi, 1952)

and N = Avogadro's number

Z = Atomic number of target material

A = Mass number of target nucleons

$r_e = e^2/m_e c^2$ = classical radius of the electron

$\beta = v/c$ = velocity of incident particle

E = energy of incident particle

E' = energy of secondary electron

Evaluating this integral for the 96 layers of flash tubes (plus aluminium electrodes) in F2+F3 gives the total number of electrons produced with energy greater than 1 MeV to be 6.8. For e/3 quarks the figure would be 6.8/9 = 0.76.

It is necessary to know the variation of the number of knock-ons seen in F2+F3 with time delay $T_D$ in order that old muon tracks simulating quarks can be recognised. For this purpose two definitions of a knock-on electron were adopted. A Type 1 knock-on was defined as $\geq 1$ flash lying adjacent to but off the track of the parent particle, a Type 2 knock-on being defined as $\geq 2$ adjacent flashes in any layer where one flash lies on the trigger particle track. The muon tracks photographed at different time delays for the determination of the efficiency - time delay variation (see section 2.2.4) were re-scanned,

the total number of Type 1 and Type 2 K.O.'s per track being counted. Figure 4.6 shows the frequency distributions obtained for the number of Type 1 K.O.'s for different time delays, and also for a sample of EAS muon tracks taken at a time delay of 20 μS.

In Figure 4.6, no correction has been made for spurious background flashes, attributed mainly to natural radioactivity in the glass. This background was measured for events at two different time delays, to establish whether there was any variation. Figure 4.7 shows the result for events at 20 and 200 μS. As expected there is no significant difference. The most probable number of background flashes is 47.5, out of a total of 8,112 flash tubes in the 96 layers of F2+F3, hence the most probable number of background flashes lying alongside a track is

$$\frac{2}{84.5} \times 47.5 = 1.09$$

(The number 84.5 is the mean number of flash tubes in a layer).

Figures 4.8 and 4.9 show the variation of K.O. number as a function of time delay, corrected for background. The full curves drawn through the points correspond to a value of $af_1Q_1 = 9$, the Lloyd parameter describing the flash tube behaviour as determined in section 2.2.4. Note that in Figure 4.9 the curve has been expressed as $(af_1Q_1 = 9)^2$ since both the tube on the track and the tube adjacent to it are required to flash.

Now the experimental points in these figures, while having basically the same shape as the fitted curves, appear to fall off rather more sharply after extending to longer time delays. This reflects the fact that the ionisation produced by low energy, stopping electrons is greater than that produced by the relativistic muons for which the value of $af_1Q_1 = 9$ was determined. Since the value of $af_1Q_1$ is proportional to the number of ion pairs initially produced in the gas, a

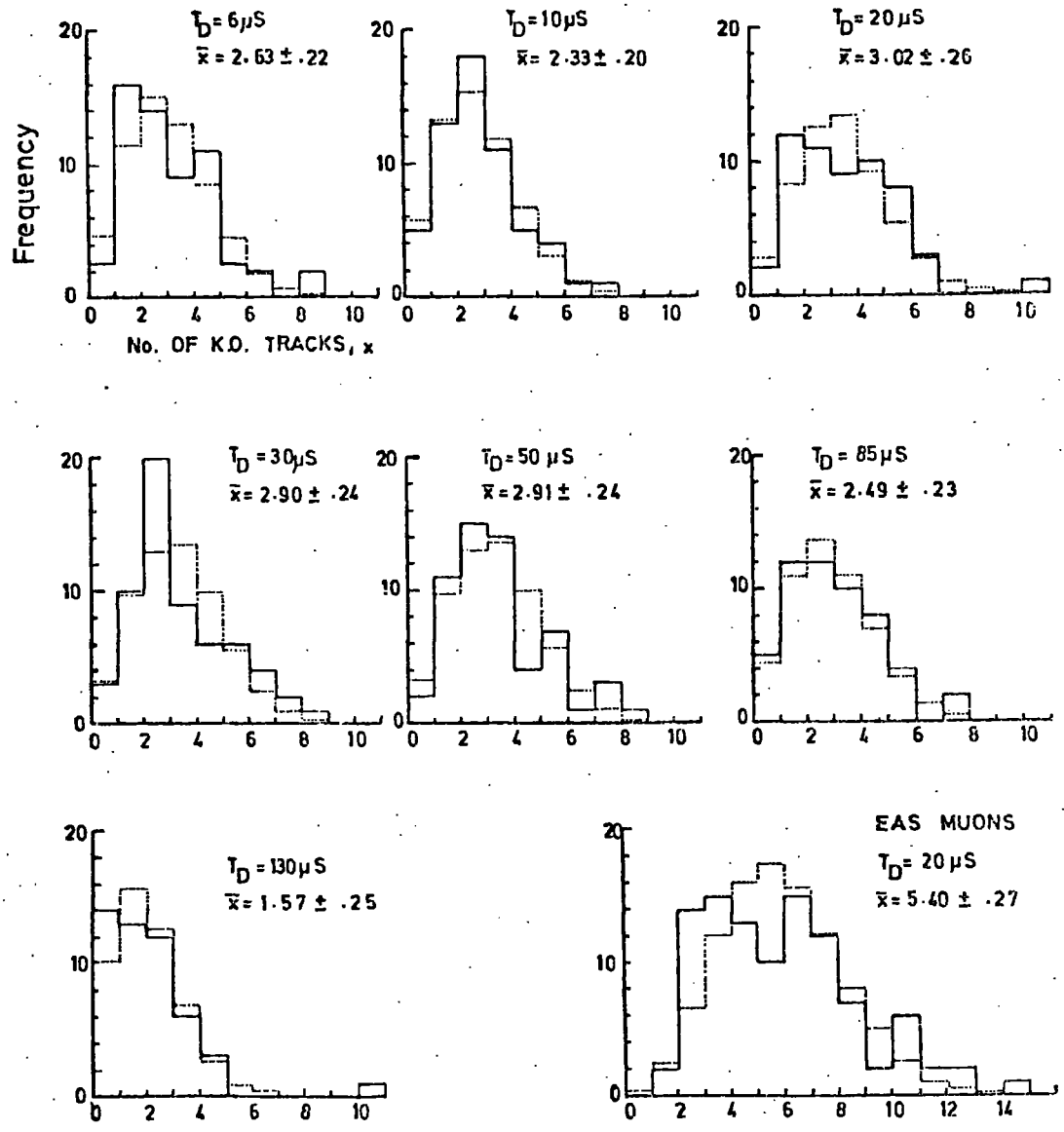


Figure 4.6 The distributions of Type 1 knock-on electrons at different time delays, $T_D$. The measurements were made on single muon tracks and EAS tracks traversing the 96 layers of flash tubes comprising $F_2 + F_3$. No correction for background has been applied.

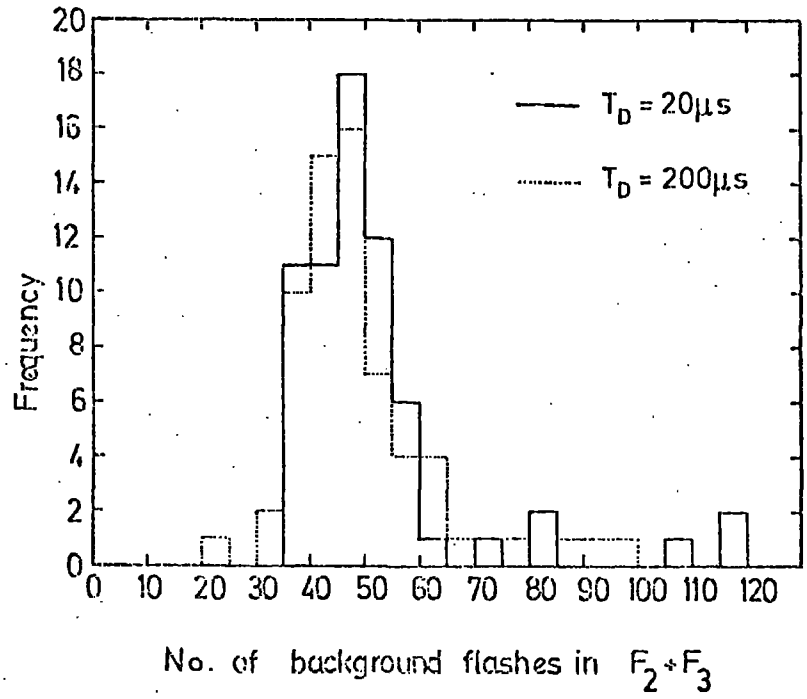


Figure 4.7 The distribution of the number of background flashes in $F_2+F_3$ for two different time delays, $T_D$ = 20 μs and 200 μs. The most probable number of background flashes is 47.5.

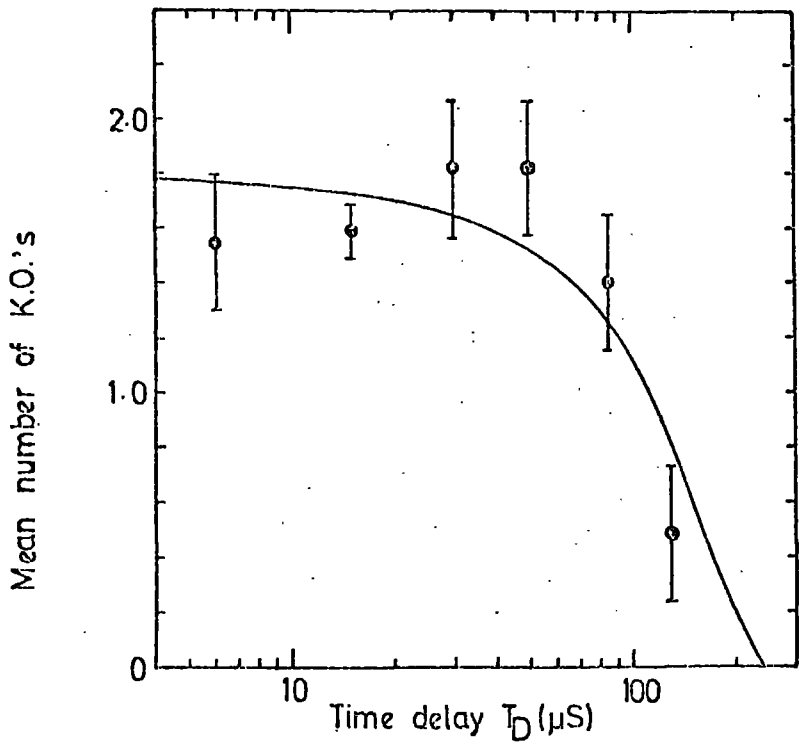


Figure 4.8 The variation of the number of Type 1 knock-on electrons with time delay.

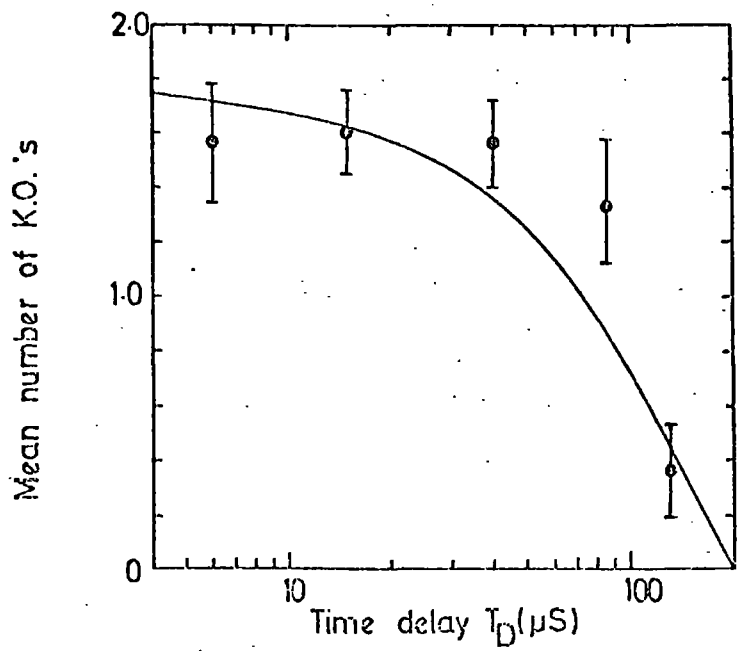


Figure 4.9 The variation of the number of Type 2 knock-on electrons with time delay.

higher value for the Lloyd parameter would be expected to fit the points shown in Figures 4.8 and 4.9, although this value could not be predicted with great accuracy since the statistical errors on the experimental points are large.

The large difference between the observed number of knock-ons at small time delays and the number predicted with energy >1MeV is presumably due to the fact that most electrons, produced typically within 20 degrees of the muon direction, never travel beyond the flash tubes defining the muon track.

In Figure 4.6, the difference between the mean number of K.O.'s obtained for single muons at $T_D = 20\,\mu S$ and air shower tracks at the same time delay is attributed to the fact that in EAS events the number of background flashes is somewhat greater, presumably because of the presence of low energy photons in the shower. Taking the observed number of Type 2 K.O.'s per track at small time delays to be 1.6 (see Figure 4.9), the expected number of K.O.'s along a quark track should be essentially zero, while for background muons at long time delays the mean number is ~ 0.4 - 0.8. The number of Type 2 K.O.'s were counted for the six remaining quark candidates and also for the 14 events rejected as being background tracks. Figure 4.10 shows the distribution of Type 2 K.O.'s for these 20 tracks. It can be seen that two of the six quark candidates have no knock-on electrons, while 3 of the 14 background tracks are free from K.O.'s. Details of the six quark candidates are given in Table 4.2. Now rather than subtract the background flashes from each track, which because of the large statistical uncertainty is not really justifiable, the six quark candidates were compared directly with the 14 background tracks, the number of spurious flashes assumed to be similar for all 20 events. The two quark candidates having no K.O.'s cannot be excluded from being possible quarks, although they are most likely background muons. Taking the predicted number of muons which could satisfy all other

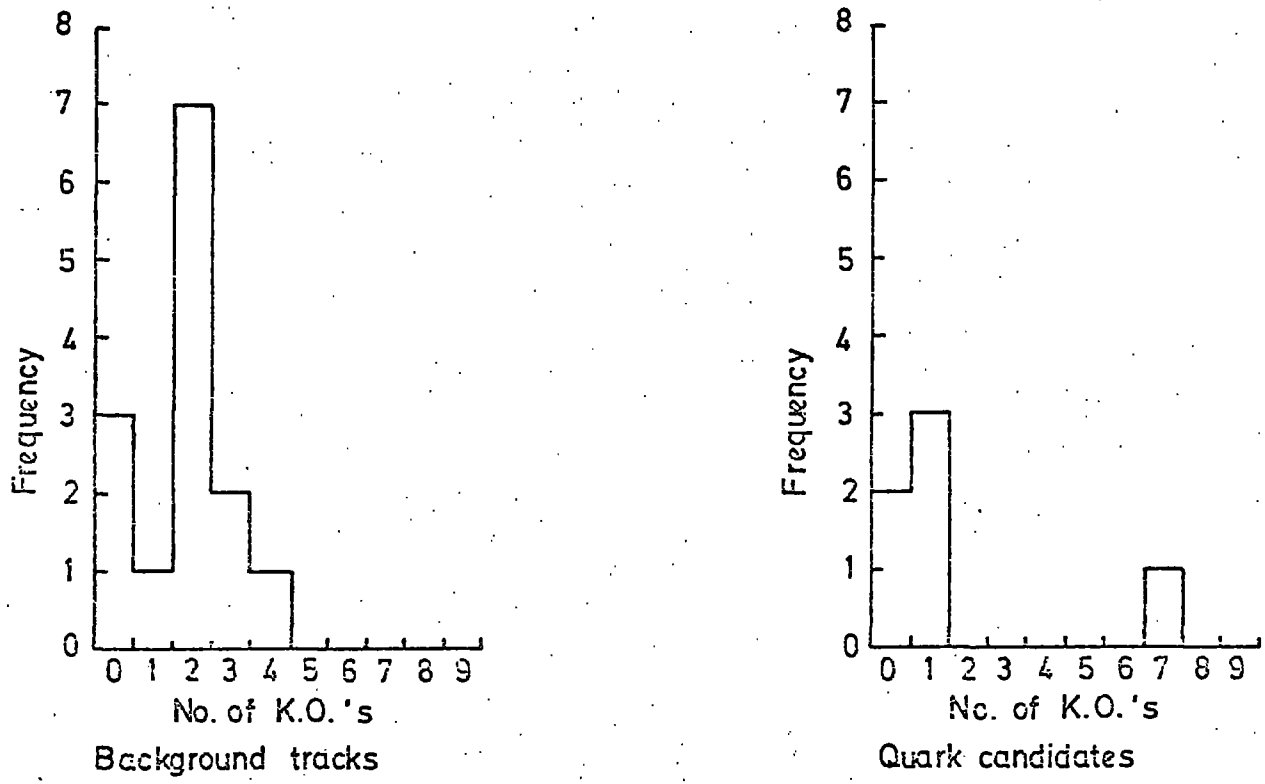


Figure 4.10 The distribution of knock-on electron number along a track for the background tracks and quark candidates.

| Event | F2+F3 for quark Candidate | No. of shower tracks in picture excluding quark candidate | Angle quark candidate track makes to other shower | No. of K.O.'s (i.e.pairs of adjacent flashes) |
|---|---|---|---|---|
| E8-48 | 31 | 1 | $3^{o}$ | 1 |
| E16-66 | 39 | 2 | $4^{o}$ | 7 |
| E19-45 | 28 | 3 | $5^{o}$ | 0 |
| E34-117 | 38 | 3 | $5^{o}$ | 0 |
| E53-125 | 47 | 2 | $0^{o}$ | 1 |
| E69-95 | 41 | 2 | $0^{o}$ | 1 |

Table 4.2 Details of the 6 events shown in Fig.4.3 with F2 + F3 $\leq$ 50.

quark tests to be 2.2 (section 4.3.1), since 3/14 of the observed background tracks had no K.O.'s the expected number of muons simulating quarks will be 2.2. x 3/14 = 0.47. Thus the probability of observing two pseudo-quarks will be ~8%, although there will be a large error on this figure. One of the two remaining quark candidates is shown in Plate 4.1.

Since two events could not be excluded from possibly being quarks, the upper limit obtained, based on these events, is less than $1.4.10^{-11}$ $cm^{-2}sec^{-1}st^{-1}$. This limit does not take account of the loss of quarks due to interactions in the chamber. Assuming the quark-nucleon inelastic cross-section to be 11 mb (section 3.2.3), the probability of a quark traversing the chamber without interacting is calculated to be 0.165. This raises the upper limit of the quark flux to less than $8.10^{-11}cm^{-2}sec^{-1}st^{-1}$

## 4.4 Conclusion

While the two quark candidates could not be excluded from being genuine quarks, the background due to muons simulating quarks is at approximately the same level. Hence it was concluded that no advantage could be gained from operating the flash tube chamber for a longer period of time without modifying it in such a way that the background from muons was either removed or substantially reduced.

One way in which it was thought the signal-to-noise ratio could be improved was to look at a smaller distance from the core of the showers, and also to increase the mean shower energy. This was achieved by increasing the local electron density trigger theshold. Two runs were performed with which the author was associated to a certain extent but which will not be described here. Briefly, electron density thresholds of $\Delta_e \cong 160m^{-2}$ (Ashton et.al. 1973b) and $\Delta_e \cong 500\ m^{-2}$ (unpublished) were chosen for new experiments. It was found that with these triggers the obscuration due to nuclear-electromagnetic cascades (produced by pions associated with the air shower interacting in the absorber above the chamber) increased, consequently reducing the efficiency for detecting quarks. Thus

Plate 4.1 Event E19-45. A possible quark track is indicated.

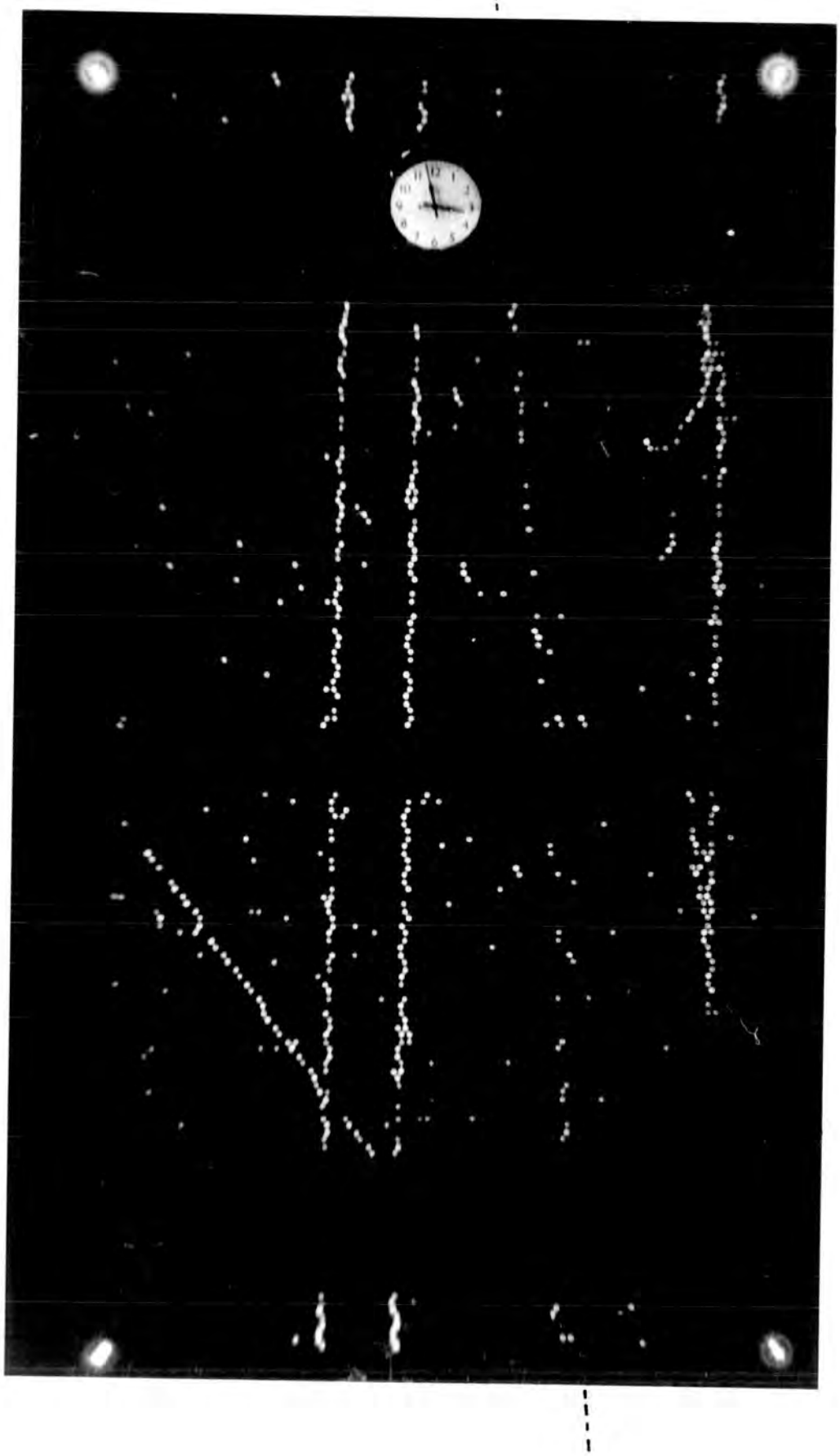

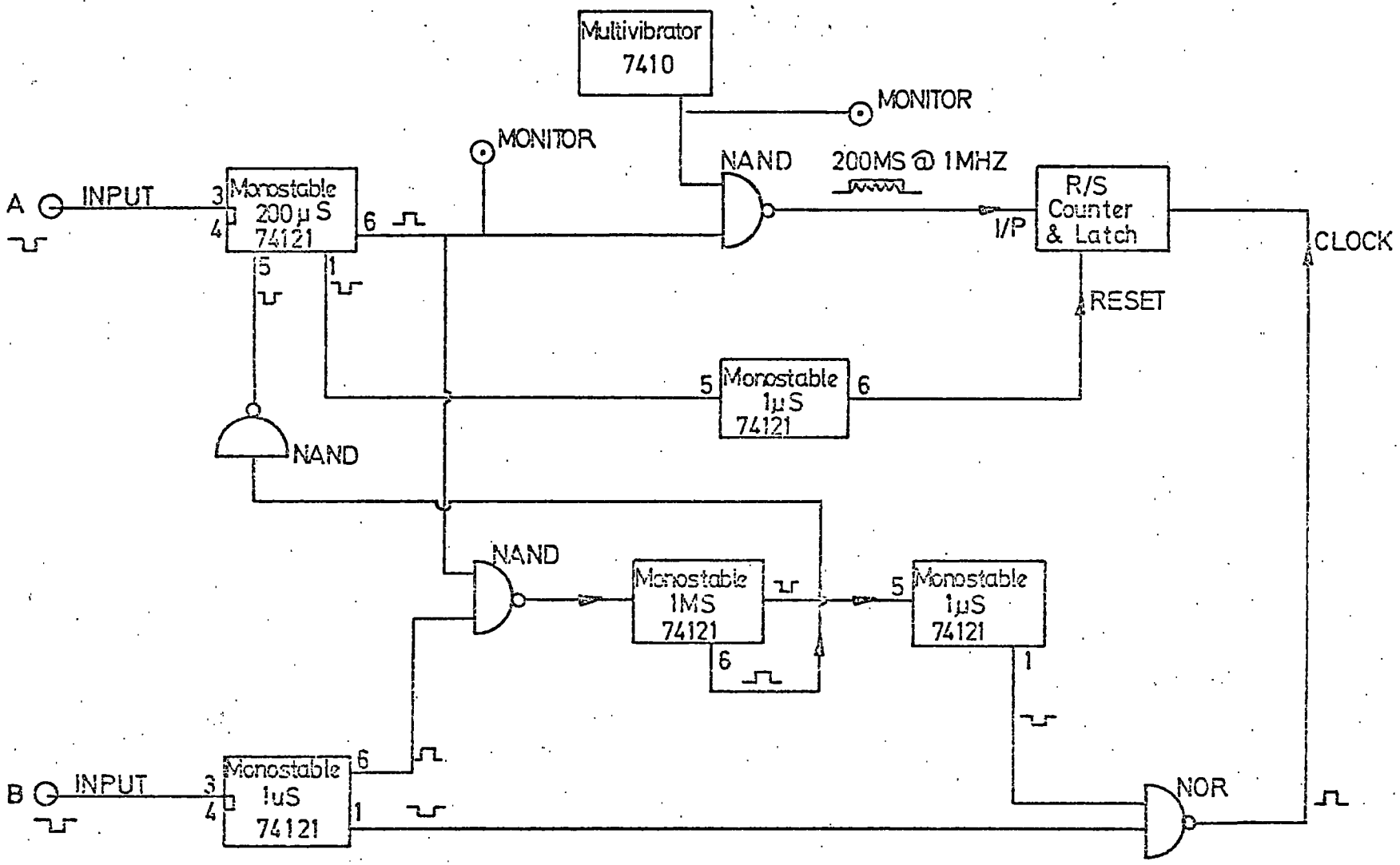


Figure 4.11 Suggested circuit for a previous particle detector.

it is concluded that of the three values of $\Delta_e$ studied so far $\Delta_e \geqq 40\ m^{-2}$ is the optimum density for the quark search.

If the detector were taken underground, thus cutting out most of the shower accompaniment while not being at so great a depth that too large a fraction of the quarks would be lost, quarks could in theory be seen very close to the shower core. The same argument would apply to an experiment in which the detector was turned onto it's side, horizontal showers being observed (in this case the increased atmospheric depth acts as an additional absorber).

While the methods named above would enable the search for quarks to be extended into the very core of EAS, hence improving, hopefully, the signal-to-noise ratio, it should be possible to almost eliminate background in the present detector by incorporating a previous particle indicator. This would consist of two layers of plastic scintillators completely covering the sensitive area of the flash tubes. For this purpose the two plastic scintillators A and B (see Figure 2.1) would be extended. The passage of single particles through A and B in coincidence would be recorded if a shower triggered the chamber in the following 200 μS, thus allowing background tracks due to "old" muons to be recognised and rejected. A possible circuit for a previous particle indicator is shown in Figure 4.11.

# CHAPTER 5

## THE PRODUCTION OF NUCLEAR-ELECTROMAGNETIC BURSTS IN THICK ABSORBERS

### 5.1 Introduction

During the Extensive Air Shower experiment described in preceding chapters, it was noticed that a considerable number of events photographed contained dense showers of particles directly below the lead shielding and also below the 15 cm. layer of iron near the top of the chamber, the bursts sometimes traversing the whole chamber. These particles form an electromagnetic cascade, produced by the passage of hadrons or muons through the absorber, and since it can be seen from the results of calculations described in Chapter 2 than when an air shower trigger occurs the mean distance from the core is only a few metres, it is thought that the majority of these bursts were produced by hadrons rather than by muons, due to the high energy transfer involved. This is discussed further in Chapter 7.

The cascade of particles produced when a hadron interacts strongly with a target nucleus can yield information about the energy of the particle if the physical processes occurring are understood and can be predicted. In this chapter a method of obtaining the energy of the interacting particle will be described, based upon assumptions about the physical processes and utilising the information about the cascade which can be obtained from the flash tube chamber. Initially pure electron-photon cascades will be discussed, consideration then being extended to nuclear-electromagnetic cascades.

### 5.2 Qualitative description of the cascade process

Consider a hadron incident on a dense absorber, of depth comparable with or greater than the interaction length of the hadron. The probability that it undergoes a strong interaction follows an exponential distribution

with the amount of absorber traversed. When it interacts, depending on the energy, a number of secondary particles are produced, mainly pions. If the incident particle is a charged pion it can be considered to lose all of its energy in the interaction. A nucleon would lose some fraction of its energy and continue through the absorber, possibly to interact again. The fraction of energy lost in an interaction is carried away by the secondary particles. Now the charged pions will travel some distance through the absorber in almost the same direction as the parent particle until they in turn interact or are lost from the absorber (decay probabilities can be neglected for charged pions in a dense material). The neutral pions, however, will decay more or less instantaneously into two photons. These photons will either materialise or undergo a Compton collision. The electrons and positrons produced will, if their energy is above the critical energy for the medium, lose energy predominantly by radiation, the photons in turn producing more electrons. Now since the processes involved produce secondaries with energies of the same order of magnitude as that of the primaries, the energy degradation in the cascade is relatively slow and allows a significant increase in the total number of particles to occur as the cascade develops with depth. Eventually the point is reached when the mean energy of the electrons falls below the critical energy, collision losses become more important than bremstrahlung, and the total number of particles in the cascade decreases. The cascade eventually degenerates until the energy input to the cascade has gone either into the excitation and ionisation of atoms in the absorber or the cascade emerges from the absorber.

Now in the above description the cascade has been considered as a one-dimensional process whereas it does in fact exhibit a lateral spread. The angular divergence is produced by

(a) the traverse momentum distribution of produced $\pi^{o}$'s

(b) multiple scattering of the strongly interacting particles

(c) the angular separation of photons from $\pi^{o}$ decay

(d) the angular separation of the electrons created in pair production

(e) multiple scattering of electrons in the electron-photon cascade.

The cascade can be considered in two parts. The nuclear cascade is effectively the skeleton of the total cascade and determines the depth of production and energy input to the electron- photon cascades produced by $\pi^0$ decay. These cascades then develop according to the laws governing electromagnetic processes and can be considered separately.

## 5.3 The one-dimensional development of electron-photon cascades

### 5.3.1 Introduction

The general problem to be solved in any attempt to describe the development of electromagnetic cascades is the following: assuming an electron or photon of known energy to be incident on an absorber, what is the distribution, for electrons and photons at depth t, of energy, angle and lateral displacement ? Restricting the problem to the one-dimensional development of the cascade, diffusion equations can be set up of the form (Rossi, 1952)

$$\frac{\partial \pi(E,t)}{\partial t} = \int_E^\infty \gamma(E',t)\, \varphi_p(E',t)dE' + \int_E^\infty \pi(E't)\, \varphi_e(E',E'-E)dE'$$

$$- \int_0^E \pi(E,t)\, \varphi(E,E')dE' - \beta \frac{\partial \pi(E,t)}{\partial E}$$

$$\frac{\partial \gamma(E,t)}{\partial t} = \int_E^\infty \pi(E',t)\, \varphi_e(E',E)\, dE' - \int_0^E \gamma(E,t)\, \varphi_p(E,E')dE'$$

where $\pi(E,t)$ represents the number of electrons of energy E at depth t, $\gamma(E,t)$ is the number of photons of energy E at depth t, $\beta$ is the average ionisation loss per radiation length, $\varphi_e(E,E')$ is the differential probability per radiation length for the production of a photon of energy E' by an electron of energy E, and $\varphi_p(E,E')$ is the differential

probability per radiation length for the production of an electron of energy E' by a photon of energy E.

To solve these equations analytically certain simplifying assumptions can be made. Alternatively the equations can be solved by numerical integration using exact probabilities. Finally, a totally different approach that has been used is the Monte Carlo technique, in which individual particles are followed through the absorber, the competition between the various processes being represented by weighted random choices.

5.3.2 Solution of the diffusion equations under Approximation A and Approximation B

Approximate solutions of the diffusion equations are possible if assumptions are made concerning the physical processes involved. In Approximation A ionisation losses and Compton scattering are ignored, while the probabilities for pair production and bremsstrahlung are described by their asymptotic values for complete screening. Approximation B makes the same simplifying assumptions except that a constant collision loss is included. The approximations made limit the applicability of the results of these calculations. Both theories are applicable only to light absorbers since in high-Z materials the total photon absorption coefficient is strongly energy dependent. In addition, Approximation A is only valid at energies well above the critical energy due to the neglection of ionisation losses. Hence in general this treatment is used to describe the early development of a cascade. While the results of Approximation B tend to be about 10% low in the number of electrons predicted (Thielheim and Zöllner, 1972), the neglection of ionisation losses in Approximation A tends to produce an overestimate in electron numbers.

Rossi (1952) deals in detail with the solution of the diffusion equations under the different approximations, while Thielheim and Zöllner (1972) present a useful review of Approximations A and B.

It should be noted that because of the assumptions made, the results

of Approximation A are independent of absorber if depth is measured in radiation lengths. Similarly, Approximation B yields results independent of absorber if depth is measured in radiation lengths and energies are expressed in units of the critical energy.

5.3.3 Numerical solution of the diffusion equations

Thielheim and Zöllner (1972) have been able to solve the diffusion equations without assuming asymptotic cross-sections by employing a method of numerical integration. They have been able to use exact cross-sections and include all relevant processes, namely bremstrahlung, pair production, Møller and Bhahba scattering (high energy transfers), ionisation loss (low energy transfers), Compton scattering and the photoeffect. Their paper presents a detailed tabulation of the cross-sections used in calculations for lead, and also compares results obtained with those of Approximations A and B, Monte Carlo methods and several experiments. Results of their calculations are estimated to be accurate to within 1%.

5.3.4 The Method of Moments

An analytical approach to the solution of the cascade diffusion equations has been used by Ivanenko and Samosudov (1959, 1967a and 1967b). Unlike Approximations A and B this treatment can take account of the energy dependence of the total photon absorption coefficient, and also includes the effect of the increased track length due to multiple scattering of the shower electrons. This allows the results to be applied to dense absorbers. The approach, the method of moments, calculates the average behaviour of the cascade by evaluating the cascade moments. These moments are simpler to calculate than the terms on the right hand side of the diffusion equations in section 5.3.1.

The degree of accuracy attainable with this method depends on the order to which the moments are calculated. Ivanenko and Samosudov evaluate the first four moments, enabling an accuracy of 5 - 10% to be obtained. They present results covering a wide range of energies for iron, lead, copper, aluminium and graphite absorbers. Results are given

for different energy cut-offs for the electrons.

5.3.5 Monte Carlo simulations

With the advent of modern computers it has become possible to simulate the cascade processes directly, enabling exact interaction probabilities to be used and hence in theory to produce very accurate results. Unfortunately, the amount of computing time that is needed to simulate a cascade increases rapidly as the energy of the primary particle is increased, thus in general only relatively low energy cascades have so far been simulated for dense absorbers.

Because of the statistical nature of the method, results concerning the mean shower behaviour are subject to fluctuations, the resulting error depending on the number of simulations performed at each energy. At low energies, however, it must be considered the most reliable method of studying electromagnetic cascades.

Groups producing results for heavy absorbers include Zerby and Moran (1963), Völkel (1965) and Messel and Crawford (1970).

5.3.6 Comparison of theoretical predictions with experiment

Figures 5.1 and 5.2 show a compilation of results from theory and experiment for a lead absorber. The calculations at low energies (Figure 5.1) can be seen to show quite close agreement. Two of the experimental curves, however, are well above both the calculations and the experimental curve of Heutch and Prescott. This apparent disagreement between the experimental results is likely to be due to experimental difficulties in defining the cut-off energy. At high energies (Figure 5.2) there are no direct experimental results or Monte Carlo results. The numerical calculations of Thielheim and Zöllner are shown along with the predictions of Ivanenko and Samosudov. Also shown is the curve predicted by Müller. This curve was obtained by fitting data from an accelerator experiment performed at energies up to 15 GeV. The results of Approximation A were modified to fit this data, which then allowed Müller to extrapolate up to energies of 1000 GeV. It appears that the

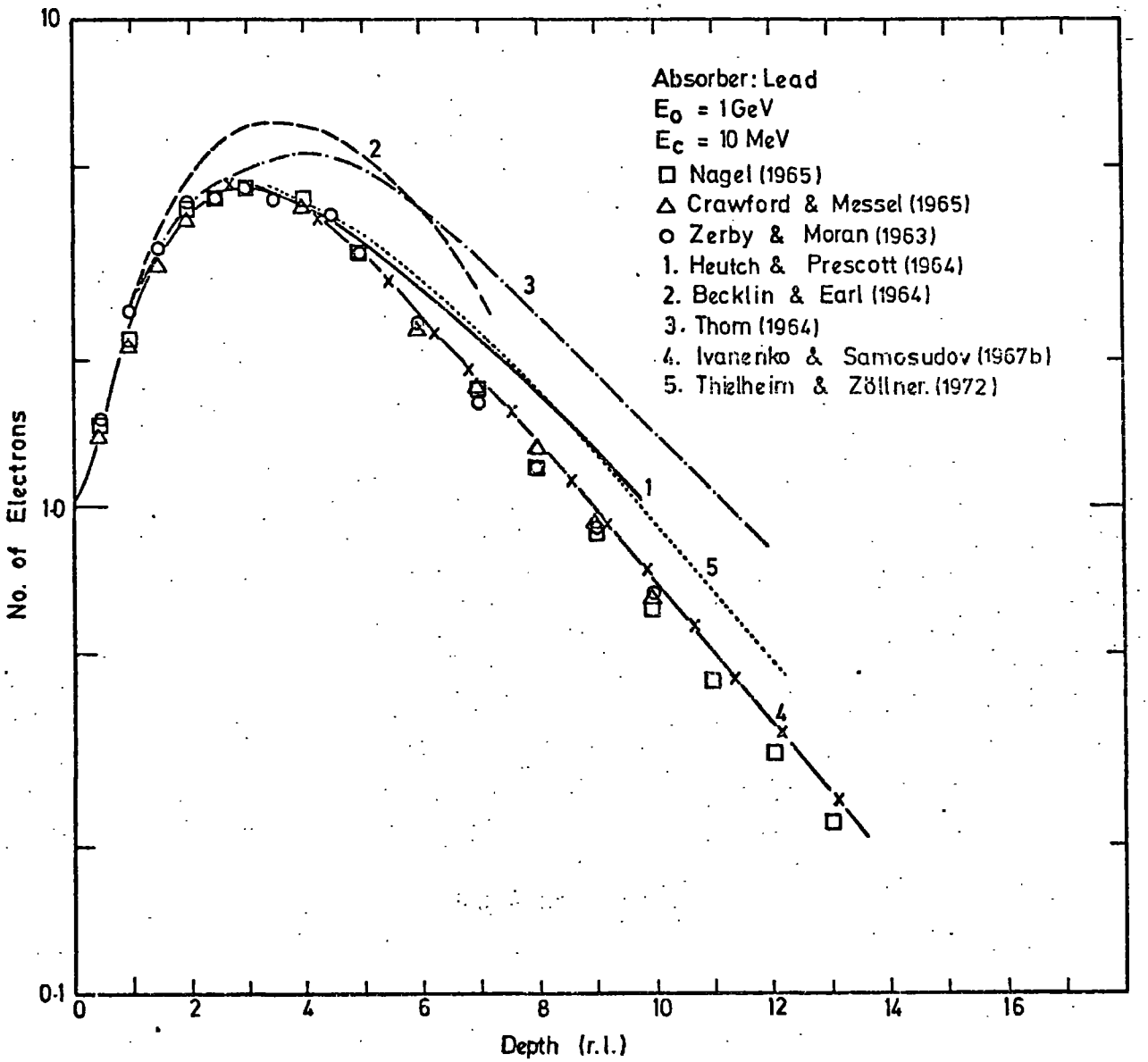


Figure 5.1 Transition curves in a lead absorber for primary electrons of 1 GeV. The cut-off energy $E_c$ is 10 MeV. The points are results of Monte Carlo calculations, curves 1, 2, and 3. refer to experiments and curves 4 and 5 are the results of calculation. See text for details.

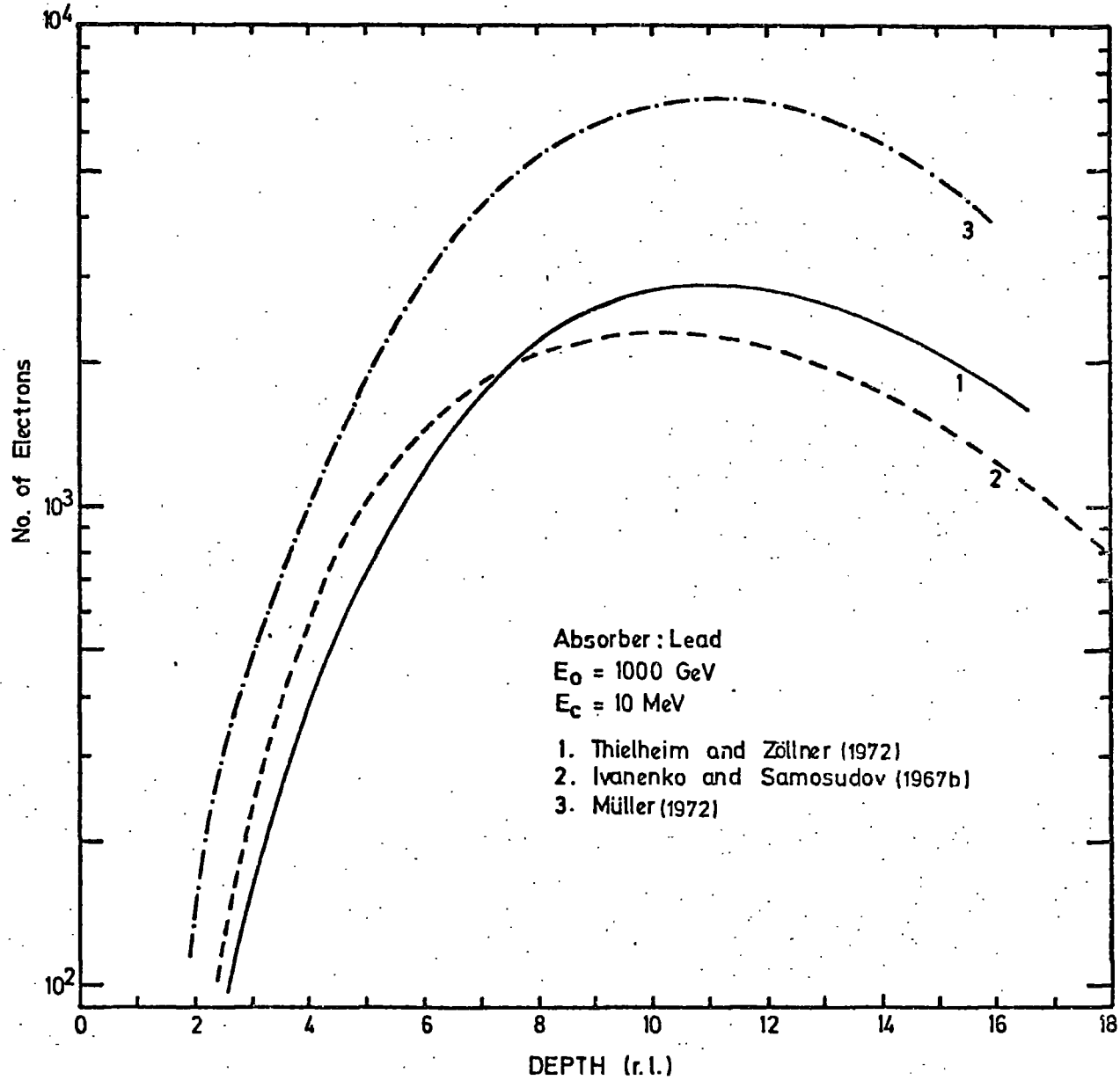


Figure 5.2 Transition curves in a lead absorber for primary electrons of energy 1000 GeV. The cut-off energy $E_c$ is 10 MeV. Curves 1 and 2 are the results of calculations. Curve 3 is based on an extrapolation of accelerator data.

results may be slightly high - certainly higher than the other predictions. This would be consistent with the fact that Approximation A overestimates electron numbers due to the neglect of ionisation losses.

Coats (1967) compares the results of Ivanenko and Samosudov for iron with experimental results obtained at intermediate energies and finds reasonable agreement, indicating that these calculations are valid for the wide range of energies required in the present experiment for both lead and iron. In addition, Ivanenko and Samosudov quote results for an energy cut-off relevant to the present experiment, ~1 MeV. This corresponds approximately to the energy needed by an electron to traverse one flash tube. Hence it was decided to adopt the transition curves of Ivanenko and Samosudov for the present calculations.

Figures 5.3 and 5.4 show the transition curves for photon-initiated cascades in iron and lead for an energy cut-off of ~1 MeV.

## 5.4 One-dimensional Simulation of Nuclear-Electromagnetic Cascades in a Thick Absorber

### 5.4.1 Introduction

Since in the present application the bursts being dealt with are not purely electromagnetic in nature but have a nuclear cascade superimposed, we must consider how this affects the overall cascade. Now while electromagnetic interactions are thought to be well understood, strong interactions are far less perfectly comprehended. This means that results obtained by calculation are strongly model dependent.

Calculations have been carried out by several workers. Jones (1969a and 1969b) has used Monte Carlo simulations of the hadronic cascade to predict cascade curves for protons in iron. These were compared with the results obtained when an iron ionisation spectrometer was exposed to protons of momentum 10,20.5 and 28 GeV/c at an accelerator. Reasonable agreement was found, although since Jones uses Approximation B to convert photon energies to cascade particles he might be expected to

Figure5.3 Transition curves for photon-induced cascades in iron, predicted by Ivanenko and Samosudov. The numbers by each curve refer to the energy of the primary photon. All energies are in units of $0.437\beta$, where $\beta$ is the critical energy and is taken as 21 MeV. The cut-off energy $\epsilon$ is 0.1 or ~ 0.92 MeV. Lines of constant s (age parameter) have been calculated from Approximation A.

Figure 5.4 Transition curves for photon-induced cascades in lead, predicted by Ivanenko and Samosudov. The numbers by each curve refer to the energy of the primary photon. All energies are in units of $0.437\beta$, where $\beta$ is the critical energy and is taken as 7.6 MeV. The cut-off energy is 0.35 or ~ 1.16 MeV. Lines of constant s were calculated as for Figure 5.3.

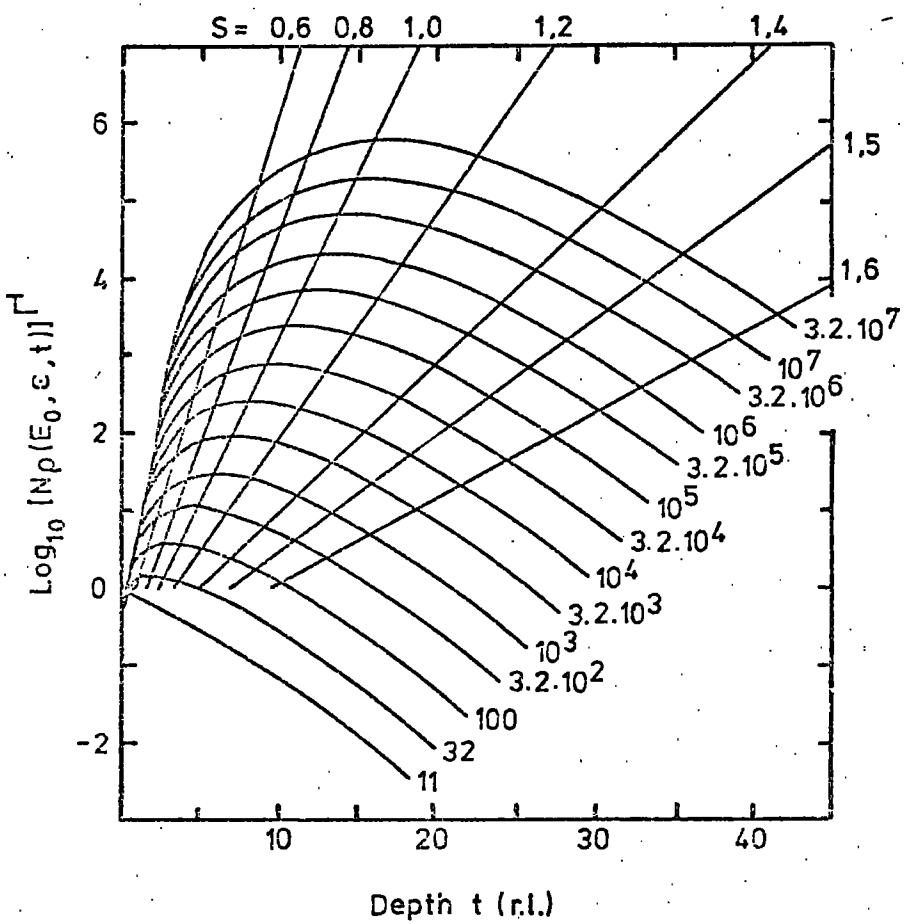
S = 0,6 0,8 1,0 1,2 1,4
1,5
1,6
3.2.10^7
10^7
3.2.10^6
10^6
3.2.10^5
10^5
3.2.10^4
10^4
3.2.10^3
10^3
3.2.10^2
100
32
11
6
4
2
0
-2
10
20
30
40
Log10 [Nρ(E0,ε,t)]^Γ
Depth t (r.l.)

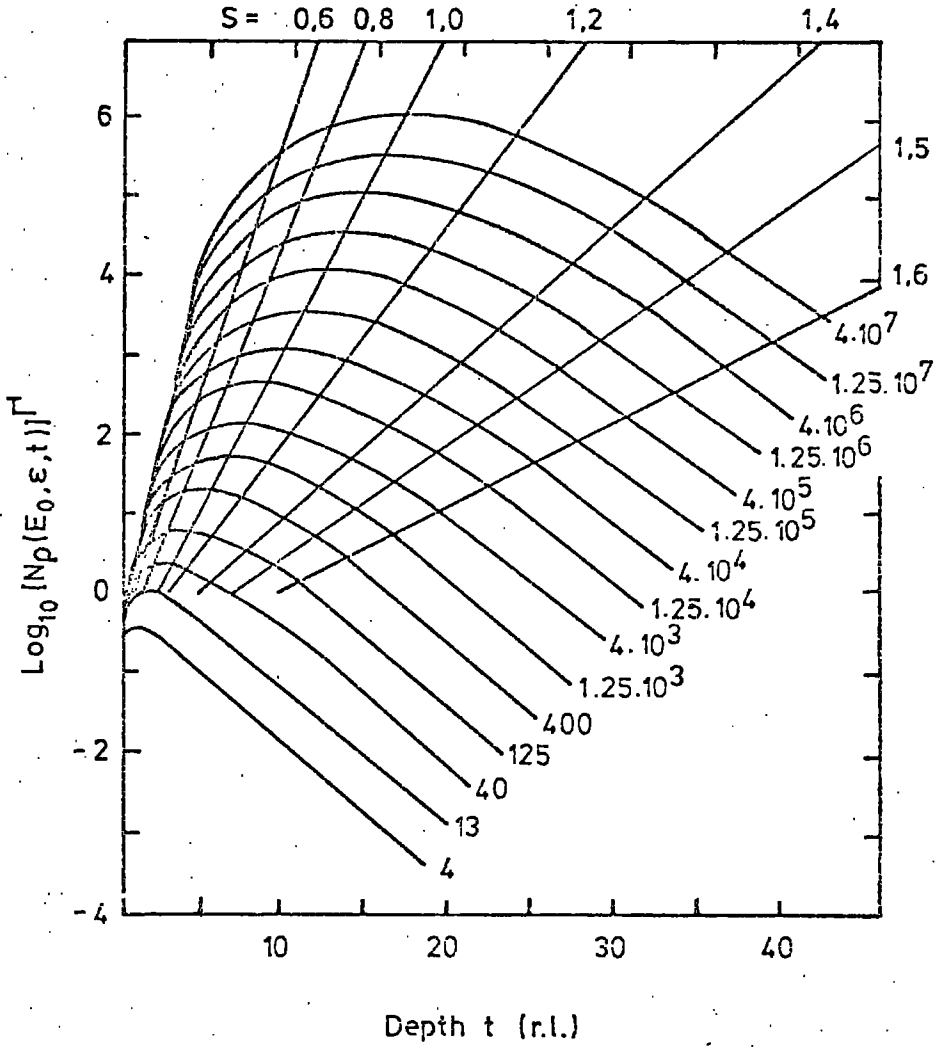
S = 0,6 0,8 1,0 1,2 1,4
1,5
1,6
4.10^7
1.25.10^7
4.10^6
1.25.10^6
4.10^5
1.25.10^5
4.10^4
1.25.10^4
4.10^3
1.25.10^3
400
125
40
13
4
6
4
2
0
-2
-4
10
20
30
40
Log10 [Nρ(E0,ε,t)]^Γ
Depth t (r.l.)

slightly underestimate electron numbers. There are several similarities between the model Jones uses and that adopted in the present calculations, hence results would not be expected to differ very markedly between the two methods (although there are significant differences, such as the energy going into heavy fragments which Jones considers and which has been neglected in the present calculations).

Vatcha et.al. (1972) have performed full Monte Carlo calculations in iron for three different nuclear interaction models up to hadron energies of 1000 GeV. The simulations were performed for the same geometry as was used in a multiplate cloud chamber operated at Ootacamund, India. From the results obtained Vatcha et. al. conclude that the absorption of cascades in the TeV region is much faster than that predicted by any of the models used, and suggest that one possible interpretation is the gammanisation process suggested by Nikolski (1967) in which high energy photons are produced directly in nuclear interactions above some threshold. Alternatively, Vatcha et.al. suggests that a higher inelasticity combined with a higher multiplicity could explain their observations. This conclusion is consistent with the observation that the cascades studied at Ootacamund in the high energy region are almost certainly pions which can be considered to undergo totally inelastic collisions with the iron nuclei. In addition, the models employed by Vatcha et.al. do not contain a term in the multiplicity distribution of secondary pions to include the intra-nuclear cascading which will increase the multiplicity. Hence it is concluded that the results of the Indian group are consistent with accepted theories of nuclear interactions.

Calculations have also been carried out by Pinkau and Thompson (1966) using a straightforward CKP model (to be discussed in the next section) and evaluate electron numbers as a function of depth in different absorbers for several values of the inelasticity K and multiplicity $n_T$.

In the present work a conservative model has been adopted since this appears to produce reasonable agreement with experiment, especially air

shower work, and is based on the model used by the Durham EAS group (Turver, 1973). The procedure adopted was to simulate, using Monte Carlo techniques, the nuclear cascade to the point at which the $\pi^0$'s produced decay into two photons. These photons were then converted into electron numbers below the iron or lead absorber by interpolating from the curves of Ivanenko and Samosudov (Figures 5.3 and 5.4).

5.4.2 Nuclear interaction model

The model used in the calculations was based upon the empirical CKP (Cocconi, Koester and Perkins) model (1961) used in cosmic ray physics a great deal over the past few years. Modifications to it include revised values for the nucleon inelasticity in dense materials and allowance for the effect of intra-nuclear cascading on the multiplicity of secondary pions. Calculations were carried out for four cases; pions and protons incident on iron and pions and protons incident on a lead absorber. In all cases the absorber thickness was taken to be 15 cms. A full list of values of constants used is given in Table 5.1. The assumptions made were the following.

(a) Ionisation losses for the hadrons were neglected

(b) The particle, incident vertically on the absorber, was allowed to interact at successive depths t (radiation lengths) according to the probability distribution

$$p(t)\,dt = \frac{1}{\lambda}\, e^{-t/\lambda}\, dt$$

where $\lambda$ is the interaction length of the primary particle in radiation lengths.

(c) For a primary pion the interaction was assumed to be totally inelastic (K = 1). For protons the mean inelasticity was assumed to be a function of the absorber material (Pinkau et.al., 1969). The distribution in the inelasticity is a parameter not well defined experimentally. Some workers have assumed a beta distribution (Jones, 1969), a sinusoidal

| Material | Density ($g.cm^{-3}$) | Radiation length $X_o$ ($g.cm^{-2}$) | $\lambda_\pi$ | $\lambda_p$ | Moliere unit |
|---|---|---|---|---|---|
| Fe | 7.6 | 14.1 | $11.6X_o$ | $9.94X_o$ | 1.53 cms. |
| Pb | 11.34 | 6.5 | $34.54X_o$ | $33.08X_o$ | 1.38 cms. |
| Al | 2.5 | 28.4 | | | |
| Glass | 2.7 | 26.3 | $4.9X_o$ | | |

Table 5.1(a) A list of constants used throughout the calculations.

| Material | Mean inelasticity of protons $\bar{K}_p$ | Mean inelasticity of pions $\bar{K}_\pi$ |
|---|---|---|
| Fe | 0.63 | 1.0 |
| Pb | 0.80 | 1.0 |

Table 5.1(b) Values of the mean inelasticities adopted for proton-nucleus and pion-nucleus collisions. See Figures 5.5 and 5.6.

variation of the form Sin $\theta$ about the mean ($\theta = \pi/2$) between the values 0.2 to 1.0 (Vatcha et.al. 1972), a flat distribution between $\bar{K} - 0.25$ and $\bar{K} + 0.25$ (Bradt and Rappaport, 1967), or a distribution of the form

$$f(K) = - (1 + \alpha)^2 (1 - K)^{\alpha} \ln (1 - K)$$

adopted by Brooke et.al. (1964) to define nucleon-air nucleus collisions. This expression is not valid, however, for $\bar{K}$ much greater than 0.5. It appears that the results of calculations do not depend critically on the shape of the distribution. The distributions adopted for the present work are shown in Figures 5.5 and 5.6. These step functions were derived from binomial distributions with the required mean. The distribution is represented by the successive terms in the expansion of $\left[p+(1-p)\right]^n$, where the product np defines the mean. The parameter n was varied (keeping the product np constant) to provide a reasonable spread about the mean, whence the function was re-normalised to restrict K to the range 0.0 to 1.0.

(d) The mean multiplicity of created pions was taken to be

$$\bar{n}_s = 3.0\ A^{0.19}\ (KE)^{0.25}$$

where E is the energy of the incident particle and A is the mass number of the absorber material. In addition, at low energies the mean multiplicity was constrained by conservation of energy considerations. This equation is based on a combination of surveys (e.g. Greider, 1971, Wdowczyk, 1973) and on the hydrodynamical model of Belenkji and Landau (1956). This mean multiplicity was used to determine the mean energies of the forward and backward cones of created pions. Individual pions, after being assigned with equal probability to either of these cones, were allocated an energy E' at random from the distribution

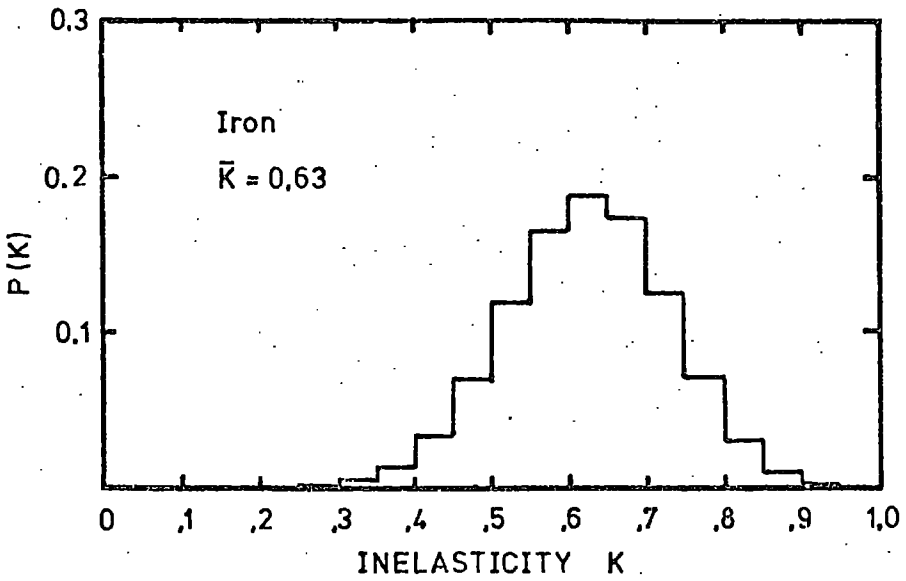


Figure 5.5 The inelasticity distribution for proton-iron nucleus collisions

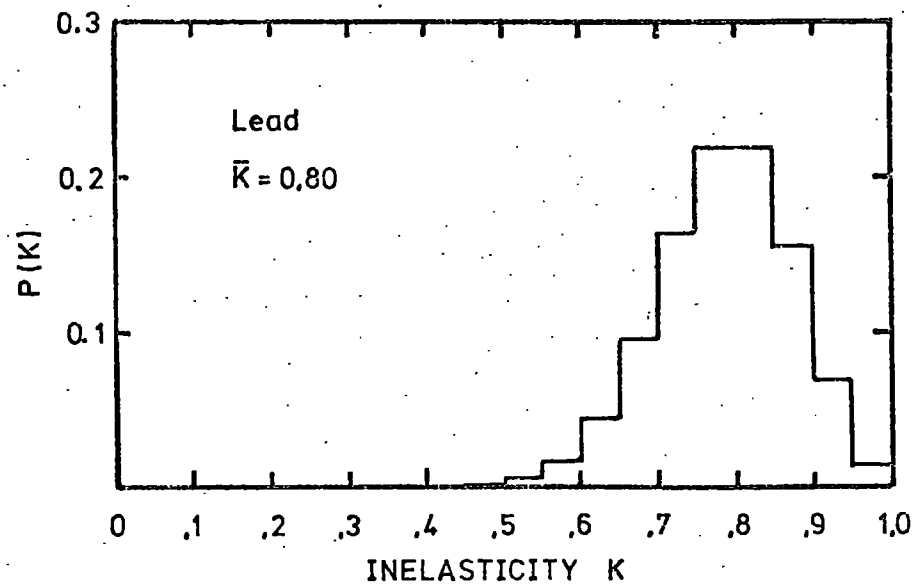


Figure 5.6 The inelasticity distribution for proton-lead nucleus collisions.

$$g(E')\,dE' = \frac{1}{U} e^{-E'/U}\,dE' + \frac{1}{T} e^{-E'/T}\,dE'$$

where U is the mean energy of the forward cone and T the mean energy of the backward cone.

Pions were selected and assigned energies from the above distribution until the total remaining energy (KE) fell below a cut-off energy of 0.2 GeV. In this way a multiplicity distribution was generated. The pion energy distribution obtained is shown in Figure 5.7.

(e) The created pions were assigned a charge from a flat probability distribution such that on the average one-third of the pions will be neutral and two-thirds charged (no distinction was drawn between positive and negative pions). If the energy of the created $\pi^o$ was less than 0.2 GeV the particle was ignored, since the photons, produced by the decay of the $\pi^o$ almost at rest, would not contribute significantly to the electromagnetic cascade. Similarly, if the total energy of the charged pion created was less than 1 GeV it was ignored since the inelastic cross-section drops very sharply at this value (Hayakawa, 1969), hence the particle would not contribute to the cascade.

(f) Charged pions were allowed to interact at greater depths determined at random from the distribution

$$p(t)\,dt = \frac{1}{\lambda_\pi} e^{-t/\lambda_\pi}\,dt$$

and the interaction characteristics were assumed to be identical to those described above.

(g) Neutral pions were assumed to decay instantaneously into two photons of equal energy which then initiated electron-photon cascades. The total number of electrons arriving at the bottom of the absorber was calculated for each photon by interpolating from the curves of Ivanenko and Samosudov shown in Figure 5.3 and 5.4.

(h) The hadronic cascade terminated when all of the hadrons (primary and produced) had either passed out of the absorber or their

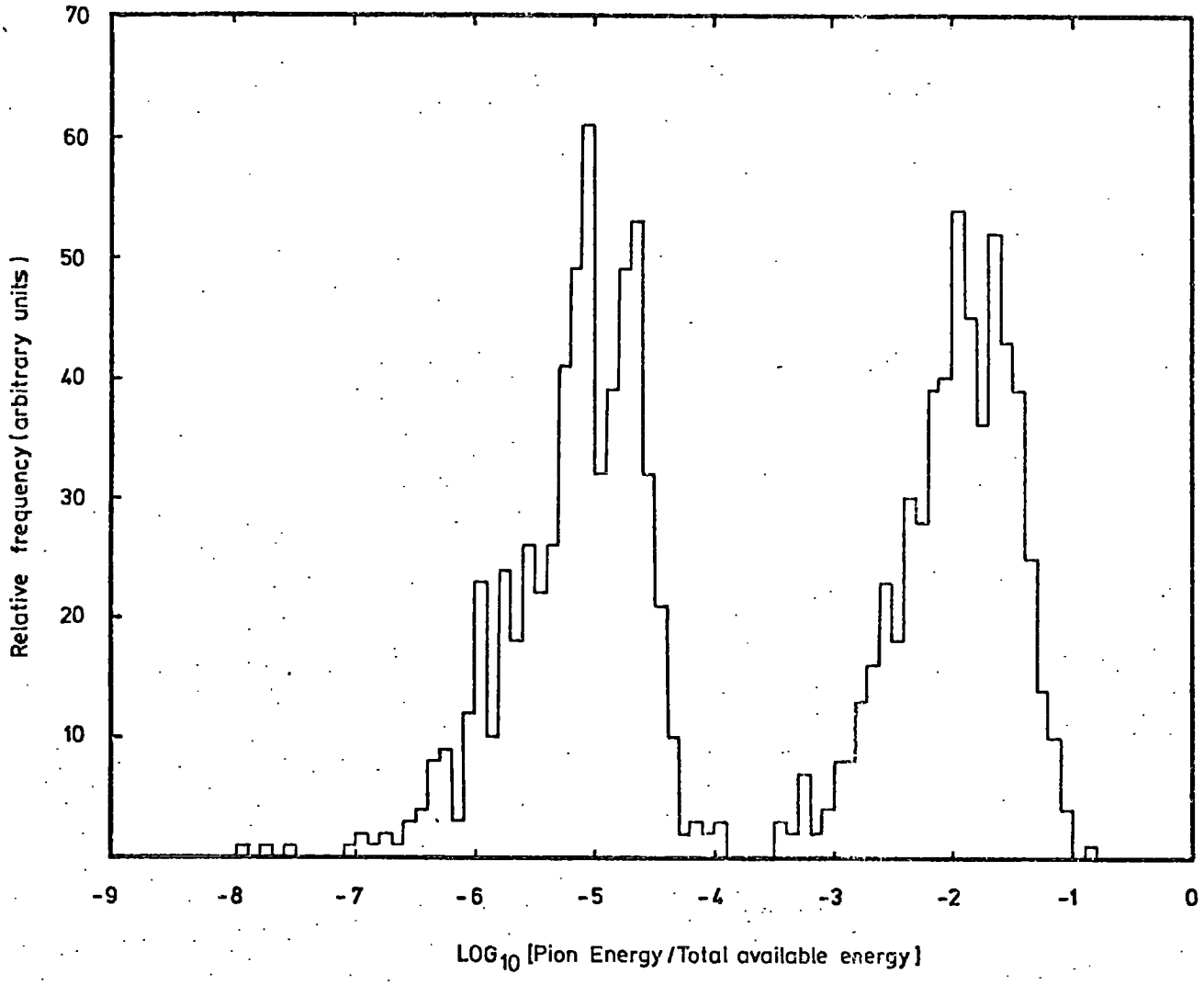


Figure 5.7 The energy distribution of secondary pions in the laboratory system, expressed as a fraction of the total available energy. The forward and backward cones can clearly be seen.

Figure 5.8 Flow diagram of Monte Carlo program, showing the simulation of one proton-induced cascade.

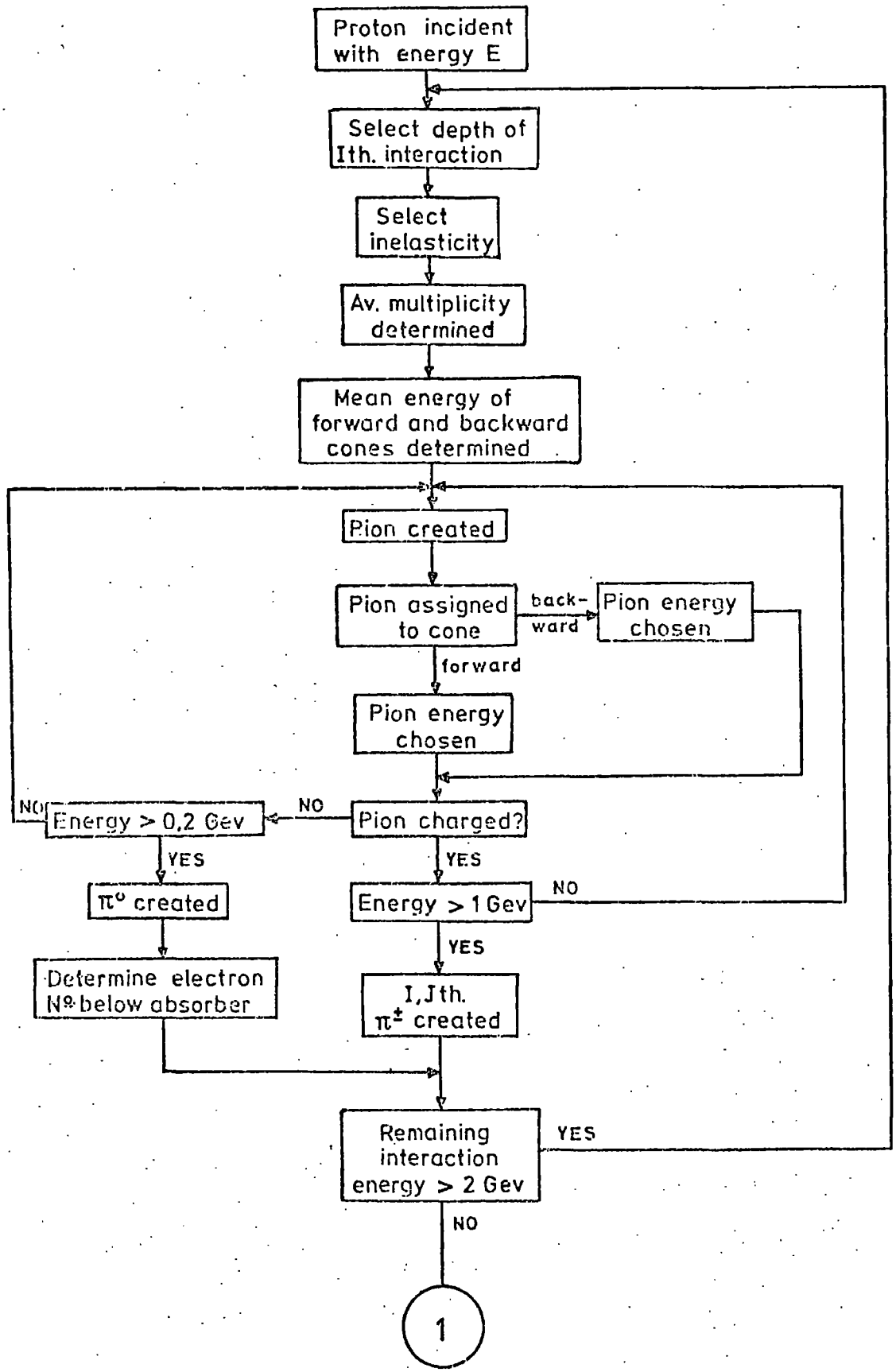
Proton incident with energy E
Select depth of Ith. interaction
Select inelasticity
Av. multiplicity determined
Mean energy of forward and backward cones determined
Pion created
Pion assigned to cone
back-ward
Pion energy chosen
forward
Pion energy chosen
NO
Energy > 0,2 Gev
NO
Pion charged?
YES
YES
π° created
Energy > 1 Gev
NO
YES
Determine electron Nº below absorber
I, Jth. π± created
Remaining interaction energy > 2 Gev
YES
NO
1

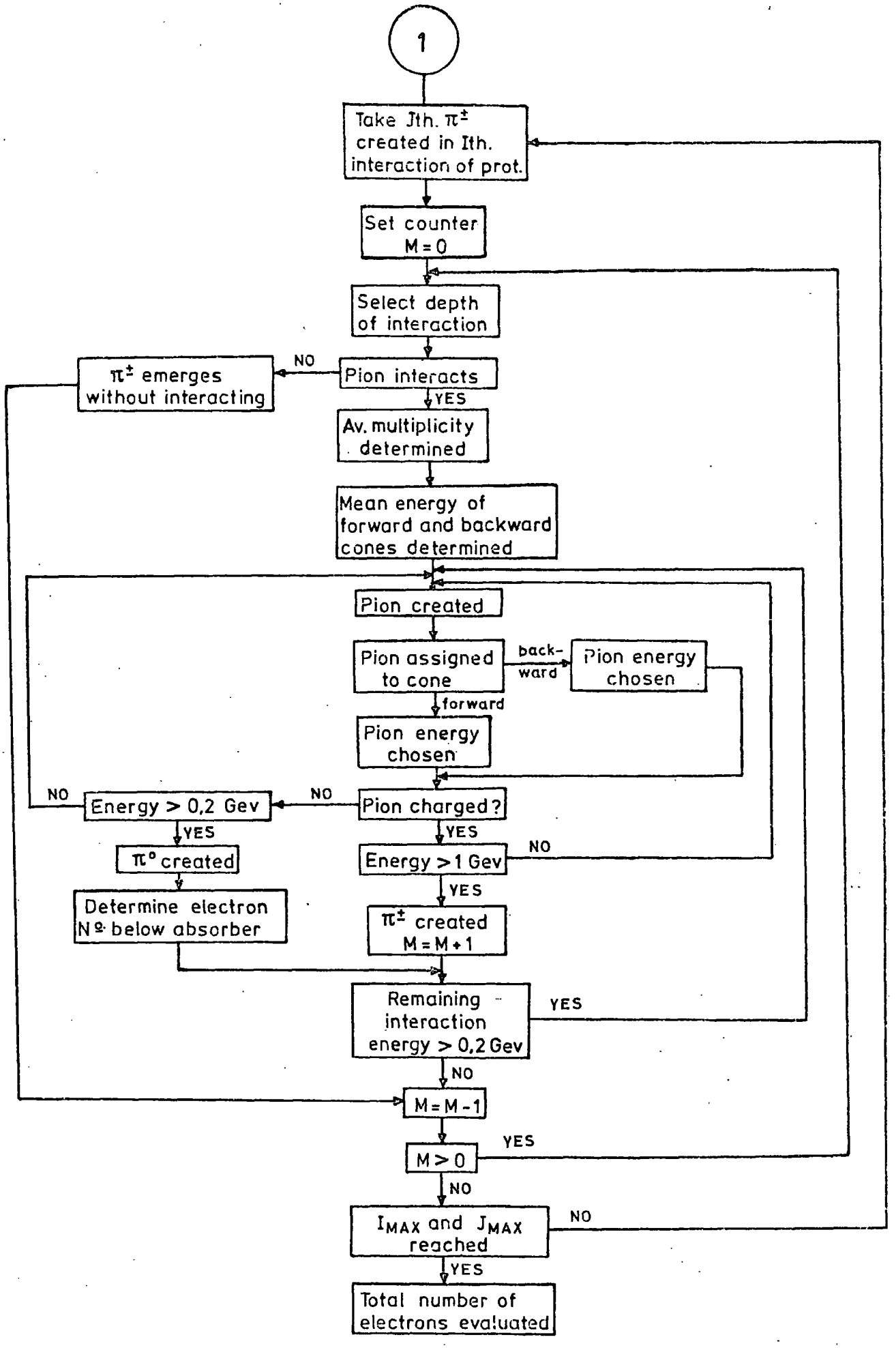
1
Take Jth. π± created in Ith. interaction of prot.
Set counter M = 0
Select depth of interaction
Pion interacts
NO
π± emerges without interacting
YES
Av. multiplicity determined
Mean energy of forward and backward cones determined
Pion created
Pion assigned to cone
back-ward
Pion energy chosen
forward
Pion energy chosen
Pion charged?
NO
Energy > 0,2 Gev
NO
YES
π° created
Determine electron N° below absorber
YES
Energy > 1 Gev
NO
YES
π± created M = M + 1
Remaining interaction energy > 0,2 Gev
YES
NO
M = M - 1
M > 0
YES
NO
IMAX and JMAX reached
NO
YES
Total number of electrons evaluated

energy had fallen below 0.2 GeV. At this point the total number of electrons emerging from the absorber, summed over all electron-photon cascades, was evaluated.

A flow diagram of the computer program is shown in Figure 5.8.

## 5.5 Results of the Calculations

### 5.5.1. Introduction

For the four cases considered, pions and protons incident on lead and iron absorbers, approximately 1000 cascades were generated at each of four energies: 10 GeV, 100 GeV, 1 TeV and 10 TeV. It was necessary to simulate a large number of cascades in order to determine average characteristics because of the large fluctuations in individual cascades. Since the analytical results of Ivanenko and Samosudov were used to evaluate electron numbers no fluctuations were included in the electron-photon cascade. This was dictated by limitations imposed on total computing time (the time required to fully simulate the highest energy cascades would have been prohibitive). However this approach can be justified, since fluctuations in the electromagnetic component will be small compared to the effect of fluctuations cased by the distribution of the depth of interaction, inelasticity and energy of the secondary pions.

### 5.5.2 The average behaviour of the cascade

The mean numbers of electrons obtained as a function of incident particle energy are shown in Figures 5.9 to 5.12. The dashed curves represent the one standard deviation limits. Smooth curves have been drawn through the points obtained. The standard error on the points is given approximately by the expression

$$\alpha = \sigma/(1000)^{1/2}$$

where 1000 is the number of cascades simulated.

It can be seen that for a given material the pion and proton curves are almost parallel, the reduction in electron number at a given energy

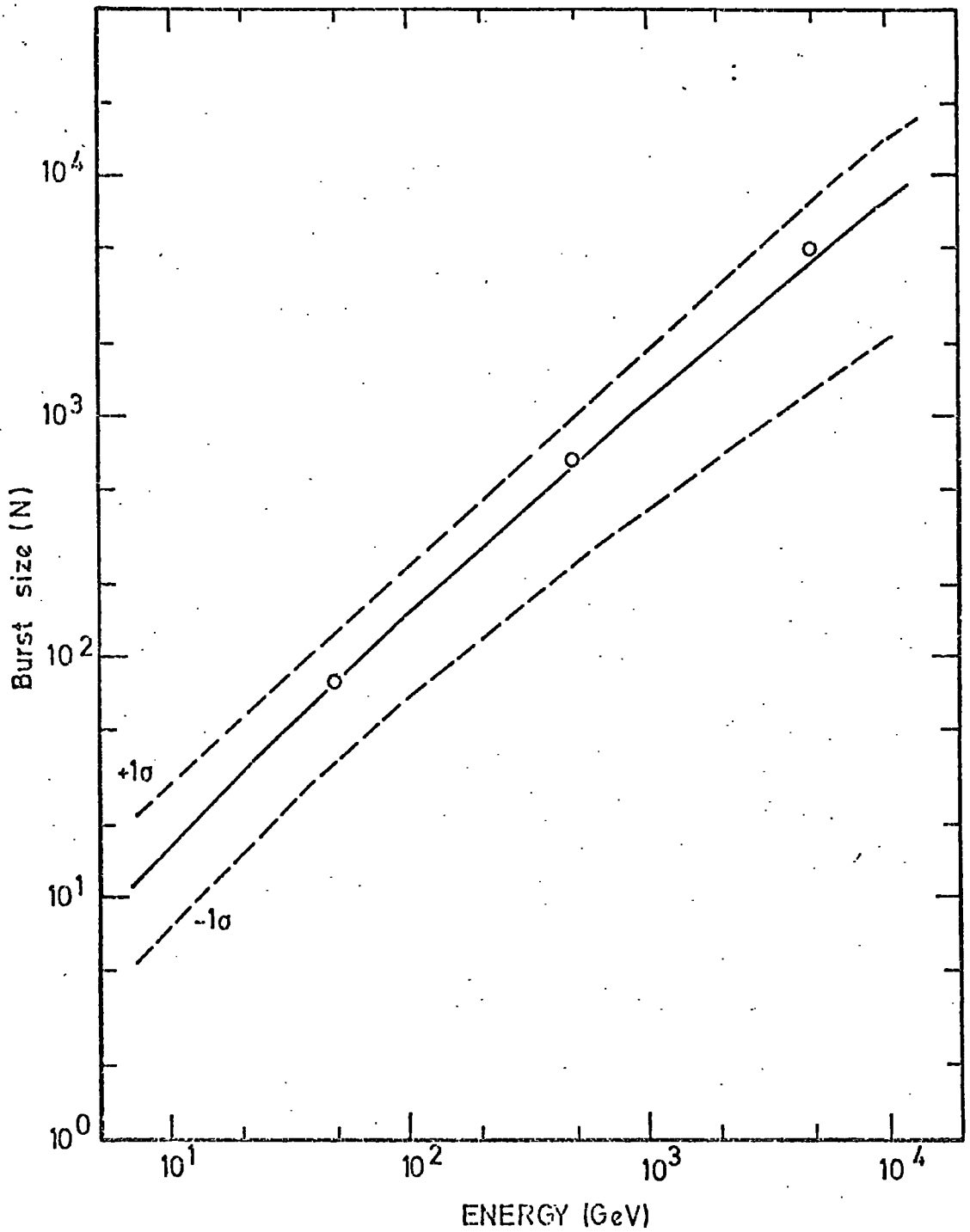


Figure 5.9 The mean burst size (N) produced by a pion of a given energy in 15 cms. iron. The one standard deviation limits of the distribution are shown. The open circles represent simulations performed for pions incident at a zenith angle of $30^{o}$.

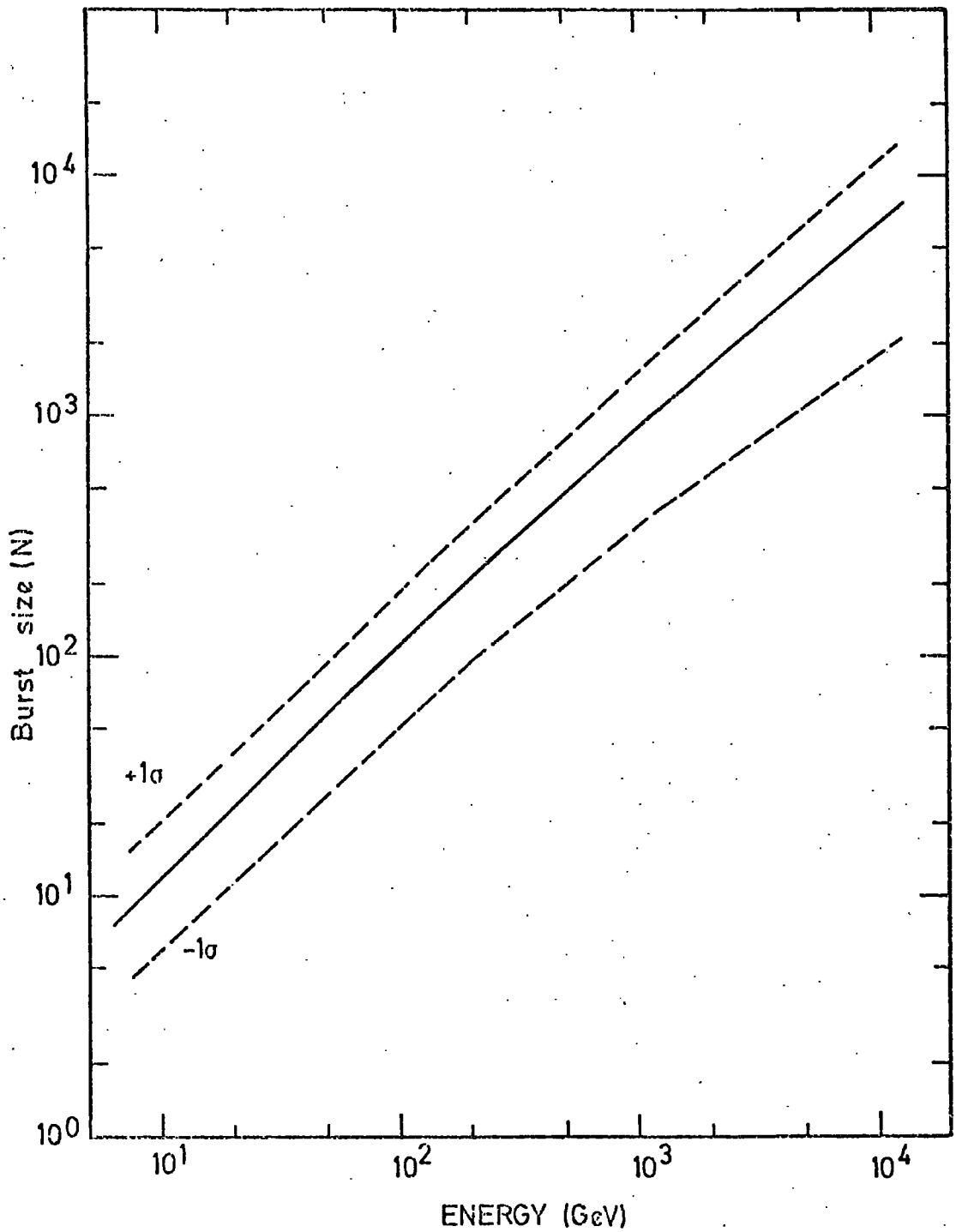


Figure 5.10 The mean burst size (N) produced by a proton of a given energy in 15 cms. iron. The one standard deviation limits of the distribution are shown.

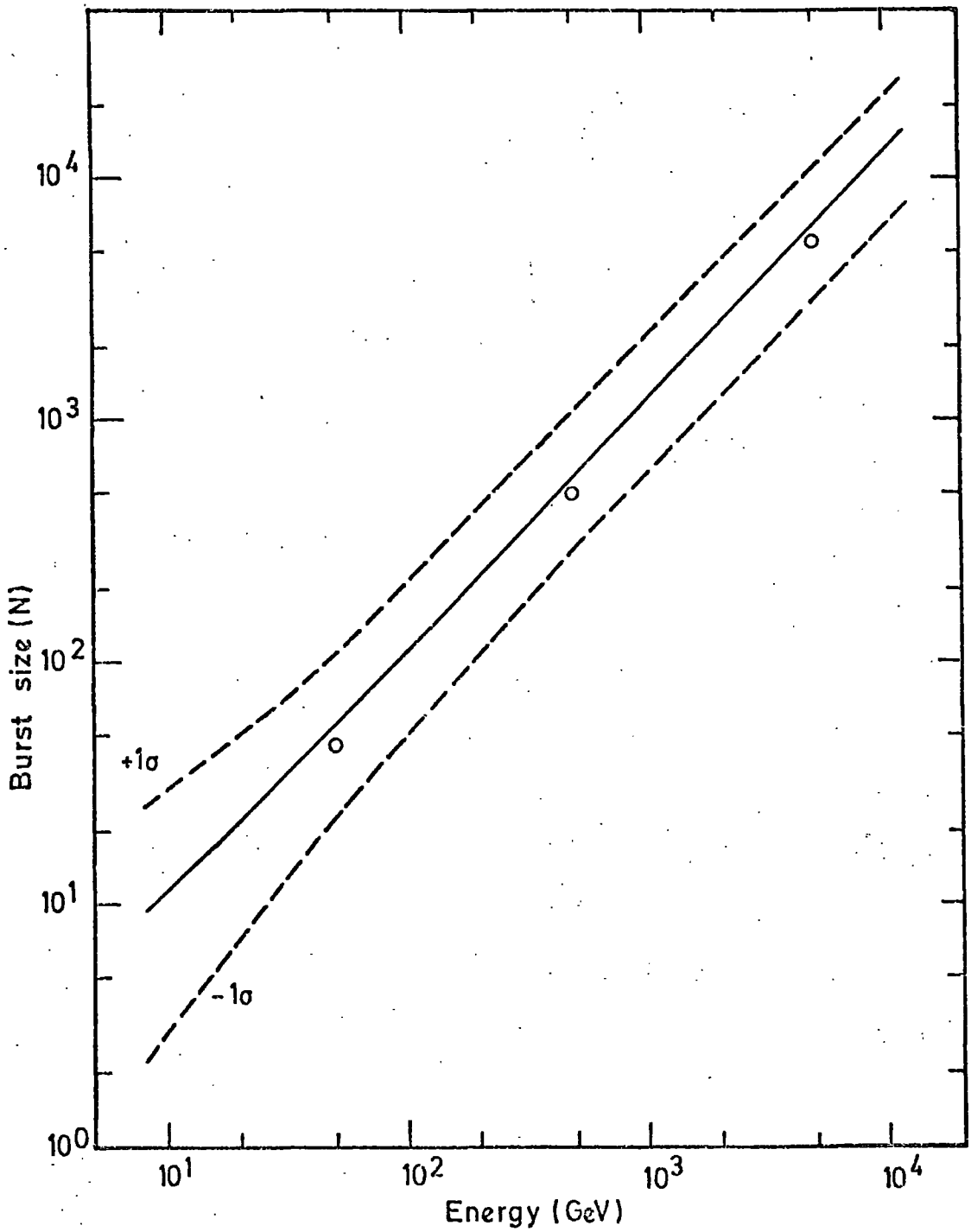


Figure 5.11 The mean burst size (N) produced by a pion of a given energy in 15 cms. lead. The one standard deviation limits of the distribution are shown. The open circles represent simulations performed for pions incident at a zenith angle of $30^{\circ}$.

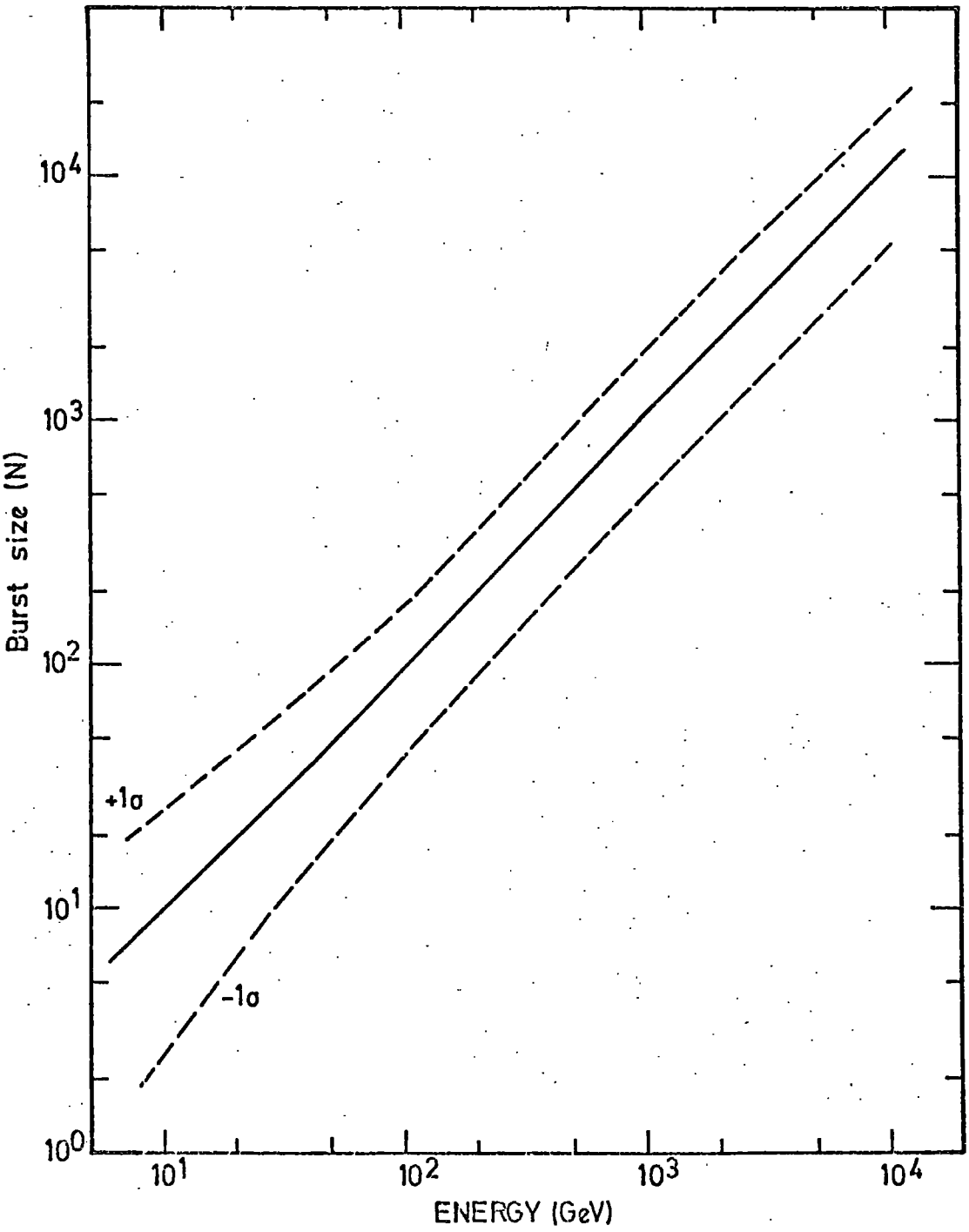


Figure 5.12 The mean burst size (N) produced by a proton of a given energy in 15 cms. lead. The one standard deviation limits of the distribution are shown.

being approximately proportional to the inelasticity. It should be noted that while up to the highest energy simulated in the lead absorber there is a scaling relationship between burst size and energy, the curves in iron show a definite flattening at high energies. This is interpreted as being due to the fact that at high energies the cascades cannot fully develop in the relatively thin iron absorber (8.19 radiation lengths), whereas in the lead saturation is not reached because of the relatively greater depth available for cascade development (32.17 radiation lengths). The open circles in Figures 5.9 and 5.11 represent cascades simulated at a zenith angle of $30^{\circ}$, performed in order to estimate the sensitivity of the results to the zenith angle. These results are consistent with the conclusions reached above. In the lead target the cascades incident at $30^{\circ}$ produce less electrons below the absorber because of the greater depth through which the cascade passes. In the iron, however, the increased path length allows the cascade to develop more fully at high energies, producing larger burst sizes.

5.5.3 The burst size distribution

While the Monte Carlo technique predicts the average properties of the cascade, it also provides direct information on the fluctuations inherent in the cascade and can thus produce the distribution in burst size for a fixed primary energy. Figures 5.13 to 5.16 show the integral probability that $\geqq N$ electrons will be produced below the absorber by a primary particle of energy E. To show more clearly the way in which the width of the distribution varies with energy, the results can be represented as shown in Figure 5.17. It can be seen that in general the widths of the distributions decrease as the energy increases, due to the averaging which occurs when a large number of electromagnetic cascades are superimposed. This is not true in the iron, however, where the width of the distribution has a minimum between 100 GeV and 1 TeV and then increases again as the energy increases. This is due to the fact that the electromagnetic cascades cannot develop fully.

Figure 5.13 The integral probability that a pion of energy $E_\pi$ will produce a burst of size >N below 15 cms. of iron.

Figure 5.14 The integral probability that a proton of energy $E_p$ will produce a burst of size >N below 15 cms. of iron.

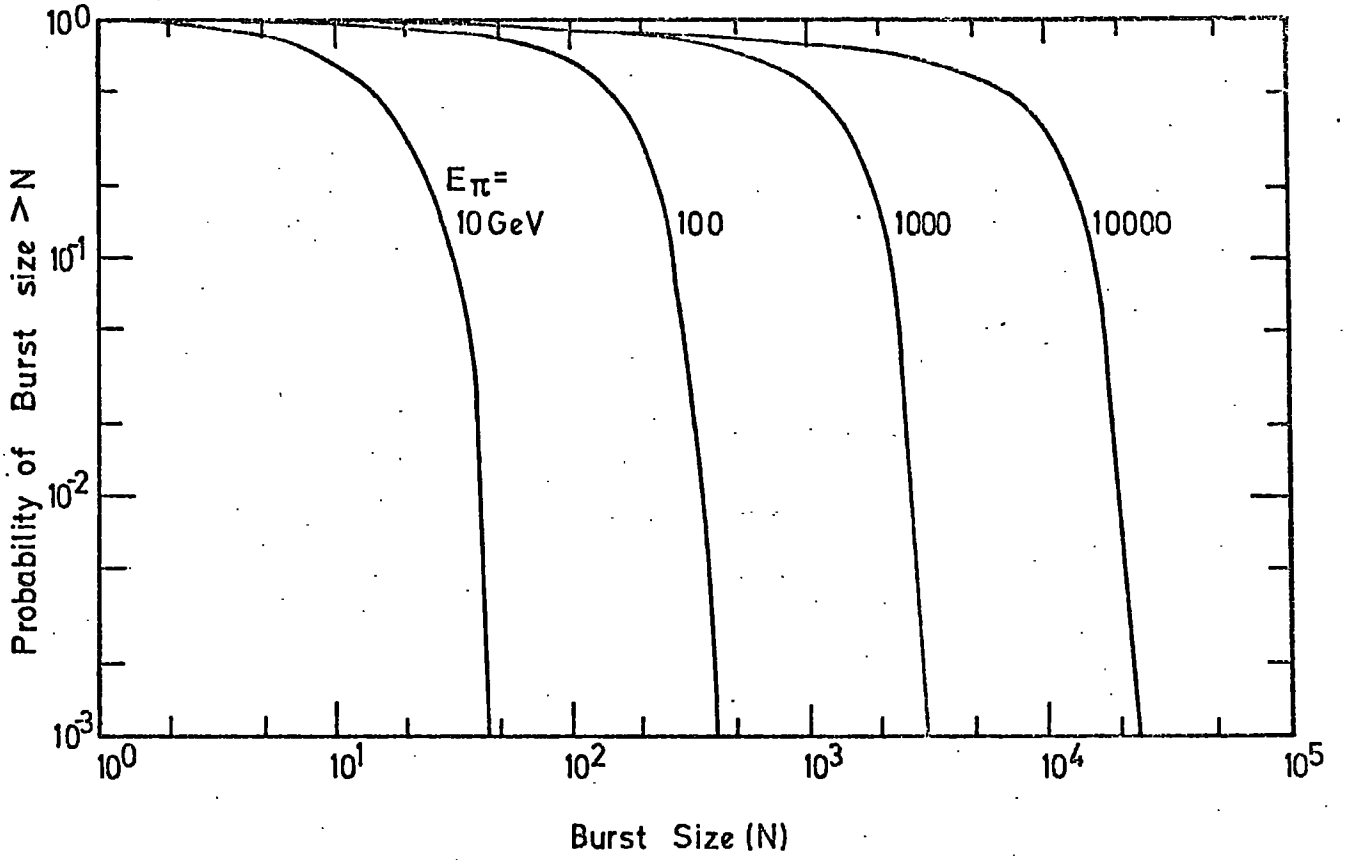
Probability of Burst size >N
$10^0$
$10^{-1}$
$10^{-2}$
$10^{-3}$
$E_\pi$=
10 GeV
100
1000
10000
$10^0$
$10^1$
$10^2$
$10^3$
$10^4$
$10^5$
Burst Size (N)

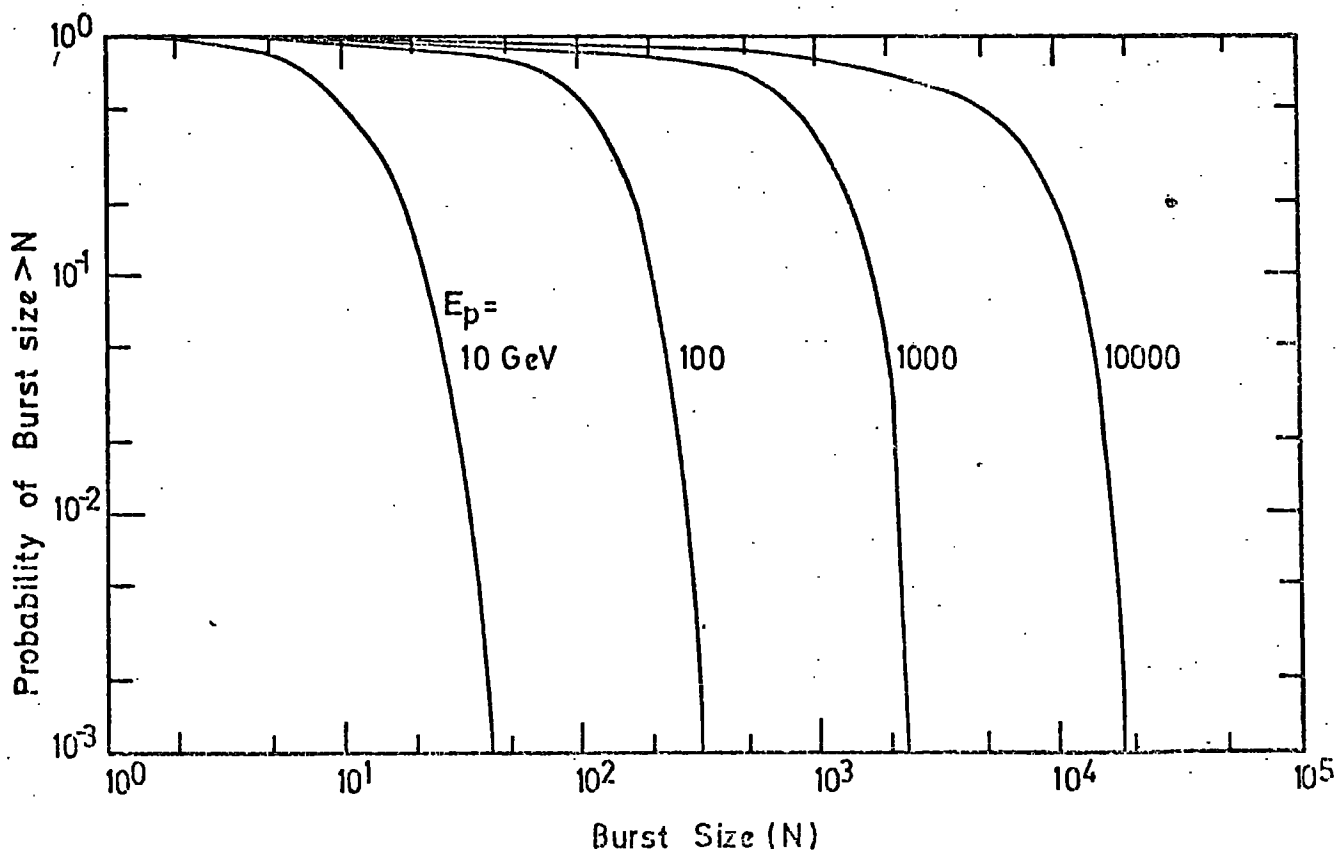
Probability of Burst size >N
$10^0$
$10^{-1}$
$10^{-2}$
$10^{-3}$
$E_p$=
10 GeV
100
1000
10000
$10^0$
$10^1$
$10^2$
$10^3$
$10^4$
$10^5$
Burst Size (N)

Figure 5.15 The integral probability that a pion of energy $E_\pi$ will produce a burst of size > N below 15 cms. of lead.

Figure 5.16 The integral probability that a proton of energy $E_p$ will produce a burst of size >N below 15 cms. of lead.

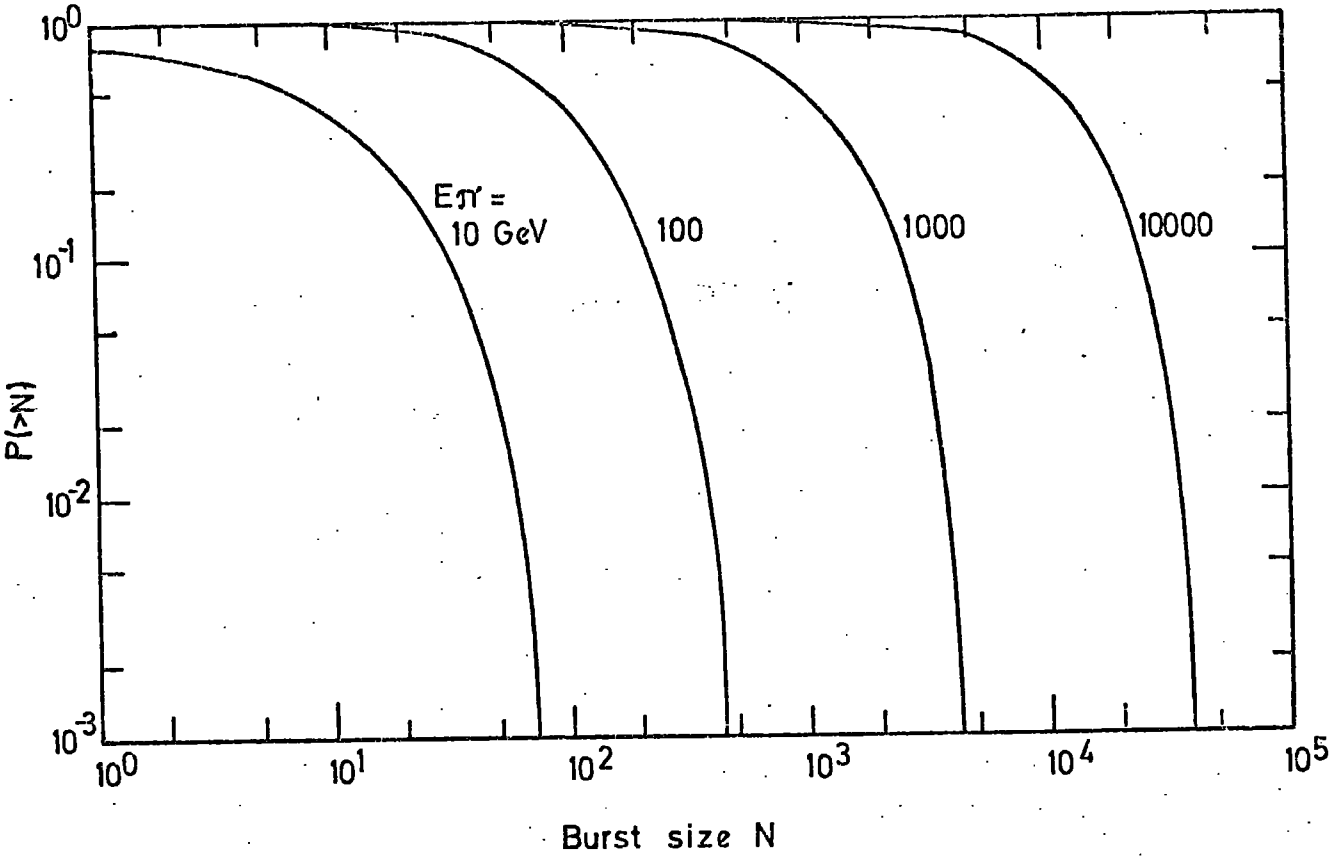
$10^0$
$10^{-1}$
$10^{-2}$
$10^{-3}$
P(>N)
Eπ⁰ =
10 GeV
100
1000
10000
$10^0$
$10^1$
$10^2$
$10^3$
$10^4$
$10^5$
Burst size N

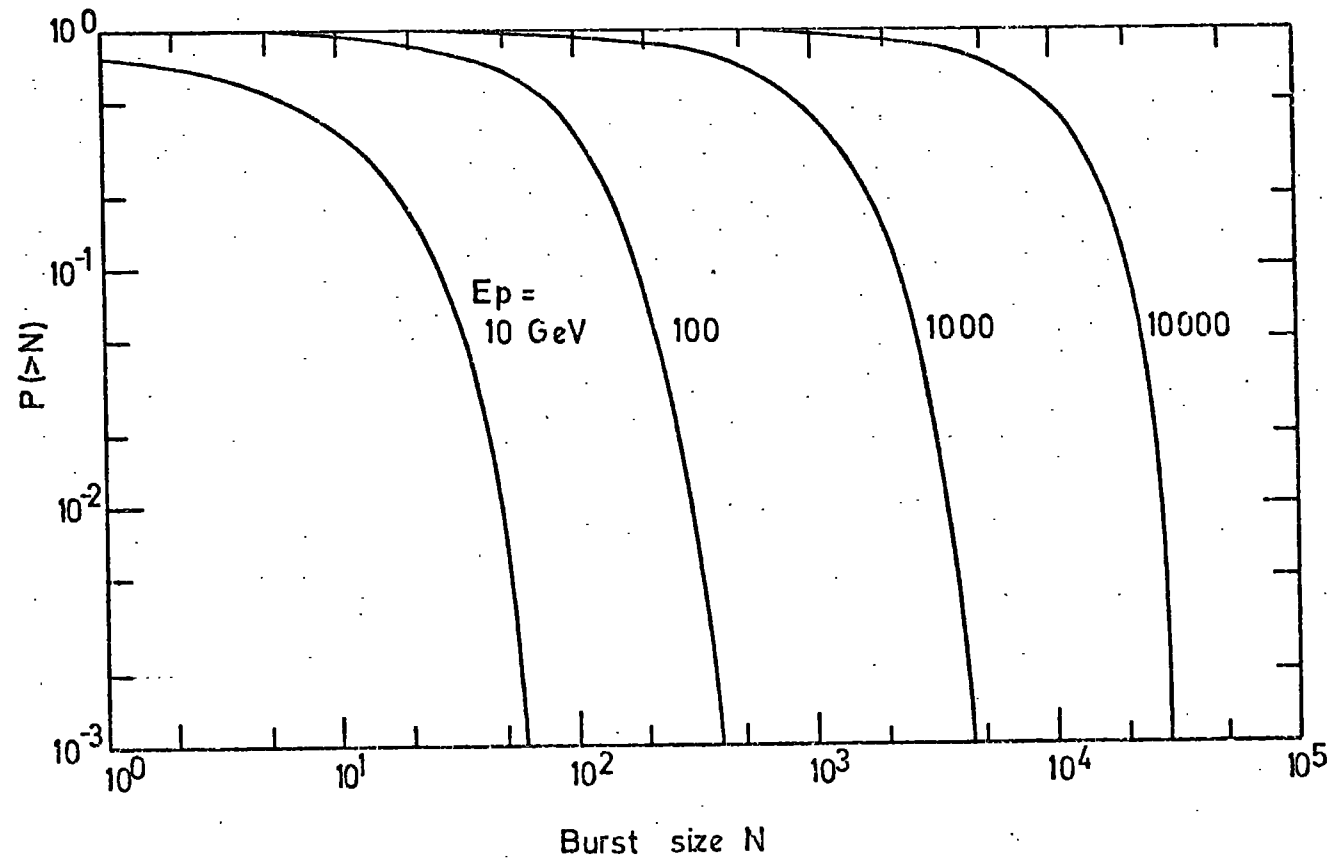
$10^0$
$10^{-1}$
$10^{-2}$
$10^{-3}$
P(>N)
Ep =
10 GeV
100
1000
10000
$10^0$
$10^1$
$10^2$
$10^3$
$10^4$
$10^5$
Burst size N

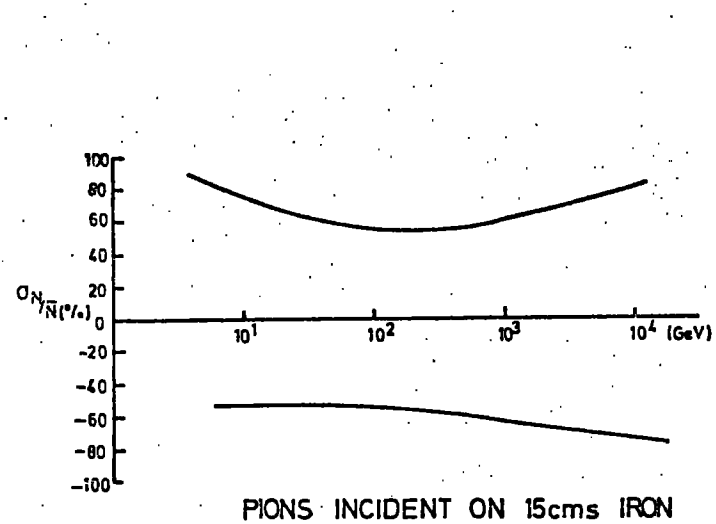


PIONS INCIDENT ON 15cms IRON

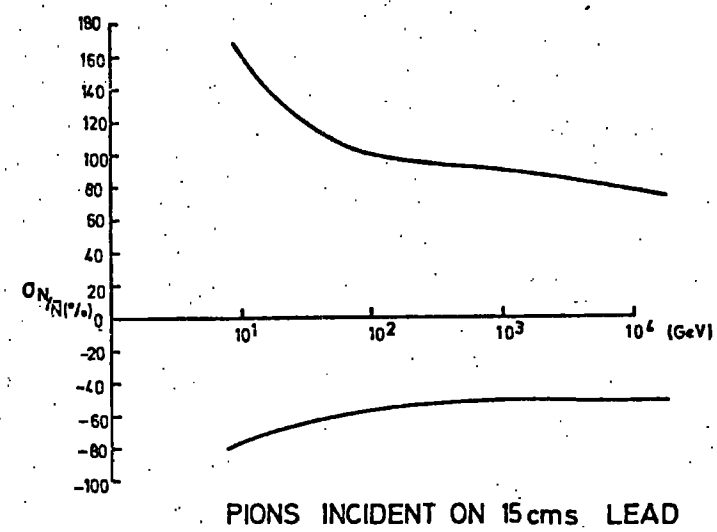


PIONS INCIDENT ON 15cms LEAD

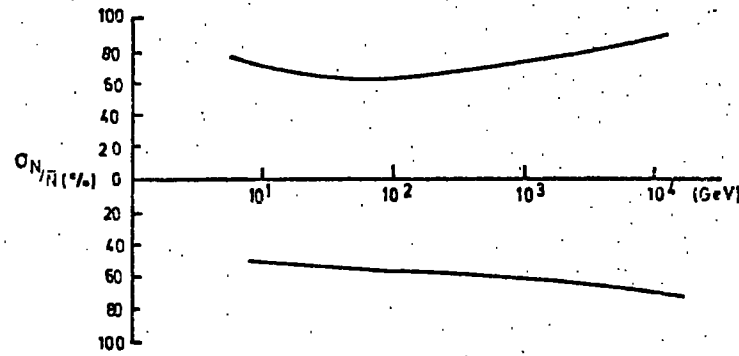


PROTONS INCIDENT ON 15 cms IRON

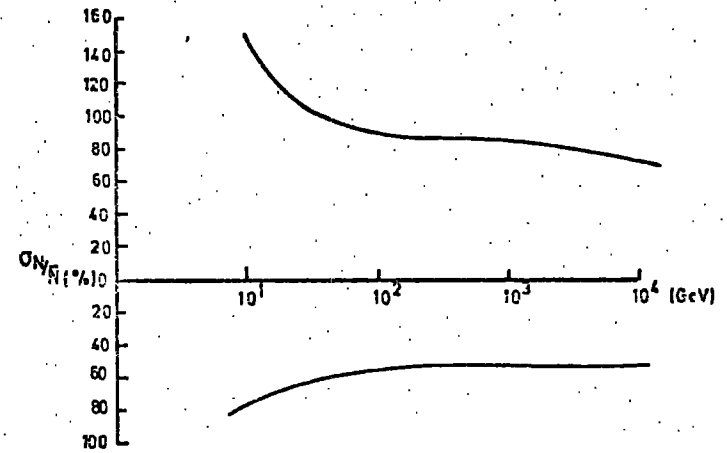


PROTONS INCIDENT ON 15 cms LEAD

Figure 5.17 The variation of the burst size distribution with energy.

The results of the Monte Carlo calculations have been compared with results obtained using an approximate numerical method (Saleh, private communication). Similar nuclear-physical assumptions were made in both cases, such that the two approaches should be directed comparable. The approach adopted in the numerical method was to divide the absorber into several layers and consider the cascade which would develop from an interaction produced in the middle of each layer. Mean multiplicities, inelasticities etc. were put into the calculations. Distributions in these parameters could not easily be included. To compare the results obtained by the two methods the variation of electron number with depth of the initial interaction was studied. Figure 5.18 shows this comparison for pions interacting in 15 cms. of iron. A total of 200 cascades were simulated at each energy and are shown in the form of a scatter plot. The full curves are the results of the numerical method. It can be seen that the results are quite close, although the small discrepancies at the highest energies are to be expected. These scatter plots clearly show that at high energies no maximum is reached in the burst size distribution as a function of depth. For comparison, Figure 5.18 (c) shows the prediction of Vatcha et.al. for a 1000 GeV pion in iron (their model C).

## 5.6 The Lateral Spread of Bursts

### 5.6.1 Introduction

To estimate the energy of bursts occurring in either the iron or lead absorbers it is necessary to relate the number of electrons emerging from the absorber to a parameter which is measurable in the flash tubes. Now since the amount of material represented by the glass of the flash tubes is small the cascade cannot develop significantly in the flash tubes themselves. Hence the parameter most accessible to measurement below both the lead and iron is the width of the burst directly below the absorber. To relate this to the burst size it is necessary to adopt

Figure 5.18 Scatter plots showing the correlation between the depth of the initial interaction and the burst size below 15 cms. of iron for pions at four energies. The smooth curves are predictions for an average treatment. The results of calculations by Vatcha et.al. are shown for comparison for 1 TeV pions.

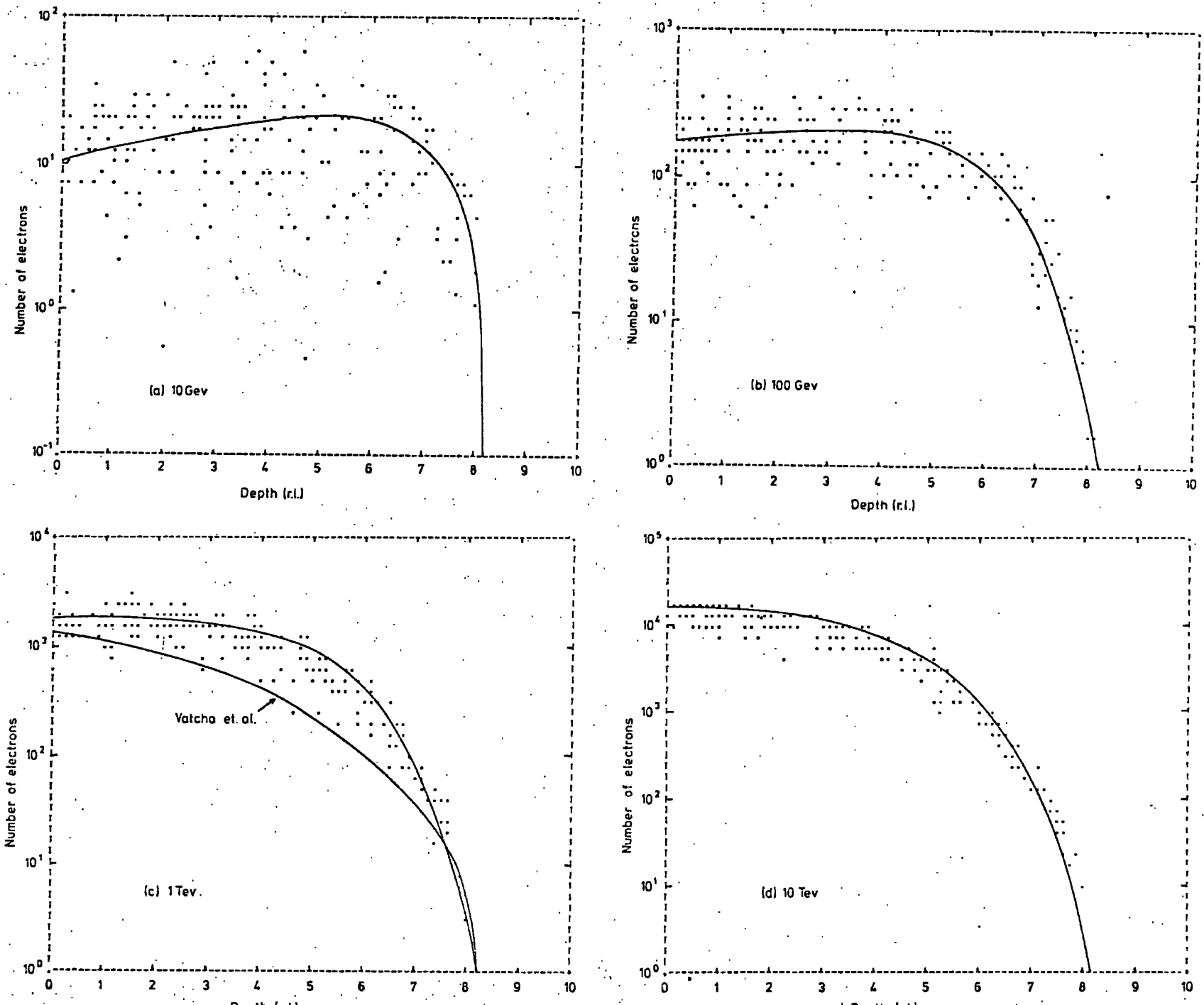
Number of electrons
Depth (r.l.)
(a) 10 Gev
(b) 100 Gev
(c) 1 Tev.
Vatcha et. al.
(d) 10 Tev

some definition of burst width. Thus the width of the burst was defined as that width in the flash tubes within which all of the flash tubes had flashed. Thus tubes flashing away from the core of the bursts, produced say by a single electron or perhaps a large angle charged pion, would not be considered when the width of the burst was measured.

The lateral spread of low energy electrons might be expected to be dominated by the effect of multiple scattering of the cascade electrons rather than by effects connected with the nuclear cascade. Thus an attempt was made to predict the lateral spread of pure electromagnetic cascades.

5.6.2 Calculation of the lateral spread of electromagnetic cascades

Nishimura and Kamata (1952) have obtained a theoretical expression for the lateral structure function of pure electromagnetic cascades. This rather complex expression has been approximated by the empirical expression by Greisen (1956):-

$$f(r/r_1) = c(s)\ (r/r_1)^{s-2}(1 + r/r_1)^{s-4.5}$$

where s is the age parameter and radii are measured in Moliere units ($r_1$). The function is normalised by the constant c(s) such that

$$\int_0^\infty 2\pi x\ f(x)dx = 1 \qquad \text{where } x = (r/r_1)$$

By a simple argument one can obtain the approximate form of the width dependence on burst size. We can write

$$f(x) \propto x^{s-2}\ (1 + x)^{s-4.5} \approx x^{(2s-6.5)} \text{ for } x \gg 1$$

Now the density at a distance x from the core is given by

$$\Delta(x) = \frac{N\ f(x)}{r_1^{\,2}}$$

$$\therefore \Delta(x) \propto N\ x^{(2s-6.5)}$$

Consider that s is a slowly varying function for the range of N being considered and is equal to one (this can be shown to be a reasonable assumption). Then the distance at which the density falls to $\Delta(x)$ is related approximately to the burst size by the power law dependence

$$r \propto N^{1/4.5} \approx N^{0.22}$$

In order to calculate the dependence more accurately the Nishimura - Kamata - Greisen (NKG) formula was integrated for three different age parameters. Now the electron density is effectively measured by the flash tubes, therefore to calculate the density of electrons per tube the integration must be carried out not radially but along strips corresponding to flash tube cross-sections. The results of the integrations are shown in Figure 5.19. To obtain the distance from the core at which the density per strip (of width one Moliere unit) falls to a certain density the ordinate should be multiplied by the burst size (the number of electrons at the measuring level of energy greater than the minimum energy required to traverse one tube). The conversion to flash tube diameters is simply performed, therefore it is possible to plot the width in flash tube diameters as a function of burst size. This is done in Figure 5.20. Also shown are the results of two experiments performed by Coats (1967) in which the burst spectra of horizontal muons (electromagnetic) and vertical particles (mainly nuclear-electromagnetic) were measured in iron of thickness 25 cms. Flash tubes were utilised in these experiments to aid in the identification of spurious events, but Coats presents the relationship between burst size and burst width in a form which can be compared with the above calculated relationship.

The lack of agreement between these curves can largely be explained by the spreading of the low energy electrons in the air gap between the absorber and the flash tubes. These low energy electrons have an almost isotropic angular distribution (Messel and Crawford, 1970) and will thus cause a considerable broadening of the cascade. It is noticeable, however,

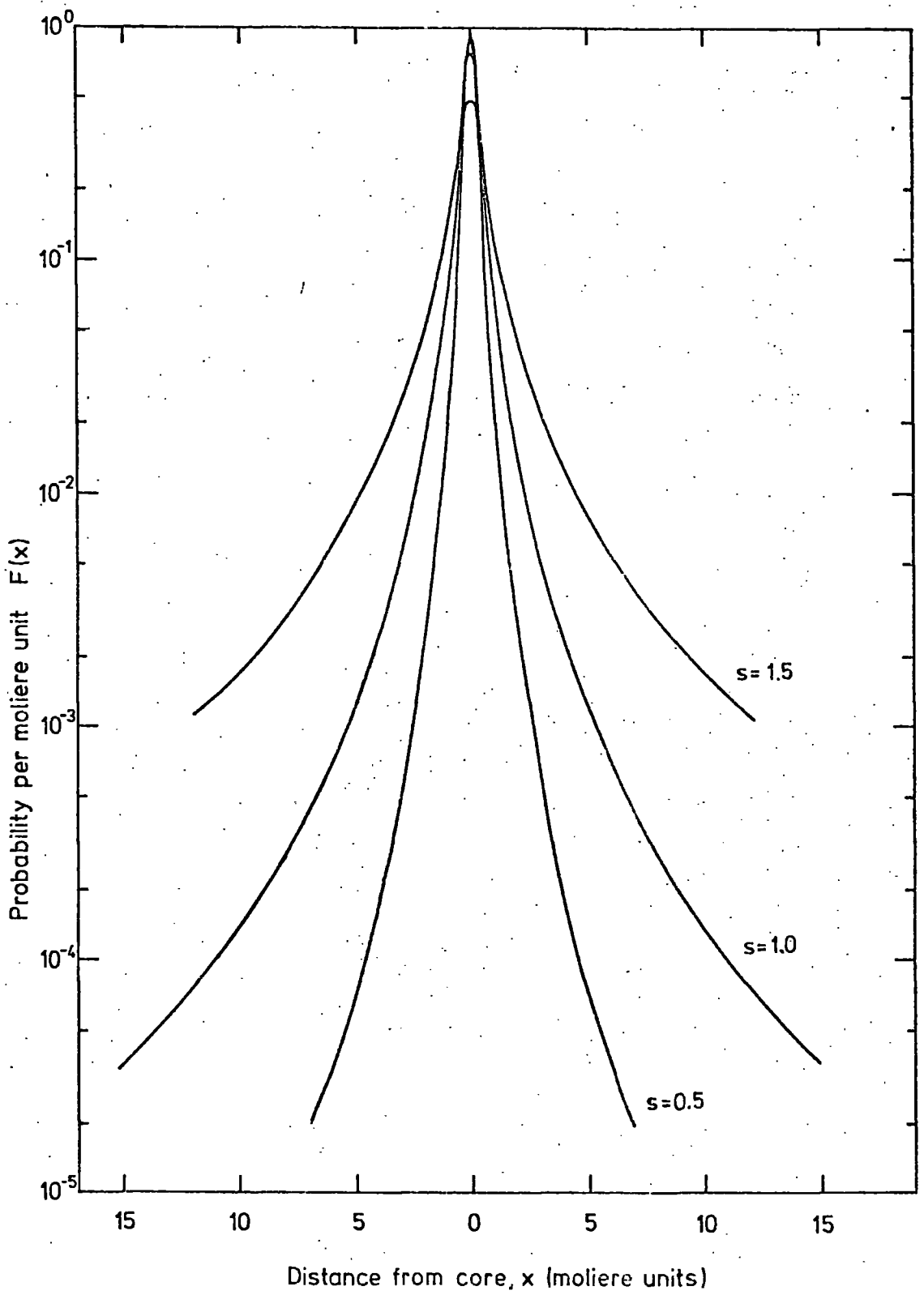


Figure 5.19 The probability of a particle traversing a flash tube as a function of distance from the core, expressed with width in Moliere units. The number of particles falling on a strip of width 1 Moliere unit as a distance x from the core is NF(x), where N is the burst size.

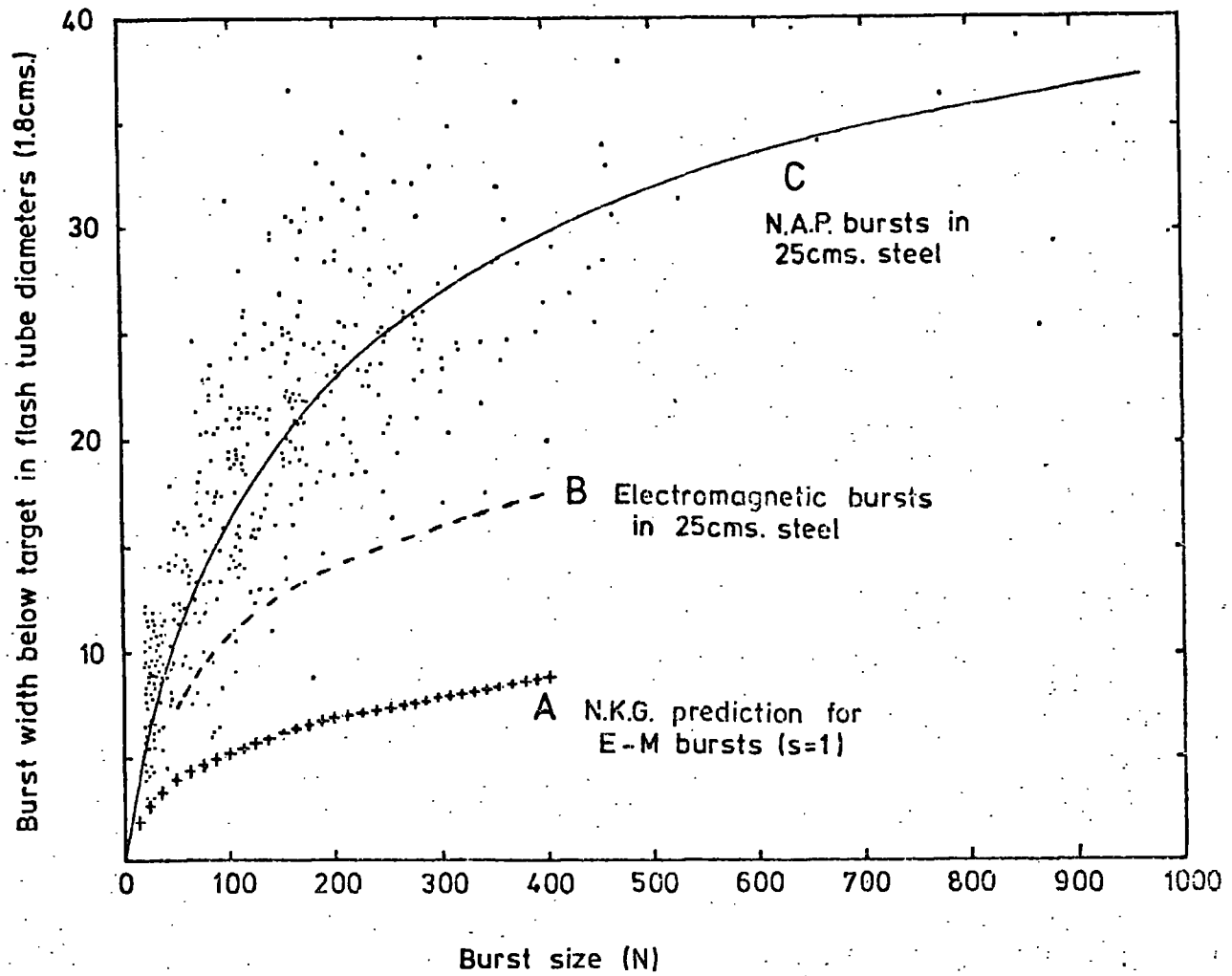


Figure 5.20 Correlation between the width of a burst emerging from a thick steel target and the number of particles in the cascade. Curve A - prediction for a pure electron-photon cascade; Curve B - measured relationship for electromagnetic bursts from muons (Coats, 1967); Curve C - as B but for nuclear-electromagnetic bursts. ~~The points were obtained in C.~~

that for similar geometries the nuclear-electromagnetic cascades are significantly wider than the pure electromagnetic cascades as measured by Coats. This is attributed to the angular divergence of the cascade caused by the effects (a) to (c) mentioned in section 5.2. It is apparent that transition effects are extremely important in determining the burst width, making a direct measurement of the burst width-burst size relation for the particular geometrical arrangement used in the present experiment a necessity.

## 5.7 Conclusion

It has been possible to predict the development of nuclear-electromagnetic cascades in the iron and lead absorbers of the flash tube chamber. It has also been shown that there exists a correlation between the width of the burst measured in the flash tubes directly below the absorbers and the burst size, hence in principle the energy of an interacting particle can be estimated from a measurement of the burst width. However the exact form of this relationship between burst width and burst size is not known. This fact was the motivation behind the construction and operation of an experiment designed to measure this relationship. The vertical unaccompanied hadron spectrum was used for this purpose. The experiment and results are described in the following chapter.

# CHAPTER 6

## THE VERTICAL BURST EXPERIMENT

### 6.1 Introduction

It was shown in Chapter 5 that the energy of a hadron can be determined from the size of the cascade that it produces below an absorber of lead or iron. It was also shown that there is a strong correlation between the size of the burst and the lateral width of the burst as measured in flash tubes directly below the absorber. In order to obtain the conversion relationship for the flash tube chamber an experiment was performed to directly measure this relationship.

Bursts produced by single hadrons in the near-vertical direction were chosen as the most appropriate source, hence modifications were made to the flash tube chamber which allowed bursts in either the iron or lead absorber to be selected.

In addition to the primary aim, to obtain a calibration for the data obtained on bursts occurring close to the core of EAS, the recently reported anomaly in the vertical burst spectrum (Kellerman, 1973) has prompted fresh interest in the high energy part of this spectrum. It was hoped that data could be obtained which would provide information on this region.

### 6.2 Experimental Arrangement

#### 6.2.1 Modification to the flash tube chamber

The flash tube chamber described in Chapter 2 was modified to allow near-vertical bursts in the iron or lead to be selected. A suitably positioned plastic scintillation counter was already in place below the iron absorber (scintillator A - see Figure 2.1). Therefore it was necessary only to position another similar scintillator (designated scintillator C) below the lead, in line with scintillator A. Fortunately

there was sufficient space for the scintillation counter to be positioned without the necessity of having to raise the lead roof. This meant that the geometry would not be changed - an important factor. Also, in order to facilitate the recognition of neutral particle-induced events, the upper eight layers of flash tubes (constituting Fla) were brought forward by 15 cms., thus completely covering the iron.

This new arrangement is shown in Figure 6.1. In addition it was decided to operate the centre liquid scintillator, M, to obtain information on the EAS accompaniment (if any) when a particle produced a burst.

6.2.2 Calibration of the scintillators

The scintillation counters have been described in Chapter 2. For this experiment the two central photomultiplier tubes in both plastic scintillators were not used. This was necessary since while five of the photomultiplier tubes used in each scintillator were 53 AVP tubes, the sixth tube, in the middle at one end of the plastic scintillator had been designed for fast timing measurements and was a 56 AVP tube. Since the voltage output - H.T. characteristic was to be utilised this tube could not be used as its performance would differ from the other tubes. To symmetrize the counter the opposing photomultiplier tube was not used. The response of these scintillation counters has been described by Ashton et.al. (1967). The linearity should not be greatly affected by the modification.

For the calibration of the three scintillation counters, single penetrating particles were selected by a small geiger telescope. In order to use the geiger coincidence system the scintillator pulses were delayed by means of a delay line by approximately 1 μs. For the calibration of the scintillators it was necessary to know the loss in pulse height for a pulse transmitted from the photomultipliers to the output of the delay line. For this purpose square pulses of 100 ns width (about the same width as the plastic scintillator pulses)

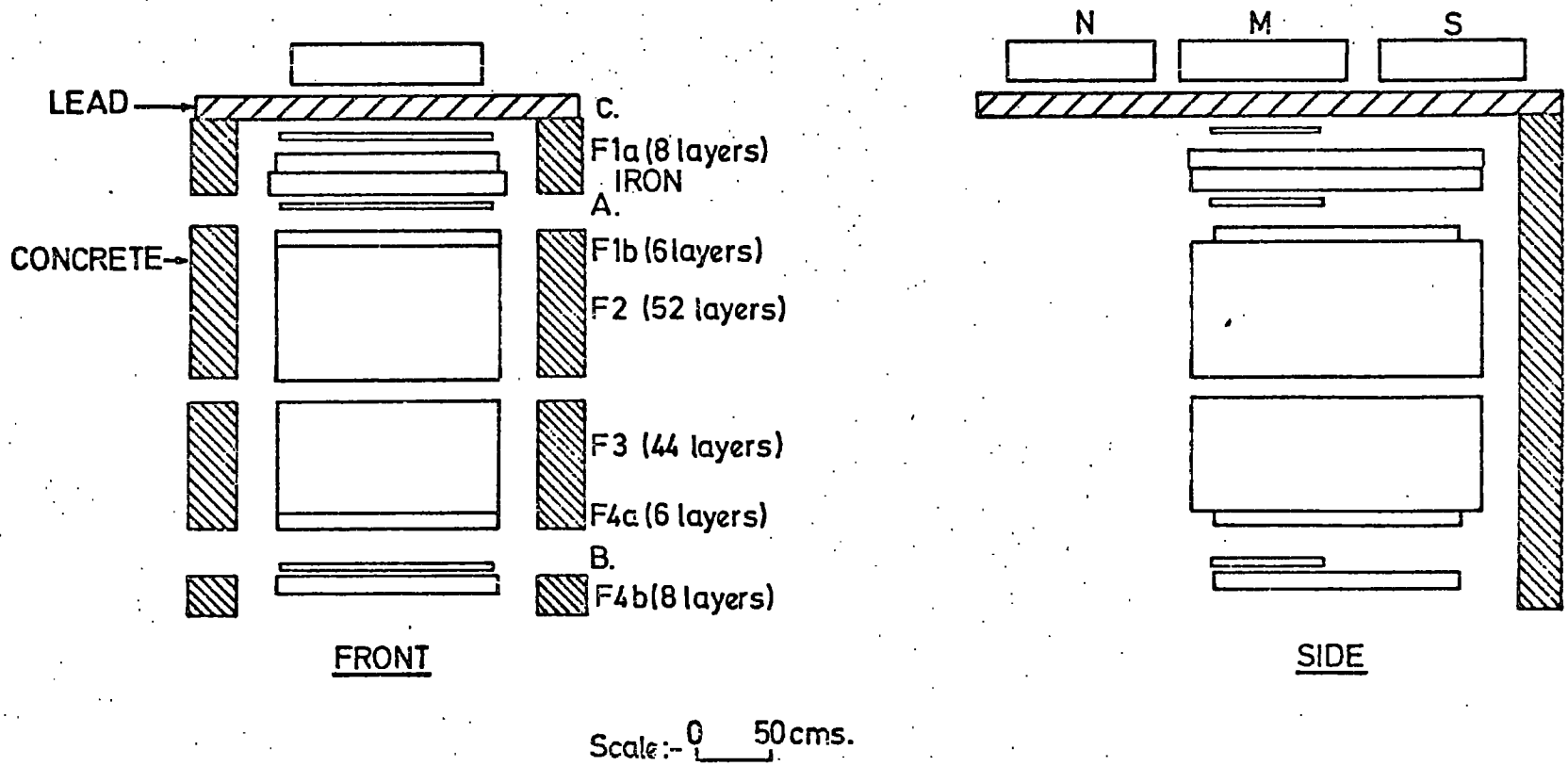


Figure 6.1 Scale diagram of modified flash tube chamber.

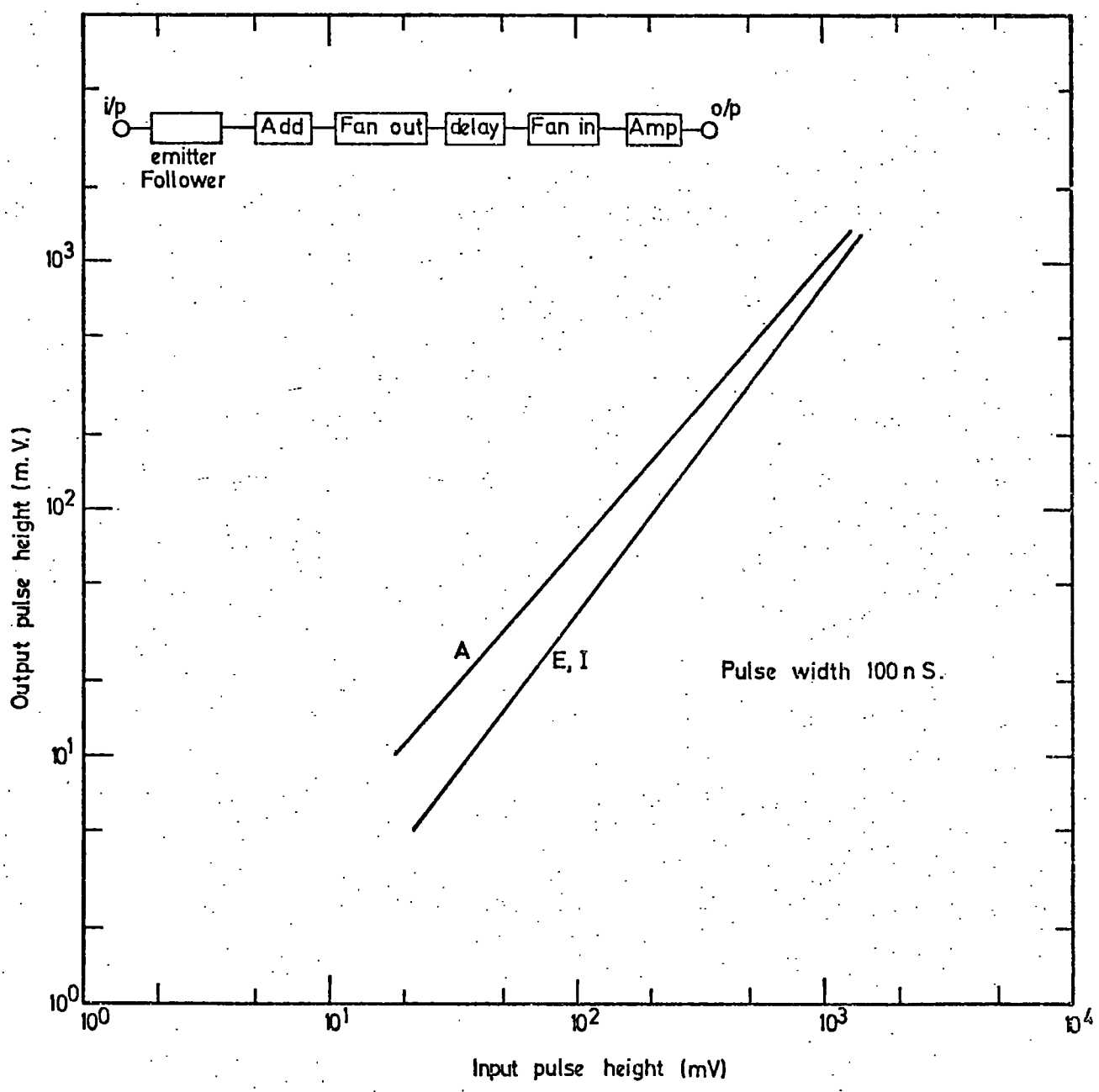


Figure 6.2 The input-output characteristics for the circuitry associated with scintillators A and M (E and I photomultipliers).

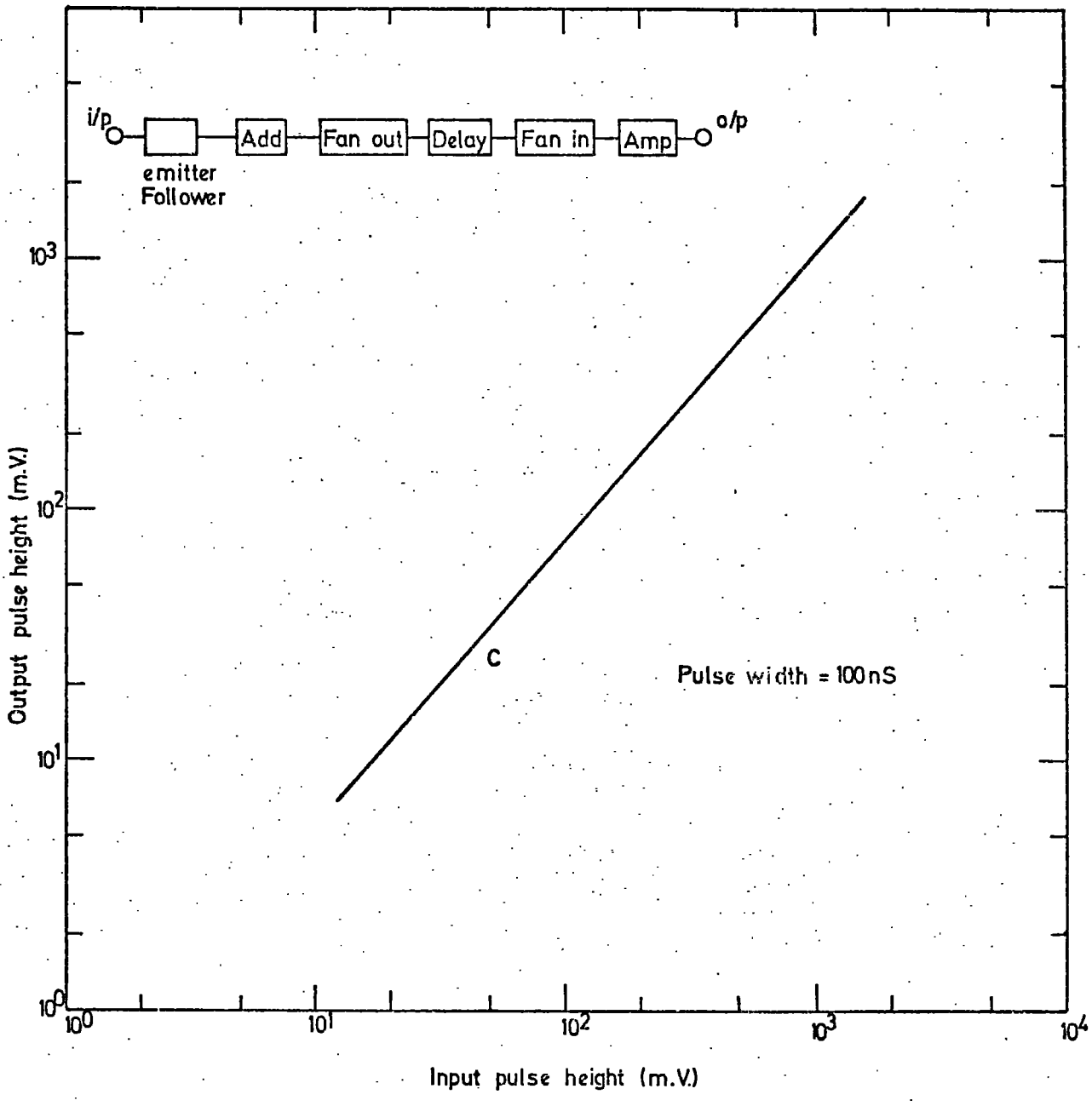


Figure 6.3 The input/output characteristics for the circuitry associated with scintillator C, measured for square pulses of width 100 ns.

were fed into the line and the input/output characteristics shown in Figures 6.2 and 6.3 were obtained. Also shown in these diagrams is the circuitry used.

For each of the photomultipliers the single particle pulse height distribution was measured for different valuesof the H.T. voltage applied to the tubes, for particles traversing the centre of each scintillator at vertical incidence. The results obtained can be seen in Figure 6.4, where the means of each distribution are shown plotted against the voltage applied to the photomultiplier tubes. It can be seen that for each scintillator all of the photomultiplier tubes produced approximately the same slope. Hence by supplying all the tubes from each scintillator from a single power supply unit via potentiometers it was possible, by adjusting the potentiometers for each tube separately, to normalise all tubes from one scintillator to produce identical output pulse heights for a charged particle traversing the centre of the scintillator. After this had been achieved it was then possible to calibrate the complete scintillator by adding the outputs from the photomultiplier tubes. The pulse height distributions obtained for scintillators A and C are shown in Figures 6.5 and 6.6 The means of these distributions were then converted using Figures 6.2 and 6.3 to pulse heights at the outputs of the photomultiplier tubes. The characteristics of the three scintillation counters obtained in this way are shown in Figures 6.7 and 6.8. Since the photomultiplier tubes for both plastic scintillators were operated from a single power supply the characteristic for the two counters should be identical. It can be seen that this is so within the limits of experimental error. The responses of the scintillators obey a power law dependence of the form $v = v_0 V^n$, where n for the plastic scintillators with 53 AVP photomultiplier tubes is 7.8, and for the liquid scintillators with EMI 9583B tubes is 7.5.

6.2.3 Experimental details

The trigger required was a burst of greater than a certain size in

Figure 6.4 The variation of single particle pulse height as a function of H.T. applied to the photomultiplier tubes for each photomultiplier tube in the three scintillators. (a) scintillator A, (b) scintillator C and (c) scintillator M. The pulse height mean was determined from the distribution for single penetrating particles at vertical incidence. Pulse heights are those measured at the output of the amplifier (see Figures 6.2 and 6.3).

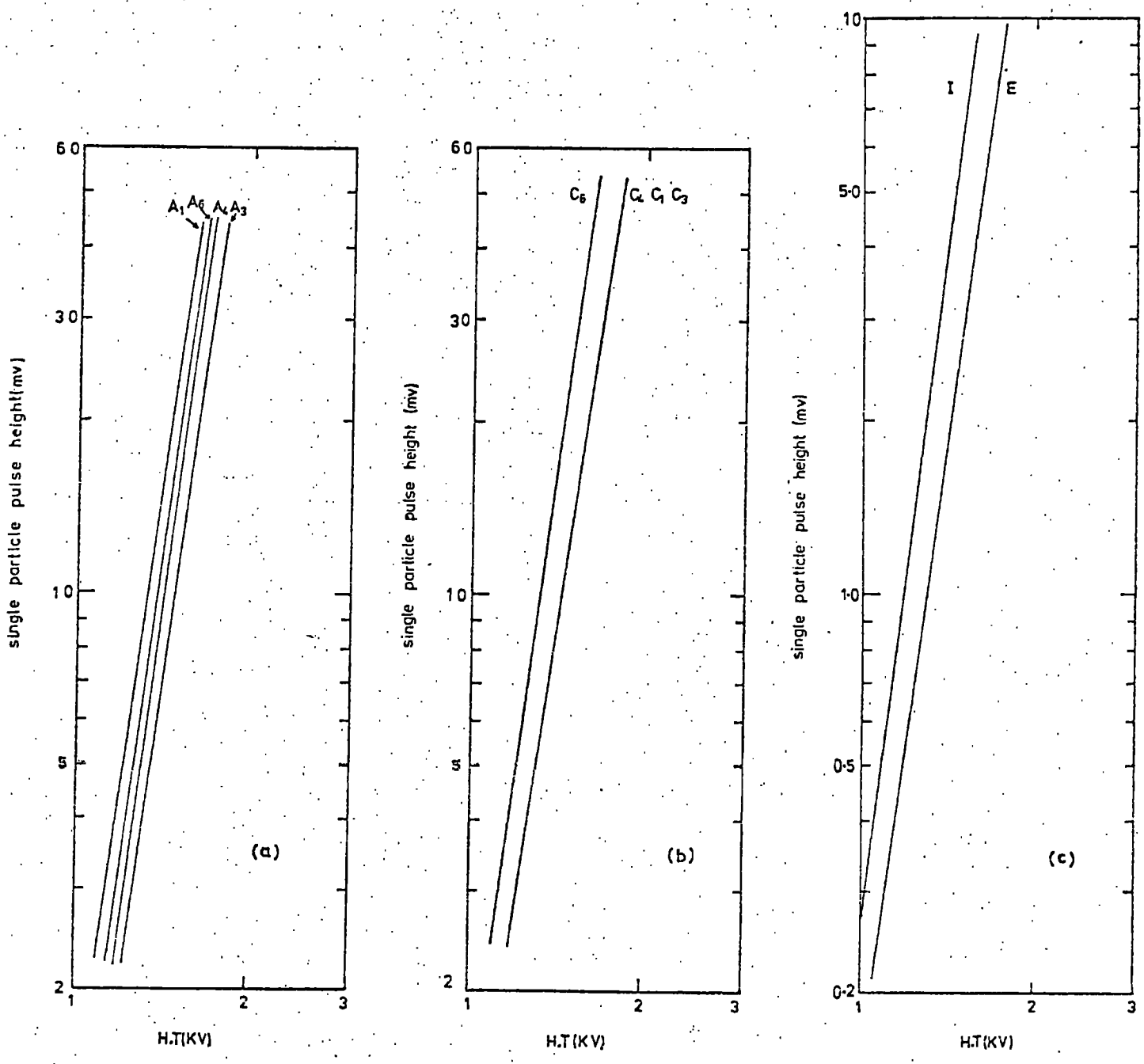
single particle pulse height(mv)
60
30
10
5
2
1
2
3
H.T(KV)
A1 A6 A4 A3
(a)
single particle pulse height (mv)
C6
C4 C1 C3
(b)
single particle pulse height (mv)
10
5·0
1·0
0·5
0·2
I
E
(c)

Figure 6.5 The single particle pulse height distribution for scintillator A, measured at the output of the amplifier (see Figure 6.4).

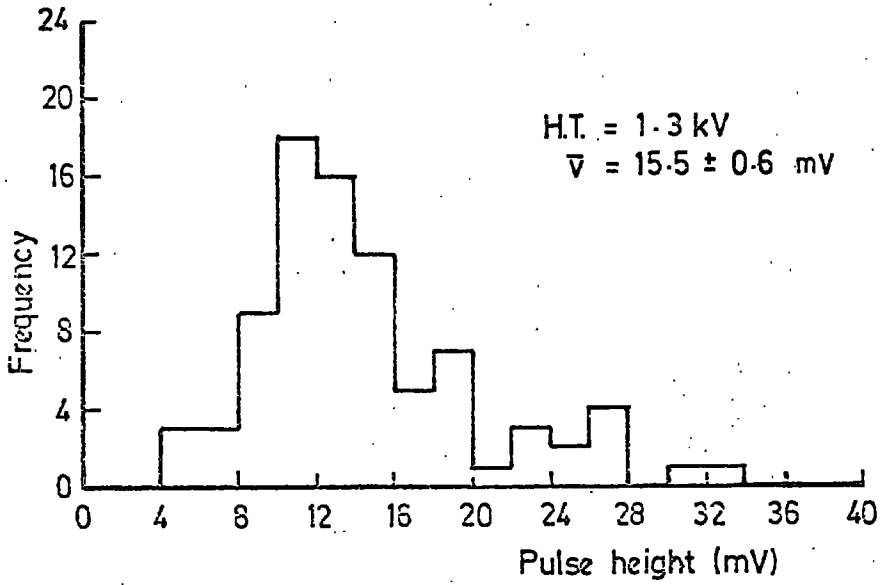
H.T. = 1·3 kV
$\bar{v}$ = 15·5 ± 0·6 mV
Frequency
Pulse height (mV)

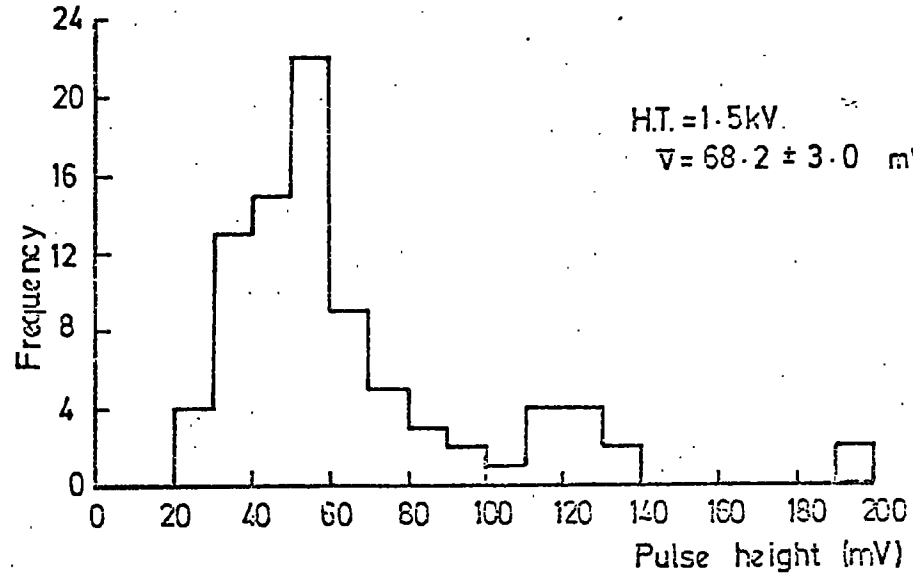
H.T. = 1·5kV
$\bar{v}$ = 68·2 ± 3·0 mV
Frequency
Pulse height (mV)

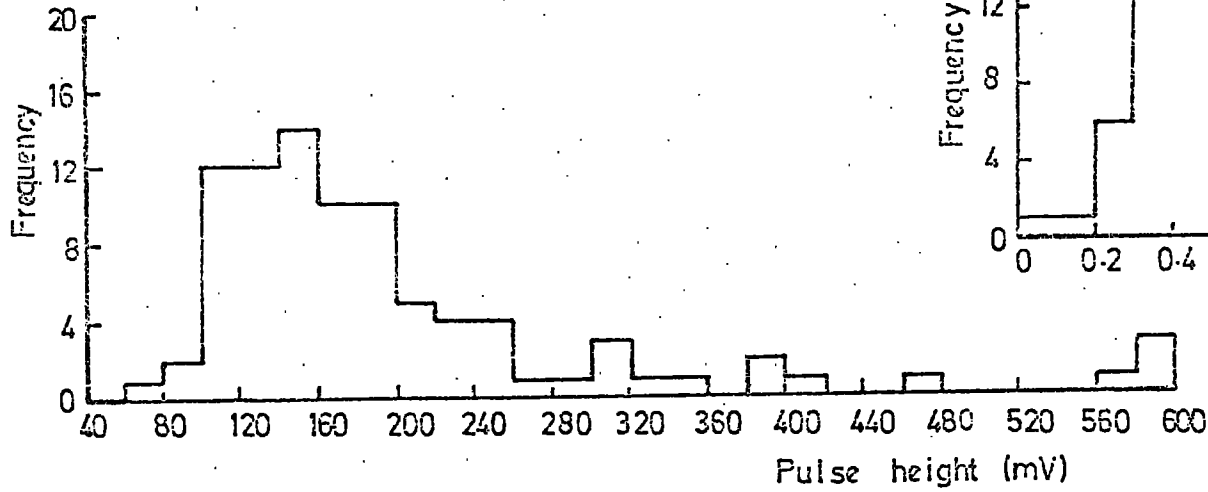
H.T. = 1·7 kV
$\bar{v}$ = 212 ± 11·6 mV
Frequency
Pulse height (mV)

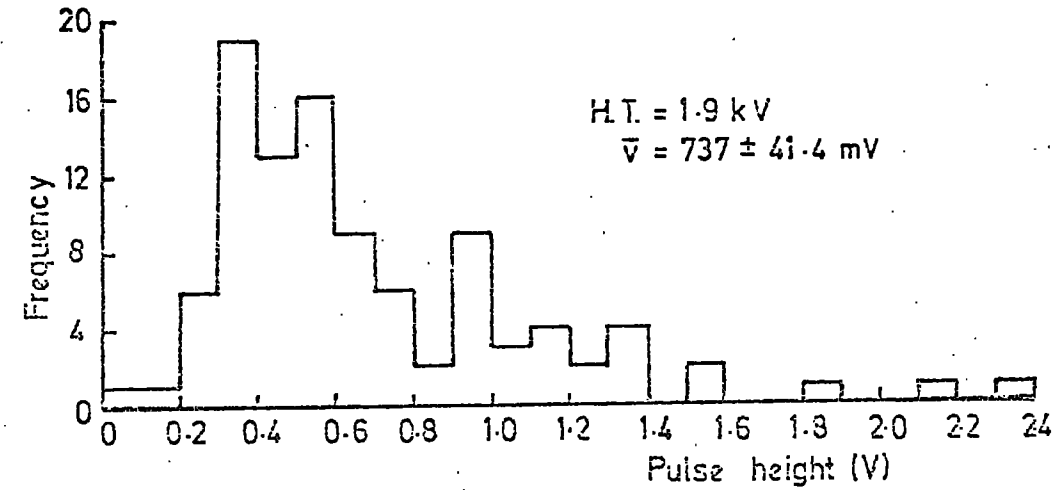
H.T. = 1·9 kV
$\bar{v}$ = 737 ± 41·4 mV
Frequency
Pulse height (V)

Figure 6.6 The single particle pulse height distribution for scintillator C, measured at the output of the amplifier (see Figure 6.3).

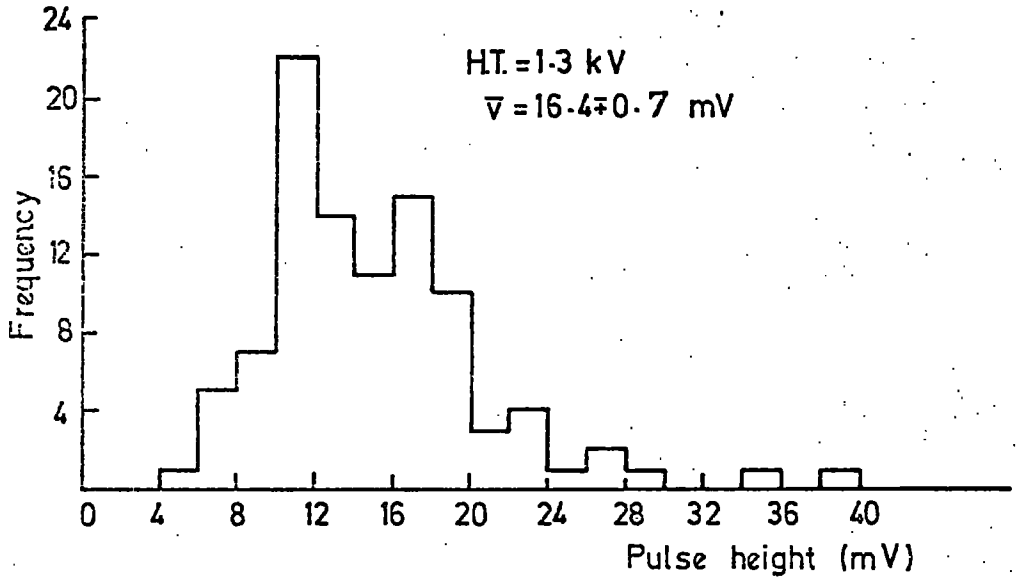
H.T. = 1·3 kV
$\bar{v}$ = 16·4∓0·7 mV
Frequency
Pulse height (mV)

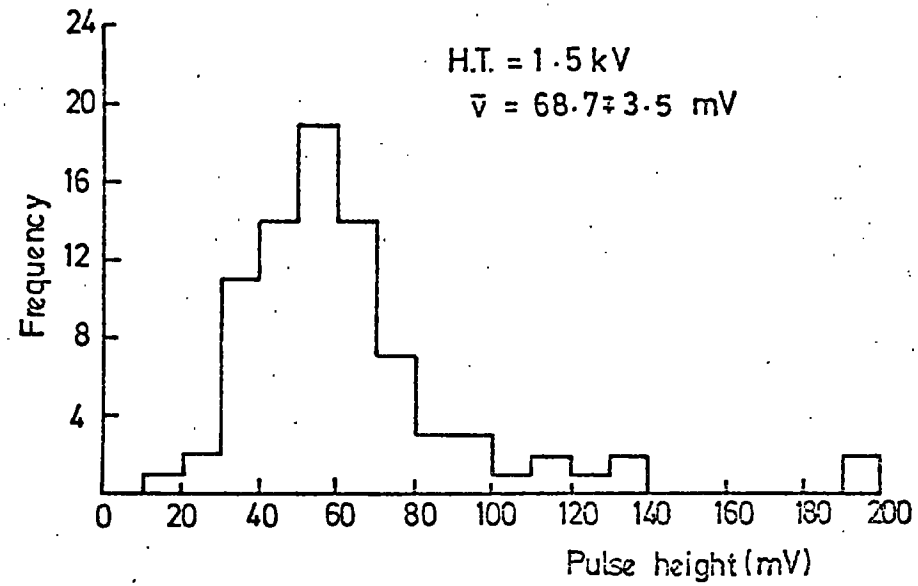
H.T. = 1·5 kV
$\bar{v}$ = 68·7∓3·5 mV
Frequency
Pulse height (mV)

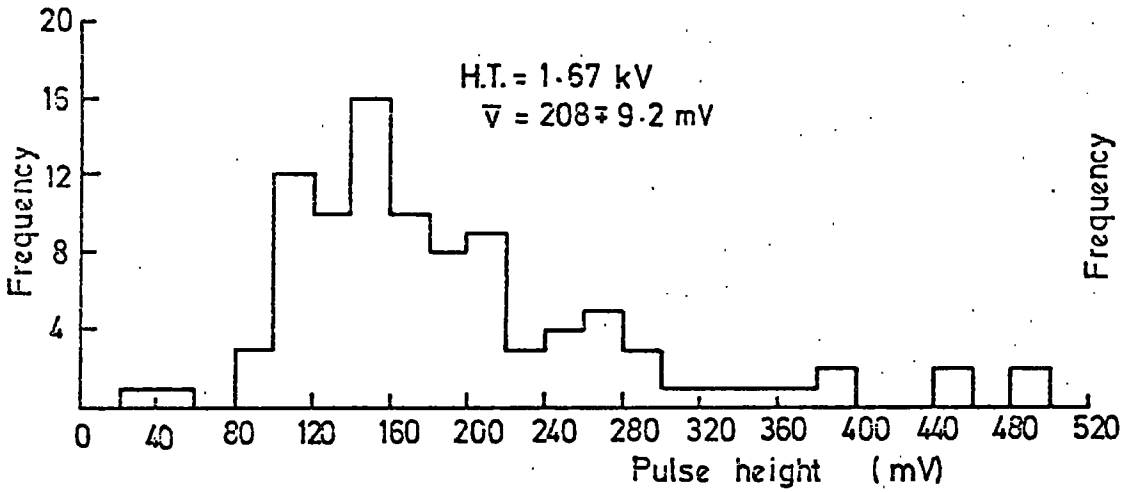
H.T. = 1·67 kV
$\bar{v}$ = 208∓9·2 mV
Frequency
Pulse height (mV)

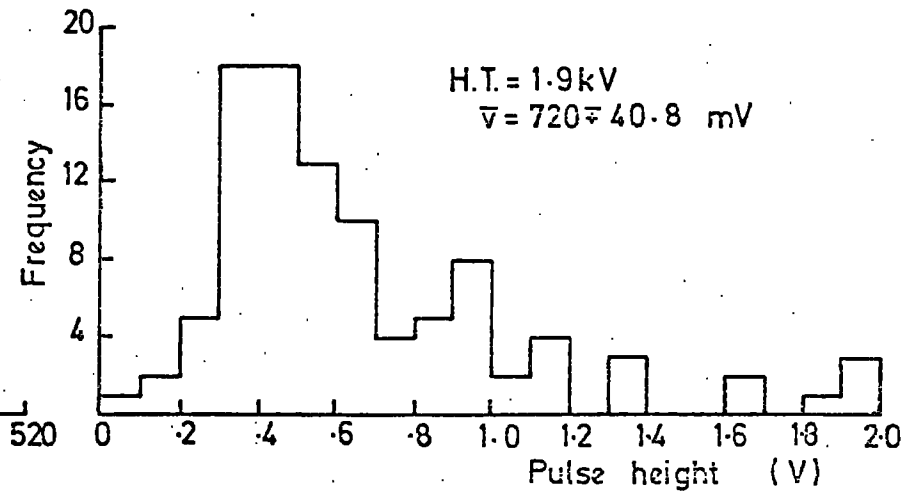
H.T. = 1·9 kV
$\bar{v}$ = 720∓40·8 mV
Frequency
Pulse height (V)

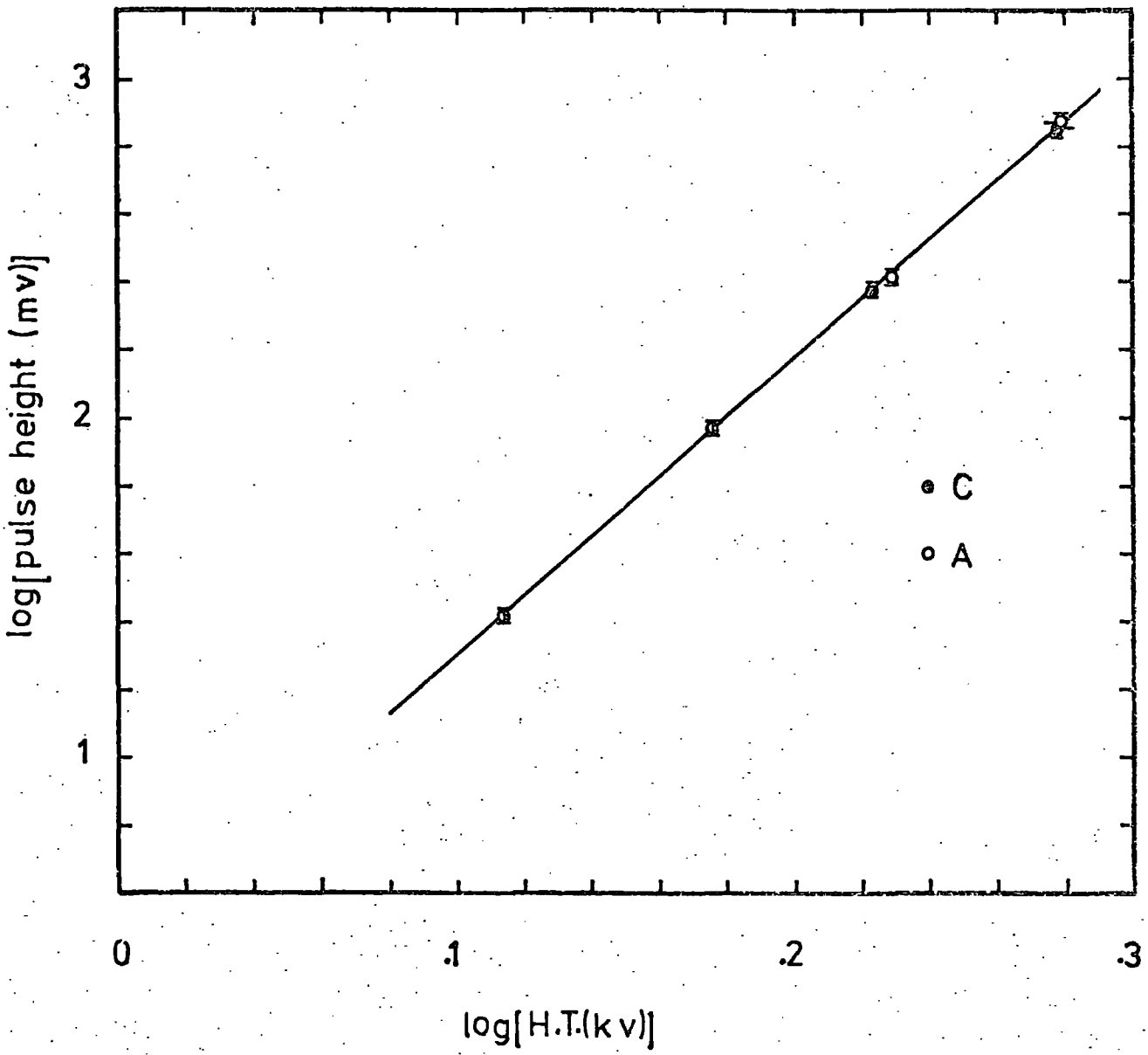


Figure 6.7 Variation of output pulse height with photomultiplier H.T. for scintillators A andC. The pulse height is the voltage at the output of the photomultipliers, for single penetrating particles traversing the centre of the counter at vertical incidence.

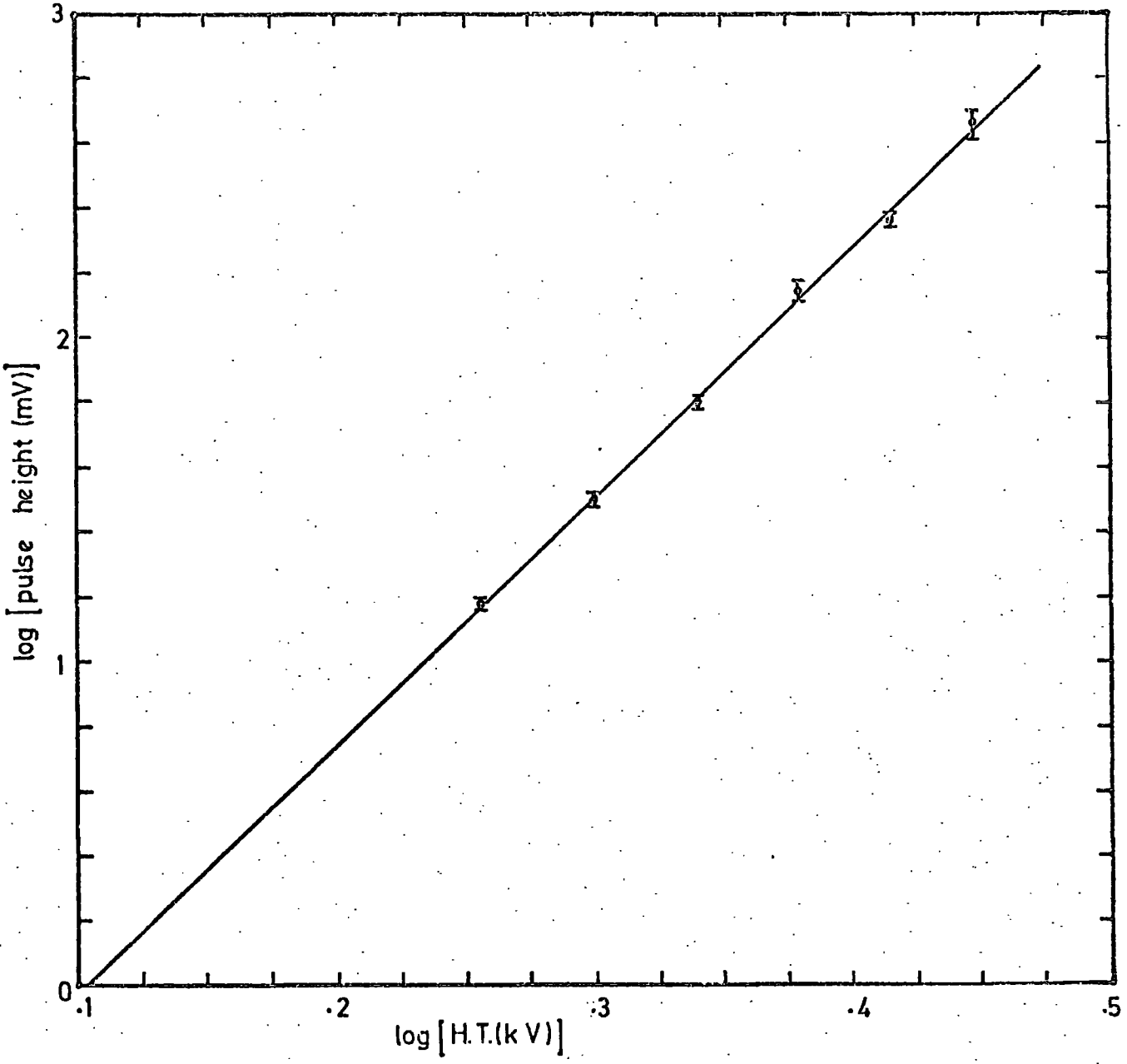


Figure 6.8 Variation of output pulse height with photomultiplier H.T. for scintillator M. The pulse height is the voltage at the output of the photomultipliers, for single penetrating particles traversing the centre of the counter at vertical incidence.

either scintillator A or C. The burst size N was defined as a burst which produced a pulse height of N times the single particle pulse height. When this occurred the pulse heights from the three scintillators A, C and M were displayed on an oscilloscope and photographed. At the same time the flash tubes were triggered and photographed. The logic for the experiment is shown in Figure 6.9.

The discriminators determining the triggering threshold were set to a predetermined level using a pulse generator. It was then possible to select a minimum burst size by altering only the H.T. applied to the photomultiplier tubes. The H.T. supplying the photomultiplier tubes of the liquid scintillation counter was set to record particle numbers in the range 5 particles to 36.

Using this arrangement the chamber has been operated from April 1974 until the present time. Data was obtained at different threshold burst sizes enabling burst sizes from approximately 20 particles up to a few thousand particles to be studied.

6.2.4. The analysis procedure

Examples of the events obtained are shown in Plates 6.1 to 6.3. The analysis consisted of projecting both films of each event onto scanning tables. From the oscilloscope film the pulse heights in the scintillators could be measured, the origin of the burst established and the existence of any air shower accompaniment determined. The flash tube film was scanned and the width of the bursts were measured according to the criteria adopted in Chapter 5. The burst widths were expressed in centimetres on the scanning table, hence to transform to real space the widths must be multiplied by a factor of 20, the scale of reduction of the projection system.

## 6.3 Experimental Results

### 6.3.1 The burst width - burst size relation

In order to establish the relationship between the width of the

Plate 6.1 Event H13 - 77.

A burst produced in the lead which penetrated the iron, producing outputs from scintillators C and A. There is also EAS accompaniment, seen in the liquid scintillator M. From left to right of the oscilloscope trace, the scintillator outputs are:-

A, C and M

C = 420 Particles

A = 650 "

M = 19 "

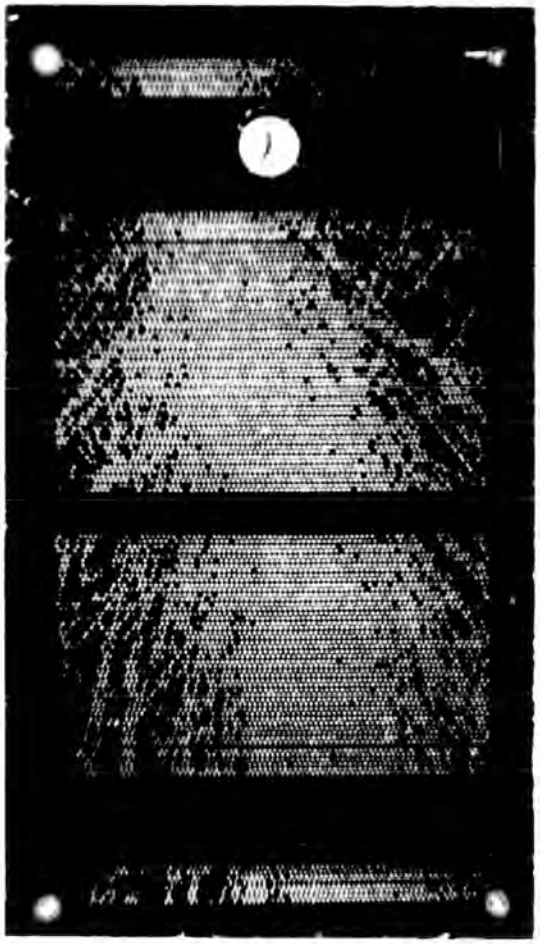

Plate 6.2 Event H.33 - 35

A burst, produced in the lead which penetrates the iron, giving pulses from scintillators C and A. There is no EAS accompaniment.

C = 940 particles

A = 1480 Particles

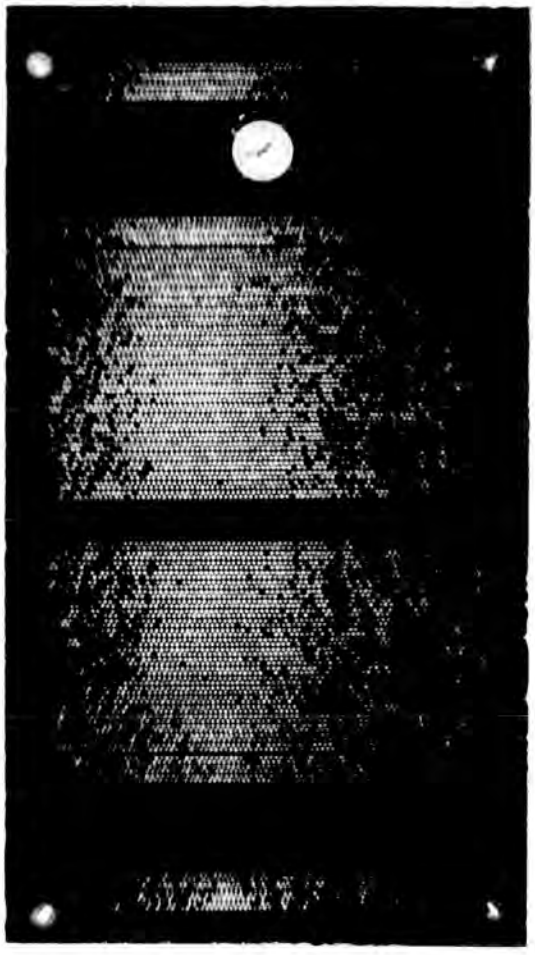

Plate 6.3 Event H.13 - 45

A burst produced in the iron.

The oscilloscope trace shows

a pulse from scintillator A.

A = 600 Particles

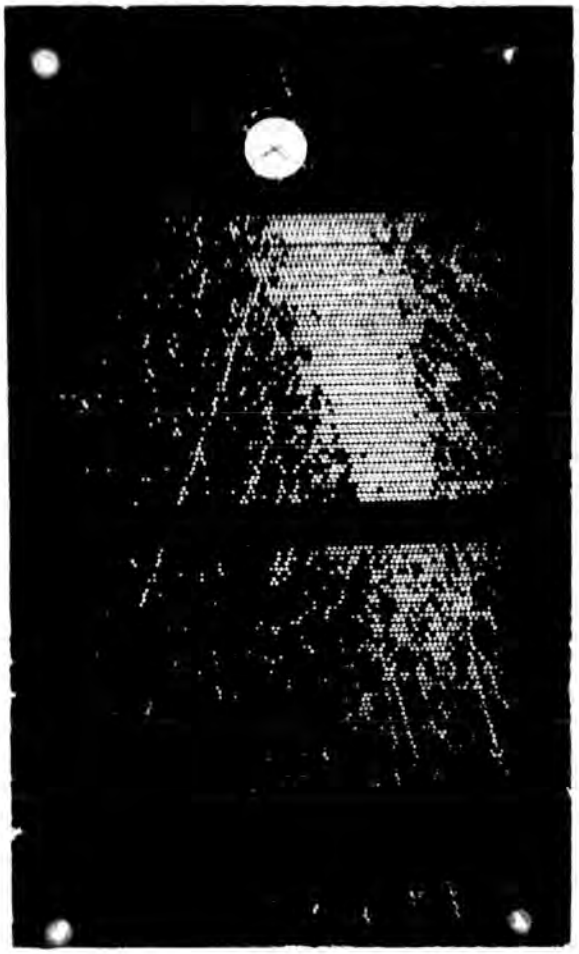

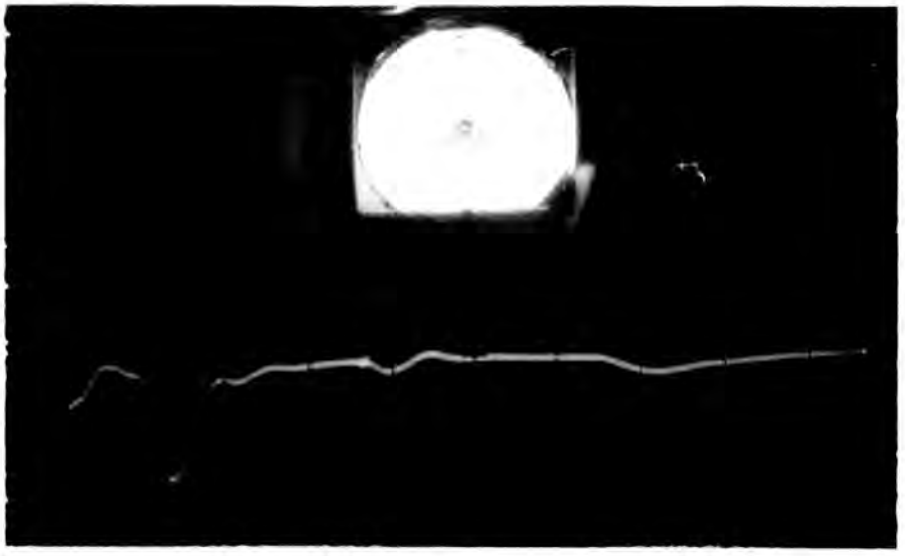

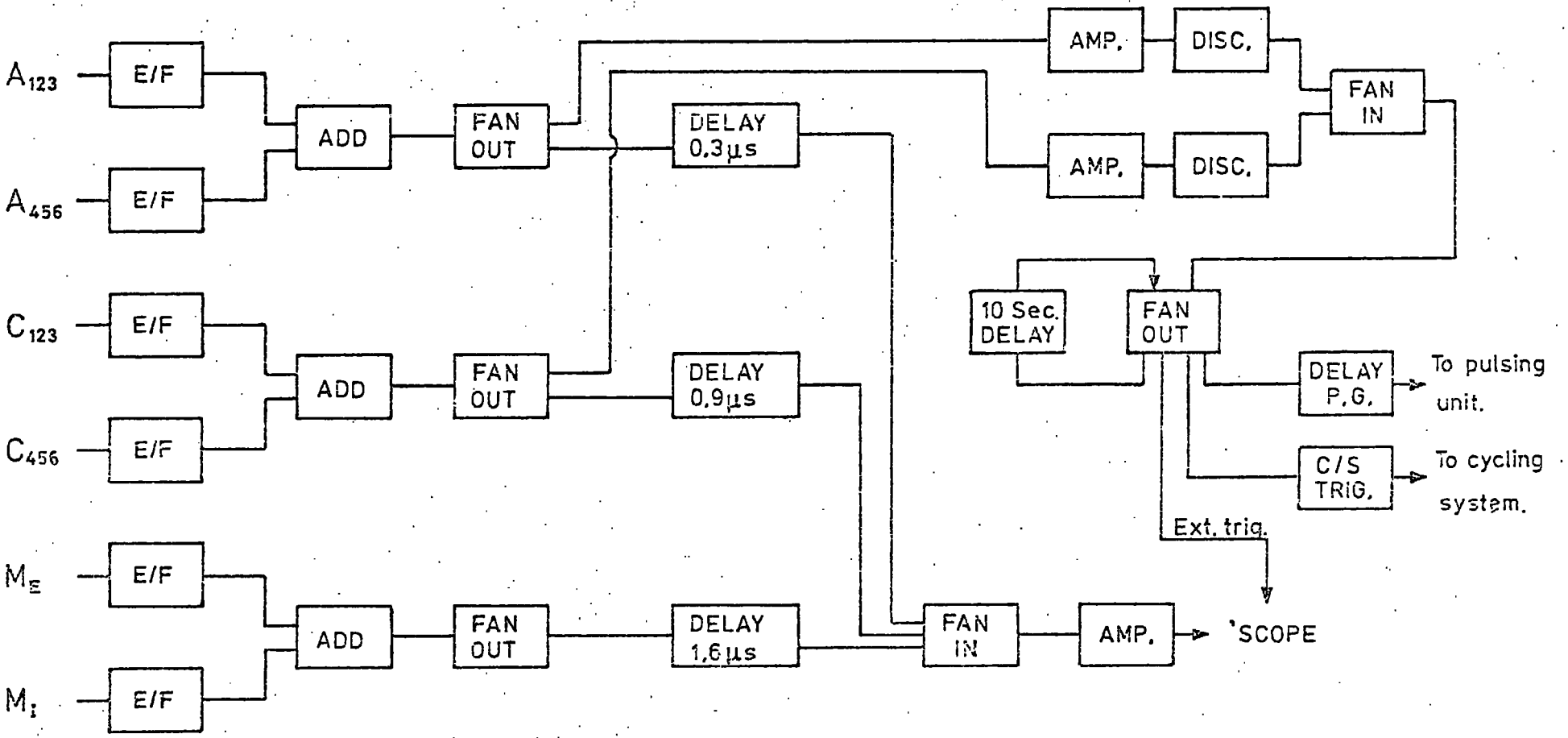


Figure 6.9 Experimental logic for vertical burst experiment.

burst and the burst size (N), scatter plots were produced for the iron and lead absorbers. These scatter plots are shown in Figures 6.10 and 6.11. The points were binned and their means found. A correction was applied, however, since for a certain burst size there is a bias towards smaller burst widths. This arises because the probability that an event is accepted is a function of the width of the burst. An acceptable event is one in which the whole width of the burst can be seen in the flash tubes, while as the burst width increases the probability that the whole of the burst will be contained in the flash tubes decreases. The amount by which the flux will be reduced is equal to (D-d)/D, where D is the width of a layer of flash tubes and d the width of the burst. Thus the burst width distribution was corrected by dividing each burst width cell by the loss factor. This is valid up to the largest burst sizes where very few events are accepted and an accurate correction is not possible. For this reason the few events at the largest burst sizes are not included in the burst width - burst size graphs shown in Figures 6.12 and 6.13. It can be seen from these figures that the power law dependence predicted in Chapter 5 holds only in the mid-range of burst sizes. For comparison the results of the experiments of Coats (1967) for bursts produced in 25 cms. of iron and predictions of the NKG lateral distribution function are included in Figure 6.12 for an iron absorber. It can be seen from this comparison that transition effects play an important role in determining the lateral spread of a cascade. The deviation of the present experimental curves is attributed to the steadily changing value of the age parameter s, being less than one for large bursts and greater than one for small bursts. The resulting curves lie somewhere between a power law relationship and a logarithmic law. It is interesting to note that Vatcha et.al. (1973) predict a logarithmic dependence from the results of their Monte Carlo simulations.

No correction has been applied to the burst size obtained to allow for cascade development in the plastic scintillators. It is predicted

Figure 6.10 Scatter plot of burst width measured in the flash tube on the scanning sheet versus burst size measured in scintillator A for bursts in the iron. To obtain the true burst width the ordinate should be multiplied by 20.

Figure 6.11 Scatter plot of burst width measured in the flash tubes on the scanning sheet versus burst size measured in scintillator C for bursts in the lead. To obtain the true burst width the ordinate should be multiplied by 20.

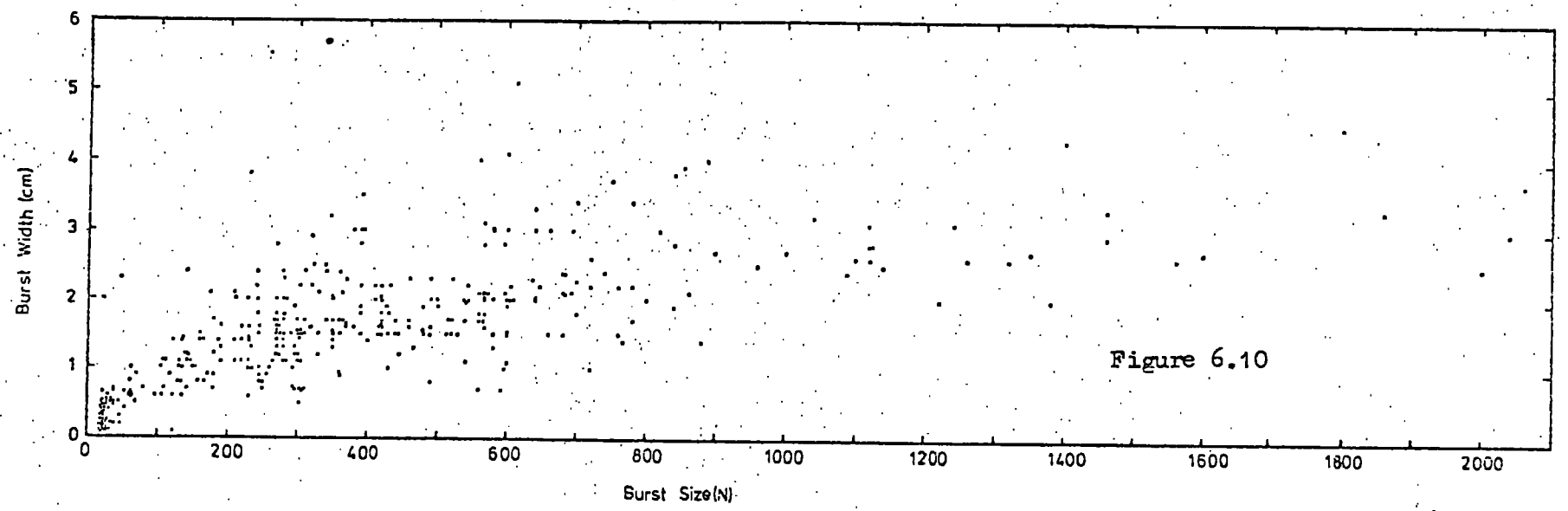


Figure 6.10

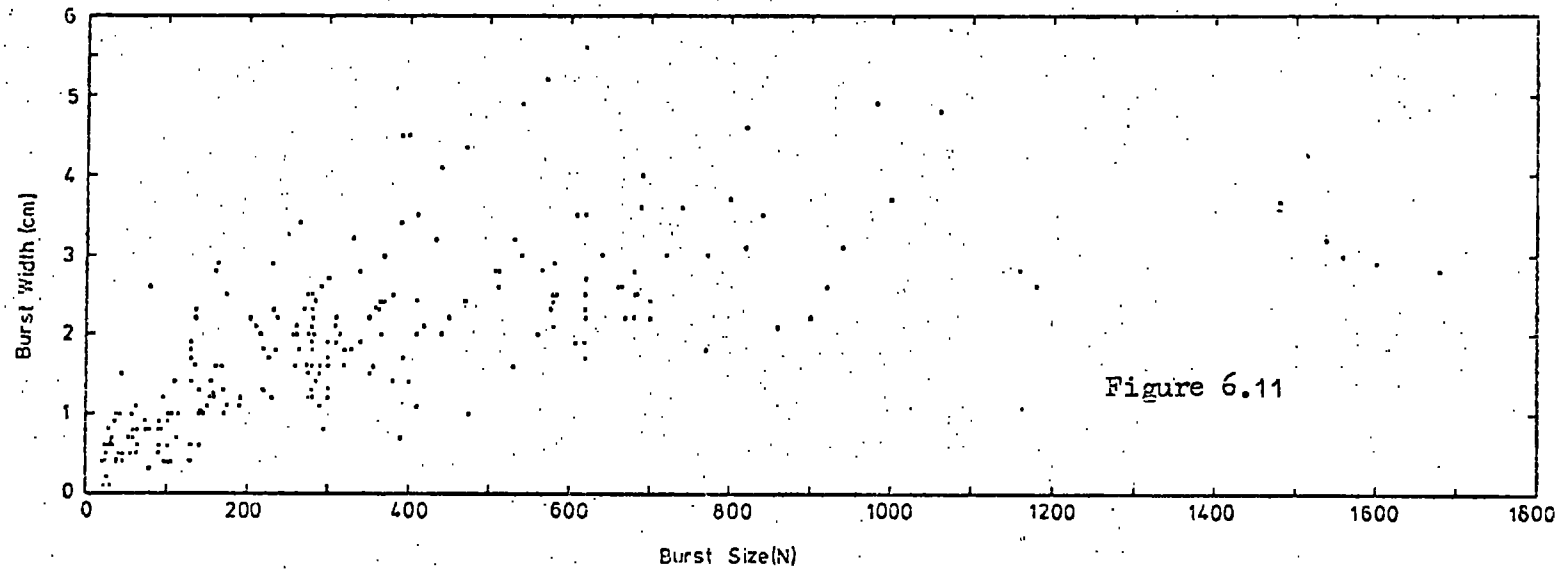


Figure 6.11

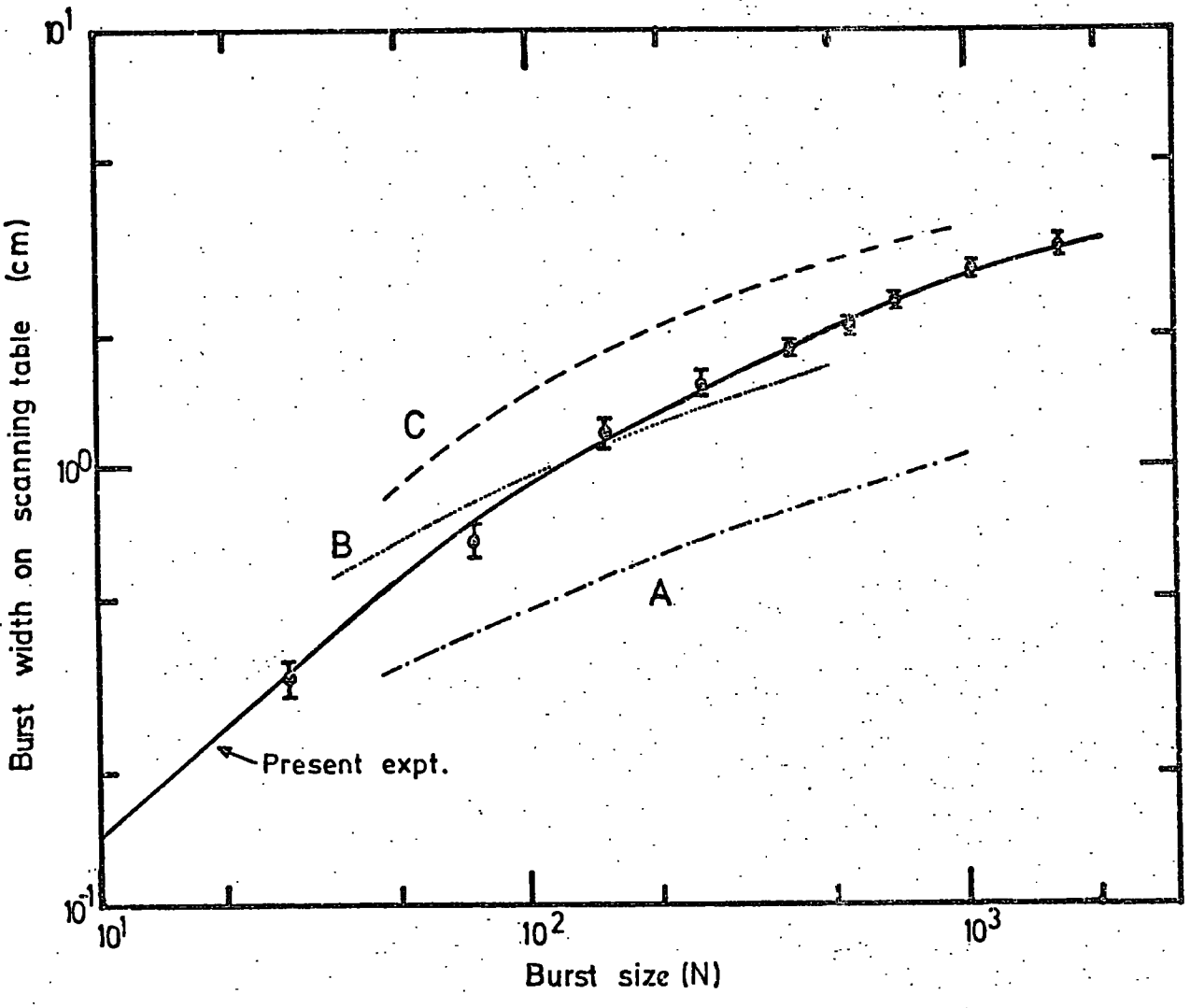


Figure 6.12 Burst width (as measured on the scanning sheet) variation with burst size (N) for Iron. To obtain the true burst width in cm, the ordinate should be multiplied by 20. Curve A - prediction for a pure electron photon-cascade; Curve B - measured relationship for electromagnetic cascades (Coats 1967); Curve C - measured relationship for nuclear-electromagnetic cascades (Coats, 1967). See Figure 5.20. The experimental points refer to the present measurements.

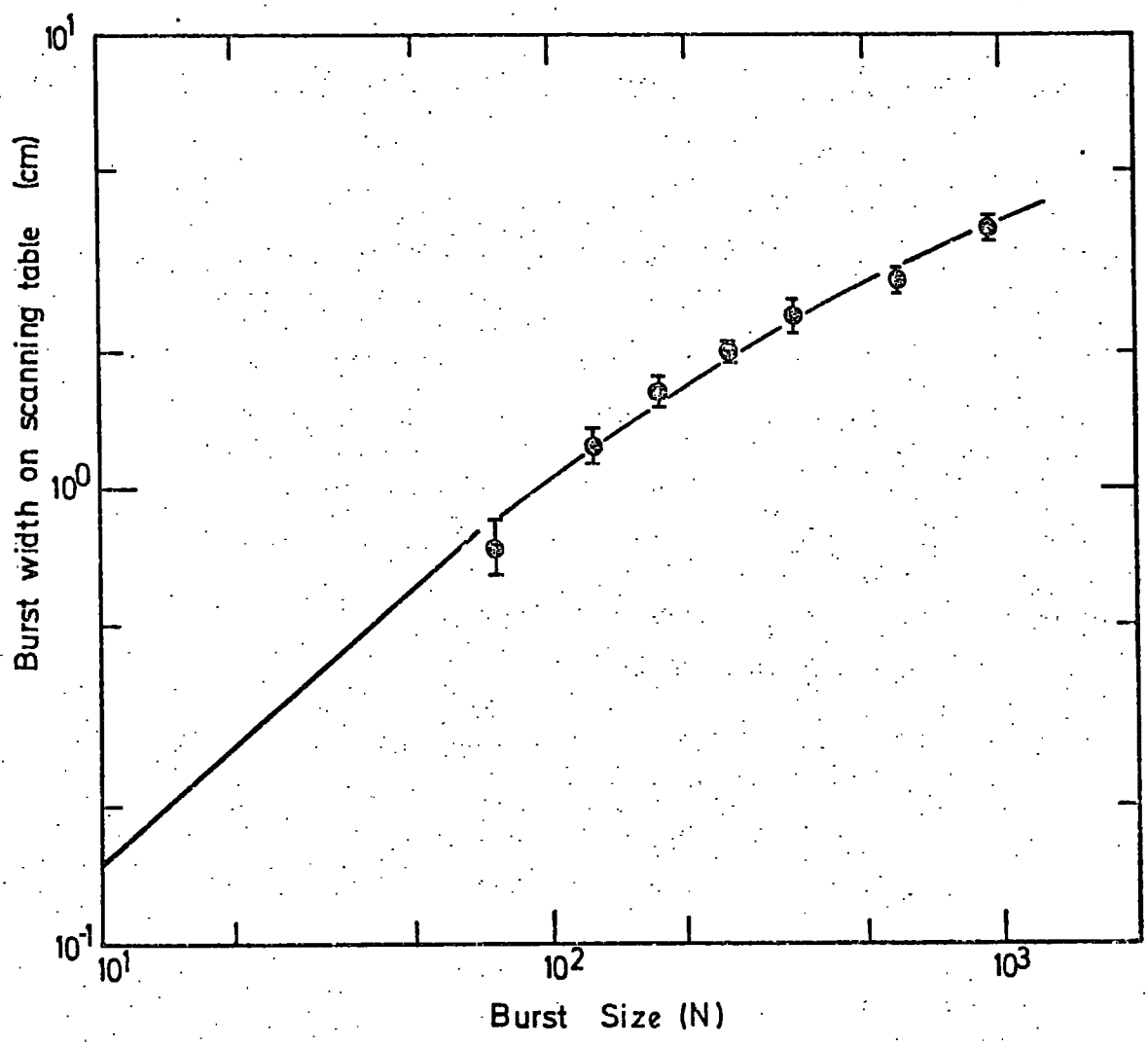


Figure 6.13 The burst width (measured on the scanning sheet)-burst size relationship measured under 15 cms. of lead. To obtain the true burst width the ordinate should be multiplied by 20.

that for the plastic scintillators in use the effect will overestimate burst sizes by approximately 10%, and will tend to nullify the reduction in electron number produced by transition effects in passing from the absorber into an air gap and then into the scintillator.

The burst size-burst width relations determined for the iron and lead absorbers should be applicable to the interpretation of the bursts observed in the air shower experiment. However, it is possible to check the absolute calibration of the scintillators and hence avoid the incorrect energy determination that would result from systematic errors in the burst size measurements. This is possible by producing the burst spectrum of events obtained during the present experiment and comparing the spectrum with that of other workers.

6.3.2 The burst spectrum of charged particles

Too few neutral bursts were obtained during the running time of the experiment to produce a burst spectrum for them, therefore it was necessary to use the charged events to produce the spectrum. This means that rather than measuring a single component, as would be done if the neutral bursts were taken (that is, neutrons), several different types of particle are responsible for the bursts. Coats (1967) has calculated the relative contributions of different particles and concludes that significant contributions arise from charged pions, protons and muons. For a 25 cm. target of iron, above about 100 GeV he concludes that pions dominate the burst spectrum due to their higher inelasticity. Coats measured the angular distribution of charged particles and neutral particles, and assuming a $\cos^n\theta$ angular variation of intensity he found $n=8.7\pm2.1$ for neutral particle bursts and $n=3.8\pm1.3$ for charged particle bursts. The difference is attributed to the muon contribution to the charged particle bursts, since the calculated values for pions and nucleons are $n=8.15$ and $n = 8.65$ respectively.

Now since the aperture of a detector (as opposed to the geometrical acceptance) is a function of n, it is necessary that this parameter is

known. The method used by many workers is that proposed by Lovati (1954). Lovati calculates the absolute magnitude of the projected angular distribution, for events falling within the acceptance geometry of the detector, for different values of n. Thus by comparing the experimentally observed projected angular distribution with those predicted for different n and minimising using a $\chi^2$-test, the best value of n and hence the absolute aperature of the apparatus can be obtained. An alternative approach is to use the Monte Carlo technique to produce the aperture and projected angular distribution that would be obtained in the detector for different n.

In the present experiment, an acceptable burst in the iron was one in which the incoming particle track was observed in the flash tubes comprising F1a and the whole burst width was seen in F1b, the layer of flash tubes located directly below the iron (and had passed through the scintillator). This clearly implies that the aperture is a function of the lateral width of the burst. Furthermore, the angular distribution of events will vary as a function of burst width independently of n. The situation is similar for bursts produced in the lead absorber. Here the geometry is defined as the two planes comprising the middle of scintillator C and the top layer of the flash tubes in F1a. Now since the lateral structure function in the electron-photon cascade is very steep, the vast majority of electrons will be contained inside a cylinder of diameter one Moliere unit, or less than 2 cms. for both the iron and lead. Hence the burst width in the scintillator can be neglected. Again, however, the burst width measured in the flash tubes affects the aperture.

There are therefore several difficulties in obtaining n:-

(a) In order to exclude side bursts produced in the walls of the chamber (barytes brick) by high energy muons, only events in which the projected zenith angle was less than $30^\circ$ were accepted. Now within this restricted angular range there is little sensitivity to variations in the exponent n

of the $\cos^n \theta$ variation. It is necessary to look at large angles to obtain an accurate determination of this quantity.

(b) Since the aperture is a function of the burst width a different geometry could be defined such that this was not so. Thus events could be restricted to the geometry shown in Figure 6.14, only bursts of width less than d' being considered and requiring that the core of each burst falls within the limits defined. The method would be applicable when sufficient data was available, but this cut was not feasible with the present data.

(c) The angular distribution could be grouped for different burst width ranges and n found in this way. Again, insufficient data was available and the restricted angular range would make any results obtained in this way subject to large uncertainties. An added complication is that since the composition changes with energy, it is to be expected that n will also change slowly.

In view of these considerations it was decided that the absolute aperture of the apparatus should be obtained as a function of the burst width (d) for the value of n obtained by Coats for charged particle bursts in his experiment.

The aperture was calculated using the Monte Carlo technique. Particles were generated in a random position in the upper geometry-defining plane. They were then given a zenith angle $\theta$ determined randomly from a distribution of the form

$$I = I_o \cos^n \theta$$

Each particle was also assigned a randomly chosen rotation angle $\alpha$ relative to the plane of projection. From this information the projected angle was determined. An event was then accepted if it crossed the area of the lower geometry-defining plane. The fraction of events accepted, $f(d,n)$, after normalising the total number of events to a constant value of $I_o$ is then related to the aperture by the relation

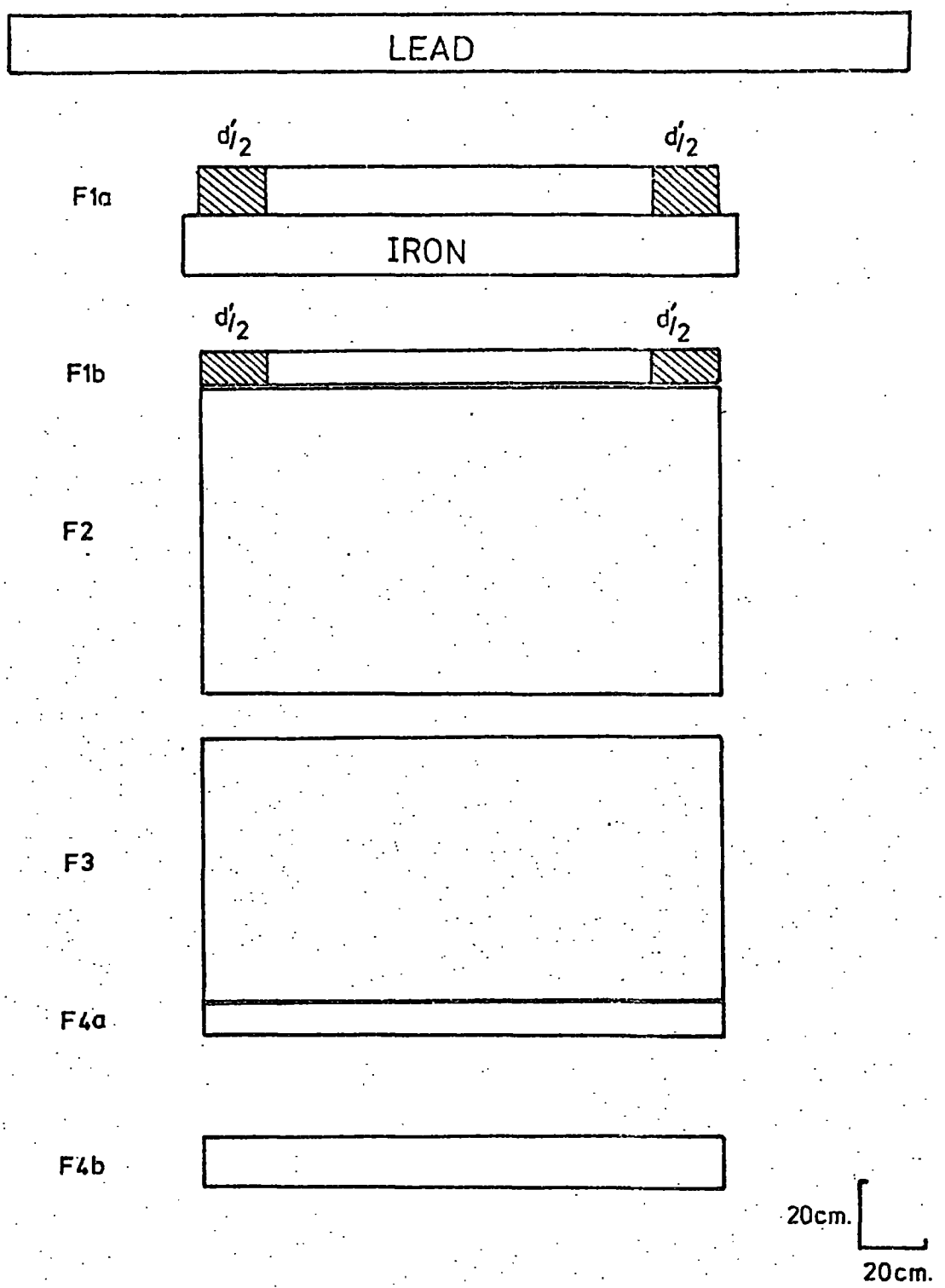


Figure 6.14 Scale diagram of the front of the chamber, showing the restricted acceptance geometry. To be accepted, the core of a burst must lie between, but not in, the shaded areas.

$$\text{Aperture} = f(d,n).\ 2\pi A_1$$

where $A_1$ is the area of the upper plane.

Apertures were calculated as a function of d for different n, the results being shown in Figures 6.15 and 6.16 for bursts in the iron and lead respectively.

The value of n was taken to be 4, after Coats. Figure 6.17 shows the predicted projected angular distribution with n = 4 for three burst widths.

Using the relevant curves in Figures 6.15 and 6.16 the burst spectra obtained from the iron and lead absorbers were calculated. Burst widths and burst sizes were correlated using Figures 6.12 and 6.13, such that the burst sizes determined from the scintillators were assumed to have an aperture corresponding to the mean burst width shown in these figures.

The integral burst spectra obtained are shown in Figures 6.18 and 6.19. Also given are the corresponding energies assuming (a) that all events are pionic, and (b) that all events are protonic. The energy conversions used are those of Figures 5.9 to 5.12.

It can be seen that the rates are the same in both the lead and the iron, while if the bursts were purely pionic there should be approximately twice as many bursts in the lead as in the iron absorber. The apparent discrepancy is interpreted as being due to the muon contamination. Since muons will not be significantly attenuated in the lead the proportion of muon-induced bursts in the iron will possibly be greater than in the lead, even when the effect of increased cross-section in the lead is allowed for. If this is so, since the angular distribution of muons is very flat the mean value of the exponent n will decrease, producing an increase in the aperture (see Figures 6.15 and 6.16) and consequently a higher rate of bursts in the iron. The correctness of this assumption can be verified by comparing the angular distributions of measured bursts below the two absorbers, and from Figure 6.20 it can be seen that the distribution in

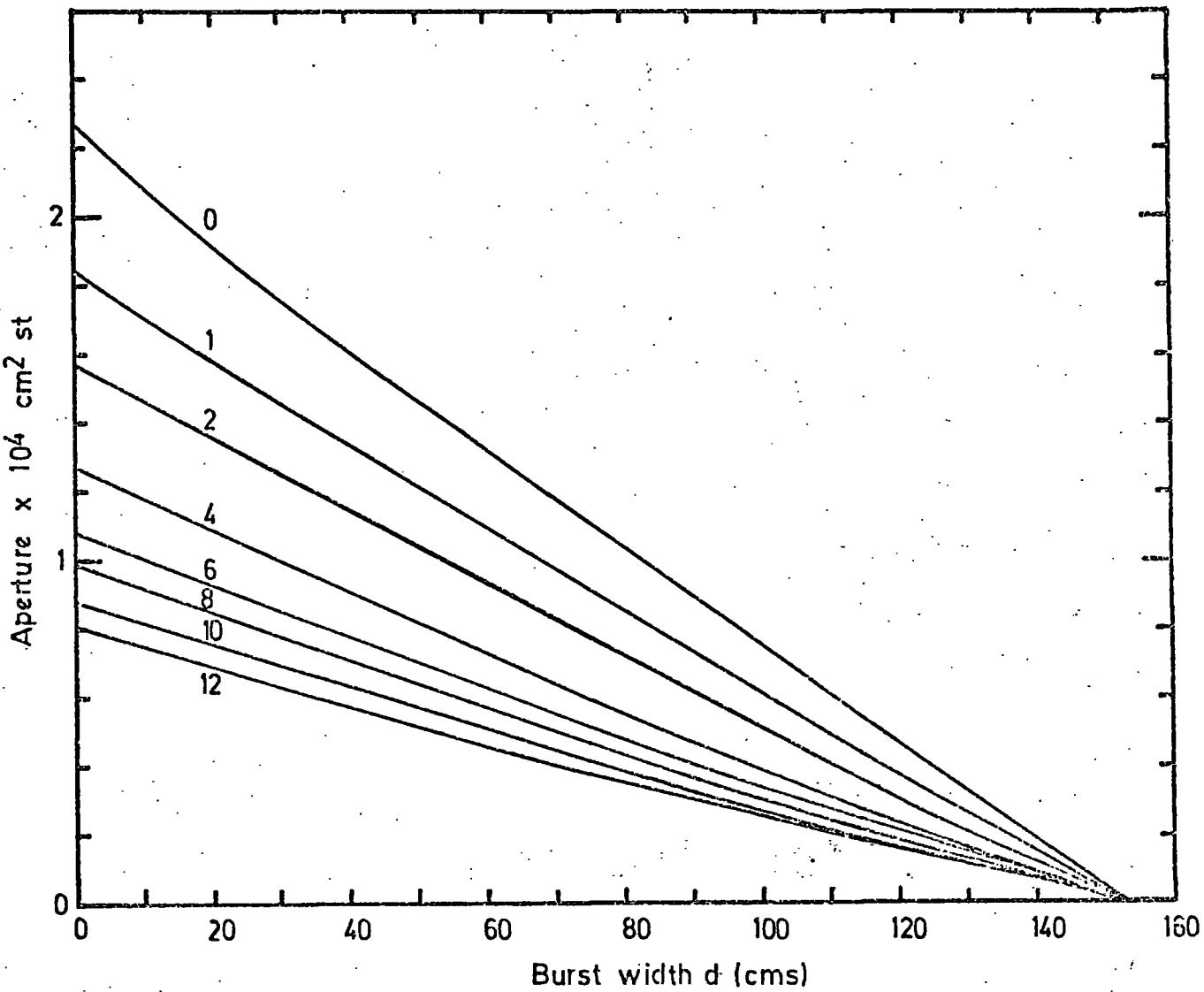


Figure 6.15 The aperture of the detector for bursts produced in the iron, as a function of the burst width, Numbers by the curves represent different values of n, the exponent in the assumed expression for the angular variation of intensity.

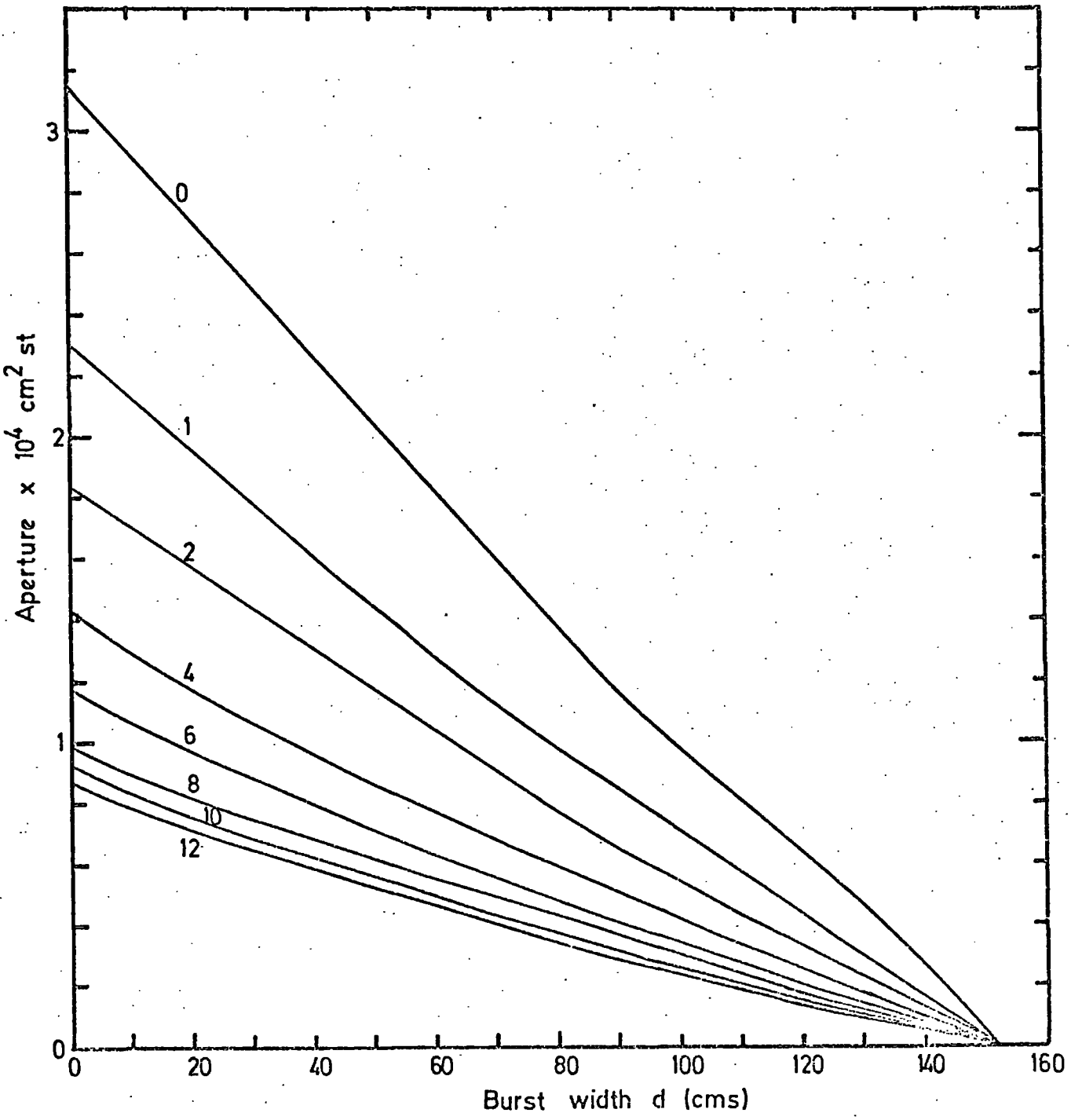


Figure 6.16 The aperture of the detector for bursts produced in the lead, as a function of the burst width. Numbers by the curves represent different values of n, the exponent in the assumed expression for the angular variation of intensity.

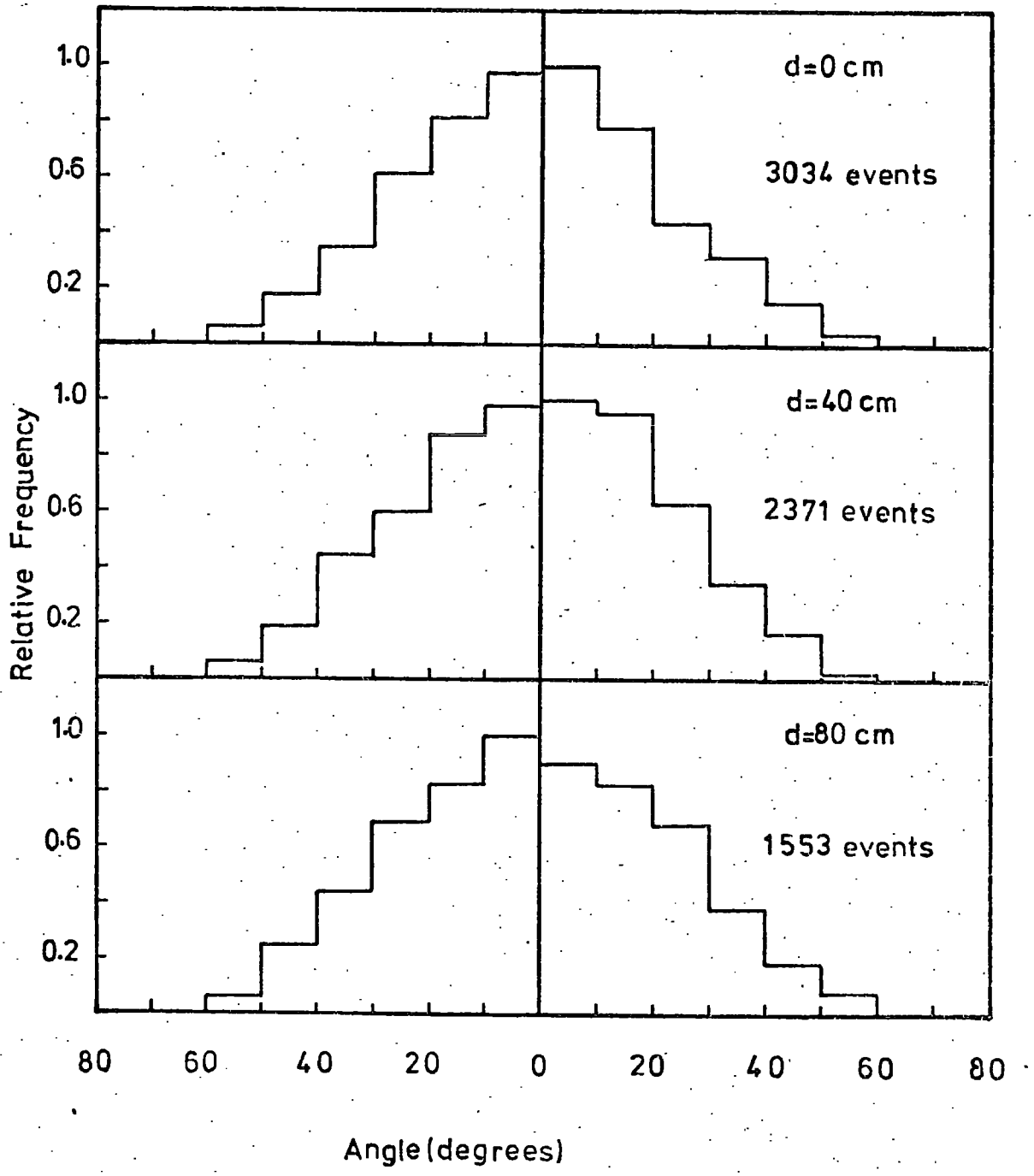


Figure 6.17 The predicted angular distribution in the projected plane for three bursts widths (d).

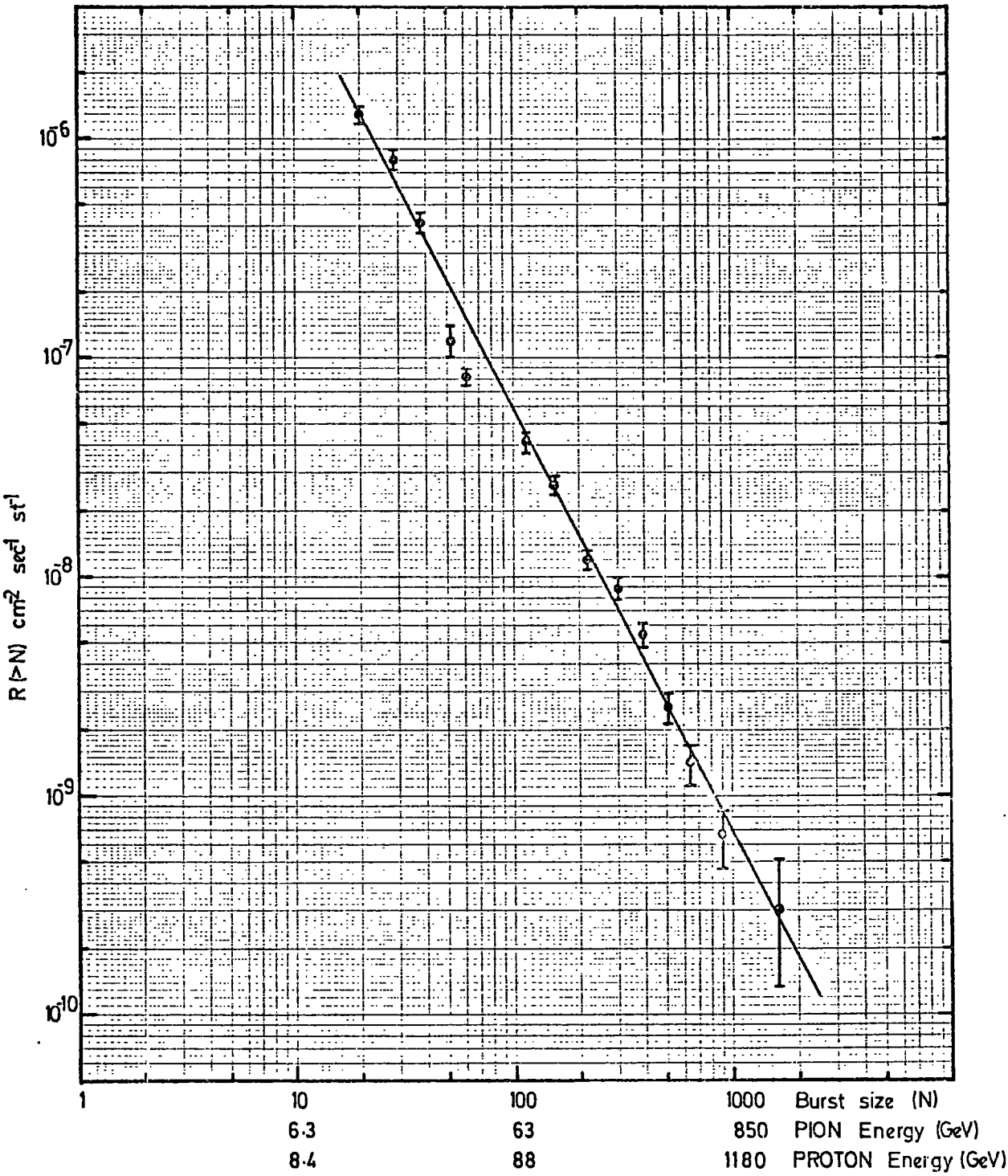


Figure 6.18 The integral burst spectrum measured in the iron. The pion and proton energy scales represent the integral energy spectra obtained assuming all bursts to be produced by pions and protons respectively.

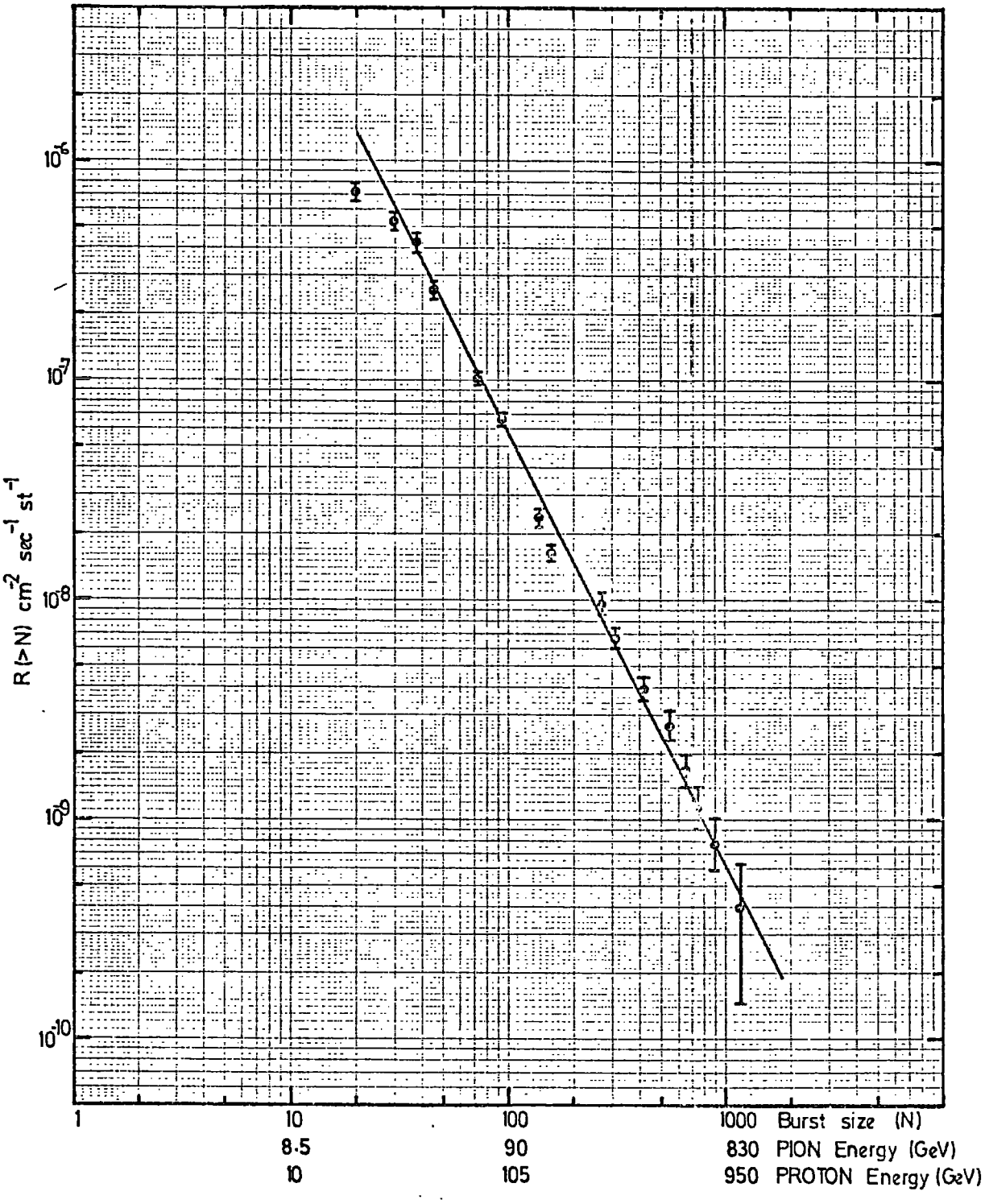


Figure 6.19 The integral burst spectrum measured in the lead. The pion and proton energy scales represent the integral energy spectra obtained assuming all bursts to be produced by pions and protons respectively.

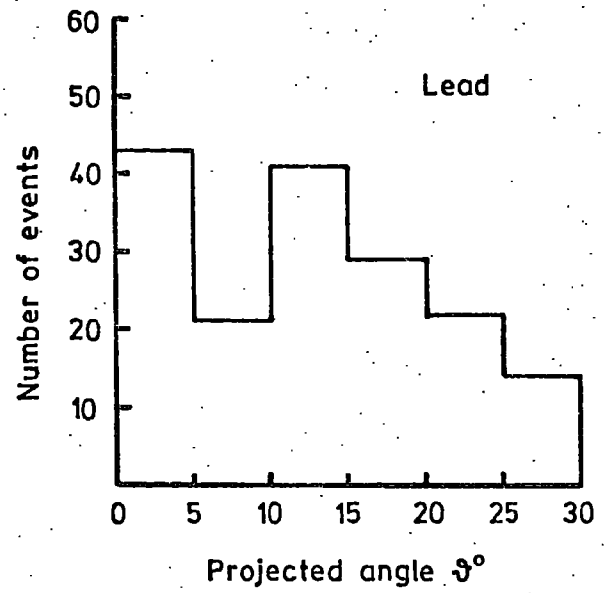


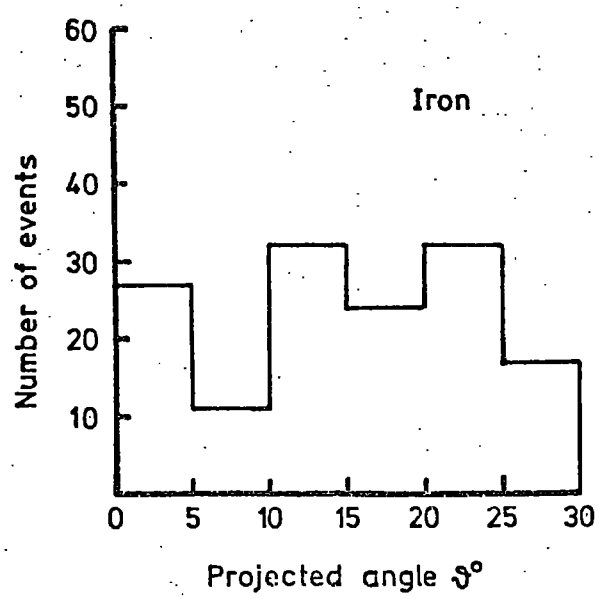


Figure 6.20 The angular distributions of accepted bursts in the lead and iron absorbers.

the iron is indeed flatter, as expected.

6.3.3 Comparison with other results

The burst spectrum in lead was converted to a differential energy spectrum in order that a comparison couldbe drawn between the results of the present experiment and results obtained from other experiments, in particular the results of Baruch et.al. (1973), who have suggested that there may be a "knee" in the spectrum at an energy of a few TeV.

While Baruch et.al. have assumed the bursts to be proton-induced, it was decided that a more reasonable assumption is that at high energies two components dominate, protons and pions, and that pions will be more important in producing bursts (Nam et.al., 1971, Cowan and Matthews, 1971, Coats, 1967). Therefore for the energy conversion it was assumed that all of the bursts were pion-induced, and further that 53% of hadrons incident on the lead were detected. The differential energy spectrum obtained is shown in Figure 6.21, and is compared with two previous experiments, Cowan and Matthews (1971) and Baruch et.al. (1973). Where the spectra of the present experiment and that obtained by Baruch et.al. overlap there is good agreement (although it must be remembered that Baruch et.al. have assumed proton-induced bursts), and the spectrum of Cowan and Matthews is also close. Thus it was concluded that the calibration of the plastic scintillators was satisfactory. The energy at which the "kink" reported by Baruch et.al. occurs has not been reached.

6.4 Extension to higher energies

Since with the arrangement described above the rate of high energy events measured was very low due to the small aperture for wide bursts, the operation of the flash tube chamber was modified to allow the accessible energy region to be extended. For this the variation of flash tube efficiency with the time delay $T_D$ was utilised.

It was shown in Chapter 2 that the probability that a tube flashes (the internal efficiency) decreases with the time delay between the

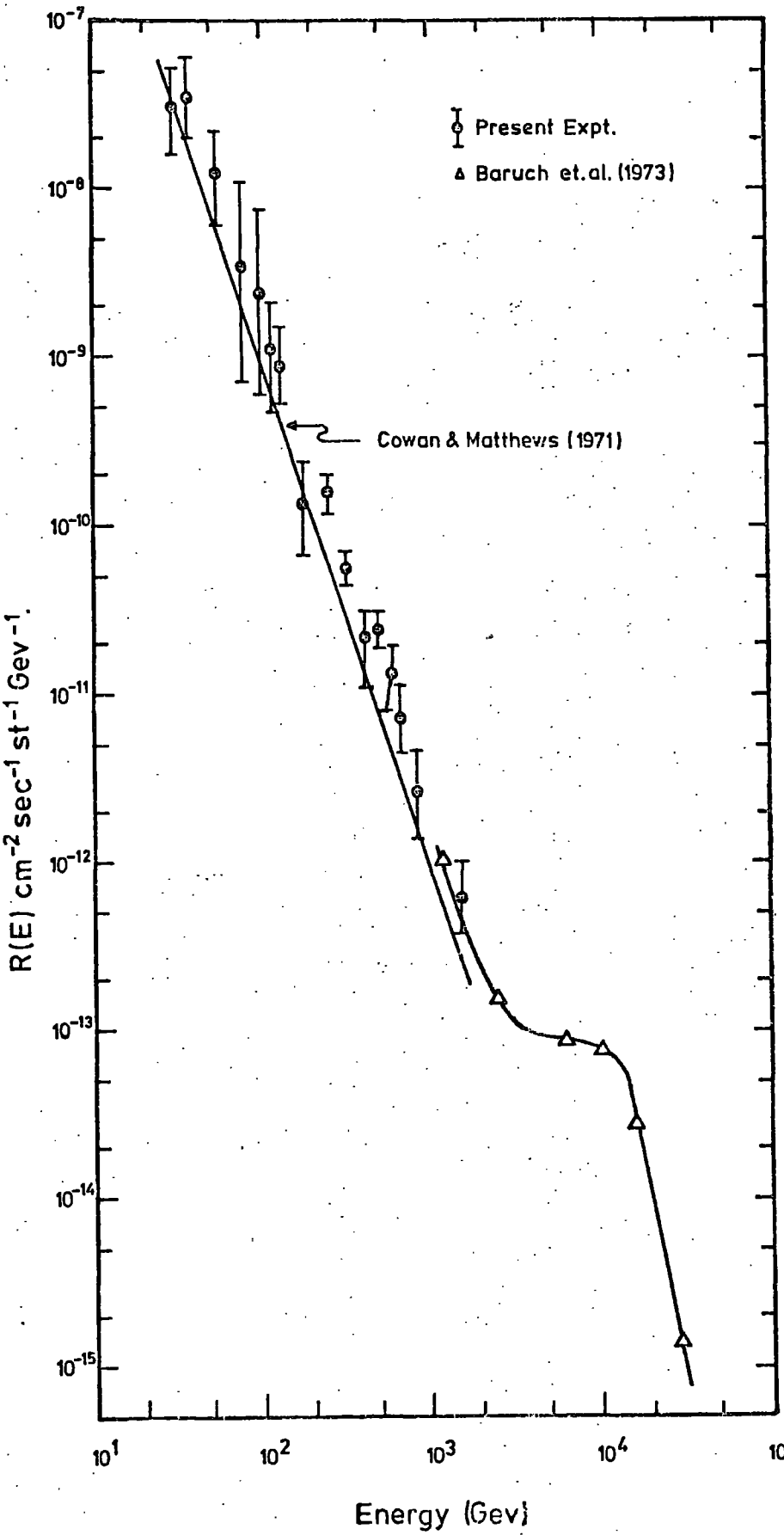


Figure 6.21 The differential energy spectrum measured in the present experiment and comparison with others. The data obtained in the present experiment was converted into an energy spectrum by assuming a 100% pion contribution.

initial ionisation being deposited and the high voltage pulse being applied to the electrodes, and that this behaviour can be predicted by the application of Lloyd's theory of electron diffusion in flash tubes. Now since at high energies the cascade width becomes too great, a knowledge of flash tube behaviour allows the width of the burst to be decreased by a controlled amount by substantially increasing the time delay $T_D$.

From Figure 5.19 it can be seen that the density per tube decreases rapidly with distance from the core, hence if instead of allowing single electrons to define the edge of a burst a larger density were required, the width of the burst would be reduced. Now the Lloyd parameter appropriate to the traversal of a flash tube by a relativistic charge e particle was found to be $af_1Q_1 = 9$, and since the parameter is a linear function of the amount of ionisation produced, the value for traversal by say ten charge e particles would be $af_1Q_1 = 90$. The variation of internal efficiency with $af_1Q_1$ at several time delays is shown in Figure 6.22 for $af_1Q_1$ values in this range. For a given time delay it can be seen that the sensitivity to different electron densities ($af_1Q_1$ values) is not great, therefore the flash tube pattern should be diffuse rather than having a well-defined edge.

With the flash tube burst widths thus reduced, the information on burst position can be used for defining the geometry while the energy is measured by the pulse height information from the scintillators. Initially a time delay of 330μS was used, an example of the flash tube photograph obtained being shown in Plate 6.4. The experiment is continuing.

## 6.5 Conclusion

A calibration of the burst width-burst size relation was obtained, the results of which should be directly applicable to the data obtained in the air shower experiment. In conjunction with the energy-burst size dependence calculated in Chapter 5 this should be sufficient to determine the energy of the EAS bursts.

Plate 6.4 Event H. 38 - 28

This event shows two parallel bursts, detected using a time delay $T_D$ of 330 $\mu$S.

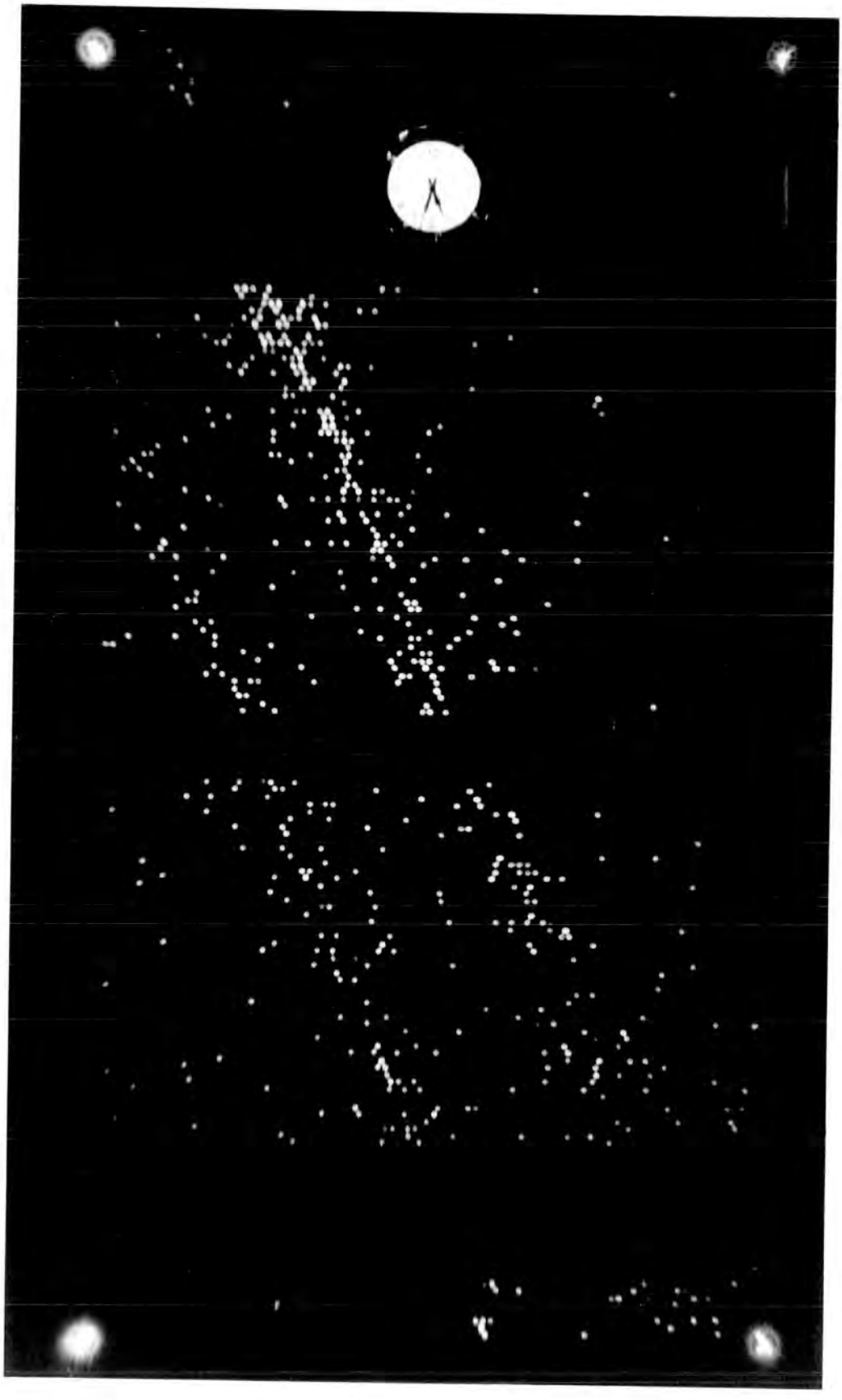

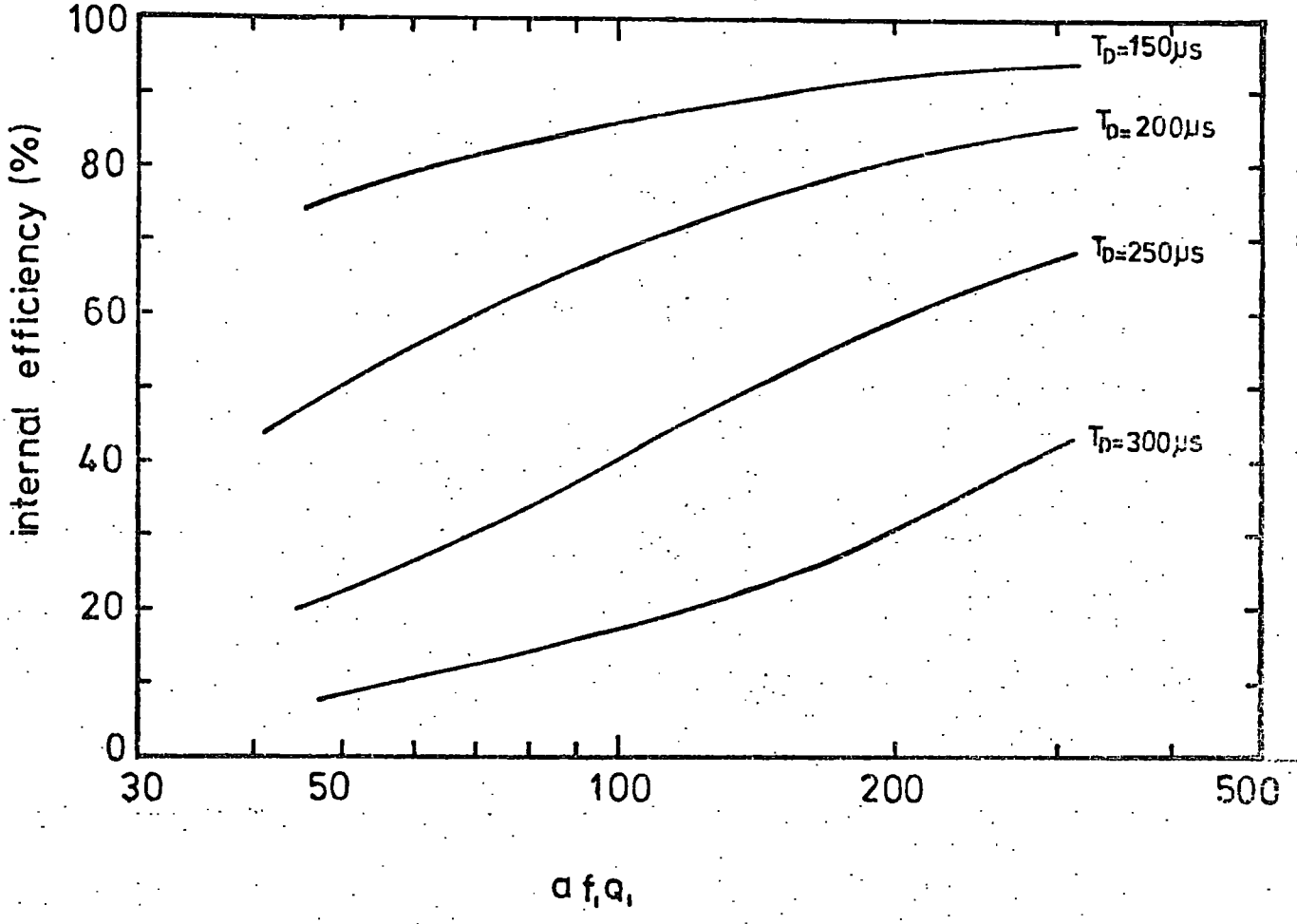


Figure 6.22 The variation of the internal efficiency of flash tubes with $af_1Q_1$ for large values of $af_1Q_1$, at different time delays $T_D$.

In addition, the vertical charged particle burst spectrum at sea-level was measured and found to be in agreement with the spectra obtained by other groups. The region of immediate interest, in which Baruch et.al. have found an anomalous "kink" in the spectrum, was not reached. The operation of the chamber was modified to enable this high energy region to be investigated, and the experiment will continue for some time to obtain data at these energies.

# CHAPTER 7

## THE ENERGY SPECTRA OF NUCLEAR-ACTIVE PARTICLES IN EAS

### 7.1 Introduction

The hadron component of an extensive air shower (EAS) determines the way in which the shower as a whole develops. In fact the development of an air shower is identical to the development of the nuclear-electromagnetic cascade discussed in Chapter 5 with reference to iron and lead absorbers, except that since air is a low density medium the competition between interaction and decay probabilities for charged pions becomes important, certainly for low energy pions.

Measurements of the hadron component provide the most direct way of studying the nuclear-physical processes occurring at these extremely high energies, thus obtaining information about this component is of considerable importance. In addition, one of the most important questions to be answered with regard to the astrophysical aspects of high energy cosmic ray particles is - What is the mass composition of these high energy particles? The hadrons can provide a means of determining the answer.

Probably the reason why few reliable experiments have been performed to study this component of EAS is the difficulty in making accurate measurements.

In this chapter a measurement of the charged and neutral hadron energy spectra will be described, as measured by the flash tube chamber, employing a local electron density detector to provide the EAS trigger. These measurements will then be related to general shower characteristics, the significance of which will be examined.

## 7.2 Analysis of the Data

### 7.2.1 Scanning technique

The 12,057 events photographed in the air shower run designated the E-series and described in section 2.5 were the source of data for this experiment. Table 7.1(a) shows the number of bursts observed in the lead and iron, and Figure 7.1 shows the basic data on the burst width distributions. Table 7.1(b) shows the probability of incident protons and pions interacting in the different parts of the chamber.

The negatives of the films were projected onto a scanning table, the reduction in scale being 20:1. The burst widths were measured in the flash tube layers below the iron and lead absorbers according to the definition adopted in Chapter 5. For an event to be accepted the whole width of the burst was required to be contained within the width of the uppermost flash tube layer. Only those events were measured which had a definable width. For each event a small-scale diagram was drawn.

### 7.2.2 Charge determination

The charge of the particle initiating a burst in the lead could not be determined, since no flash tubes were located above the lead absorber. However, for bursts occurring in the iron charge identification was possible in the eight layers of flash tubes (Fla) situated directly above the iron. The definition adopted for a burst produced by a charged particle was that it must have an observable track in Fla parallel to the burst direction and coincident with the middle of the burst. A neutral particle burst was defined as one for which the above definition of a charged particle was not satisfied.

Since no three-dimensional information was available, and hence the position of the burst in the back plane could not be determined, it was possible for a charged particle burst to simulate a neutral particle burst by entering the iron either at the extreme front or rear of the chamber where the iron was not completely covered by the flash tubes

| Total No. of triggers with $\Delta_e \geqq 40\ m^{-2}$ | Running time (hours) | No. of bursts observed in the lead with E>16GeV assuming produced by $\pi^{\pm}$ | No. of bursts observed in iron. | |
|---|---|---|---|---|
| | | | Charged $\pi^{\pm}$ with E > 12 GeV | Neutral nucleons with E >16 GeV |
| 12,057 | 2,570 | 681 | 313 | 34 |

Table 7.1(a) Basic experimental data.

| | Lead | Iron | Glass and aluminium electrodes in $F_2+F_3$ (Figure 2.1) |
|---|---|---|---|
| Proton | 0.55 | 0.25 | 0.12 |
| Pion | 0.53 | 0.23 | 0.12 |

Table 7.1(b) The probability of incident protons and pions interacting in different parts of the chamber.

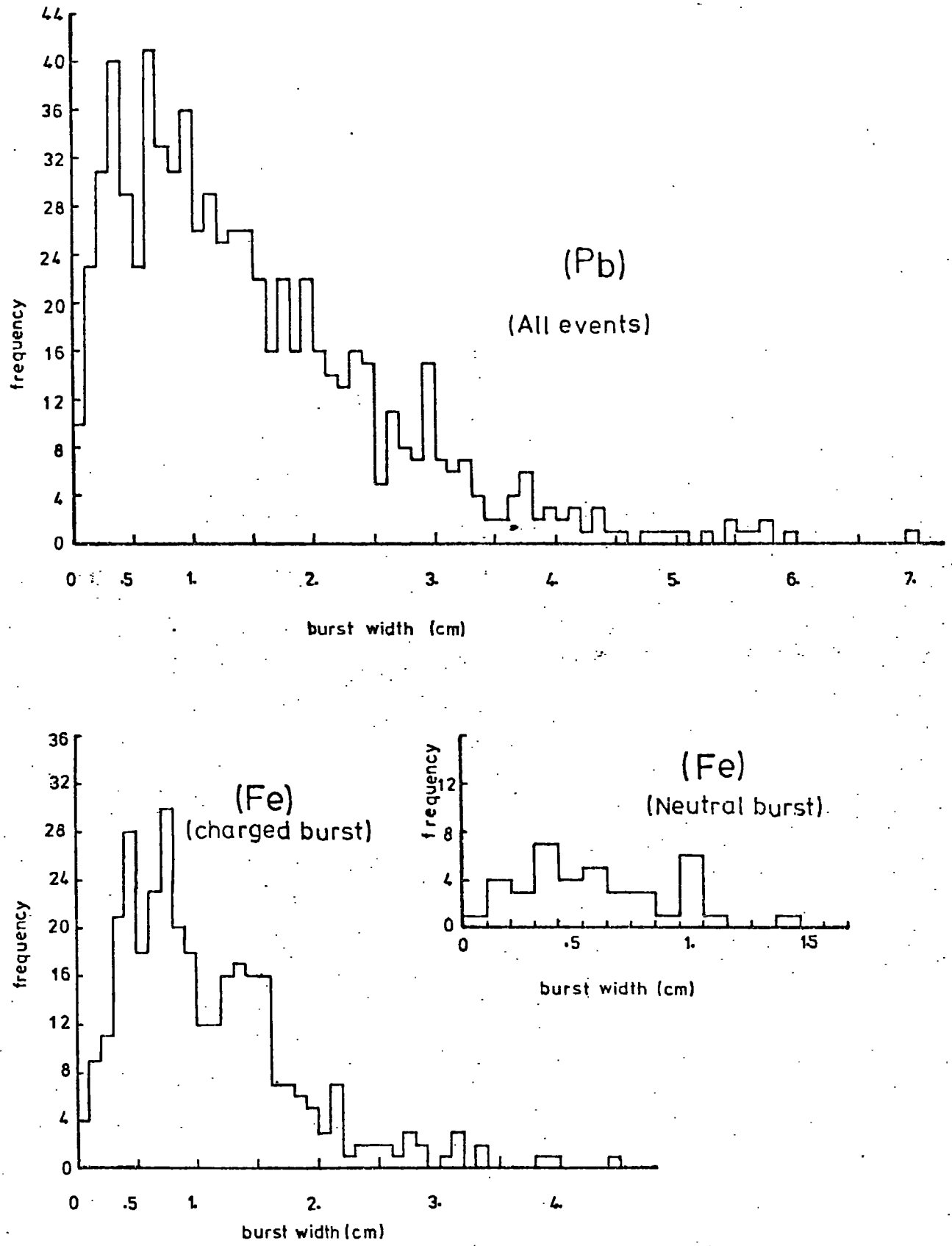


Figure 7.1 The measured burst width distributions obtained below the lead and iron absorber. From 12,057 events selected by the local density triger where $\Delta e \cong 40\ m^{-2}$. See Table 7.1(a) for further details. For the true burst width, multiply by 20.

(Figure 2.1). It was felt, however, that this type of event could be recognised and eliminated by the characteristic shape of the burst produced in this way. Plate 7.1 shows the effect. A particle has interacted in the iron without producing a track in the upper layer of flash tubes. However, when the burst reaches the bottom of the iron it also misses the measuring layers of flash tubes, F1b, and produces a characteristic step in the width of the burst in going from the recessed layers of flash tubes of F1b to the projecting layers of F2 where the full width of the burst is displayed. Thus this event is almost certainly not produced by a neutral particle and would be rejected by the scanning procedure. Edge effect events not detected by this method should be rare due to the very peaked angular distribution of the hadrons about the zenith in the EAS detected (measured to vary as $\cos^{10}\theta$ - Parvaresh, private communication).

7.2.3 Energy determination and production of spectra

The burst widths measured were converted into particle numbers using the relationship measured for unaccompanied vertical bursts and described in Chapter 6. The scintillator through which the bursts were required to pass in the vertical burst experiment will modify the form of the burst width-burst size relationship. This effect is likely to be small, however, since in the experiment performed by Coats (1967) with a thick iron absorber above two measuring levels of flash tubes, a liquid scintillator being positioned between the two layers, the difference in burst width measured at the two flash tube levels was small. An analogous effect can be seen in the glass of the flash tubes which constitutes an absorber not too dissimilar from the plastic scintillator, where once the burst has reached shower maximum the width of the burst is almost constant. Hence the conversion to burst size was made directly.

To convert the burst size obtained to an energy it was first necessary to assume an identity for the incident particles. Thus all bursts produced in the lead were taken to be pion-induced while in the iron charged bursts were assumed to be pion-induced and neutral particle bursts were

Plate 7.1 Event E 28 - 68

An edge effect event, simulating a neutral particle burst. The width of the burst increases immediately on passing from F1b to F2.

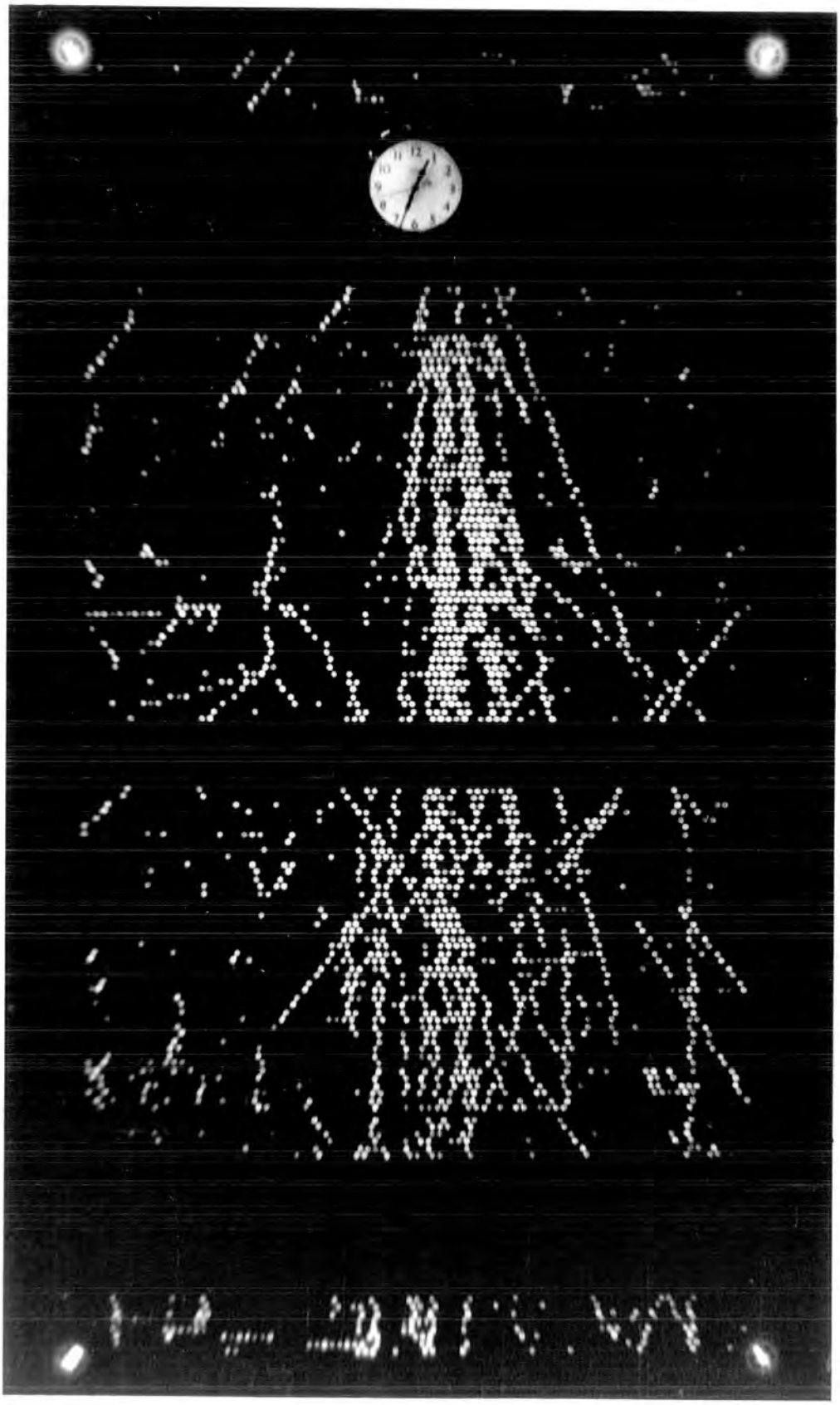

treated as neutrons (neutral kaons were neglected). With these assumptions it was possible to use the energy conversions calculated in Chapter 5 and hence produce the energy spectrum of all nuclear-active particles producing bursts in the lead and the spectra of charged and neutral particles producing bursts in the iron. Examples of the different classes of burst are shown in Plates 7.2 to 7.5.

## 7.3 Results

### 7.3.1 Corrections to the neutral particle energy spectrum

The neutral particle spectrum measured will be an underestimate of the true spectrum due to losses caused by mis-identification of a neutral burst (burst induced by a neutral particle) as a charged burst. This arises when the density of penetrating charged particles becomes such that there is a significant probability that there will be an unassociated charged particle track in the flash tubes directly above the neutral burst and with approximately the same direction. When this occurs the neutral burst will be wrongly identified as due to a charged particle.

An attempt was made to estimate the magnitude of this effect. Charged bursts were scanned for this purpose. The procedure adopted was to ignore the charged particle track in the flash tubes of Fla which had been taken to be the initiator of the burst, and then to see whether there was another particle track in Fla which could have been identified as the parent particle. The fraction of events with this ambiguous origin was then estimated as a function of energy. The result is shown in Figure 7.2. It can be seen that the effect increases with increasing energy, consistent with the fact that the mean energy of the hadrons increases at small distances from the core, where the particle density is higher.

Thus this correction can be applied to the neutral particle spectrum if it is assumed that the losses at each energy are those given by Figure 7.2. The assumption made here is that the lateral structure functions of neutrons

Plate 7.2 Event E 23 - 144

A charged particle burst produced in the iron.

N=135 particles

E=88GeV

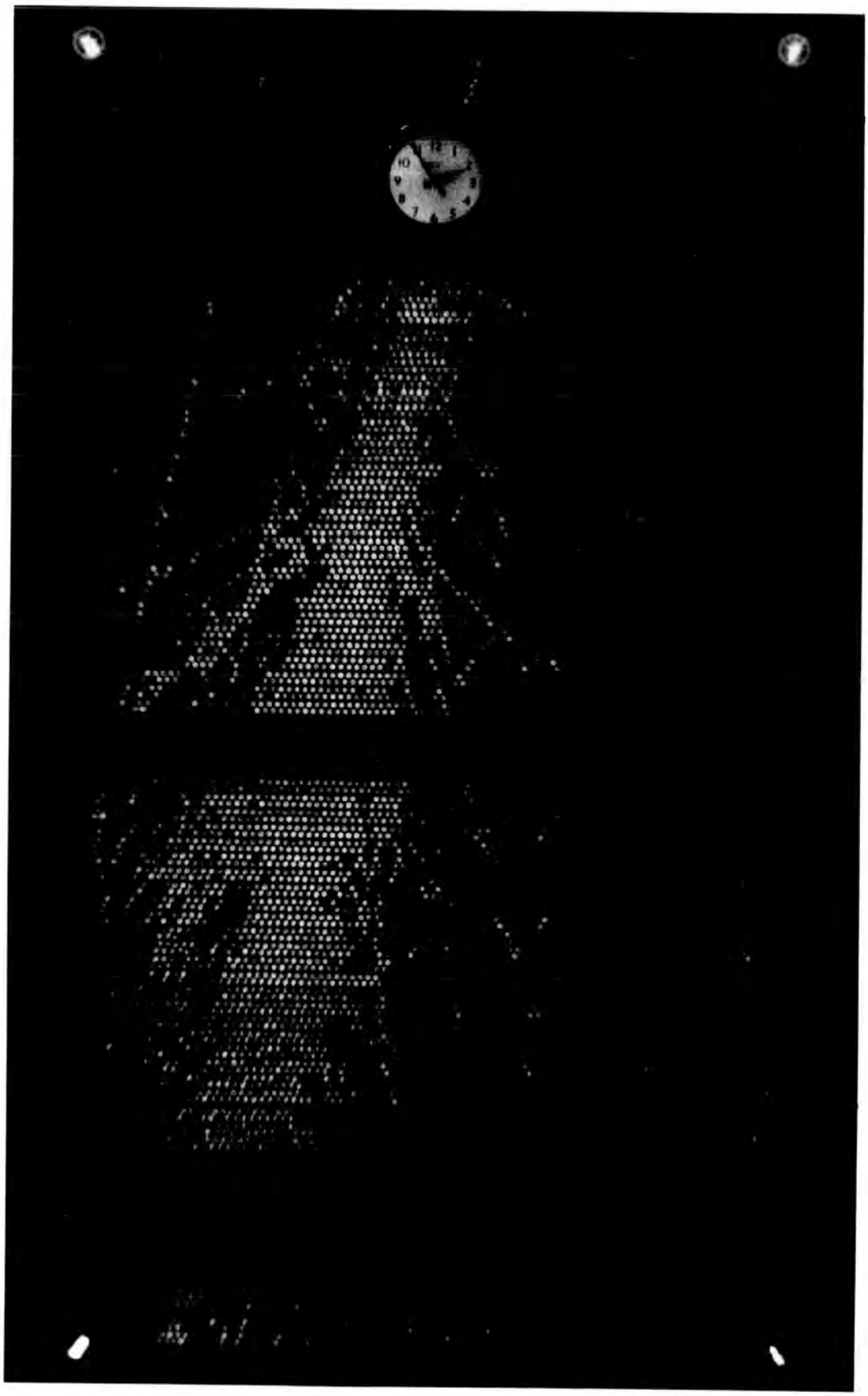

Plate 7.3 Event E 25 - 65

A burst produced in the iron by a neutral particle.

N=54 particles

E = 33 GeV

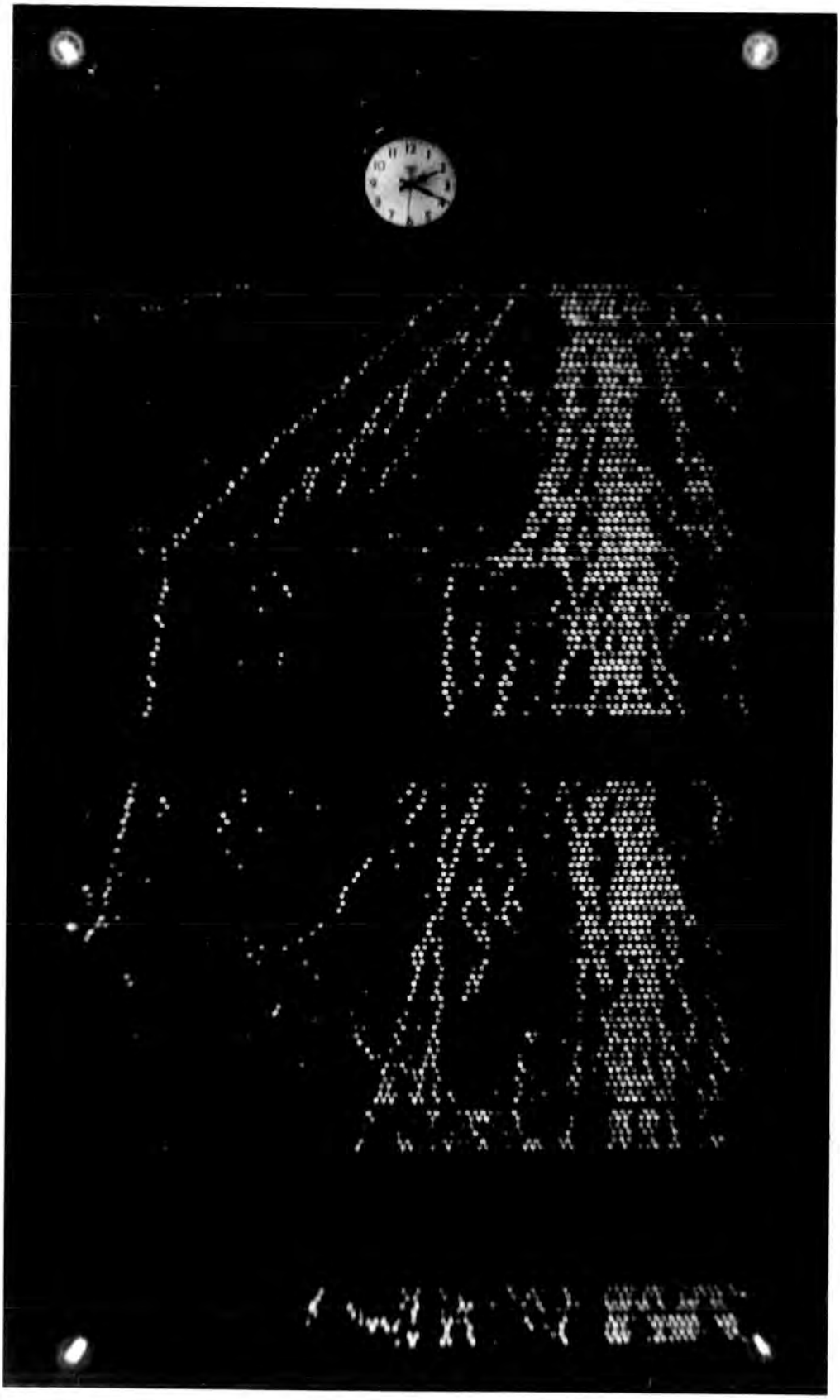

Plate 7.4 Event E 25 - 144

A burst produced in the lead and penetrating the iron.

N = 250 particles

E = 215 Gev

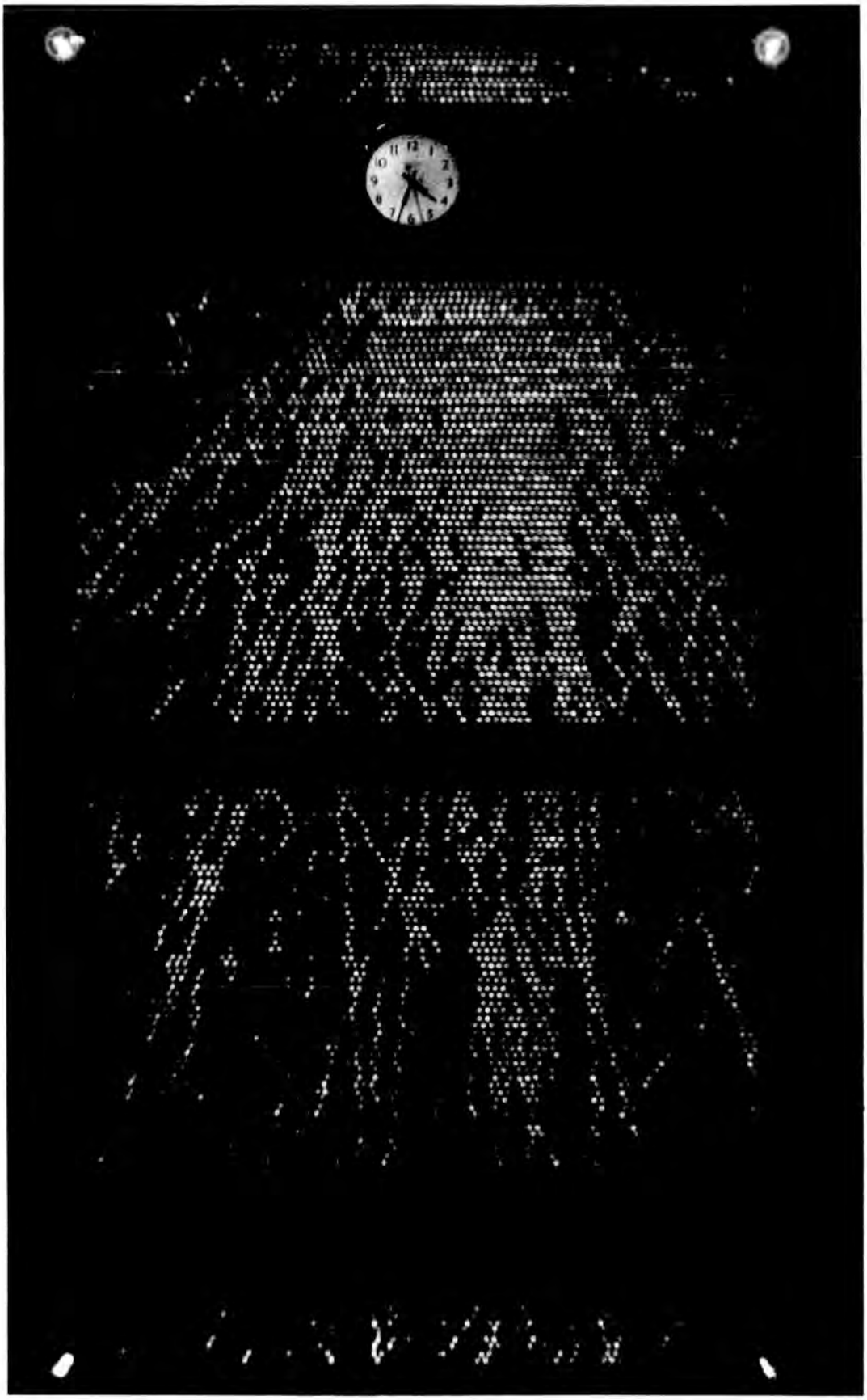

Plate 7.5 Event E 5 - 21

An example of an event in which three distinct cascades can be seen.

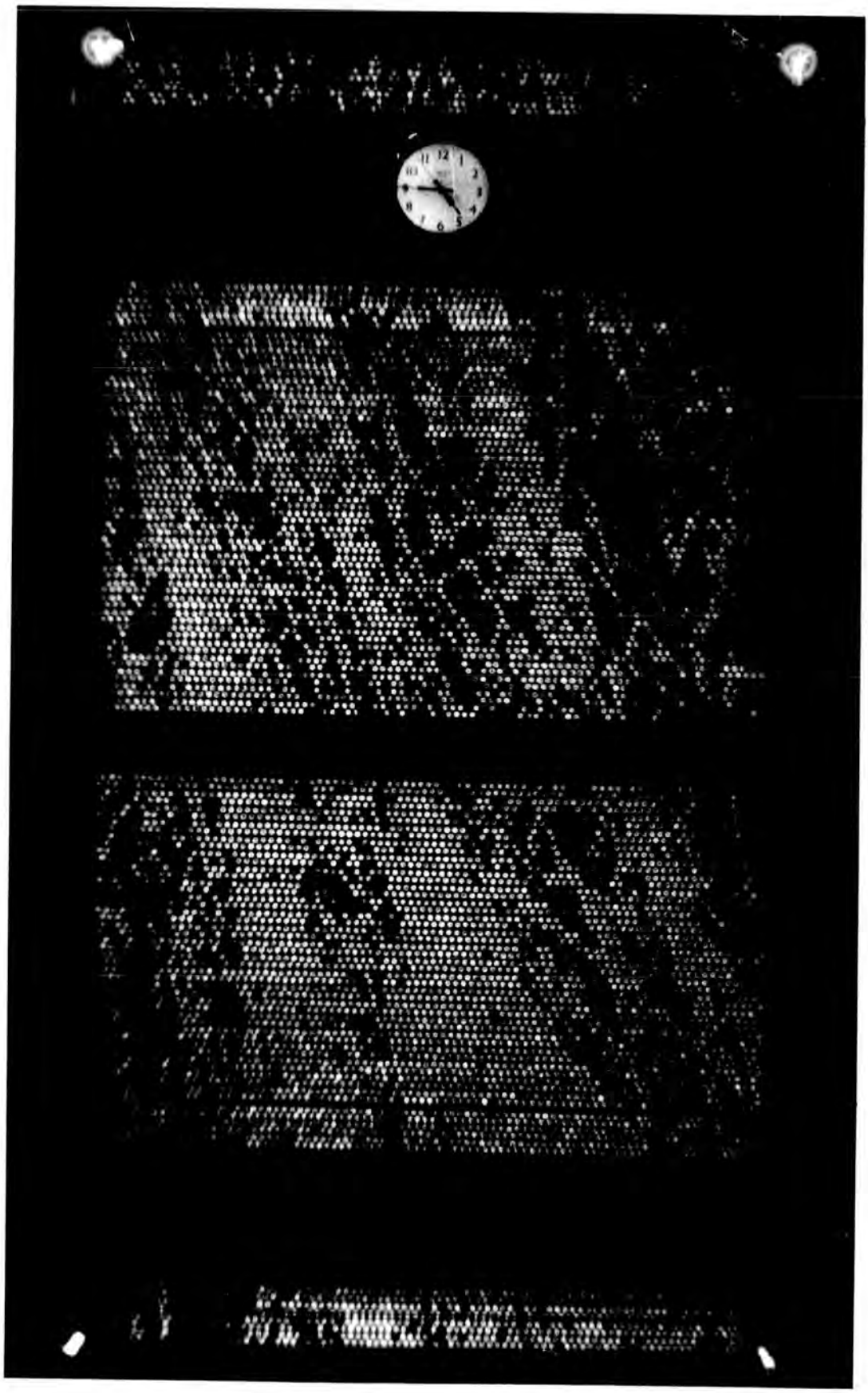

and charged pions are the same at a given energy in a particular shower. Now this is obviously an approximation. The lateral structure function of neutrons and its energy dependence is an unknown parameter. Theoretically, the shape of this function depends on the model of high energy interactions adopted. For the CKP theory, in which the surviving nucleon (neutral charge probability about one-half) is the only nucleon in the shower, the probability of observing the nucleon a significant distance outside the core will be very low, producing a steep structure function. Baryon-antibaryon production will produce a greater lateral spread, but the energy of the neutrons and antineutrons produced by this mechanism will be predominantly low energy (Jabs, 1967). It is thus felt that applying the correction factor estimated from Figure 7.2 to the neutral particle spectrum will probably lead to an underestimate of the spectrum by perhaps some tens of percent. It is also possible that the shape of the spectrum could be altered. The corrected spectrum should therefore be considered as a lower limit.

7.3.2 The energy spectra

Figures 7.3 and 7.4 show respectively the differential and integral forms of the energy spectra obtained in the present experiment. Three spectra are presented: the energy spectrum of all bursts produced in the lead, the spectrum of charged bursts produced in the iron and the spectrum of neutral bursts produced in the iron. All spectra have been corrected for the energy dependence of the aperture due to the reduced probability of an event being accepted as the burst width increases, and represent the total number of hadrons falling on (and interacting in) the detector, independent of burst width. The integral spectra of bursts in the lead and charged bursts in the iron can be represented by a power law of constant exponent above about 200 GeV, the value of the exponent being $-1.05 \pm 0.10$. The spectrum of the neutral particles appears to be somewhat steeper than this. The significance of this will be discussed later.

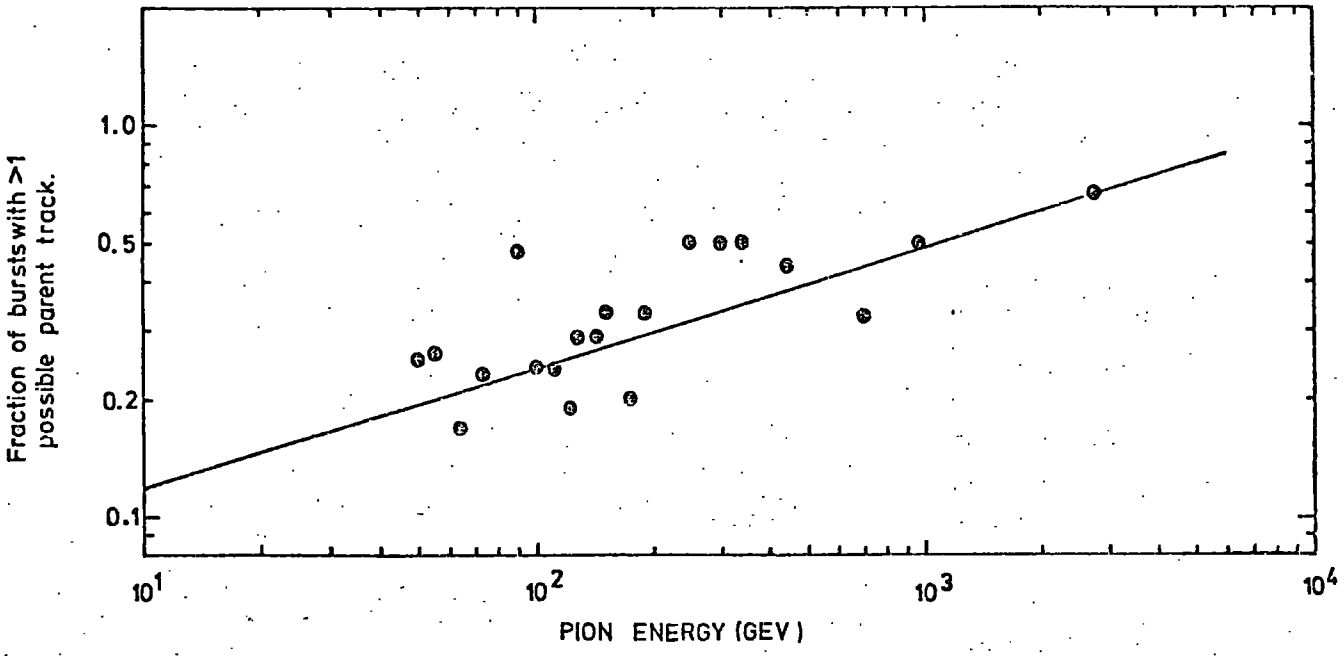


Figure 7.2 The fraction of charged bursts for which the parent track in Fla could not be uniquely defined, expressed as a function of energy.

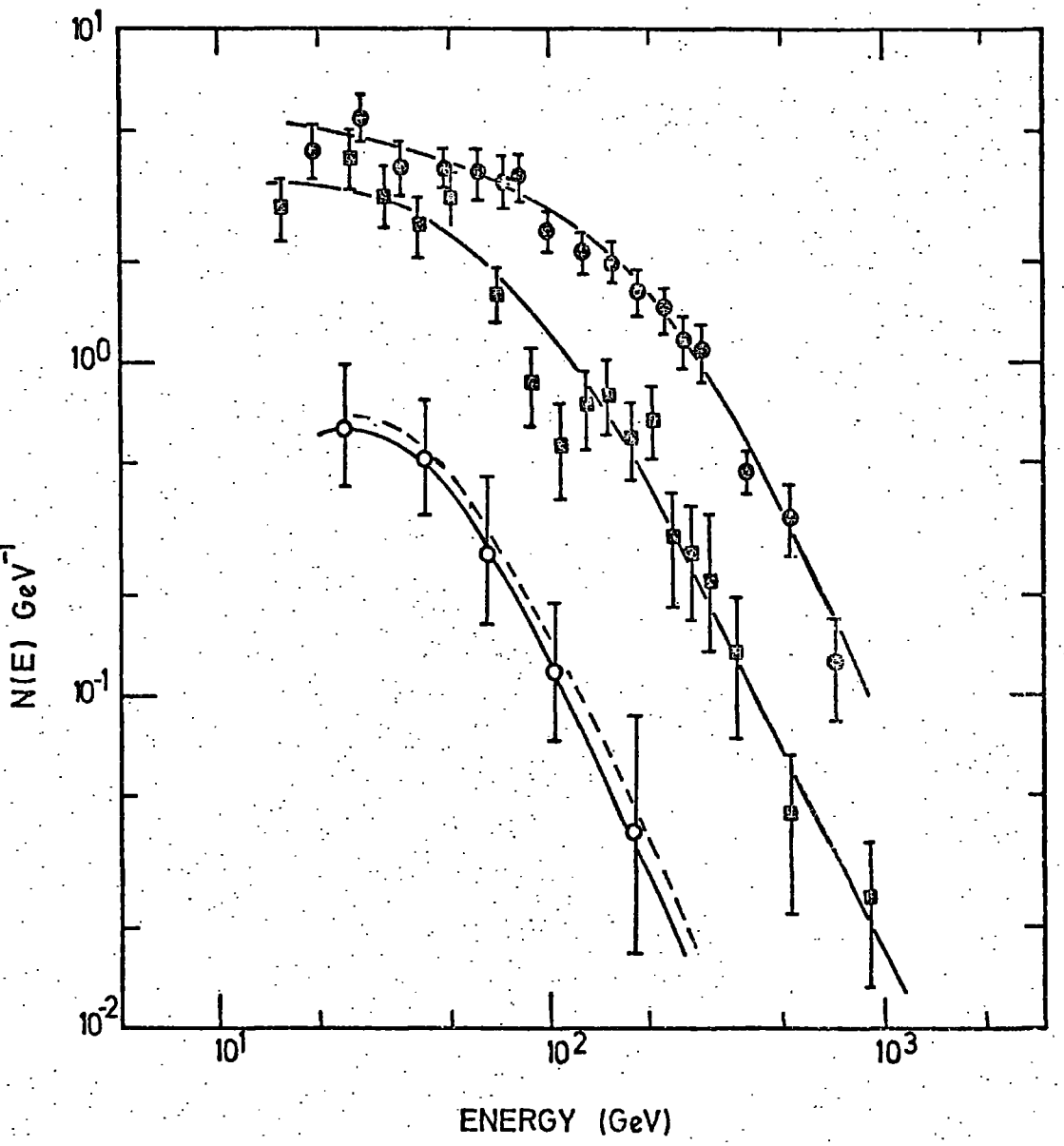


Figure 7.3 Differential energy spectra of hadrons in regions of EAS with $\Delta e \geqq 40$ m$^{-2}$ observed in a running time of 2570 hours. All spectra have been corrected for aperture effects and represent the flux falling on a detector of area 1.7x1.15 m$^2$. $\Phi$ = bursts in the lead, $\Phi$ = charged bursts in the iron, and $\Phi$ = neutral bursts in the iron. The dashed line indicates the corrected neutral spectrum.

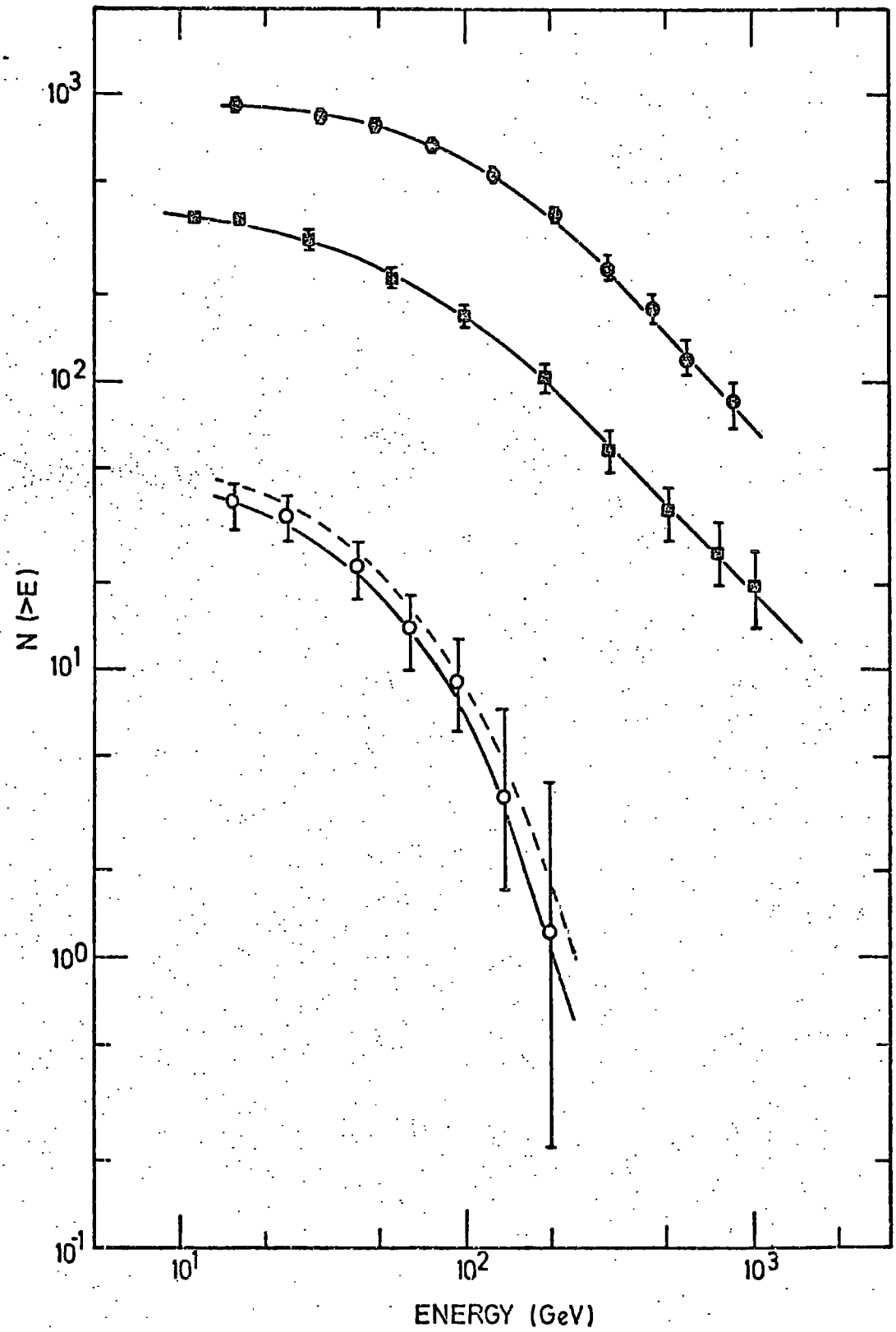


Figure 7.4 Integral energy spectra of hadrons in EAS with $\Delta e \geqq 40$ $m^{-2}$ observed in a running time of 2570 hours for a detector of total sensitive area 1.7x1.151 $m^2$. ⊕ = bursts in the lead, ⊞ = charged bursts in the iron, and ⊖ = neutral bursts in the iron. The dashed line indicates the corrected neutral spectrum.

The effect of folding the distribution of burst size (for an incident particle of a given energy) into the energy spectrum has been investigated using the distributions generated by the Monte Carlo program described in Chapter 5. It was found that the effect was minimal. Fluctuations in burst width were not considered separately since the high degree of correlation existing between the fluctuations in burst width and those in burst size renders this unnecessary.

7.3.3 Comparison of the bursts produced in the lead and iron absorbers

The relative frequency of bursts in the two absorbers provides information about the contribution to the burst spectra by muon-induced bursts. Assuming the bursts to be all pion-induced, the ratio of the number of bursts in the iron to the number in the lead should be 0.45. Figure 7.5 shows this ratio as a function of energy. While there appears to be some systematic variation, the points mostly lie within a standard deviation of the expected value. Any systematic variation can be attributed to effects of the energy conversions used, which were totally independent for the two absorbers. There is no evidence for significant muon contamination, which would be expected to produce a different ratio, caused not by attenuation of the muons in the lead but by the different interaction probabilities in lead and iron.

7.3.4 Bursts produced in the flash tubes.

Additional experimental evidence against the presence of a large muon contamination is afforded by a measurement of the interaction length of particles producing bursts in the glass of the flash tubes. The total amount of absorber represented by the flash tubes in F2+F3 (see Figure 2.1) in the vertical direction is 91.5 $g.cm^{-2}$. By measuring the variation of the frequency of interactions with depth in the flash tubes the interaction length can be determined. This has been carried out by Nasri and Parvaresh (1974, private communication). Acceptable events were those which had traversed both the iron and lead absorbers,

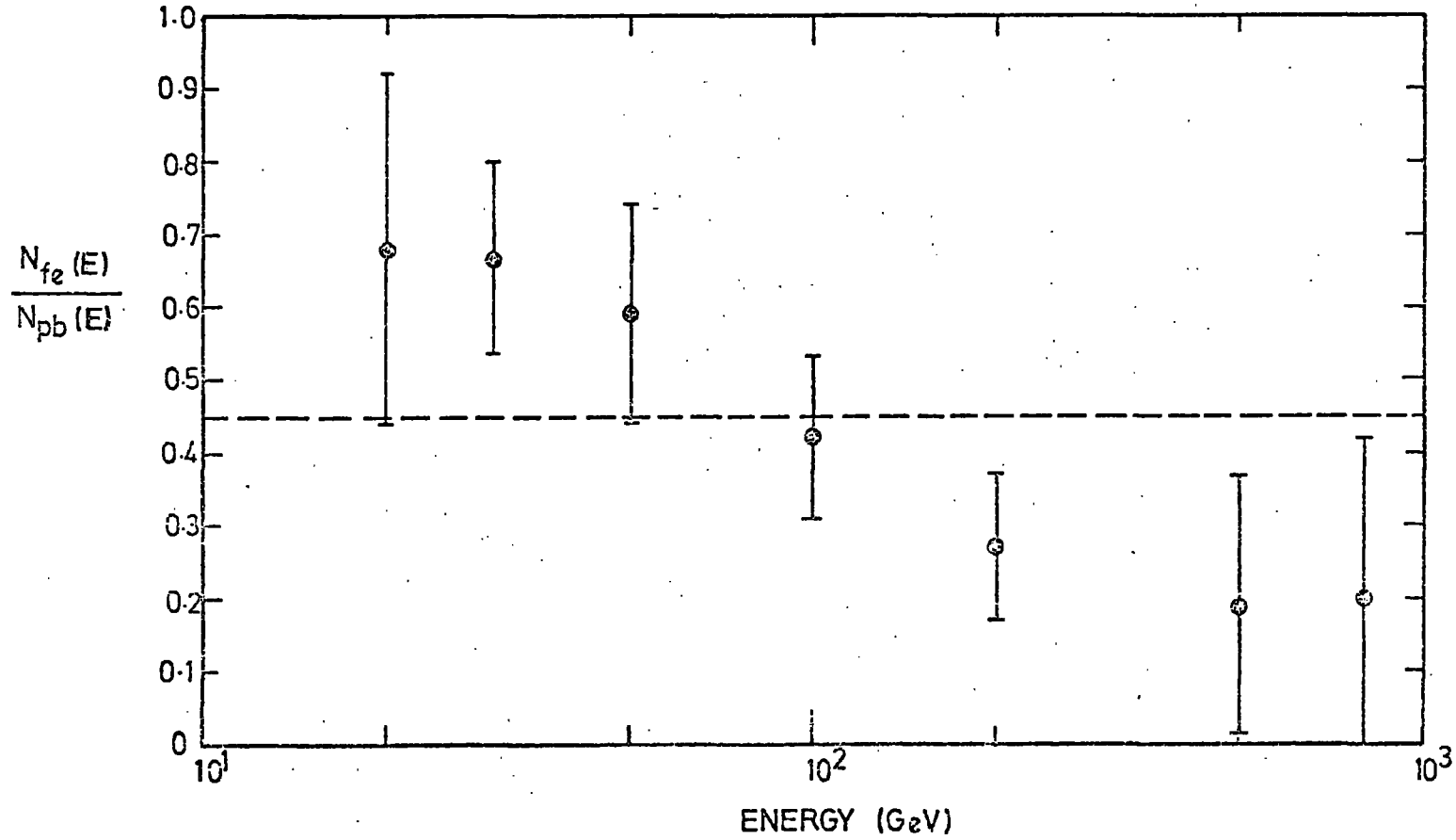


Figure 7.5 Ratio of the number of bursts observed in the iron to the number of bursts observed in the lead. The dashed line is the prediction for a 100% pion beam.

the track being visible in the flash tubes of Fla and Flb. Measurements were made on bursts occurring in F2 and F3. The correction for aperture was made after the method of Lovati (1954), the value of n found being 10 (where n is the exponent in the $\cos^n\theta$ angular distribution assumed). The results are shown in Figure 7.6. Fitting an exponential to the points and minimising using the $X^2$-test, the interaction length was found to be $119\pm44$ g.cm$^{-2}$, and is consistent with the value of 130 g.cm$^{-2}$ calculated from the paper of Alexander and Yekutielli (1961). For neutral particles the same analysis procedure cannot be carried out since the direction of the interacting particle cannot be accurately defined. Hence the data presented in Figure 7.7 is uncorrected for aperture effects and no acceptance geometry has been defined. The best estimate of the interaction length of neutral particles from this data is 115 g.cm$^{-2}$, subject to large errors, to be compared with a predicted value of 102g.cm$^{-2}$ for neutrons.

Since the interaction length of the charged particles is consistent with them being pions, it is concluded that muons (with a much longer mean free path) do not contribute greatly to the production of the bursts in the glass. It should be remembered, however, that the probability of a muon interacting is approximately proportional to $Z^2/A$, hence the relative contribution in the lead and iron absorbers will be greater than that in the glass. This should be largely compensated for, though, since the charged particles are required to have passed through 15 cms. of iron and 15 cms. of lead before interacting in the flash tubes, thus reducing the pion contribution by about 75% and effectively enhancing the muon contribution. Thus a measurement of the interaction length in the flash tubes is relevant to the consideration of the muon burst contamination in the lead and iron absorbers. Examples of charged and neutral bursts are shown in Plates 7.6 and 7.7.

## 7.4 Determination of air shower characteristics

### 7.4.1 Introduction

The energy spectra measured in the flash tube chamber with a local

Plate 7.6 Event E 4 - 100

An example of a burst produced when a charged particle interacts in the glass of a flash tube.

Plate 7.7 Event E 69 - 76

An example of a burst produced when a neutral particle interacts in the glass of a flash tube.

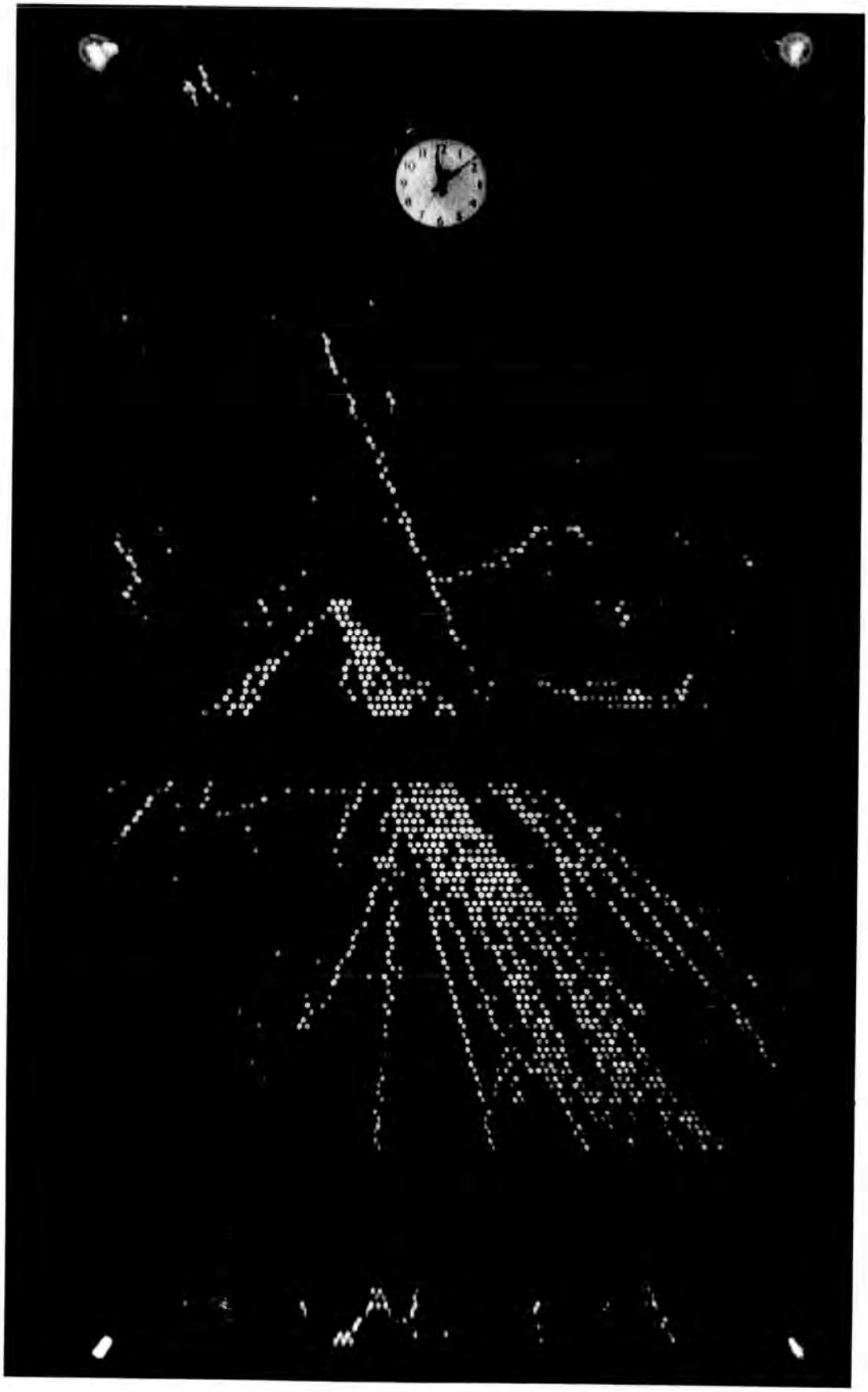

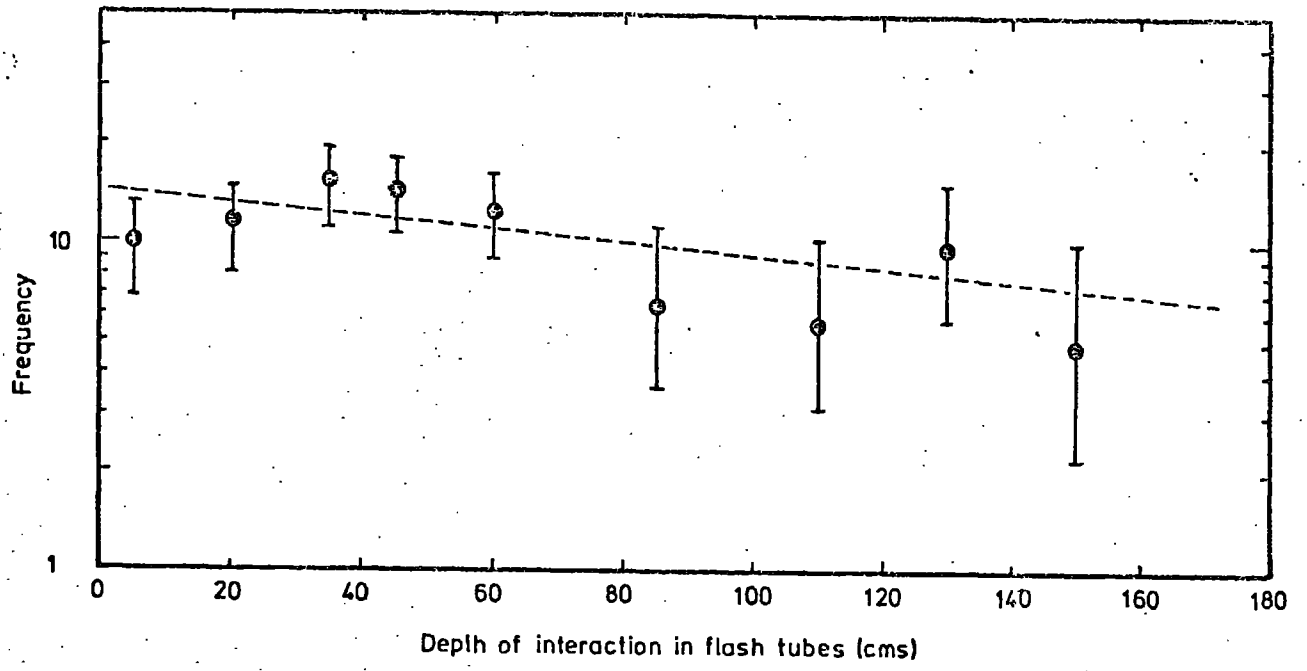


Figure 7.6 The interaction length of charged particles in the flash tubes. $\lambda = 119 \pm 44$ g.cm$^{-2}$.

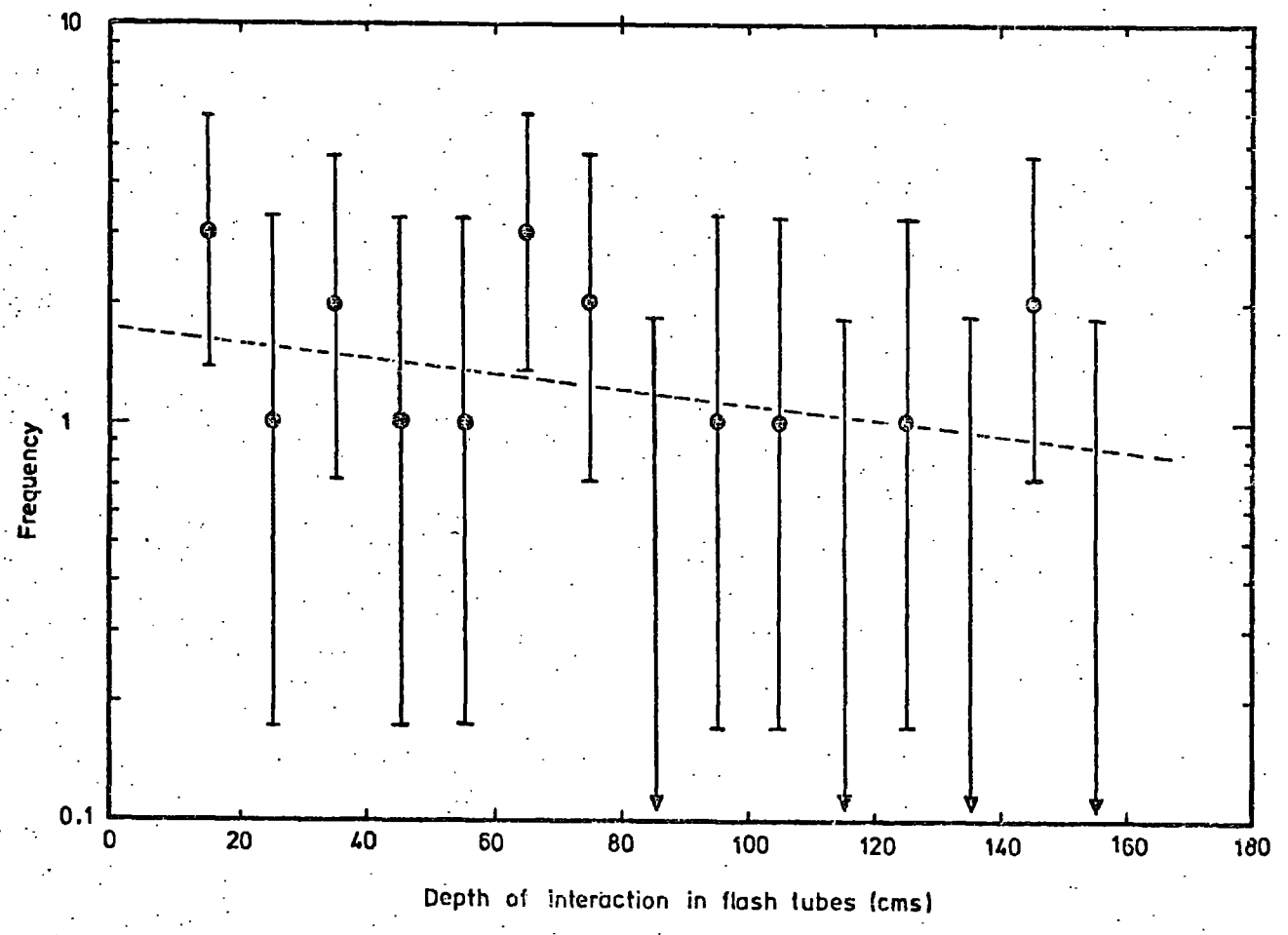


Figure 7.7 The interaction length of neutral particles in the flash tubes. $\lambda = 115$ g.cm.$^{-2}$.

density trigger must be related to the overall characteristics of EAS before any attempt to interpret the data is made. As can be seen from Figures 2.13 and 2.14, the type of EAS trigger used introduces a bias into the measurements. Rather than obtaining a measurement of all hadrons in an air shower for different shower sizes, the trigger provides selective information over a range of shower sizes and core distances. This information cannot immediately be unfolded from the results since for individual events no information was available on shower size or the distance of the detector from the shower core. Therefore an indirect method must be used.

7.4.2 Parameterisation of the data

To relate the data obtained using the flash tube chamber (with a local electron density trigger of $\Delta e \geq 40 m^{-2}$) to mean shower characteristics it is necessary to know how the density of hadrons in a shower depends on hadron energy, core distance and the size of the shower. As this information was not available in the present experiment it was necessary to adopt a general expression describing hadrons in EAS which could then be modified to fit the present data.

For this purpose the results of Kameda et.al.(1965) were used. Kameda et.al. studied hadrons of energy greater than 100 GeV in EAS of size $4.10^4$-$4.10^6$, using a multiplate cloud chamber situated in an air shower array at sea-level. By combining the information obtained from their detector with the information on shower size and core distance obtained from the air shower array, they were able to produce an empirical expression describing the hadrons in a form suitable for use in the present application.

The expression they give is for the density of nuclear active particles of energy (E,E+dE) at a distance (r,r+dr) from the axis of a shower of size $(N/10^5)$ particles, and is

$$n(E,r,N)dE\,dr = 0.35\ N^{0.35}\ E^{-1.2}\ \exp(-r/r_o)\ dEdr$$

where $r_o = 2.4\ N^{0.32}E^{-0.25}$

and E is in units of 100 GeV and r in metres.

This, however, is not consistent with a statement in the text of the paper, which states that the size dependence of the number of hadrons with energy greater than 100 GeV was found to be

$$n_N\ (>100\ \text{GeV}) = \left(\frac{N}{10^5}\right)^{1.0\pm0.15}$$

where C is given as $7.2\pm1.5$.

Assuming this latter statement to be correct, the Kameda expression was modified to fit this value, the expression obtained being

$$n(E,r,N) = 0.14\ N^{0.35}E^{-1.2}\exp(-r/r_o)\ m^{-2}\ (100\ \text{GeV})^{-1}$$

where $r_o = 2.4\ N^{0.32}\ E^{-0.25}$

and E is in units of 100 GeV and r in metres.

This represents the density of hadrons per square metre with energy (E,E + dE) at a core distance r in a shower of size $(N/10^5)$.

For ease of calculation in the present application, the units were converted, such that N is the shower size in units of single particles and E is in GeV. The resulting expression for the hadron density is

$$\Delta(E,r,N) = 6.26.10^{-3}N^{0.35}E^{-1.2}\ \exp(-r/r_o)m^{-2}GeV^{-1}$$

where $r_o = 0.19\ N^{0.32}E^{-0.25}$

When integrated over all core distances, for a particular shower size the exponent of the energy spectrum of hadrons is obtained from this equation to be -0.75, to be compared with (negative) values of 1.0 - 1.2 found by most other workers (Chatterjee et.al., 1968, Fritze et.al., 1969, Tanahashi, 1965 and Bohm et.al., 1968).

While the N-dependence of the relation cannot be checked in the present experiment, nor the value of the parameter $r_o$, the overall energy dependence can be. Thus, assuming the N-dependence and $r_o$ to be

correct, a two-parameter fit to the data obtained in the present experiment was attempted. For this purpose, a parameterisation of the following form was adopted:-

$$\Delta(E,r,N) = A\ N^{0.35}\ E^{-\alpha} \exp(-r/r_o)\ m^{-2}\ GeV^{-1}$$

where $r_o = 0.19\ N^{0.32}\ E^{-0.25}$, where r is in metres and energy in GeV.

To evaluate A and $\alpha$ appropriate to the present experiment the following integral was solved.

$$r(E, \Delta e \geqq 40)dE = \int_{r=0}^{r_{max}} \int_{n=N_{min}}^{N_{max}} 2\pi r.\Delta(E,r,N).R(N)dEdNdr$$

where R(N) is the rate of showers of size N, $N_{min}$ is the minimum shower size at a core distance r which can produce a local electron density of $\geqq \Delta e$, and $N_{max}$ is an arbitrarily large shower size, taken to be $5.10^9$ for the present calculations. The value of $r_{max}$ was taken to be 50 metres, beyond which the number of energetic hadrons was assumed to fall to zero. The number spectrum of EAS used was a derived differential form of the integral spectrum given by Hillas (1970), and was taken to be

$$R(N)dN = 78.26N^{-2.5}dN\ cm^{-2}sec^{-1}st^{-1} \qquad N<5.10^5$$

$$R(N)dN = 5.5610^4N^{-3.0}dN\ cm^{-2}sec^{-1}\ st^{-1} \qquad 5.10^5<N<3.10^7$$

$$R(N)dN = 10.17\ N^{-2.5}dN\ cm^{-2}sec^{-1}st^{-1} \qquad 3.10^7<N<5.10^9$$

The integrations were performed for a series of values of the exponent $\alpha$, the slope of the energy spectrum which would be obtained with the local electron density trigger $\Delta e \geqq 40\ m^{-2}$ being evaluated for each value of $\alpha$. It was found that a value $\alpha = 1.7\pm0.1$ would produce an energy spectrum measured with this trigger of $1.05\pm0.1$, the value measured in the present experiment. For this value of $\alpha$ the constant A was calculated to be 0.252, the value required for the expression to predict the number of hadrons, with energy greater than 200 GeV falling

on the $1.7 \times 1.5 m^2$ area of the flash tube chamber in a running time of 2570 hours, to be 600. This number was obtained from Figure 7.4 by adding the total number of bursts observed in the iron to the number in the lead and correcting for the fraction of hadrons which will traverse both absorbers without interacting (assuming a 100% pion contribution). Other losses were assumed to be small. The value of the exponent of the hadron angular distribution in the showers was taken to be n = 10 (Parvaresh, 1974 - private communication).

Thus the expression obtained, normalised to the data of the present experiment, gives the density of hadrons of energy E GeV a distance r metres from the core of a shower of size N to be

$$(E,r,N) = 0.252\ N^{0.35}\ E^{-1.7}\ \exp(-r/r_o) m^{-2} GeV^{-1}$$

where $r_o = 0.19\ N^{0.32}\ E^{-0.25}$.

Integrating this expression over core distance gives the energy spectrum of hadrons in a shower of size N, the value of the exponent being $1.2 \pm 0.1$, in good agreement with the references quoted earlier in this section, and also with the predictions of Thielheim and Beiersdorf (1969), Bradt and Rappaport (1967) and Greider (1970).

It should be noted that the exponent of the energy spectrum measured with the local electron density trigger (1.05) is not very different from the value per shower of 1.2.

From the above expression the total number of hadrons of energy greater than 200 GeV per shower has been determined for the mean shower size observed in this experiment, $2.10^5$, to be 16. Figure 7.8 shows this value and compares it with results obtained at sea-level from other experiments and from various predictions. These predictions will be discussed in greater detail in section 7.5.2.

7.4.3 Muon contamination

In sections 7.3.3 and 7.3.4 it was concluded that the muon

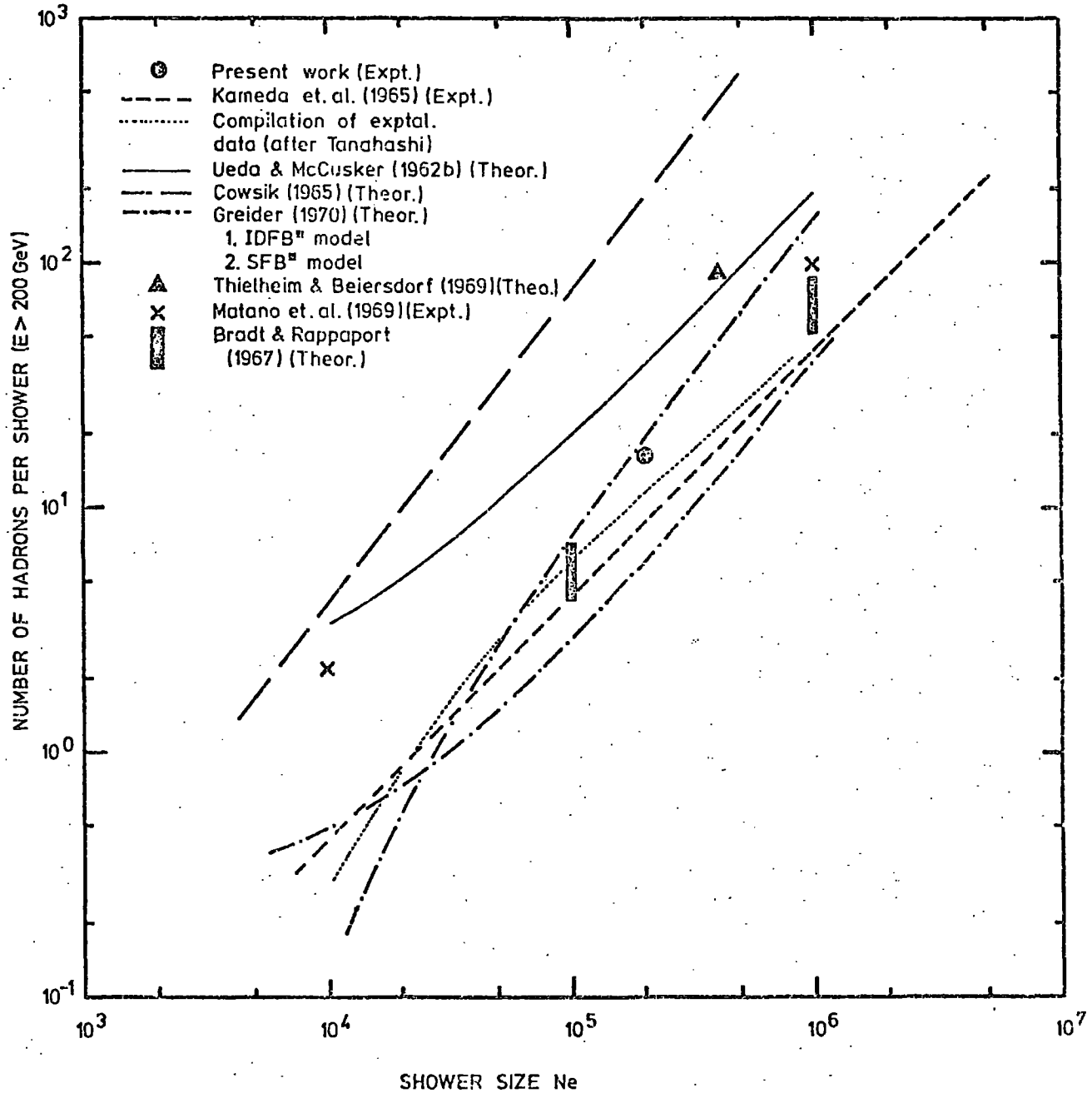


Figure 7.8 The number of hadrons, in a shower of size Ne, with energy >200 GeV. The point obtained in the present experiment has been evaluated at the mean shower size obtained in the experiment ($2.10^5$). The compilation of experimental data by Tanahashi is taken from Greider (1970). The data of Matano et.al.(1969) has been extrapolated.

contribution to the burst spectrum would not be large, from considerations of the ratio of bursts occurring in the lead to those occurring in the iron absorber, and also from a measurement of the interaction length of burst-producing particles in the glass of the flash tubes. A more direct attempt can, however, be made to predict the contribution quantitatively.

The energy spectrum of muons above the flash tube chamber detected with the trigger employed in the present experiment was calculated in much the same way as was the hadron spectrum. The parameterisation used was that of Greisen (Bennett et.al., 1962), and gives the density of muons as

$$\rho_\mu(>E,r,N)dr = \frac{14.4r^{-0.75}}{(1+r/320)^{2.5}} \left(\frac{N}{10^6}\right)^{0.75} \left(\frac{51}{E+50}\right)\left(\frac{3}{E+2}\right)^{0.14r^{0.37}} dr$$

where r is in metres and the energy E in GeV.

This empirical formula was derived for the shower size range appropriate to the present experiment, but was evaluated from data for muons of energy only up to 10 GeV. The large extrapolation made here is justified in that the formula is not inconsistent with the data presently available at small core distances (Goorevitch and Peak, 1973, Barnavelli et.al., 1965), and should be correct to within the accuracy required in the present calculation. Greider (1970) compares the results of Monte Carlo simulations with Greisen's expression, concluding that the limit of reliability of the Greisen formula is at about $10^3$GeV.

The conversion from a muon energy spectrum to a burst spectrum has been performed for the iron absorber, neglecting the lead above the iron. Results of calculations carried out by Hansen (1974, private communication), predicting burst probabilities below a thick iron absorber as a function of muon energy, have been used for the conversion. For a sufficiently thick absorber the burst size distribution produced by muons will be almost independent of the thickness up to some limiting energy, due to

the great absorption length of muons. The limiting energy is determined approximately by the maximum energy cascade which can develop to shower maximum in the whole depth of the absorber. The 8.19 radiation lengths of iron in the flash tube chamber can be seen from the transition curves of Ivanenko and Samosudov (Figure 5.3) to be sufficient up to about 1 TeV, thus the results of calculations carried out for a very thick iron absorber should be applicable. After evaluating the detailed cross-sections for the relevant processes (knock-on electron production, bremstrahlung, direct pair production and photo-nuclear production - see Hansen, 1974 for details of cross-sections used), Hansen solves the integral

$$\theta\,(E,N)dN = \int_t \phi\,(E,N,t)\,\frac{\partial E'(N,t)}{N}\quad dNdt$$

where $\phi(E,N,t)$ is the probability that a muon of energy E will produce a burst of size N below the iron absorber, initiated by an energy transfer E' to a photon or electron a distance t from the bottom of the absorber (the cascade curves of Ivenenko and Samosudov (1967) were used).

The results of these calculations were made available as probability distributions for a muon of energy E to produce a burst size below the absorber of N particles. These distributions were then folded into the energy spectrum of muons predicted above, allowing the contribution to the burst spectrum obtained in the present experiment to be evaluated. The results are shown in Figure 7.9. It can be seen that muon contamination is small and can be neglected.

## 7.5 Interpretation of the results

### 7.5.1 Introduction

The number of hadrons with energy greater than 200 GeV in a shower of size N was determined in section 7.4.2 from the results of the present experiment, and is shown in Figure 7.8. It can be seen that this is slightly higher than most other experiments have found, but could be due

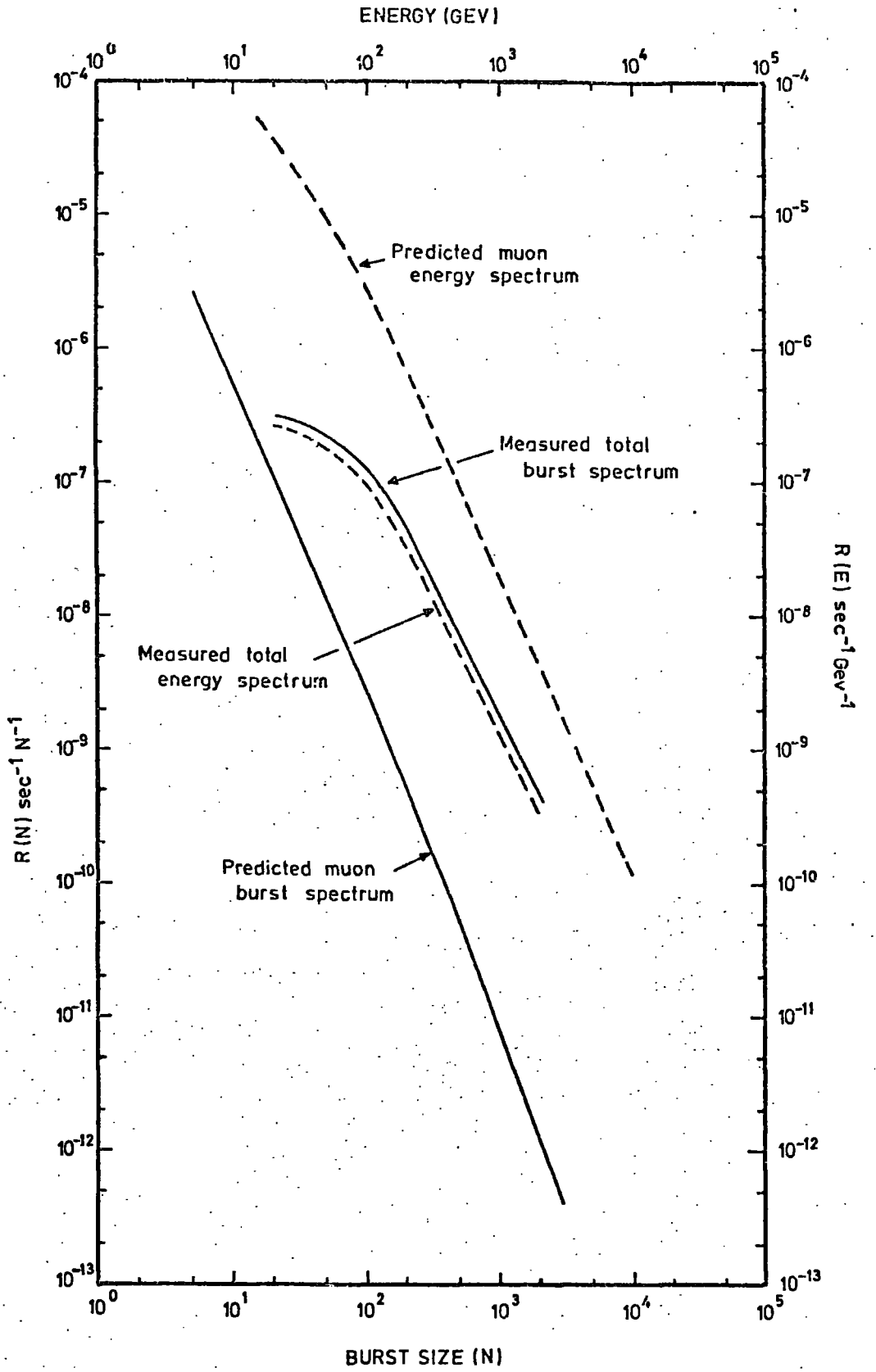


Figure 7.9 A comparison of the total burst spectrum obtained in the iron of the detector with the predicted contribution from muons. The dashed lines refer to the respective energy spectra.

to the way in which the Kameda expression was modified to fit present data. In particular there is some evidence that the N-dependence found by Kameda et.al. is incorrect, leading to an error when a two-parameter fit of the type adopted in the present work is utilised.

Models of the nuclear interactions of nucleons can, in general, be divided into three main groups. First is the CKP model discussed in earlier chapters, which envisages fireball production (two-centre) as the source of thepions (Cocconi, 1965). An extension to this theory is the inclusion of isobar production (Pal and Peters, 1964), in which the nucleon (leading particle) emerges from the interaction with a certain probability of being in an excited state. This then decays to the ground state emitting pions. The fraction of energy going into isobar excitation and into fireball production is usually a free parameter in interaction models. While the pion multiplicity increases as $E^{1/4}$ in the CKP model, isobar production produces a stronger dependence of the form $E^{1/2}$.

At high energies there appears to be an additional process occurring, that of baryon-antibaryon ($N\bar{N}$) production (Bertin, 1972). Thus the fireball emits not only pions (and kaons) but also nucleons and anti-nucleons. This mechanism has been incorporated into several models, usually by including an energy dependent term which will saturate at very high energies at a level of about 15% of the total secondary energy.

7.5.2 Total numbers of hadrons in a shower

Predictions of several models are shown in Figure 7.8 for comparison with experiment. The Monte Carlo calculations of Theilheim and Beiersdorf (1969) and Bradt and Rappaport (1967) do not include $N\bar{N}$ production, whereas all other models shown do. The predictions of four models of Bradt and Rappaport are shown, representing two centre and isobar production for protons and iron nuclei. There is little sensitivity to these different models. Thielheim and Beiersdorf find a similar lack of resolution for the mass of the primary cosmic ray particles,

although at high energies conservation of energy produces a steepening of the energy spectrum of hadrons for high -A showers (A is the mass number). Two models are shown from the Monte Carlo calculations of Greider (1970); the single fireball model and the intermediate double fireball model. Both include $N\bar{N}$ production.

Numerical calculations which include the effects of $N\bar{N}$ production have been carried out by Ueda and McCusker (1962a,b) and by Cowsik (1965). These, however, produce considerably higher hadron numbers than the Monte Carlo calculations, and in the calculations of Cowsik in particular the nucleons dominate the hadron spectrum at all energies. This is perhaps unexpected, since $N\bar{N}$ production would be expected to enhance mainly the low energy part of the spectrum (Jabs, 1968, Greider, 1970). It appears that these numerical calculations may overestimate hadron numbers,

Most of the theoretical predictions are given in terms of the primary particle energy, rather than shower size, hence the conversion to shower size had been made assuming 10 GeV per electron (Grieder, 1970). This, however, is an oversimplification.

It can be seen that there is little sensitivity to the different interaction models in the total number of NAP's, although Greider concludes that the double fireball model (which shows an $E^{1/4}$ multiplicity dependence) is unable to produce sufficient particle numbers in the smaller air showers, due to the fraction of the energy going into heavy particle production. What is important is that the relative contributions of nucleons and charged pions changes significantly, depending on whether or not baryon-antibaryon production is included.

It should be noted that another parameter open to investigation is the time delay spectrum of hadrons in EAS. For hadrons of a given energy, the time delay distribution will depend on the types of particle present and their mode of production. While Tonwar and Sreekantan (1971) interpret their results in terms of an isobar-pionisation model, Greider

(1970) concludes that the time delay spectrum is not very sensitive to his different models although it is useful in the classification of particle type.

7.5.3 The ratio of charged to neutral hadrons

As mentioned above, the ratio of the total number of nucleons (and antinucleons) to charged pions in a shower depends on the nuclear interaction model. This ratio can be broken down into the number of neutral hadrons (neutrons and antineutrons - kaons being neglected) to the number of charged hadrons (pions, protons and antiprotons) present in a shower.

Using the data of Figure 7.3 the charge to neutral ratio obtained in the present experiment was evaluated as a function of energy, and is shown in Figure 7.10. It can be seen that the ratio increases from about 4.5:1 at low energies to ~12:1 at energies of ~200 GeV, although the errors on these values are large. This is in disagreement with the results of other experiments (Vatcha and Sreekantan , 1973a and Kameda . et.al., 1965). Kameda et.al. find a charge to neutral ratio in showers at sea-level of size $4.10^4$ - $4.10^6$ (independent of shower size) of $4.5 \pm 0.5$ for all events, changing from $6 \pm 1$ at energies less than 500 GeV to $2.5 \pm \frac{1.5}{0.5}$ above 500 GeV and $1.5 \pm 0.5$ above 1000 GeV. Vatcha and Sreekantan (at 800 $g.cm.^{-2}$) find a shower size dependence, being $6.2 \pm 1.3$ for hadrons of energies greater than 25 GeV in showers of size less than $3.2.10^5$, and $3.1 \pm 0.5$ for hadrons of energy greater than 25 GeV in showers of size $3.2.10^5$ - $1.8.10^6$. For all shower sizes the ratio falls from $5.2 \pm 1.7$ for hadrons of energy 10 - 25 GeV to $1.1 \pm 0.5$ for energies >200 GeV, a somewhat faster fall than that found by Kameda et.al. While the discrepancy between these results and those obtained in the present experiment can be explained by assuming a steep lateral structure function for the high energy neutral particles (as discussed in section 7.3.1), leading to an underestimate of the absolute number of these high energy particles, it is interesting to note that the model

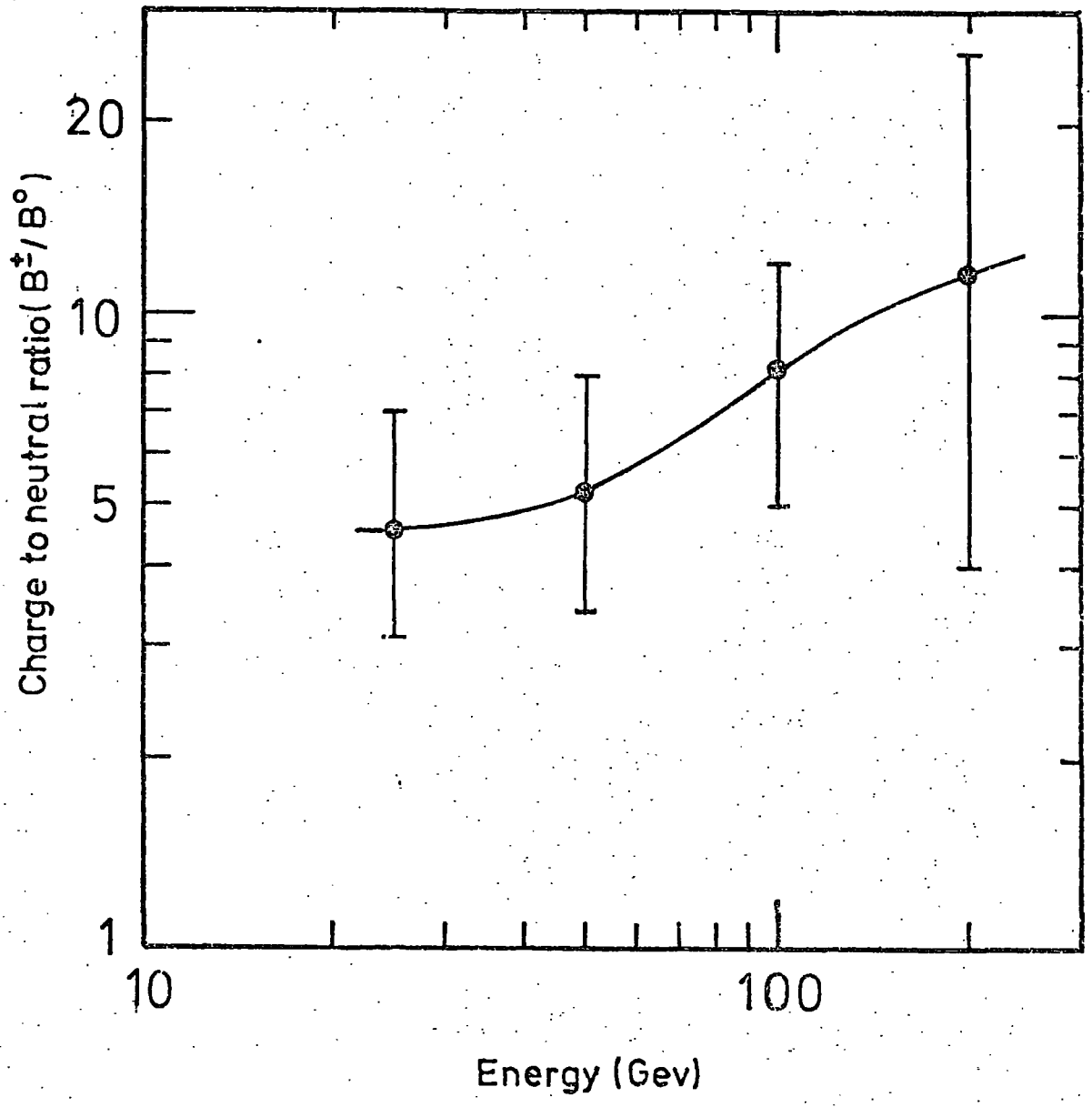


Figure 7.10 The ratio of charged particle bursts to neutral particle bursts observed below the iron absorber. No correction has been made for possible different interaction probabilities.

of Greider (1970) shows the same trend as that observed in this experiment - an increase in the ratio with increasing energy. The charge to neutral ratio has been deduced from Greider's simulation of a $10^7$GeV shower for the IDFB model. This predicts that the ratio for hadrons of energy greater than 10 GeV is ~ 6.4, increasing to ~ 13.6 for hadron energies greater than 1000 GeV. Since $N\bar{N}$ production principally enhances the numbers of low energy hadrons (Jabs, 1968), this is not unexpected. The model produced by Vatcha and Sreekantan (1973c), however, produces the opposite trend. This model, though, while including $N\bar{N}$ production has some rather novel features; for example, pion collisions are assumed to be partially inelastic and the interaction length of pions exhibits an energy dependence, decreasing from 130 g.cm$^{-2}$ at energies less than $10^{11}$eV to 70 g.cm$^{-2}$ at energies above $2.10^{11}$ eV. This latter effect will tend to degrade the pion spectrum more quickly. Clearly this is an area which requires detailed investigation.

One fact that does emerge from the results shown in Figure 7.10 is the low value of the ratio. Assuming the primary particles to be protons, Vatcha and Sreekantan (1973b) show that significant $N\bar{N}$ production is necessary to produce a charge to neutral ratio of this order. Even with 100% iron primaries, they conclude that $N\bar{N}$ production is necessary.

## 7.6 Conclusions

The energy spectra of charged and neutral hadrons in EAS of mean size $2.10^5$ have been obtained by the technique of measuring burst widths below thick iron and lead absorbers. The charged energy spectrum was related to overall shower characteristics by adopting a parameterisation of the form obtained by Kameda et.al. (1965).

The results obtained provide information on the nuclear-physical process occurring in EAS. In particular, it is necessary to assume the presence of significant baryon-antibaryon production in high energy collisions to account for the low value obtained for the ratio of charged

to neutral hadrons. There is a discrepancy in the energy dependence of this ratio found in the present experiment compared with that found by two previous experiments. This could be explained by the loss of high energy neutral hadrons which will occur close to the core of the shower, although the dependence found in this experiment is in agreement with predictions which include $N\bar{N}$ production. At sea-level there is little sensitivity to the mass composition of the primary particles, although the study of the fluctuations involved should yield information regarding the composition. This would require the monitoring not only of the hadronic component of the air shower, but also of the other components (Bradt and Rappaport, 1967 and Thielheim and Beiersdorf, 1969).

# CHAPTER 8

## SUMMARY AND DISCUSSION OF FUTURE WORK

A study of the particles close to the core of extensive air showers has been carried out in an attempt to investigate sub-nuclear structure and the nature of strong interactions at high energies.

(a) The search for quarks did not reveal their existence, even though, as was argued earlier, the cores of air showers are perhaps the most likely place for quarks to be found. An upper limit was placed on the flux of e/3 quarks selected by a local electron density trigger with $\Delta e \geqq 40\ m^{-2}$, of $8.0.10^{-11} cm^{-2} sec^{-1} st^{-1}$. At the time of the termination of this experiment, June 1973, this was the lowest intensity limit for e/3 quarks obtained by any group. The limit has since been depressed to $\leqq 4.0.10^{-11} cm^{-2} sec^{-1} st^{-1}$ by a group operating a 2.5 $m^2$ area cloud chamber (Hazen et.al., 1973).

Thus while the theoretical basis of the quark model is quite sound, continued attempts to detect free quarks have failed. Accelerator experiments to detect free quarks give null results. However experiments on deep inelastic lepton-hadron scattering appear to have confirmed that nucleons are composed of fundamental (?) point-like particles while electron-positron annihilation experiments produce results inconsistent with the naiive quark model. Possibly quarks do exist, but only in the bound state, as has been suggested recently by Kauffmann (Feynman, 1974). This requires a novel field of force such that the potential energy <u>increases</u> linearly with distance. An alternative solution is that quarks are bound so tightly that energies so far explored are insufficient to split the nucleons into their component parts.

Possible modifications to the flash tube chamber or its location were suggested in section 4.4. Since flash tubes are relatively inexpensive, it is conceivable that a very large area ($\sim 10\ m^2$) chamber

could be built, perhaps underground. Only in this way can intensities of the necessary order be investigated.

(b) It has been shown that the technique of measuring cascade widths below thick absorbers is a valid method of measuring the energy spectra of hadrons. Flash tubes again have an advantage over more conventional detectors in that large areas can be readily covered. The energy spectra of nuclear-active particles measured close to EAS cores have been used to derive information about strong interactions at very high energies.

At present, the experiment measuring the energy spectrum of unaccompanied hadrons in the near-vertical direction is continuing, in order that the energy of the "kink" found by Baruch et.al. (1973) may be investigated, enabling the measurements of Baruch et.al. to be checked.

In the longer term, a small air shower array is being constructed at Durham around the flash tube chamber and M.A.R.S., the solid iron muon spectrograph (e.g. Ayre et.al. 1972 a,b). When this is completed, shower size and core distance information will be available for each event. This will allow a more detailed study of hadrons in air showers to be made. As the chamber was primarily designed for use as a quark detector, several improvements could be made for the study of hadrons. Crossed flash tubes in the part of the chamber where charge determination is made would improve the resolution of neutral particle bursts. In addition, while the fluctuations associated with individual energy determinations are large with the present experimental arrangement ($\sim 100\%$), this is due mainly to the uncertainty in determining the depth of interaction of the incident particle. Thus a more suitable arrangement would be to have many layers of iron or lead with perhaps two layers of flash tubes below each layer of absorber. The energy should then be resolvable to better than 50% if the width is measured below each layer of absorber.

A feature which emerges from the operation of the flash tubes, using a long time delay before applying the high voltage pulse, is that multiple bursts which could not be resolved with the normal mode of operation of

the flash tube, can be seen as separate bursts at these long time delays (for example, see Plate 6.4 ). This could be useful in resolving bursts in the core of a shower, perhaps counting the total number of flash tubes which flash over a certain number of layers rather than defining a width to determine their energy.

Another application which presents itself is in the detection of highly ionising particles such as magnetic monopoles or Yock's sub-nuclear particles (see Chapter 3). The paths of these particles should be seen as high efficiency tracks at these long time delays, whereas normal tracks due to charge e particles will not be seen.

Finally, with the information provided by the air shower array, M.A.R.S. and flash tube chamber, it may be possible to make measurements on the fluctuations of the various components. This could provide information on the primary mass composition. In addition, fast timing measurements would allow the time delay spectrum of hadrons to be measured, providing an aid to particle identification.

# APPENDIX A

## THE DISTRIBUTION OF $N_f$ FOR BACKGROUND MUONS TRAVERSING THE FLASH TUBE CHAMBER

In order to calculate the muon background in the quark search, it is necessary to know how the number of flashes along a muon track ($N_f$) varies as a function of the time interval between the muon traversing the chamber and an air shower triggering the chamber.

Assuming muons traversing the chamber arrive randomly in time, the probability that a muon traversing the chamber a time $T_D$ before the master trigger has $N_f$ flashes along it's track can be obtained from the efficiency - time delay curve of Figure 2.10. The distribution predicted is shown in Figure A1. The curve has been normalised such that the total probability between $N_f$ = 22 and 77 is unity, $N_f$ = 22 being the minimum number of flashes for a track to be recognised efficiently against the background of spurious flashes, and $N_f$ = 77 being the maximum theoretical value.

In order to compare the form of this curve with experiment, the 1,046 events obtained in the single muon calibration run (section 2.5.1) were scanned, the in-geometry background tracks being measured. Now since the probability of two coherent muons causing a trigger is low it was assumed that in all events containing at least two in-geometry tracks with an angular separation of >5 degrees, the track with an $N_f$ value furthest from the mean of the single particle distribution for $T_D$ = 20 μs ($\overline{N}_f = 74.77 \pm 0.14$) was a background track.

The number of background tracks found was 16, to be compared with the expected number of 15.7. To compare the theoretical distribution of $N_f$ with this measured distribution, it is necessary to fold the width of the distribution of $N_f$ into the curve. The width ($\sigma N_f$) was evaluated from Figure 2.9. This new curve is also shown in Figure A1, the experimental

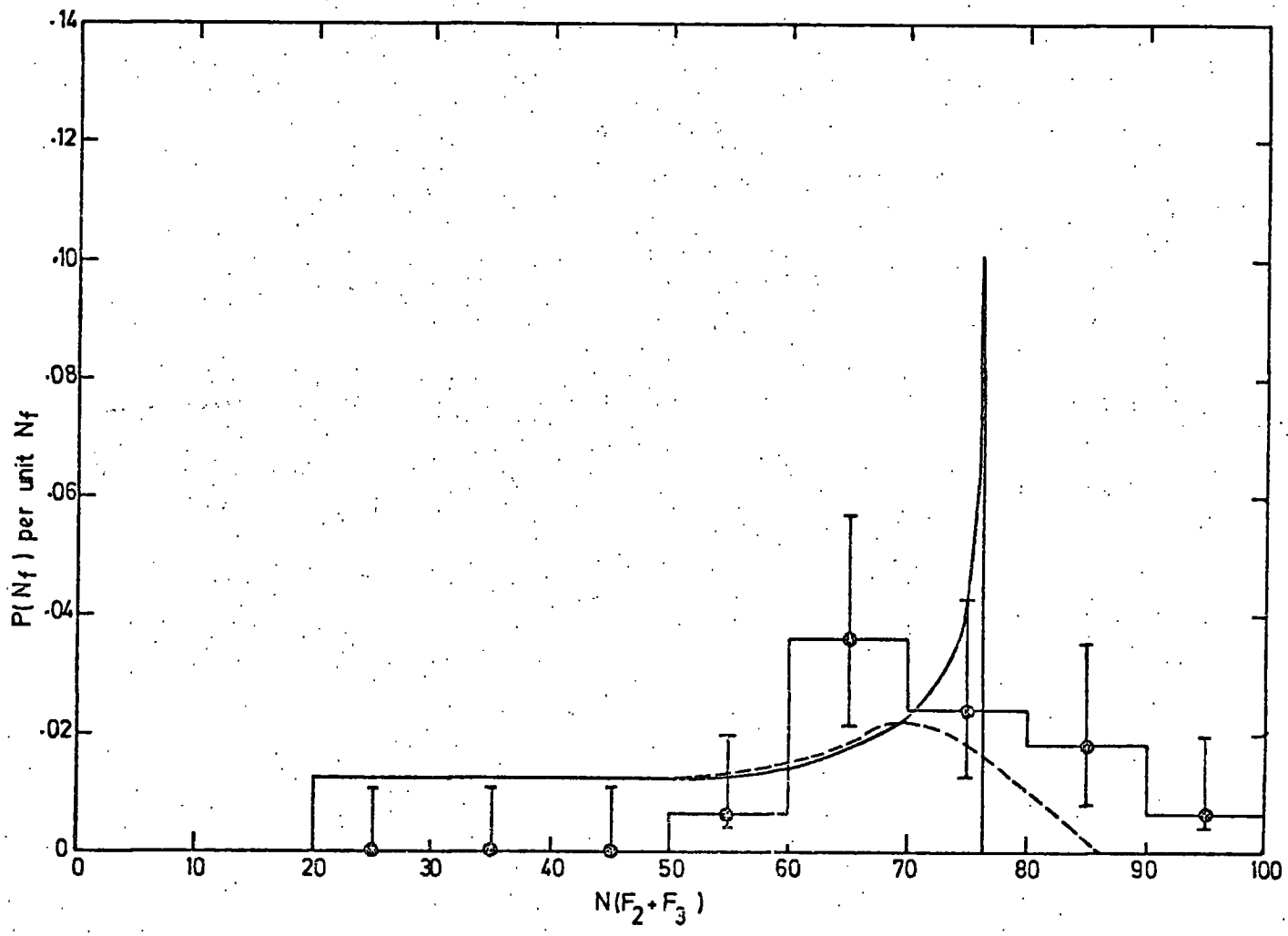


Figure A1 The distribution of N(F2+F3) for background muons. The full line shows the predicted variation. The dashed curve is the same but with the distribution of $N_f$ folded in. The histogram shows the experimental results.

distribution being included for comparison. It can be seen that the shapes of the distributions have approximately the same form, and agree within the statistical errors.

# APPENDIX B

## INVESTIGATION OF SOME PROPERTIES OF A "TRIGATRON" SPARK GAP

The operation of the triggering system for the flash tubes was described in section 2.2.2. Figures 2.4 and 2.5 show respectively the H.T. pulsing unit and the circuitry of the lumped delay line feeding the trigatron spark gap. A scale diagram of the spark gap itself is shown in Figure B.1.

It was found initially that in operation the voltage working range of the spark gap (that is the voltage range over which the gap could be triggered efficiently while at the same time not breaking down spontaneously) was narrow, and that after a short time in continuous operation the small changes in field due to slight pitting of the electrodes were sufficient to make the gap unstable. An attempt was thus made to extend the voltage working range of the spark gap.

A 5 volt square pulse was used to trigger the thyristor of Figure 2.4. Initially the transformer at the output of this stage gave a negative pulse to be fed onto the trigger pin of the spark gap, but it was arranged that trigger pulses of both polarities could be used.

The spontaneous breakdown potential for different separations of the main electrodes was measured, and is shown in Figure B.2. The triggering efficiency of the spark gap as a function of voltage was obtained next, by repeatedly applying a trigger pulse and determining the percentage of "successful" triggers. Results obtained with trigger pulses of both polarities are shown in Figure B.3(a). These results indicate the importance of the trigger pulse polarity, presumably due to the retarding field it produces. It can be seen from this figure, however, that for positive pulses there is a large range over which the spark gap triggers with reduced efficiency. This is due

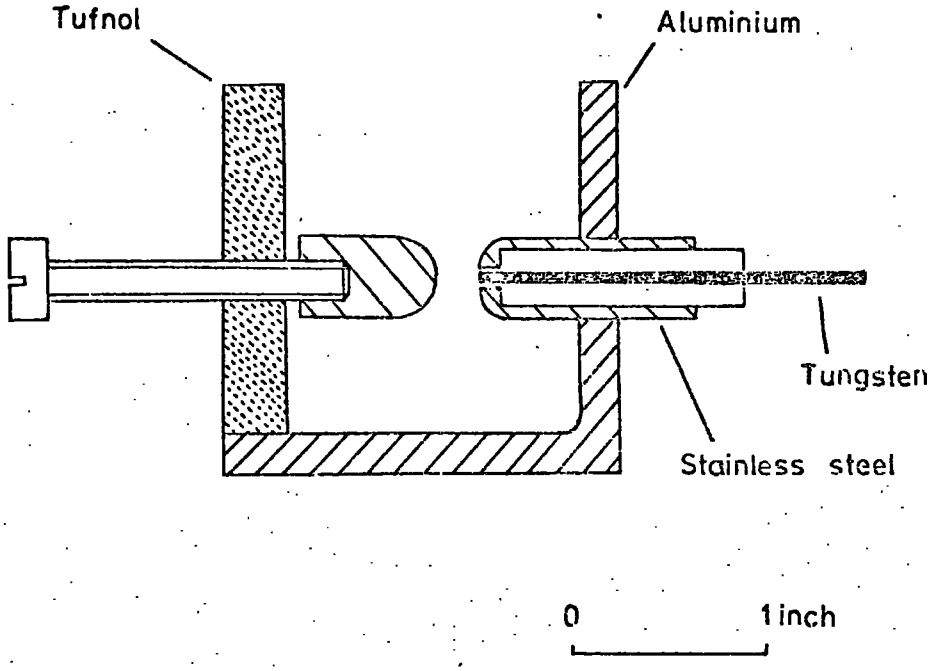


Figure B.1 Scale diagram of the triggered spark gap used in the measurements.

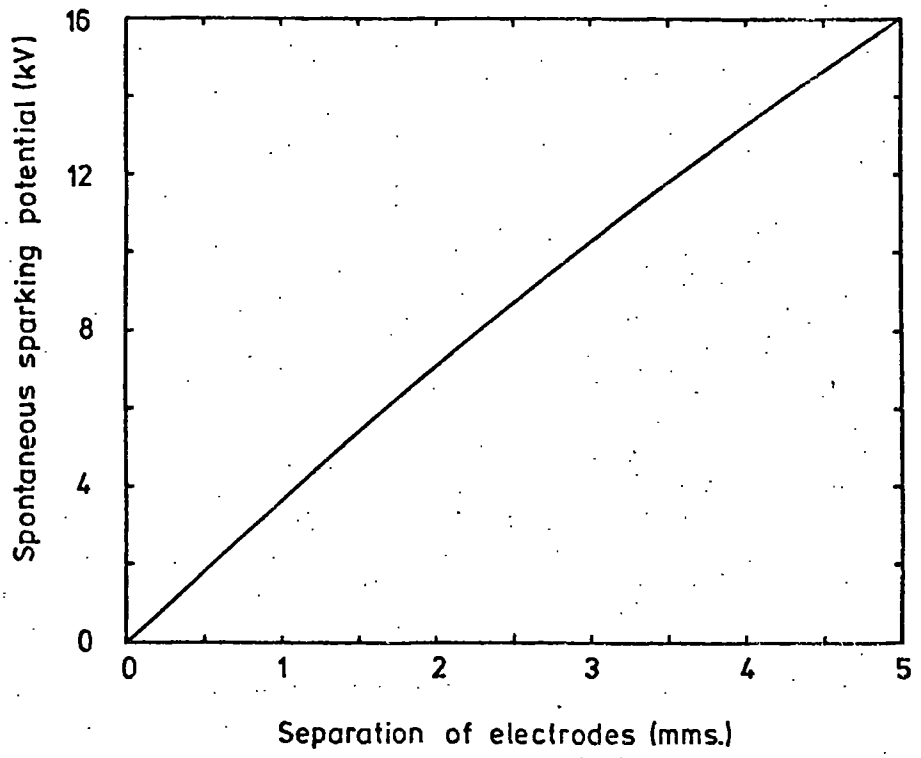


Figure B.2 The variation of the spontaneous breakdown potential with electrode separation. The curve represents the average behaviour of 5 spark gaps tested.

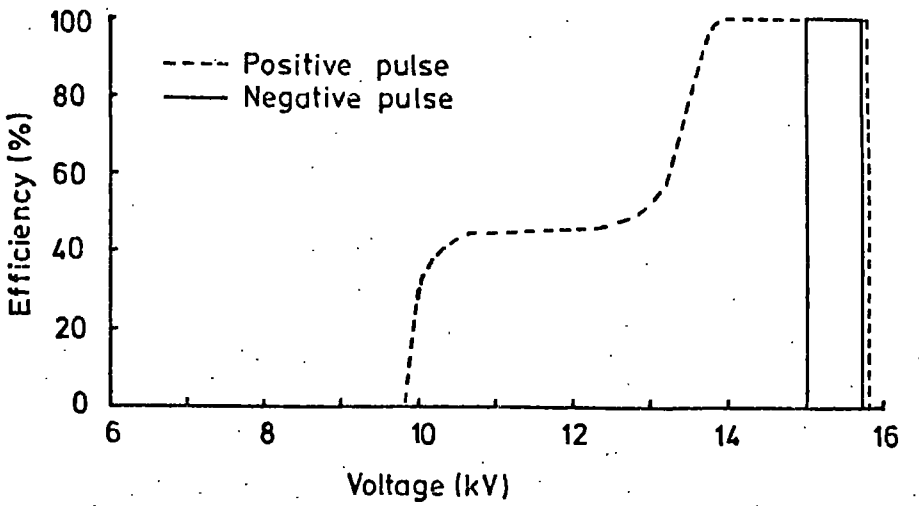


(a) Unshaped trigger electrode

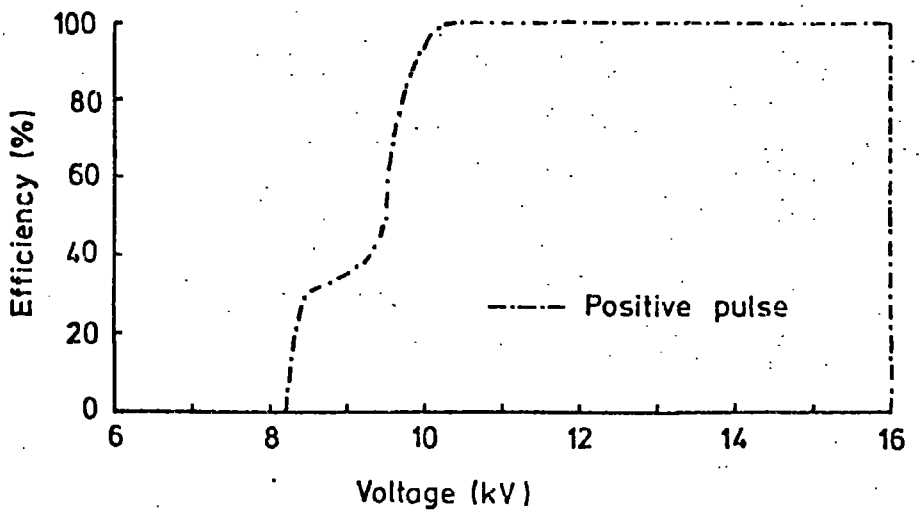


(b) Modified trigger electrode.

Figure B.3 The variation of triggering efficiency with applied voltage for different polarity trigger pulses, for the shaped and unshaped trigger electrode.

to variations in the position along the trigger electrode at which the trigger spark occurs.

It was found that the gap triggered most efficiently when the trigger spark occurred at the end of the electrode. This can be explained in terms of the photoelectrons produced by irradiation of the cathode. If the spark occurs inside the anode, the U.V. photons will be seen by the cathode with reduced intensity. In addition, Sletten and Lewis (1956) suggest that the ejection of a region of hot, low density gas into the main gap after the trigger spark has occurred is important in causing the main gap to break down. This would again be inhibited if the spark does not occur at the end of the trigger electrode.

To ensure that the spark did occur at the front of the trigger electrode, this electrode was shaped to produce a slightly conical form such that the largest cross-section was at the front, thus producing a shorter distance between the electrode and the anode at this point. With this arrangement a marked improvement was obtained. The result is shown in Figure B.3(b)

It was found that with the modification, and using a positive trigger pulse, the stability of the spark gap was greatly improved and could be used in continuous operation for longperiods of time.

# APPENDIX C

## MULTIPLE SCATTERING MEASUREMENTS ON COSMIC RAY MUON TRACKS

### C.1 Introduction

When charged particles pass through matter, small deflections occur due to electromagnetic interactions with the atoms of the medium. Because of the many deflections which occur in a small distance, the process can be considered to be continuous. The scattering probability is a function of the mass and velocity of the particle, hence if a mass is assumed for the scattering particle the momentum can be estimated, or conversely, if the momentum and range is known the mass can be estimated. The effect has been investigated by studying the tracks of 5283 unaccompanied muons traversing the flash tube chamber. Initially, 1046 events were obtained (as described in section 2.5.1) in connection with the quark search, but this was later increased to the present number to study the properties of these muon tracks.

### C.2 The Multiple Scattering Distribution of Muons

The R.M.S. projected angle of scattering of a charged particle traversing t radiation lengths of material is given by (Rossi, 1952)

$$\langle \vartheta \rangle = \frac{1}{2^{1/2}} \quad \frac{Kt^{1/2}}{p\beta c}$$

where K is a constant equal to 21 MeV, p is the particle momentum and $\beta c$ is the velocity of the particle. Now the multiply-scattered tracks were observed to approximate well to arcs of circles. Thus it was possible to define a sagitta d as the maximum distance between the track and a chord joining the ends of the track at the top of F2 and the bottom of F3 (see Figure 2.1). For the 5283 tracks photographed, the sagitta d was measured by projecting the negative of the film obtained onto a scanning table. The smallest measurable value of d corresponded to a

distance in real space of 2 cms. The distribution of d obtained is shown in Figure C.1. The dashed histogram in this figure is the theoretical prediction. This was obtained by simulating the trajectories of muons through the absorber represented by the 96 layers of flash tubes (and associated aluminium electrodes) of F2+F3. The Monte Carlo technique was used, the sensitive volume being divided into thin layers, the spaces between the glass (mainly neon gas) were allowed for geometrically, though no scattering was considered to take place in the gas. The scattering formula given above was used, a constant energy loss being assumed. The sagitta distributions were obtained for different muon momenta and then folded into the momentum spectrum of Hayman and Wolfendale (1962) for muons at sea-level. The distribution was broadened by including a measuring error of 1.1 cms., the final result being the dashed histogram of Figure C.1. It can be seen that the agreement is good.

C.3 The Mass Distribution of Stopping Particles

Of the 5283 tracks recorded, 27 were produced by stopping particles (presumed to be muons) exhibiting noticeable multiple scattering along their track, which then decayed with the emission of a decay electron. Since the range of these particles can be measured, it is possible to estimate their mass.

Consider the R.M.S. scattering angle to be given by the formula of section C.2. The energy loss of a low energy charged particle is given by

$$-\frac{dE}{dx} = \frac{1}{\beta^2} f(\beta)$$

writing $E = Mc^2(\gamma-1)$ and integrating, the range is given by

$$R = A\,Mc^2\,g(\beta) \text{ where A is a constant}$$

writing $\frac{R}{p\beta c} = \frac{A\,Mc^2 g(\beta)}{\gamma\beta^2\,Mc^2} = \frac{Ag(\beta)}{2}$ - which is independent

of mass and depends only on $\beta$.

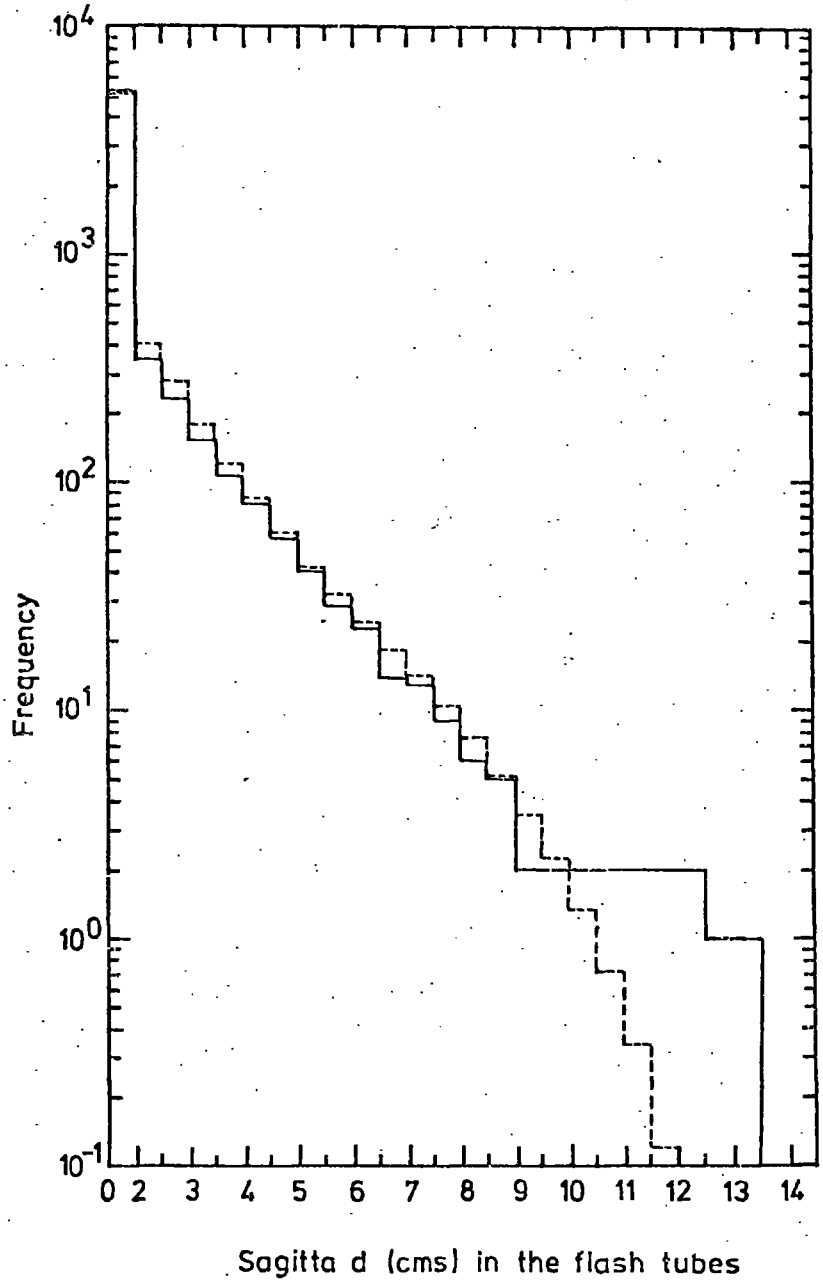


Figure C.1 Distribution of sagitta measured for 5283 muon tracks. The dashed histogram shows the predicted distribution.

Figure C.2 shows this dependence, evaluated from the range-energy tables of Serre (1967) for aluminium (similar to glass in atomic number). From this curve it can be seen that once $R/p\beta c$ is known, $\beta$ can be evaluated and hence the mass of the particle can be found from

$$Mc^2 = p\beta c \frac{(1-\beta^2)^{1/2}}{\beta^2}$$

To evaluate $p\beta c$ for the 27 stopping particles, it was assumed that the trajectories of the multiply-scattered muons formed arcs of circles, a good approximation until close to the end of their range. Then, using the notation of section C.2

$$\theta = \frac{8}{l} \cdot d$$

Thus by measuring d, l and the corresponding value of t for a part of the track in F2+F3, and identifying $\theta$ with $\theta$, it was possible using the formula of section C.2 to obtain the $p\beta c$ value for the middle of the arc taken. Then, measuring the range from this point to the stopping point of the track, it was possible to obtain a mass estimate as above. The 27 points obtained are shown on a scatter plot in Figure C.3. Also shown are predicted curves for different particles. It can be seen that most of the stopping particles lie close to the muon curve, as expected, although three events with apparent mass less than 10 electron masses were obtained. These could be interpreted as pions, in which a large angle nuclear scatter is superimposed on the continuous multiple scattering, causing an underestimate of $p\beta c$ and hence a spuriously low mass value. The maximum value of $p\beta c$ measurable in F2+F3 was 710 MeV.

The curve in Figure C3 labelled 10 Mp corresponds to the expected position for a massive particle of ten proton masses. It suggests that the method, with modifications, might be used in a search for massive particles. Possibly alternate layers of absorber and flash tubes could be used to extend the range of $p\beta c$ that can be investigated.

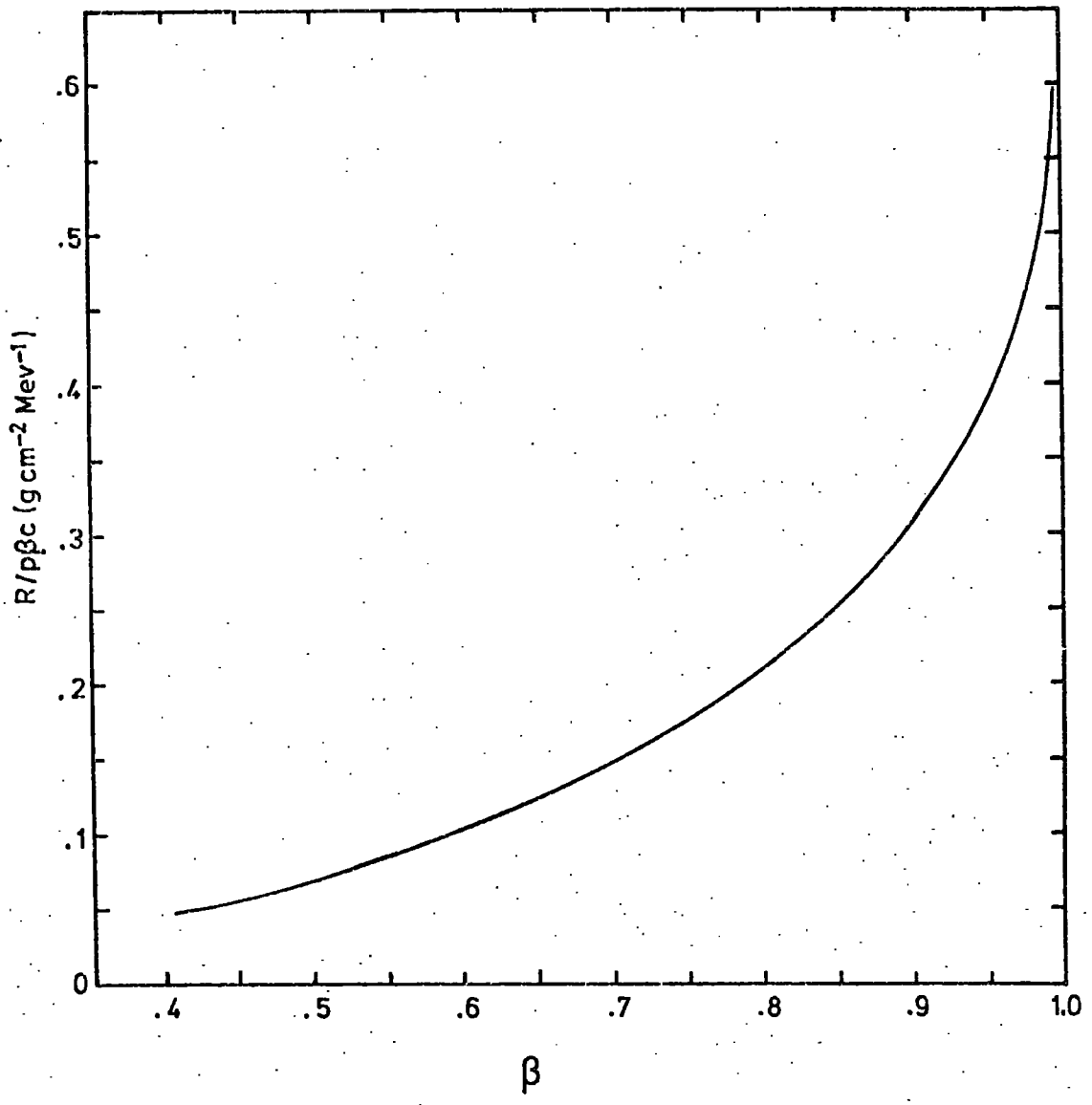


Figure C.2 $R/p\beta c - \beta$ curve calculated for aluminium. The curve is valid for any particle rest mass and is also closely valid for glass, which has a similar average Z and A to aluminium.

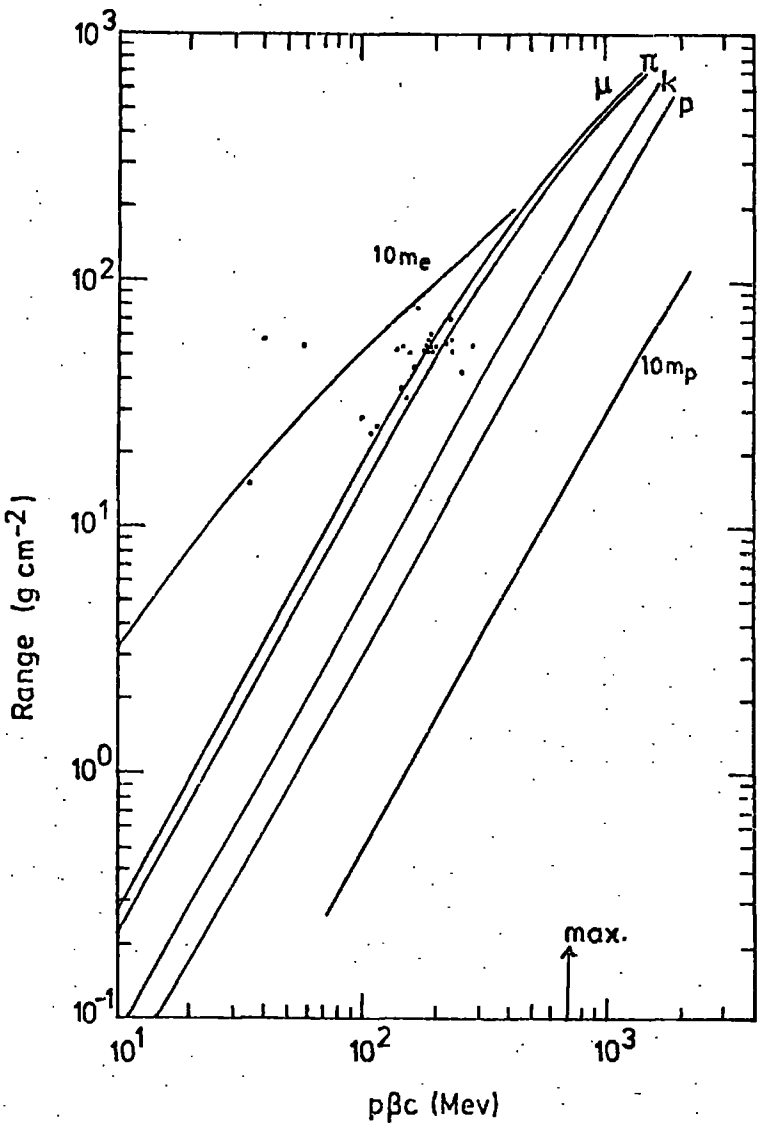


Figure C.3 The range - pβc plot for the 27 stopping particles. The full curves represent constant masses for 10 me, $\mu$, $\pi$, K, p and 10 mp particles.

## ACKNOWLEDGMENTS

The author wishes to thank Professors G.D. Rochester, F.R.S. and A.W. Wolfendale for the provision of the facilities for this work, and for their interest and support.

He is extremely grateful to his supervisor, Dr. F. Ashton, for his continued help and guidance throughout the work.

Many members of the Cosmic Ray Research Group, staff and research students, are thanked for helpful and stimulating discussions, and especially Mr. A. Parvaresh and Mr. A.J. Saleh for their friendly assistance.

The technical staff of the Physics Department, in particular Mr. W. Leslie, Mr. M. Lee, Mr. K. Tindale and Mr. J. Storey are thanked for their willing help, and Mrs.A. Gregory for her invaluable help in drawing many of the diagrams for this thesis.

The Computer Unit is thanked for the provision of computing facilities.

The author is grateful to Mr. S. Jobling for her patient work in typing this thesis.

Finally, the Science Research Council is thanked for the provision of a Research Studentship.

## REFERENCES

PICCR = Proceedings. Int. Conf. Cosmic Rays

Adair, R. and Price, N., (1966), Phys. Rev. 142, 844.

Adair, R. and Kasha, H., (1969), Phys. Rev. Lett., 23, 1355.

Alcock, C.R., Chisholm, A., Tyndel, M. and Yock, P.C.M., (1974), Nucl. Inst. and Meth., 115, 245.

Alexander, G., and Yekutieli, G., (1961), Nuovo Cim., 19, 103.

Allaby, J.V. et.al. (1969), Nuovo Cim., 64A, 75.

Antipov, Yu. M. et.al. (1969), Phys. Lett., 29B 245.

Ashton, F., Coats, R.B., Kelly, G.N., Simpson, D.A., Smith, N.I. and Takahashi, T., (1967) PICCR, Calgary, (1968) Canad. J. Phys., 46, S1125.

Ashton, F., Coats, R.B., Kelly, G.N., Simpson, D.A., Smith, N.I. and Tanahashi, T., (1968), J. Phys. A., 1,569.

Ashton, F., Edwards, H.J. and Kelly, G.N., (1969), Phys. Lett., 29B, 249.

Ashton, F., Breare, J.M., Holroyd, F.W., Tsuji, K. and Wolfendale, A.W., (1971), Lett. Nuovo Cim., 2, 707.

Ashton, F., Coats, R.B., King, J., Tsuji, K. and Wolfendale, A.W., (1971), J. Phys. A, 4, 895.

Ashton, F., (1973a), Cosmic Rays at Ground Level, Ed. Wolfendale, A.W., (Inst. Phys).

Ashton, F., (1973b), unpublished.

Ashton, F., Cooper, D.A., Parvaresh, A. and Saleh, A.J., (1973a), J. Phys. A, 6, 577.

Ashton, F., et.al., (1973b), PICCR, Denver, 3, 2096.

Ashton F., et.al., (1973c) PICCR, Denver, 4 2610.

Ashton, F., et.al., (1973d), PICCR, Denver, 4 2993.

Ashton, F., et.al., (1973e), PICCR, Denver, 4, 2997.

Ashton, F., et.al. (1973f), PICCR, Denver, 4, 3000.

Ashton, F., et.al., (1973g) PICCR, Denver, 4, 3003.

Ashton, F., et.al., (1973h), PICCR, Denver, 3, 2032

Auger, P., Ehrenfest Jr., Maze, R., Dandin, J., Robley and Freon, A., (1939), Rev. Mod. Phys., 11, 288.

Ayre,C.A., Hamdan,M.A., Hume,C.J., Stubbs,F.W., Thompson,M.G., Wells,S.C. and Whalley,M.R., (1972), Nucl. Inst. and Meth, 102,19-44.

Bacci,C., et al., (1972),Laboratori Nazionali di Frascati rep. No. LNF 72/68 (unpublished).

Bacry, H., Nuyts, J. and Van Hove, L., (1964), Phys. Lett., 9, 121.

Barger, V., (1974), Phys. Lett., 49B, 43.

Barish, B.C., et.al., (1973), Phys. Rev. Lett., 31, 566.

Barnavelli, T.T., Bibilashviti, M.F., Grubelashviti, G.A., Dzhavrishviti, A.K., Kazarov, R.E., Kuridze, R.V. and Khaldeeva, I.V., (1965), Bull. Acad. Sci. U.S.S.R., (Phys.Ser.), 28, 1782.

Bartoli, B., et.al., (1972), Phys. Rev., D6, 2374.

Baruch, J.E.F., Brooke, G. and Kellerman, E.W., (1973), Nature Phys. Sci., Lett., 242, 6.

Becklin, E.E., and Earl, J.A., (1964), Phys. Rev., 136B, 237.

Belenkji, S.Z. and Landau, L.D., (1956), Nuovo. Cim. Suppl., 3, 15.

Bennett, S., Delvaille, J., Greisen, K., Kendziorski, F., (1962), J. Phys. Soc. Japan, 17, 196.

Bennett, W.R., (1966), Phys. Rev. Lett., 17, 1196

Benevenuti, et.al., (1973), Phys. Rev. Lett., 30, 1084.

Bertin, A., et.al., (1972), Phys. Lett., 38B, 260

Bingham, H.H., et.al., (1964), Phys. Lett., 9, 201.

Bjorken, J.D. and Glashow, S.L., (1964), Phys. Lett., 11, 255.

Bjorken, J.D., (1969), Phys. Rev., 179, 1547.

Bjorken, J.D., (1973), SLAC - pub - 1318.

Blum, W., et.al., (1964), Phys. Rev. Lett., 13, 353.

Bohm, E., et.al., (1968), Canad. J.Phys., 46, S50.

Bott-Bodenhausen, M., et.al., (1972), Phys. Lett., 40B, 693.

Bradt, H.V. and Rappaport, S.A., (1967), Phys. Rev., 164, 1567.

Brooke, G., Hayman, P.J., Kamiya, Y. and Wolfendale, A.W., (1964), Proc. Phys. Soc., 83, 853.

Bussian, A.E., (1974), Phys. Rev., 9, 1384.

Chanowitz, M.S. and Drell, S.D., (1973), Phys. Rev. Lett., 30, 807.

Chatterjee, B.K., Murthy, G.T., Naranen, S., Sreekantan, B.V., Srinivasa Rao, M.V., Tonwar, S.C. and Vatcha, R.H., (1968), Canad. J. Phys., 46, S136.

Chin, S., Hanayama, A.,Hara, T., Higashi, S., and Tsuji, K.,(1971), Nuovo Cim., 2A,419.

Chukpa, W., Schiffer,J.,and Stevens,C., (1966), Phys. Rev. Lett.,17,60.

Clark, A.F., Ernst, R.D., Fin, H.F., Griffith, C.F., Hansen, N.E. and Smith, D.E., (1973), PICCR, Denver, 3, 2090.

Coats, R.B., (1967), Ph.D. thesis, Durham, unpublished.
Cocconi, G., Handbuck der Physik, Vol. XLVI/I, 215-271.
Cocconi, G., (1965), PICCR, London, 2, 616.

Cocconi, G., Koester, L.S. and Perkins, D.H., (1961), UCRL High Energy Physics Study Seminars, 28, (UCID - 1444).

Cook, D.D., De Pasquali, G., Framfelder, H., Peacock, R.N., Steinrisser, F. and Wattenburg, A., (1969), Phys. Rev., 188, 2092.

Cosme, G., et.al., (1972), Phys. Lett., 40B, 685.

Cowan, E.W., and Matthews, K., (1971), Phys. Rev., D4, 37.

Cowsik, R., (1965), PICCR, London, 2, 656.

Crawford, D.F. and Messel, H., (1965), Nucl. Phys., 61, 145.

Crispin, A. and Fowler, G.N., (1970), Rev. Mod. Phys., 42, 290.

Dakin, J.T., Feldman, G.J. Martin, F., Perl, M.L. and Toner, T., (1973), Phys. Rev. Lett., 31, 786.

Dardo, M., Penengo, P. and Sitte, K., (1968), Nuovo Cim., 58A, 59.

Dardo, M., Navarra, G., Penengo, P. and Sitte, K., (1972), Nuovo Cim., 9A, 319.

Dorfan, D.E., Eades, J., Lederman, L.M., Lee, W. and Ting, C.N., (1965), Phys. Rev. Lett., 14, 999.

Eichten, T., et.al., (1973), Phys. Lett., 46B, 281.

Evans, G.R., Fancey, N.E., Muir, J. and Watson, A.A., (1971/72), Proc. R.S.E.(A), 70, 143.

Elmore, W.C., and Sands, M., (1949), Electronics, (McGraw Hill).

Fermi, E., and Yang C.N., (1949), Phys. Rev., 76, 1739.

Feynman, R.P., (1969), Phys. Rev. Lett., 23, 1415.

Feynman, R.P., (1974), Science, 183, 601.

Fowler, P.H., Thorne, R.T. and Muzumdar, A.P., (1973), PICCR, Denver, 5, 3239.

Franzini, P., Leontic, B., Rahm, D., Samios, N. and Schultz, M., (1965), Phys. Rev. Lett., 14, 196.

Franzini, P. and Shulman, S., (1968), Phys.Rev.Lett., 21, 1013.

Fraunfelder, H., Kruse, U.E., and Sard, R.D., (1970), Phys. Rev. Lett., 24, 33.

Fritze, R., Samorski, M., Stauhert, R., Trumper, J., Aschenbach, B. and Bohm, E., (1970), Acta Phys. Acad. Sci. Hungaricae, 29, suppl.3, 439.

Galper, A.M., et.al., (1970), Sov. J. Nucl. Phys., 10, 193.

Gellman, M., (1953), Phys. Rev., 92, 833.

Gellman, M., (1962), Phys. Rev., 125, 1067.

Gellman, M., (1964), Phys.Lett., 8, 214.

Goldberg, H. and Ne'eman, (1963), Nuovo Cim, 27, 1.

Goldhaber, M., (1965), Phys. Rev., 101, 433.

Goorevitch, L., and Peak, L.S., (1973), PICCR, Denver, 4, 2617.

Greider, P.K.F., (1970), Inst. Nucl. Study, Tokyo, pub INS J 125.

Greider, P.K.F.,(1972), Nuovo Cim., 7A, 867.

Greisen, K., (1956), Progress in Cosmic Ray Physics, vol.3, (Amsterdam, North Holland).

Greisen, K., (1960), Ann. Rev. Nucl. Sci., 10, 63,

Grilli, M., et.al., (1973), Nuovo Cim., 13A, 593.

Gronau, M., Ravndal, F. and Zarmi, Y., (1973), Nucl. Phys., B51, 611.

Hagedorn, R., (1968), Suppl. Nuovo Cim., 6, 311.

Han, M.Y. and Nambu, Y., (1965), Phys. Rev., 139B, 1006

Hansen, J.S., (1974), Ph.D. thesis, Durham (in preparation)

Hayakawa, S., (1969), Cosmic Rays (Wiley Interscience).

Hayman, P.J. andWolfendale, A.W., (1962), Proc. Phys. Soc., 80, 710.

Hazen, W.E., (1971), Phys. Rev. Lett., 26, 582.

Hazen, W.E., Hodson, A.L., Winterstein, D. and Keller, O., (1973), PICCR, 3, 2087.

Hebard, A.F. andFairbank, W.M., (1970), Proc. Inst. Conf. Low Energy Phys., 855.

Heutch, C.A. and Prescott, C.Y., (1964), Phys. Rev., 135B, 772.

Hillas, M., (1970), Acta. Phys. Hung., 29, suppl.3, 355.

Ikeda, M., Ogawa, S. and Ohnuki, Y., (1959), Prog. Theor, Phys., 22,715.

Ivanenko, I.P. and Samosudov, B.E., (1959), Sov.Phys.JETP, 35(8), 884.

Ivanenko, I.P. and Samosudov, B.E., (1967a), Bull.Acad.Sci., U.S.S.R., (Phys.Ser.), 30, 1722.

Ivanenko, I.P. and Samosudov, B.E., (1967b), Sov.J.Nucl.Phys., 5 ,442.

Jabs, A., (1968), Z.Physik, 212, 222.

Johnson, E.W., (1969), Ph.D. thesis (Univ. of Michigan).

Jones, W.V., (1969a) Phys. Rev., 187, 1868.

Jones, W.V., (1969b), PICCR, Budapest, Acta Physica Acad. Sci. Hungaricae, (1970), 29, supp. 4, 513.

Jones, L.W., (1970), Symmetries and Quark Models, Ed. R.Chand, (Gordon and Breach).

Jones, L.W., (1971), PICCR, Hobart, Rapporteur paper.

Kameda, T., Maeda, T., Oda, H. and Sugihara, T., (1965), PICCR, London, 2, 681.

Kasha, H., Larsen, R.C., Leipuner, L.B. and Adair, R.K., (1968), Phys. Rev. Lett., 20, 217.

Kelly, G.N., (1969), Ph.D. thesis, University of Durham, (unpublished).

Kiraly, P. and Wolfendale, A.W., (1970), Phys. Lett., 31B, 410.

Kokkedee, J.J.J., (1969), The Quark Model, (Benjamin, New York)

Kurdadze, L.M., et.al. (1972), Phys.Lett., 42B, 515.

Kurti, J. and Weisskopf, V.F., (1971), Phys. Rev., D4, 3418.

Leacock, R.A., Beavers, W.I. and Daub, C.T., (1968), Ap.J., 151, 1179.

Leipuner, L.B., Chu, W.T., Larsen, R.C. and Adair, R.K., (1964), Phys. Rev.Lett., 12, 423.

Lipkin, H.J., (1968), Proc. 5th Coral Gables Conf. on Symmetries at High Energies (Benjamin New York), 261.

Lipkin, H.J., (1973), Phys. Reports, 8C, 175.

Litke, A., et.al., (1973), Phys. Rev. Lett., 30, 1189.

Lloyd, J.L., (1960), Proc. Phys. Soc., 75, 387.

Lovati, A., Mura, A., Succi, C. and Tagliaferri, G., (1954), Nuovo Cim., 12, 526.

Maksimenko, V.M., Sisakyan, I.N., Feinberg, E.L. and Chernavsky, D.S., (1966), Sov. Phys. - JETP Lett., 3, 214.

McCusker, C.B.A. and Cairns, I., (1969), Phys.Rev.Lett., 23, 658.

Messel, H. and Crawford, D., (1965), - see Crawford, D. and Messel, H., (1965).

Messel, H. and Crawford, D(1970), Tables, (Oxford, Pergamon).

Miller, G., et.al. (1972), Phys.Rev., D5, 528.

Morpurgo, G., (1967), Acta Phys. Hung., 22, 105.

Muller, D., (1972), Phys. Rev., 5, 2677.

Nagel, H.H., (1965), Z. Physik, 186, 319.

Nakato, T. and Nishijima, K., (1953), Prog. Theor. Phys., 10, 581.

Nam, R.A., Nikolski, S.I., Pavijutchenko, V.P., Sokolovsky, V.I. and Yakovlev, V.I., (1971) PICCR, Hobart, 2259.

Nash, T., et.al., (1974), Phys. Rev. Lett., 32, 858.

Ne'eman, Y. (1961), Nucl. Phys., 26, 222.

Nikolski, S.I., (1967), Sov. Phys. JETP, 24, 535.

Nir, A., (1967), Phys. Rev. Lett., 19, 336.

Nishimura, J. and Kamata, K., (1952), Prog.Theor.Phys., 1, 185.

Pal, Y. and Peters, B., (1964), Mat.Fys.Medd.Dan.Vid.Selsk., 33, No.15.

Pinkeu, K. and Thompson, K.V., (1966), Rev.Sci.Inst., 37, 302.

Rahm, D.C. and Louttit, R.I., (1970), Phys.Rev.Lett., 24, 279.

Rank, D.M., (1968), Phys.Rev., 176, 1635.

Rochester, G.D. and Butler, C.C., (1947), Nature, 160, 855.

Rossi, B., (1932), Phys. Z., 33, 304.

Rossi, B., (1933a), Z.Phys., 82, 151.

Rossi, B., (1933b), Nature, 132, 173.

Rossi, B., (1952), High Energy Particles, (Prentice-Hall).

Sakata, S., (1956), Prog.Theor.Phys., 16, 686 (L).

Schwinger, J., (1968), Phys.Rev., 173, 1536.

Serre, C., (1967), CERN report, 67-5.

Sinanoglu, O., Skutnick, B. and Tousey, R., (1966), Phys.Rev.Lett., 17, 785.

Sitte, K., (1970), Suppl.Nuovo Cim., 6, 866.

Sletton, and Lewis, (1956), I.E.E. Monograph No. 193M, 54.

Squires, E.J., (1970), Bull.Inst.Math., 7

Tanahashi, G., (1965), Proc.Phys.Soc. Japan, 20 883.

Thielheim, K.O. and Beiersdorf, R., (1969), Acta. Phys. Acad. Sci. Hung., 29, suppl. 3, 519.

Thielheim, K.O. and Zollner, R., (1972), J.Phys. A., 5, 1054.

Thom, H., (1964), Phys. Rev., 136, B447.

Tonwar, S.C. and Sreekantan, B.V., (1971), J.Phys. A, 4, 868.

Tonwar S.C., Naranan, S. and Sreekantan, B.V., (1971a), PICCR, Hobart, 3, 1171.

Tonwar, S.C., Sreekantan, B.V. and Vatcha R.H., (1973), PICCR, Denver, 4, 2616 - see Ramana Murthy, P.V., (1973), PICCR, Denver, 5, 3668.

Turver, K.E., (1973), Cosmic Rays at Ground Level, Ed. Wolfendale, A.W., (Inst. Phys.)

Vainshtein, L.A. and Pikel'ner, S.B., (1966), Zh.Eksper.Teor.Fiz.Pis'me, 4, 307.

Vatcha, R.H., Sreekantan, B.V. andTonwar, S.C. (1972), J.Phys. A, 5,859

Vatcha, R.H. and Sreekantan, B.V., (1973a), J.Phys.A, 6, 1050.

Vatcha, R.H. and Sreekantan, B.V., (1973b), J.Phys.A, 6, 1067.

Vatcha, R.H.and Sreekantan, B.V., (1973c), J.Phys.A, 6, 1078

Volkel, U. (1965), DESY report 6516.

Wazed, A., (1965), Nuovo Cim., 292.

Wdowczyk, J., (1973), Cosmic Rays at Ground Level, Ed. Wolfendale, A.W., (Inst. Phys.).

Yock, P.C.M., (1973), Ann.Phys., 82, 449.

Yock, P.C.M., (1974), 17th Int. Conf. High Energy Phys,(session B6.)

Zel'dovitch, Y.B., (1965), Sov. Phys. Usp., 8, 489.

Zerby, C.D. and Moran, H.S., (1963), J.Appl.Phys., 34, 2445.

Zweig, G., (1965), Symmetries in Elementary Particle Physics, (Acad. Press, New York), 192.